DEFECTS AND OXYGEN VACANCIES TAILORED PROPERTIES OF 4d CATIONS DOPED CeO_2 NANOPARTICLES

A

Thesis

Submitted to the

UNIVERSITY OF KOTA

In the Partial Fulfillment of the Requirements for the

Award of the Degree of

DOCTOR OF PHILOSOPHY

in

Physics

under the

Faculty of Science

Submitted by

Kiran Mahavar

Registration No.: RS/2080/19

Under the Supervision of

Dr. Saurabh Dalela

Associate Professor

Department of Pure & Applied Physics

UNIVERSITY OF KOTA
KOTA (RAJASTHAN)-324005
INDIA

July, 2025

Dr. Saurabh Dalela
Ph.D.(Material Science)
Associate Professor

Ref. No.- F.()/Phys/UOK/2025/……
Date: ……..

TELEFAX: +91-744-2471-038
E-mail: sdalela@uok.ac.in
Website: www.uok.ac.in

Department of Pure & Applied Physics
University of Kota, Kota
M.B.S. Marg, Kabir Circle, Kota

CERTIFICATE

I feel great pleasure in certifying that the Ph.D. thesis entitled "Defects and Oxygen Vacancies Tailored Properties of 4d Cations Doped CeO_2 Nanoparticles" **submitted by** Mrs. Kiran Mahavar **to the University of Kota in the partial fulfilment of the requirements for the award of the degree of Doctor of Philosophy is based on the research work carried out under my guidance.**

She has completed the following requirements as per UGC regulations and researchordinance of the University:

(a) Satisfactory Completion of the Ph.D. Course Work.

(b) Submission of Half Yearly Progress Reports.

(c) Fulfilment of residential requirement of the Research Centre (*Minimum 200 Days*).

(d) Presentation of research work before the Departmental Committee.

(e) Publication of at least one research paper in the referred research journal of nationaland international repute.

(f) Two paper presentations in the Conferences/ Seminars.

I recommend the submission of the Ph.D. thesis and certify that it is fit to be evaluated by the examiners.

Date: **Dr. SAURABH DALELA**

Place:

शोध निदेशालय
कोटा विश्वविद्यालय
एम.बी.एस. मार्ग, कोटा (राजस्थान)
324005

Directorate of Research
University of Kota
M.B.S. Marg, Kota (Rajasthan) - 3240005
Phone No.: 0744-2471037

DECLARATION

Mrs. Kiran Mahavar hereby certify that the research work presented in my Ph.D. thesis entitled **"Defects and Oxygen Vacancies Tailored Properties of 4d Cations Doped CeO_2 Nanoparticles"** Which is carried out by me under the supervision of **Dr. Saurabh Dalela** and submitted in the partial fulfilment of the requirement for the award of the degree of Doctor of Philosophy of the University of Kota, represents my ideas in my own words and where others' ideas or words have been included in this thesis, I have adequately cited and referenced the original sources.

The work presented in this thesis has not been submitted elsewhere for the award of any degree or diploma from any other institution or university in India or abroad. I declare that I have adhered to all the principles of academic honesty and integrity and have not misrepresented or fabricated or falsified any idea / data / fact / source in my submission.

I understand that any violation of the above will cause for disciplinary action by the University and can also evoke penal action from the sources which have thus not been properly cited or from whom proper permission has not been taken when needed.

Date: **Mrs. Kiran Mahavar**

Place:

This is to certify that the above statement made by **Mrs. Kiran Mahavar** (Registration Number **RS/2080/19**) is correct to the best of my knowledge.

Date:
Place:

Dr. Saurabh Dalela
Associate Professor
Department of Pure & Applied Physics
University of Kota, Kota

शोध निदेशालय
कोटा विश्वविद्यालय
एम.बी.एस. मार्ग, कोटा (राजस्थान)
324005

Directorate of Research
University of Kota
M.B.S. Marg, Kota (Rajasthan) - 3240005
Phone No.: 0744-2471037

ANTI-PLAGIARISM CERTIFICATE

It is certified that PhD Thesis entitled, **"Defects and Oxygen Vacancies Tailored Properties of 4d Cations Doped CeO_2 Nanoparticles"** submitted by **Mrs. Kiran Mahavar** has been examined by us with the following anti-plagiarism tools.

We undertake the follows:

a. Thesis has significant new work/knowledge as compared already published or are under consideration to be published elsewhere. No sentence, equation, diagram, table, paragraph or section has been copied verbatim from previous work unless it is placed under quotation mark and duly referenced.

b. The work presented is original and own work of the author (i.e. there is no plagiarism). No ideas, processes, results or words of the others have been presented as author's own work.

c. There is no fabrication of data or results which has been compiled and analyzed.

d. There is no falsification by manipulating research materials, equipment or processes, or changing or omitting data or results such that the research is not accurately represented in the research record.

e. The thesis has been checked using ***DrillBit*** tool/software and found within limits as per UGC plagiarism policy and instructions issued from time to time. Report is also enclosed along with this Ph.D. thesis.

Date: **Mrs. Kiran Mahavar**
Place:

Dr. Saurabh Dalela
Associate Professor
Department of Pure & Applied Physics
University of Kota, Kota

DrillBit

The Report is Generated by DrillBit Plagiarism Detection Software

Submission Information

Author Name	Kiran Mahawar
Title	Defects and Oxygen Vacancies Tailored Properties of 4d Cations Doped CeO2 Nanoparticles
Paper/Submission ID	4106520
Submitted by	sdalela@uok.ac.in
Submission Date	2025-07-18 16:46:19
Total Pages, Total Words	153, 41836
Document type	Thesis

Result Information

Similarity **6 %**

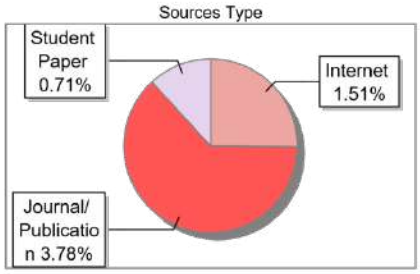

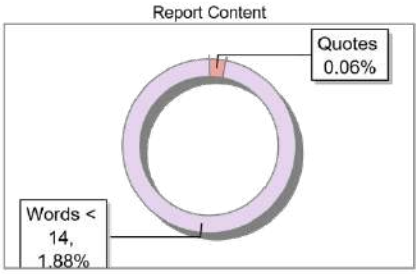

Exclude Information

Database Selection

Quotes	Excluded	Language	English
References/Bibliography	Excluded	Student Papers	Yes
Source: Excluded < 14 Words	Not Excluded	Journals & publishers	Yes
Excluded Source	**0 %**	Internet or Web	Yes
Excluded Phrases	Not Excluded	Institution Repository	Yes

A Unique QR Code use to View/Download/Share Pdf File

ACKNOWLEDGEMENT

Not all who wander are lost!

Those, whose wandering is escorted by proper encouragement, motivation, and inspiration, do find their track soon. This extensive and exhausting journey of research was not at all easy for me, but constant support and guidance from so many made this journey not just possible but effectual and exciting as well. I would like to take this opportunity to express my gratitude towards all those.

First and the foremost, I would like to express a deep sense of gratitude to my supervisor, **Dr. Saurabh Dalela**, Associate Professor, Department of Pure & Applied Physics, University of Kota, Kota. It was his motivation and encouragement that fueled me back after each mile. A balanced proportion of the freedom and assistance that he provided was the main forte throughout this journey. I do feel very privileged to be blessed with an opportunity to work under his supervision.

My heartfelt thanks to **Prof. B. P. Sarawat**, Vice Chancellor, **Prof. Reena Dadeech madam**, Director of Research, other Professors, faculty members and staff members at the University of Kota in Kota for their help and support in carrying out my research.

I express my courteous gratitude to **Prof. K. P Maheshwari (Retd.),** Visiting faculty,Department of Pure & Applied Physics, University of Kota, Kota. No matter howtrivial my doubt used to be, he was always kind and supportive. Thought provoking and deep discussions with his benevolent attitude were my constant source of inspiration that makes me believe that "*true knowledge comes from the humblest of origin"*. I extend my heart felt gratitude to the respected faculty members of the department **Prof. N. K. Jaiman (Retd.), Dr. Ghanshyam Sharma, Dr. N. L. Heda**, **Dr. Namrata Sengar** and **Mr. B. L. Suthar (Retd.)** for their invaluable suggestions, guidance, and blessings throughout this journey.

I am grateful to our research collaborator and faculty members from various research institutes and universities for facilitating the necessary instrumentation for the successful execution of my research. I would like to express my heartfelt gratitude

to **Dr. P. A. Alvi**, Associate Professor, Department of Physics, Banasthali Vidhyapith, Newai, for providing XRD, Raman and UV-Vis-NIR spectroscopy facilities to examine my samples to finish my work. I would like to give special thanks to **Dr. Shalendra Kumar**, Associate Professor, King Faisal University, Saudi Arabia; and University of Petroleum & Energy Studies, Dehradun, India, for his continuous encouragement and constant support.

A special thanks goes to **Dr. Narendra Singh Leel**, my senior and the only lab mate who went through this entire expedition with me. Be it writing my synopsis, a manuscript, investigating, data analysis, software dealing or this thesis, task could not have been completed without his support. Long time discussions on research topics, which sometimes were more like a fight, helped me alot to get an insight to proceed further. I am very pleased for his support, cooperation and suggestions during this course of work.

I am very grateful to my senior **Dr. Kuntal Kabra, Dr. H. R. Khakhal, Dr. Jyoti Sahu, Mrs. Mridula Dave** for their invaluable, insightful comments, warm encouragement, thoughtful guidance, and suggestions to improve the quality of this work. His deep knowledge on nanomaterial subject helped me a lot in concluding my research work. I warmly thank my colleagues **Dr. Pinkesh Meena, Mr. Om Prakash Soni, Mr. Mangal Chand, Mr. Koushal Shringi, Mr. Labhchand Meena** and **Mrs. Loveleena Singh** for their support my research work. I would also like to thanks my friends **Dr. Manoj Kumawat** (JNU-Delhi), **Mrs. Jyoti Arya (**Banasthali Vidhyapith), and **Mr. Giriraj Carpenter.** They always support me and encourage me to feel good. I want to express my gratitude to all of the university employees who assisted me both directly and indirectly during this research work.

An unnoticed thread of trust was always there from the family to hold me. *"Giving up is simply not an option when you do have a family to support."* I would like to acknowledge my parents **Mr. Bhim Raj Mahavar- Mrs. Vimla Mahavar** for their encouragement, unconditional love and prayers at every stage of my life and my in-laws **Dr. Mohan Lal Mahavar-Mrs. Rukmani Mahavar** whose blessings are always there. My elder sister **Mrs. Pooja Mahavar,** my elder brother **Mr. Shivanshu Mahavar** are a constant source of inspiration and motivation. I also thanks to my loving and supportive husband **Mr. Shubhendra**, who has always been there during

all ups and downs. It was his continues moral support and encouragement without which this thesis work would not have been concluded. His efforts serve as a constant source of inspiration for me to attain my goals. Joyful moments with **Takshay** (son) are like power boosters in my stressful and hectic schedules. My friends continuously tapped my back to proceed further with greater enthusiasm. I thank them all for their blessings and support.

I acknowledge UGC-JRF fellowship **(JUNE18-537794)** for financial support to carry out the thesis work. I would also like to thank the Department of Pure and Applied Physics (University of Kota) for library and computational facility.

I am grateful to all the other individuals who supported my research in various ways. Finally, I want to express my gratitude to the anonymous individuals who supported me directly or indirectly while undertaking my research work. I nevertheless hope they will understand and embrace my sincere gratitude.

- **Mrs. Kiran Mahavar**

ABSTRACT

Nanotechnology refers to the manipulation and control of matter at the nano-scale (typically below 100 nm), where unique physical, chemical, and biological features exist. Nano-materials are nano-scale-engineered materials that serve as the foundation of nanotechnology. These materials are critical to breakthroughs in material science because they enable for the creation of materials with superior characteristics and functionality. Nanotechnology and nanoparticles are transforming material science by allowing the development of materials with improved and customizable properties. Their uses range from electronics to medicine, making them vital to the advancement of next-generation technology. Nano-structuring considerably improves performance of dilute magnetic semiconductors (DMS) by expanding surface area, introducing defects, and changing electronic structures. The correlation stems from the fact that nano-scale effects enhance magnetic interactions, making nano-structured DMS intriguing for spintronics devices, sensors, and multifunctional materials.

DMS are semiconducting materials doped with a minor number of magnetic ions (such as Mn, Fe, Co, Ni, etc.) to impart magnetic characteristics while retaining their semiconducting behavior. These materials exist at the crossroads of magnetism and electronics, making them extremely important in modern material research and technology. DMS materials combine the properties of semiconductors (used in electronic devices) and Ferro-magnets (used for magnetic memory). This dual functionality opens the door to spintronics, a field that makes use of both electron charge and spin.

Cerium oxide (CeO_2), a wide band-gap semiconductor (~3.2 eV), is a promising material in the field of DMS. It can display room-temperature ferromagnetism (RTFM) when doped with transition metal (TM) or rare-earth (RE) ions. It is considered as a suitable DMS because it naturally supports oxygen vacancies, resulting in the existence of Ce^{3+} ions. The Ce^{3+}/Ce^{4+} redox pair is critical for facilitating magnetic exchange interactions. Oxygen vacancies behave as magnetic polarons, aligning neighbouring magnetic dopant spins using the Bound Magnetic Polaron (BMP) process. High vacancy concentrations can cause or improve

ferromagnetism even in the absence of exogenous doping. CeO_2 lattices may easily accommodate TM and RE dopants (e.g., Y, Ag and Cd). These dopants create localized magnetic moments that interact with carriers or defects. These properties make them valuable in a wide variety of scientific and industrial applications. It is used as an oxidation/reduction catalyst: Serves as a co-catalyst in the oxidation of CO, hydrocarbons, and alcohols. It is also effective at degrading organic pollutants under UV or visible light, particularly when doped with metals (e.g., Ag, Cd). Because of its high oxygen ion conductivity, this material can be used as an electrolyte or anode. It is used in sunscreens and protective coatings due to its excellent UV-blocking capabilities. It is used to polish glass, silicon wafers, and other high-precision optical components. It serves as a high-k dielectric in electronic components such as transistors and capacitors. Therefore, CeO_2 nanoparticles are versatile materials with uses in catalysis, energy, the environment, medicine, electronics, and magnetism. Their distinctive redox activity, oxygen storage capacity, and biocompatibility make them particularly useful in cutting-edge nanotechnology and material science applications.

Doping CeO_2 nanoparticles with TMs including Y, Ag and Cd considerably affects their structural, optical, magnetic, and electrochemical properties. This is due to changes in electrical structure, oxygen vacancy concentration, and defect chemistry caused by dopant ions. Here is a detailed look at the effects and benefits of doping CeO_2 nanoparticles with TM elements. The structural, optical, electronic, magnetic, and electro-chemical properties of undoped CeO_2 and TM (Y, Ag and Cd) doped CeO_2 nanoparticles at various dopant concentrations are thoroughly investigated. The present thesis has **six chapters**. A quick overview of each chapter is provided below.

The First chapter (Introduction) of this thesis provides the groundwork for the remainder of the work. It presents the background and motivation of the research in a clear and logical manner. It defines nano-science and nanotechnology, introduce nanoparticles, including their size range, type (metal, oxide, or semiconductor), and general properties. It explains why nanoparticles are so significant in modern materials science and how nanoparticlesare engineered to have magnetic and electronic properties. The importance of DMS and oxide-based magnetic nanoparticles is provided in this chapter. In addition, a variety of theoretical models,

such as the RKKY, FCE, and BMP models are provided in detail to better explain the genesis of ferromagnetism in undoped and doped CeO_2. This chapter also discusses the research's main objectives and conclusions.

The Second chapter (Characterization Techniques) chapter provides a detailed description of the experimental tools and methods used to analyse the structural, morphological, optical, magnetic, and electro-chemical properties of the prepared samples. Each technique has been addressed in a distinct subsection, including: Principle and Instrument details. Techniques such as XRD, TEM and EDX are addressed to study the structure properties, UV-Vis-NIR, Raman and photoluminescence spectroscopy to determine the optical properties, XPS for electronic structure and electrochemical analyser to study the electro-chemical properties. Techniques such as XRD, TEM, and EDX are used to identify the structure properties, UV-Vis-NIR, Raman, and photoluminescence spectroscopy to assess optical properties, XPS for electronic structure, SQUID- VSM for magnetic properties and an electrochemical analyzer to study electrochemistry. Several experimental procedures are given in the introduction to instrumentation, data collecting, data analysis, and information derived from the analysis.

The Third Chapter highlights the extraordinary properties of CeO_2 and $Ce_{1-x}Y_xO_2$ nanoparticles (x = 0.03, 0.05, and 0.07). The findings of XRD revealed a FCC structure of CeO_2 with reduced crystallite size. To explore surface morphology, HRTEM and SAED patterns were used. EDX studies were performed to investigate the elemental and compositional properties. The absorption spectra were studied using UV-Vis-NIR spectroscopy, revealing that red-shifted absorbance increased with decreasing band gap values for higher Y doping. The PL spectra showed diverse emissions showing the formation of various defects and oxygen vacancies with the inclusion of Y content in the lattice with CCT values below 4000 K, indicating warm yellow light for indoor applications. Furthermore, the XPS measurements revealed the valence states of elements such as Ce (3+ and 4+), Y (3+), and O (2-), as well as charged oxygen vacancies. The photo-catalytic research demonstrated that Y-doped CeO_2 nanoparticles degrade better under a variety of conditions. A degradation mechanism demonstrating the impact of oxygen vacancies induced by Y-doping on the photo-degradation process has been proposed.

The Fourth chapter details the synthesis of undoped CeO_2 and Ag-incorporated CeO2 nanoparticles with varying Ag concentrations (x = 0.03, 0.05 and 0.07) via coprecipitation technique. The XRD measurement indicates an improvement in the crystalline nature with Ag-doping and crystallite size between 13 and 9 nm. The absorption spectra show a red shift of the absorption peaks and a shortening of the band gap as the Ag concentration increases. To determine the defects and excitation wavelength, PL measurements were carried out. The prepared samples had a high colour rendering index (CRI), indicating good luminescence with white light emissions. Furthermore, the XPS measurements revealed the valence states of Ce (3+ and 4+), Ag (1+), and O (2-). The CV test confirmed that in 2 M KOH electrolyte solution, the 5% Ag-doped CeO_2 nanoparticles sample exhibited the highest specific capacitance value of 363.44 F/g at a scan rate of 10 mV/s and the best cycle stability (retaining 93.90% after 2100 cycles). The 5% Ag-doped CeO_2 nanoparticles had an energy density of 125.08 Wh/kg and a power density of 652.48 W/kg.

The Fifth chapter uses a unique co-precipitation technique to prepare Cd-doped CeO_2 varying Cd concentrations (x = 0.03, 0.06 and 0.09) nanoparticles. Powder XRD and TEM revealed fcc structures and spherical symmetry with diameters ranging from 6 to 12 nm, respectively. UV-Vis spectroscopy revealed a red shift in the absorption edge, and lower band gap energy reduced from 3.39 eV to 2.98 eV when Cd concentration increased (x = 0.00 to 0.09), the optical band gap. The increase in oxygen vacancies in the CeO_2 lattice was further supported by XPS measurements for core levels Ce 3d, O 1s, and Cd 3p and 3d. The valence states of elements including Ce (3+ and 4+), Cd (2+), and O (2-), as well as charged oxygen vacancies, were also disclosed by the XPS measurements. Cd-doped CeO_2 showed enhanced properties in magnetic studies, exhibiting RTFM behaviour. Consequently, these results show that CeO_2 nanoparticles can be customized for a variety of uses, such as optical and spintronics, through Cd doping.

The Sixth chapter of this thesis, commonly titled "Conclusion and Summary" provides a clear vision on the synthesis of the entire work, emphasizing what has been accomplished, what has been discovered, and why it is important. This chapter brings everything together and frequently recommends further directions for future.

TABLE OF CONTENTS

LIST OF TABLES

LIST OF FIGURES

LIST OF ABBREVIATIONS

AFM	:	Anti-Ferromagnetism
BMP	:	Bound Magnetic Polaron
CeO_2	:	Cerium Oxide
CV	:	Cyclic Voltammetry
DMO	:	Dilute Magnetic Oxide
DMS	:	Dilute Magnetic Semiconductor
EIS	:	Electrochemical Impedance Spectroscopy
FM	:	Ferromagnetism
FCE	:	F-Centred Exchange
GCD	:	Galvanostatic Charge Discharge
JCPD	:	Joint Committee on Power Diffraction Standards
LED	:	Light Emitting Diode
PL	:	Photoluminescence
PM	:	Paramagnetism
TM	:	Transition Metal
TEM	:	Transmission Electron Microscope
RKKY	:	Ruderman-Kittel-Kasuya-Yosida
RTFM	:	Room Temperature Ferromagnetism
SEM	:	Scanning Electron Microscopy
SC	:	Specific Capacitance
XRD	:	X-ray Diffractometer
XPS	:	X-Ray Photo Electron Spectroscopy
VSM	:	Vibrating Sample Magnetometer

Chapter 1
Introduction and Review of Literature

Chapter-1

Introduction and Review of Literature

1.1. Introduction

1.1.1. Nano-materials and Nanostructures

Recent studies have revealed that manufacturing typical semiconductor materials into nanostructures, especially three-dimensional (3-D) arrays like nanowires. The 3-D arrays of these nanostructures closely resemble natural light harvesting structures. Nanoparticles are particulate or solid particles ranging in size from 10 to 1000 nm. Nanoparticles are type of materials with properties that are distinguishable from their bulk and molecule equivalents. Nano-materials with unique properties, such as high surface-to-volume ratio and quantum confinement are being studied to developed new PV mechanisms, such as dye-sensitized solar cell and quantum dot solar cells. Many research groups are exploring the optical absorption of nanostructure arrays to optimize solar cell efficiency and various experiments have been conducted to characterize the unique optical properties of 3-D nanostructures, in addition to theoretical study [1].

Nanoparticles have numerous unique properties due to their small size such as their ability to alter absorption and emission wavelengths through surface fictionalization and particle size. The chemical composition and size of nanoparticles affect their ionic potential, electron affinity, and electron transport capabilities. Individual metallic magnetic nanoparticles may display super-paramagnetic properties [2]. Nano-material-based electrochemical signal amplification has the potential to enhance sensitivity and selectivity for electrochemical and biosensors, thanks to advancements in nanotechnology and nano-science. High-performance electrochemical sensing devices rely heavily on electrode materials to identify target molecules using diverse analytical methods. Despite their advantages, nanoparticles have limitations. To use nanoparticles in clinical or commercial settings, practical issues must be addressed [3]. Nonetheless, nanoparticles hold immense potential for environmental cleanup. There are two basic fabrication processes for arrayed nanostructures: (i) top-down and (ii) bottom-up. On the other hand, Bottom-up procedures involve

developing and assembling nano-materials at the atomic scale, such as vapor-liquid-solid (VLS) growth, vapor-solid growth, and electrochemical growth [4].

1.1.2. Dilute Magnetic Oxides (DMOs)

Recently, diluted magnetic semiconductors (DMS), have gained attention from the scientific and industrial field and their unique properties for optoelectronic devices. DMS research encompasses a wide range of material systems and theoretical techniques, all of which contribute to a better understanding of these materials and their prospective uses. Such interaction effectively modifies the energy band and electronic structural properties of semiconductors, leading to new physical consequences, especially the magnetic properties [5]. These materials can be engineered to have a band gap, making them suitable for various device applications. Growth circumstances and co-doping with shallow dopant can alter the properties of nano-crystals [6]. Single-phase dilute magnetic oxides are thought to be essential for developing practical devices due to their polarized carrier population. For ferromagnetic wide band-gap semiconductors to be helpful in spintronics applications there must be a coupling between their ferromagnetic and semiconducting properties, regardless of the system's microstructure [7].

1.1.3. Spintronics and DMOs

DMS's ferromagnetic property assists the development of high-performance magnetic random-access memory (MRAM), which can function at room temperature. Ongoing research focuses on improving the Curie temperature and understanding the ferromagnetic processes in various DMS materials, which is important for practical applications [8]. While DMS has considerable potential in spintronics, obstacles such as low Curie temperatures and the requirement for sophisticated fabrication procedures remain barriers that researchers must overcome before these applications can be completely realized.

1.1.4. Difference between Magnetic, Non -Magnetic and DMS:

DMS are semiconductors doped with magnetic elements to exhibit magnetic properties. Each variety has distinct properties and applications, particularly in domains like as spintronics and materials science. A DMS involves distributing a small concentration of magnetically atoms which are magnetically active at the cation

sites of a semiconductor. This system can exhibit combination of semiconducting as well as ferromagnetic properties, making it an appealing concept. A schematic representation of different types of magnetic materials is shown in figure 1.1.

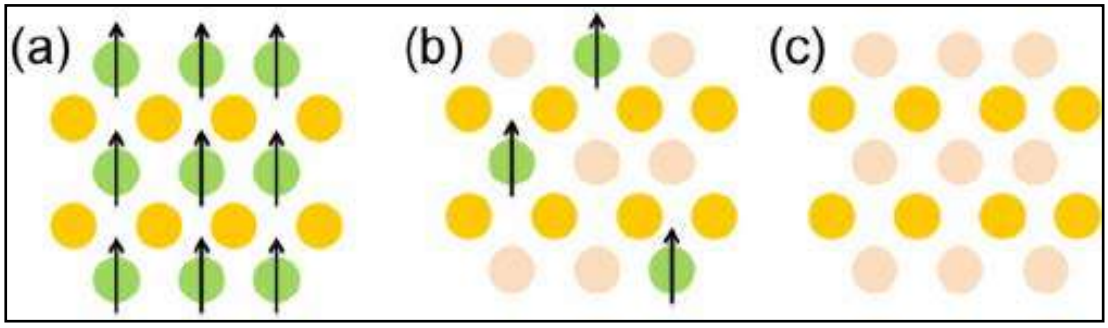

Figure 1.1: Different types of semi-conductor (a) magnetic semiconductors; (b) dilute magnetic semiconductor; (c) non-magnetic semiconductor

- **Magnetic materials**

Materials like iron, nickel, and cobalt show ferromagnetism, which occurs when magnetic moments align spontaneously, resulting in a permanent magnet even without an external magnetic field. Because of their strong magnetic characteristics, these materials are commonly used in data storage, sensors, and motors.

- **Nonmagnetic Materials**

These materials are not magnetic, while they comprise diamagnetic and paramagnetic substances whose magnetic moments are either absent or do not align to form a net magnetic field. Frequently employed in situations where magnetic interference is undesirable, such as in certain electronic components [9].

- **Diluted magnetic semiconductors (DMS)**

DMS are semiconductors doped with a trace number of magnetic elements, such as Mn, Co, or Ni, to produce magnetic characteristics. Obtaining steady RTFM and regulating the Curie temperature are key issues. Examples include ZnO-based DMS doped with Mn or Co, which exhibit different magnetic characteristics depending on the synthesis procedure and further doping. While magnetic and non-magnetic materials play distinct roles, DMSs provide a hybrid approach by combining semiconductor characteristics with magnetism, which is especially promising for advanced electronic and spintronics devices [10]. However, the development of DMS

with high Curie temperatures remains a problem, needs more study and innovation in material synthesis and doping techniques [11].

1.1.5 Why Cerium Oxide?

Cerium oxide (CeO_2) is important in many fields, including environmental applications and energy devices, because of its unique features such as redox behavior and oxygen storage capacity. CeO_2 is important in three-way catalysts (TWC) for automotive exhaust systems because its oxygen storage capacity improves the elimination of pollutants such as CO and hydrocarbons. CeO_2 nanoparticles can easily transition between Ce^{3+} and Ce^{4+} states, allowing them to scavenge free radicals and reactive oxygen species, which is important for decreasing oxidative stress in biological systems. CeO_2 nanoparticles exhibit strong antibacterial action, effectively inhibiting bacterial growth and bio-film formation, which helps in overcoming antibiotic resistance [12]. These nanoparticles are used in treating illnesses like cancer because of their capacity to scavenge free radicals and reduce oxidative stress [13]. Also, these nanoparticles increase the performance of internal combustion engines by lowering emissions and increasing fuel efficiency when used as catalysts. While CeO_2 nanoparticles offer various benefits, their possible pro-oxidant effects and toxicity must be carefully considered. Understanding how they interact with biological systems is important for developing safe and effective medical uses [14].

The problems of size and shape-based CeO_2 nanoparticles in material science are largely studied for their synthesis, characterization, and the effects of these characteristics on their catalytic properties. Controlling the size and shape of ceria nanoparticles is essential, as these variables have a substantial impact on their reactivity and performance in a variety of applications. Over the last few years, some research groups have synthesized size/shape-controlled CeO_2 nanostructures such as spherical nanoparticles, nano-rods, nanowires, nanotubes, nano-cubes, nano-spheres, and hierarchical nanostructures, as well as investigated the properties that vary with size/shape. Nanocrystalline compounds have superior optical, electrical, and structural characteristics compared to bulk counterparts due to quantum size effects and greater surface-to-volume ratios [15, 16]. More recently, the good matching of the crystal structure of undoped and TM doped CeO_2, were employed as diluted magnetic DMO in spintronics applications [17].

1.2. Structural properties of undoped and 4d cations doped CeO_2 nanoparticles.

1.2.1. Structural properties of undoped CeO_2

The structural properties of CeO_2 nanoparticles are determined by their crystalline structure, particle size and doping/synthesis processes. These nanoparticles mostly have a face-centered cubic (fcc) fluorite structure, which is validated by X-ray diffraction (XRD) and Raman spectroscopy. The bond length of Ce-O in CeO_2 nanoparticles is an important parameter that influences their structural and catalytic properties. This elongation is due to the nanoparticles' distinctive surface/core configuration, which influences their electronic and catalytic function. CeO_2 nanoparticles have a Ce-O bond length of around 2.338 Å in bulk, although this is lengthened due to surface effects. CeO_2 nanoparticles' surface atoms have distinct bonding properties than their core atoms, resulting in variances in electronic properties and reactivity. Nano-particle shape, such as the presence of various surface terminations, can influence bond lengths and overall stability [18]. CeO_2 nanoparticles could transition between oxidation states (Ce^{4+} and Ce^{3+}), making them excellent antioxidants and pro-oxidants under different conditions. This distinct redox activity is crucial for their applications in biological and environmental sciences [19]. CeO_2 nanoparticles are best known for their antioxidant activities, their dual role as both antioxidants and pro-oxidants demonstrates the complexities of their redox characteristics, which can be altered by environmental conditions such as pH and concentration.

$$\boldsymbol{CeO_{2-x} \leftrightarrow CeO_2 + \frac{x}{2}O_2 \; for \; x = 0.5, then \; CeO_{1.5} \; (Ce_2O_3)} \qquad \textbf{(1.1)}$$

This duality needs careful attention in their employment to secure desired results in therapeutic and industrial uses [20]. According to research, when grain size decreases, the lattice parameter compresses before growing at sizes smaller than 20 nm, with a minimum seen nearly about 0.5411 nm at 300 K. The morphology of CeO_2 nanoparticles has a considerable impact on their physical and chemical properties, which affects applications in catalysis and gas sensing. Different morphologies result in variable oxygen vacancy concentrations, which are necessary for catalytic oxidation reactions. For example, shuttle-shaped CeO_2 demonstrates improved catalytic performance due to its increased surface area and oxygen vacancies. CeO_2

nanoparticles' exposed facets, such as {100} and {111}, affect their catalytic effectiveness, with {100} facets demonstrating improved performance in gas sensors.

1.2.1.1. Crystalline Size (D) and other parameters:

CeO_2 nanoparticles crystallize in the fcc structure, where each O^{2-} ion coordinates with four Ce^{4+} distortions. Particle size has the primary influence on how the expansion of the lattice in ceria nanoparticles takes place. Adding Ce^{3+} ions to the crystal lattice reduces the coordination number of Ce^{4+} to O^{2-} from eight to seven [21]. The general crystal structure of CeO_2 nanoparticles is shown in figure 1.2.

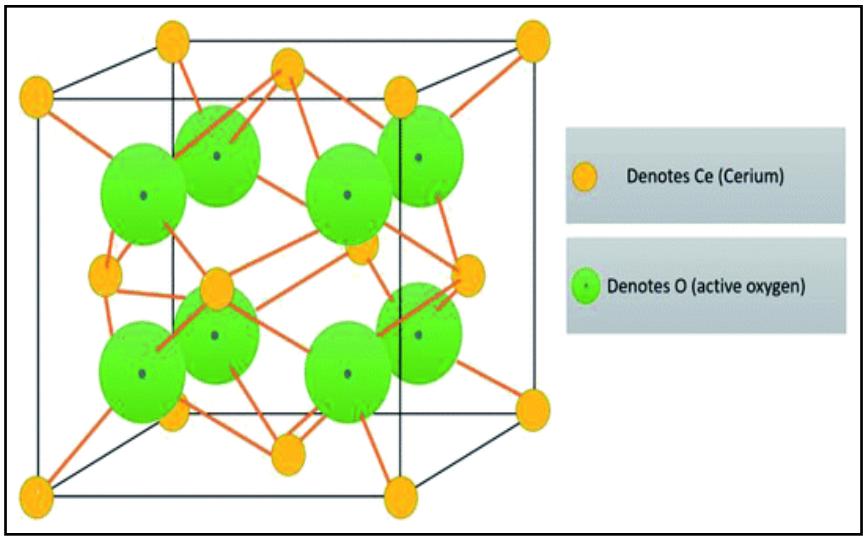

Figure 1.2: General fcc crystal structure of CeO_2 nanoparticles

The ionic radius of Ce^{3+} ions is larger (1.034 Å) than to Ce^{4+} ions (0.92 Å). The presence of oxygen vacancies and Ce^{3+} ions distorts the local symmetry. This changes both the overall lattice parameter and the Ce-O bond length lattice distortion. The lattice parameter for the (h k l plane) can be calculated using the following equation [22].

$$\frac{1}{d_{hkl}^2} = \frac{h^2+k^2+l^2}{a_{exp}^2} \qquad \textbf{(1.2)}$$

where 'a' symbolizes lattice constant, d represents the interplanar spacing and (h k l) are the miller indices. The average crystallite size (D) of the CeO_2 nanoparticles can be calculated using Scherer's formula as follows [23].

$$D = k\,\lambda / \beta\,cos\theta \qquad \textbf{(1.3)}$$

In this equation, θ represents Bragg's diffraction angle, λ is the wavelength of Cu-kα radiation (1.54060 Å), β is the peak width at half maximum (in radians), and k is the shape factor (0.9). Excessive lattice strain may cause lattice expansion to occur as a strain relief mechanism. Massive crystallites show less lattice distortion because losing a few oxygen atoms does not produce considerable lattice strain. This strain is defined by the following equation [24].

$$\boldsymbol{\varepsilon = \frac{\beta \cos \theta}{4}} \qquad \textbf{(1.4)}$$

The Debye-Scherrer formula is used to determine D and stain based on the XRD peaks (2θ). However, this technique implies peak broadening is solely due to crystallite size, neglecting micro-strain (ε) and instrumental variables. The Williamson-Hall analysis considers both size and strain-induced broadening and is used to analyze size separation and strain broadening at various θ points [25].

$$\boldsymbol{\beta \cos \theta = \frac{K\lambda}{D} + 4\epsilon \sin\theta} \qquad \textbf{(1.5)}$$

The above equation assumes that stain is uniform in all crystallographic directions is plotted against 4sinθ for CeO_2 peaks. Strain and crystallite size are calculated using the slope and y intercept of the fitted line, respectively. Thus, oxygen vacancies are formed when Ce^{4+} ions are converted into Ce^{3+} ions to maintain charge neutrality. This could lead to localized micro-strain in the samples. The theoretical density of nanoparticles can be calculated using the formula below.

$$\boldsymbol{\rho = \frac{nM_W}{N_A V}} \qquad \textbf{(1.6)}$$

Where V represents the unit cell volume, n represents the number of atoms per unit cell, M_W is the molecular weight, and N_A Avogadro's numbers [26].

1.2.1.2. Effect of annealing temperature:

Several studies have shown that the annealing temperature has a considerable influence on the various properties of nanoparticles. Higher annealing temperatures typically result in larger crystallites and higher material quality, which improves magnetic properties and modifies optical features. Annealing affects surface roughness and particle agglomeration like when surfactants are applied, higher temperatures enhance roughness and decrease agglomeration. CeO_2 nanoparticles'

optical band gap rises at increasing annealing temperatures, ranging from 2.90 eV to 3.57 eV, indicating increased electronic properties. Also, the visible range has found with high optical transmittance (~75%) with increasing annealing temperature, making it ideal for optoelectronic applications [27]. Higher annealing temperatures improve certain properties, but they can also cause undesirable effects such as increased particle size, which may limit the effectiveness of nanoparticles in specific applications such as catalysis or drug delivery. The average crystallite size of zinc ferrite nanoparticles increased from 11.8 to 18.4 nm as the annealing temperature increased as reported by ***Ansari et al.*** [28]. Despite this broad effect, the composition of the material, deposition technique, and annealing temperature all have a major influence on the development of the final CeO_2 crystal phases.

1.2.1.3. Particle Size

The size of nanoparticles has a considerable impact on their behavior in a variety of domains, including health and material research. The size of nanoparticles influences cellular absorption and bio-distribution; optimum sizes (10-60 nm) improve medication delivery effectiveness. Smaller nanoparticles are frequently preferred for their superiority while larger nanoparticles (greater than 100 nm) can overcome specific biological barriers, such as tumor vasculature, demonstrating a complex link between size and functionality in a variety of applications. Smaller CeO_2 nanoparticles have higher optical properties, as indicated by UV-Vis experiments that reveal increased light absorption and photo-catalytic activity for degradation processes like Methylene Blue degradation. The smaller particle size correlates with increased optical properties, making them more useful in applications requiring light interaction [29]. Mechanical properties, such as the coefficient of friction during polishing, are also influenced by particle size, with smaller particles yields lower friction coefficients [30]. While smaller CeO_2 nanoparticles frequently demonstrate improved catalytic and toxicological properties, larger particles may provide advantages in certain applications, such as CO_2 hydrogenation.

1.2.2. Structural Properties of 4d cation doped CeO_2 nanoparticles:

Doping CeO_2 nanoparticles with 4d cations such as silver (Ag), cadmium (Cd), and niobium (Nb) improves their physicochemical property, including photo-catalytic activity, magnetic properties, and enzyme-like behavior. The structural

properties of Nb-doped CeO_2 nanoparticles show considerable morphology, crystallinity, and electronic properties changes. Doping with niobium (Nb) affects the lattice structure and defect formation, which are critical for improving the material's functional properties. Y-doped CeO_2 nanoparticles retain fcc structure, with no impurity phases found during synthesis. Doping causes a decrease in lattice characteristics and average crystallite size, with reported values around 18.66 nm [31]. The structural characteristics of silver-doped CeO_2 nanoparticles vary significantly depending on synthesis process and dopant concentration. These nanoparticles typically have fcc structure, with crystallite sizes determined by the amount of silver present. Ag doped CeO_2 nanoparticles prepared by solution combustion method possess single-phase cubic CeO_2: Ag nanoparticles, with crystallite sizes decreasing as the Ag concentration increases. This process produces single-phase cubic CeO_2: Ag nanoparticles, with crystallite sizes decreasing as the Ag concentration increases [32]. As reported by ***Mutassin et al.*** [33], Pd doped CeO_2 nanoparticles are typically spherical in shape and range in size from 6 to 13 nm. As Pd doping increases, particle size decreases. Doping with palladium reduces crystallite size from 67.41 nm to 41.67 nm while increasing overall crystallinity of the material. Mixed phases of CeO_2 and Ce_2O_3 are observed, with the latter decreasing as Pd concentration increases. ***W. Lee et al***. [34] demonstrated that Y^{3+} substitutes Ce, causing an oxygen vacancy to form. Y^{3+} distributed irregularly throughout the particle at low doping doses. However, as the doping level increased over 11%, Y^{3+} collected on the surface, forming Y-rich clusters.

1.3. Optical properties of undoped and 4d cation doped CeO_2 nanoparticles

Doping with 4d cations, such as Y, Ag and Cd, alters the band gap, absorption characteristics, and photoluminescence properties, principally by introducing oxygen vacancies and changing the Ce^{3+}/Ce^{4+} ratio [35]. Doping with 4d cations causes the optical band gap energy to drop, depending on the doping dose, indicating a red shift in absorption spectra and attributed to the development of oxygen vacancies as Ce^{4+} ions are reduced to Ce^{3+}. The existence of oxygen vacancies has an important role in enhancing photoluminescence, where higher vacancies corresponded with improved luminous properties [36].

1.3.1. Optical properties of undoped CeO_2 nanoparticles

Undoped CeO_2 nanoparticles have unique optical properties, including wide band gap (3.0 to 3.6 eV), oxygen vacancies, and Ce^{4+}/Ce^{3+} redox activity. Quantum confinement factors frequently cause the band gap to increase as particle size decreases. CeO_2 nanoparticles exhibit optical absorption in the UV region, making it suitable for UV shielding applications. CeO_2 nanoparticles also emit photoluminescence in the UV-visible spectrum, driven by: defects (oxygen vacancies), exciton recombination and surface defects. Luminescence is commonly caused by $Ce^{3+} \leftrightarrow Ce^{4+}$ charge transfer transitions.

1.3.1.1. CeO_2 as a UV blocker

CeO_2 nanoparticles have acquired popularity as UV blockers due to their efficient UV absorption capabilities and potential for incorporation into a variety of applications, including sunscreens and coatings. CeO_2 nanoparticles have high UV absorption capabilities, especially when doped with compounds such as calcium oxide, which improves their performance. For example, CeO_2/20%CaO increased the sun protection factor (SPF) from 1.95 to 2.81, showing a 69.39% improvement in UV protection [37]. The addition of CeO_2 into polyurethane coatings resulted in 60% transmittance at 365 nm UV, demonstrating its efficiency in defensive applications. CeO_2 nanoparticles are used in a variety of formulations, including sunscreens, where they not only block UV radiation but also reduce free radical formation, hence reducing possible skin damage. CeO_2-doped glasses have been created to provide almost minimal transmission in the UV region while preserving strong visible light transmission, making them perfect for UV protection in eyewear [38].

1.3.1.2. Optical band gap:

The optical band gap (Eg) is an important property that determines the electronic and optical properties of nanoparticles, which may be controlled using different manufacturing methods and material modifications. According to research, doping, temperature, and structural properties all have a substantial impact on the band gap values of various nanoparticles systems. At low temperatures, the band gap is at 3.35 eV, which decreases to 3.29 eV at ambient temperature due to thermal effects. Doping with TM like Fe or Co can effectively lower the band gap. For

example, Fe ion implantation lowers the Eg value from 3.14 eV to 2.70 eV. Similarly, Co doping can reduce the band gap to roughly 2.0 eV [39].

1.3.1.3. Raman Spectra on undoped CeO_2 nanoparticles

The most prevalent Raman-active mode is F_2g mode (~465 cm^{-1}) is the most powerful peak, resulting from symmetric breathing vibrations of oxygen atoms around cerium atoms in the fluorite structure. Other Raman characteristics that may arise, depending on particle size, defects, and oxygen vacancies, include: (i) Defect-induced modes (~250-600 cm^{-1}) which generally occur due to oxygen vacancies or lattice distortions, (ii) Longitudinal optical mode (LO) (approx. 600-650 cm^{-1}), which is sometimes seen due to defect-induced activation, (iii) Overtones and multi-phonon modes (~1100 cm^{-1} and higher): These may arise at higher frequency [40]. In nano-sized CeO_2, the F_2g mode may move to lower wave-numbers and expand due to phonon confinement effects and increasing oxygen vacancy [41]. The Raman spectrum of undoped CeO_2 nanoparticles is shown in figure 1.3.

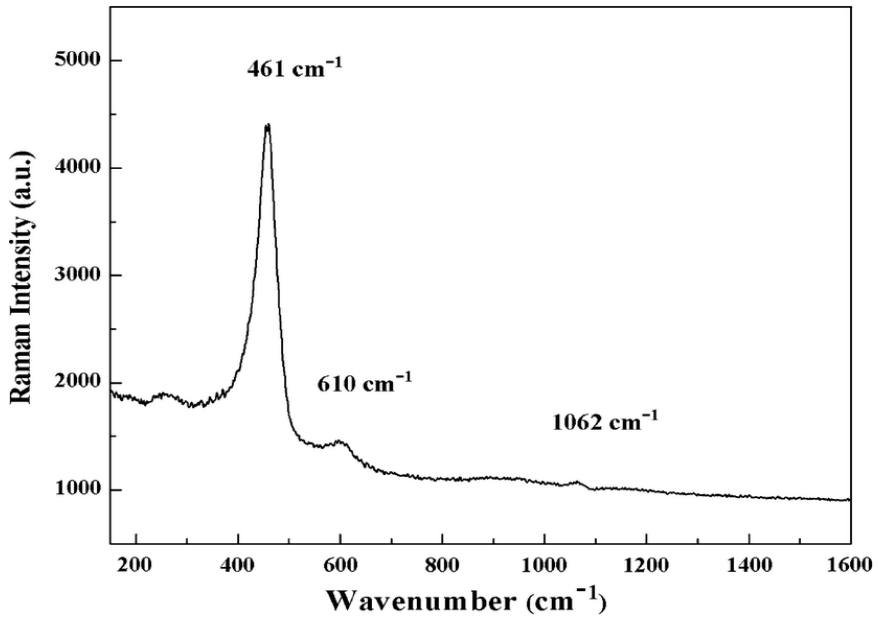

Figure 1.3: Raman spectra of CeO_2 nanoparticles

1.3.1.4. Optical properties of 4d cation doped CeO_2 nanoparticles

Doping CeO_2 nanoparticles with 4d transition metals (e.g. Zr, Mo, Tc, Ru, Rh, Pd, Ag, and Cd) affects their optical, electronic, and luminous properties. Unlike 4f rare-earth elements, 4d elements have delocalized d-orbitals, resulting in strong charge transfer interactions with CeO_2. This impacts band-gap tuning, defect state

creation, PL, and visible/NIR absorption. As reported by ***B. Xu et al***. [42] after yttrium doping, oxygen vacancies increased significantly in comparison to undoped CeO_2. A mole ratio of Ce:Y of 1:0.1 resulted in a maximum oxygen vacancy of 11.2% revealed by the Raman spectra. According to ***D. Van et al.*** [43], Ag nanoparticles promote CeO_2's visible light absorption due to the quantum confinement effect and the valence change of Ce ions. CeO_2's band gap lowers with increasing Ag concentration, showing increased optical properties. The Eg value of Cd-doped CeO_2 films ranges from 3.23 to 3.52 eV, suggesting possible applications in photo-catalysis and optoelectronics [44]. Other investigations, however, have demonstrated that the band gap can be reduced to around 2.0 eV by altering synthesis settings or using other doping techniques [45]. Doping CeO_2 nanoparticles with 4d cations such as Y, Nb, Ag, Cd, Zr has a considerable influence on their optical band-gap. This effect is primarily caused by the introduction of oxygen vacancies and defects into the crystal lattice, altering the material's electronic structure and optical properties.

1.3.1.5. Formation of defect states between the energy bands

Defect states in CeO_2 nanoparticles arise primarily from oxygen vacancies and Ce^{3+} states**,** which significantly modifies the electronic structure. These defects introduce energy levels within the band-gap**,** affecting the material's optical, electronic, and catalytic properties. Defect states in CeO_2 nanoparticles are predominantly caused by oxygen vacancies and Ce^{3+} states, which dramatically affect the electronic structure. Oxygen vacancies result in two extra electrons that can be focused on cerium ions, reducing Ce^{4+} to Ce^{3+}. These Ce^{3+} sites create more 4d states in the band-gap [46]. Shallow defect states trap electrons, resulting in better charge separation in photo-catalysis. Defect-mediated electronic transitions improve electrical conductivity in sensor and fuel cell systems. Tailoring the optical and electronic characteristics of CeO_2 nanoparticles require the creation of defect states. Oxygen vacancies and Ce^{3+} sites provide mid-gap energy levels, leading to improved visible-light absorption, photoluminescence, and charge transport.

1.3.1.6. Role of oxygen Vacancies

Oxygen vacancies significantly affect the optical behavior of CeO_2 nanoparticles. These vacancies influence the electronic structure, defect states, charge carrier dynamics, and light absorption properties. Oxygen vacancy introduces defect

states below the conduction band, leading to band-gap narrowing (red-shift in optical absorption) and enhanced visible-light absorption, making CeO_2 more useful in photo-catalytic and optoelectronic applications. These states allow for sub-band-gap electronic transitions, resulting in visible absorption (~400-600 nm). However, undoped CeO_2 has poor luminosity due to rapid charge carrier recombination but oxygen vacancies are responsible to introduce new defect-related emission peaks in the blue-green range (450-550 nm). Enhance radiative recombination by trapping electrons, resulting in higher PL intensity. Influence exciton recombination, resulting in tunable emission spectra based on vacancy concentrations [47]. Oxygen vacancies promote the $Ce^{4+} \rightarrow Ce^{3+}$ transition, which alters the electronic structure and influences optical absorption.

1.4. Electronic structure properties of undoped and 4d cation doped CeO_2 nanoparticles

Undoped CeO_2 nanoparticles have distinct electronic structural properties due to their distinctive defect surface, optical behavior, and electronic transitions. The presence of oxygen vacancies is essential because they affect charge compensation and electronic conductivity. The generation of Ce^{3+} ions from Ce^{4+} due to these vacancies improves electronic properties. Ce's 4f and 3d orbitals are principally responsible for its electronic structure [48].

1.4.1. X-ray Photoelectron spectroscopic studies of undoped CeO_2 nanoparticles

The X-ray photoelectron spectroscopy (XPS) properties of undoped CeO_2 nanoparticles provide valuable information on their electronic structure and oxidation states. XPS examination often detects the presence of Ce^{3+} and Ce^{4+} ions. The XPS results demonstrate that undoped CeO_2 contains roughly 20.5% Ce^{3+} and 79.5% Ce^{4+} ions, which are required for its catalytic characteristics. The presence of various oxidation states enhances the material's ability to engage in redox processes. The XPS spectra also demonstrate the stoichiometry of oxygen, with a ratio of around 1.9 oxygen atoms per cerium atom, indicating the presence of oxygen vacancies. According to ***R. Suresh et al.***, [49] Ce 3d core level spectra exhibit mixed valence states of Ce^{3+} and Ce^{4+} due to its non-stoichiometry nature. Ce^{4+} peaks nearly at 921 and 912 eV, while Ce^{3+} peaks nearly at 885 and 903 eV. Ce^{4+} has stronger peaks than Ce^{3+} while Ce^{4+} ions are primarily found on the surface of cerium oxide nanoparticles,

potentially contributing to their blue shift. The charge state change from 3+ to 4+ increases the charge-transfer gap between the O 2p and Ce 4f bands. The asymmetrical O 1s core level spectra in the binding energy range of 526-540 eV are deconvolute into four peaks. The peak observed at ≈528-530 is ascribed to the lattice oxygen O^{2-} (O_L) while higher binding energy peaks at ≈530-533 eV and ≈533.5-536.4 eV corresponds to oxygen vacancies (O_V) and formation of hydroxyl or absorbed H_2O species (Oα and Oβ) on their surfaces respectively [50].

1.4.2. X-ray Photoelectron spectroscopic studies on 4d cation-doped CeO_2 nanoparticles

Doping CeO_2 nanoparticles with 4d elements (e.g. Zr, Mo, Ru, Rh, Pd, Ag) changes their electronic structure, affecting band-gap, charge transport, defect states, and catalytic activity. The simpler generation of Ce^{3+} leads to an increase in oxygen storage capacity, which improves redox characteristics, making it an effective catalyst for fuel cells and exhaust gas treatment. Also, the photo-catalytic activity rises due to improved charge separation and longer light absorption. XPS demonstrates that 4d cation doping in CeO_2 alters Ce^{3+}/Ce^{4+} ratios, oxygen vacancy concentration, and dopant oxidation states, influencing catalytic and electronic characteristics. Dopants such as Mo, Ru, and Rh improve reducibility by promoting Ce^{3+} production and oxygen vacancies, while Pd and Ag alter surface chemistry and charge transfer. As reported by ***C. Sun et al.*** [51] that Y 3d doublet, having peaks at 157.4 eV ($Y3d_{5/2}$) and 159.3 eV ($Y3d_{3/2}$), indicates the presence of Y^{3+} species. Ce does not affect the position of Y 3d peaks, suggesting a modest interaction between the two elements. Increasing Y concentration does not result in a linear increase in Y/Ce atomic ratios. This effect may be caused by an uneven distribution of Y between the bulk and surface, or by larger Y_2O_3 particles in higher Y content samples. In case of Nb doped CeO_2 nanoparticles, ***W. Zhang et al.*** [52] reported that as the concentration of Nb dopant increases, Nb^{5+} ions replace Ce^{4+} ions and donate electrons into CeO_2's conduction band. This causes a change in Ce^{3+} ions, regulating the oxygen vacancy content. In case of XPS spectra of Ag-doped CeO_2 nanoparticles, ***M. Mittal et al.*** [53] have found that the surface has significantly larger concentrations of Ce^{3+} or oxygen vacancies than the interior. XPS spectra of Rh-doped CeO_2 indicates that the mobile oxygen of CeO_2 significantly affect the oxidation status of the supported metals. Elevated temperatures promote oxidation of the reduced support surface and metals

due to the separation of oxygen species from ceria at the surface. Oxidized CeO_2 surfaces can easily release oxygen in the presence of Rh, resulting in the reduction of the noble metal [54].

1.5. Magnetic properties of undoped and 4d cation doped CeO_2 nanoparticles

1.5.1. Ferromagnetism in DMOs:

DMS are materials in which a small fraction of the semiconductor's atoms is replaced (doped) with magnetic atoms, usually transition metal such as Mn, Fe, or Co. These dopants introduce localized magnetic moments and modifying carrier concentration (for example, Mn behaves as both a magnetic ion and an acceptor in GaAs). Ferromagnetism in DMS results from indirect coupling mediated by charge carriers, primarily holes, rather than direct interaction between magnetic ions. The holes interact with the localized magnetic moments through an exchange interaction. This causes the hole's spin to align anti-parallel to the spin of the magnetic ion. When multiple holes interact with many ions, the magnetic ions align parallel to one another, resulting in ferromagnetism. The spin alignment in ferromagnetic material is shown in figure 1.4.

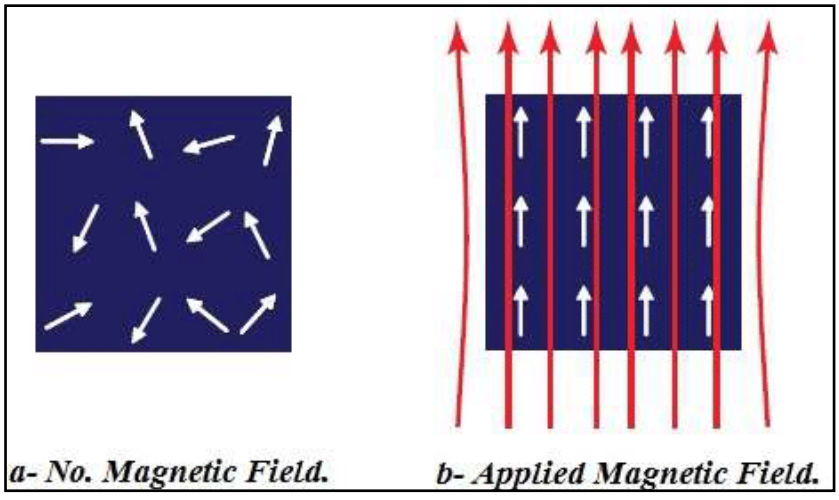

Figure 1.4: Alignment of a randomly ordered magnetic spin system: (a) in absence of an external magnetic field and (b) with an external magnetic field

There are several theoretical models, describing the origin of ferro-magnetism such as Zener model, RKKY model, BMP and FCE mechanism. The Zener Model / Mean-field Theory describe hole-mediated spin alignment and predict a reliance on

carrier concentration while RKKY Interaction is an oscillatory, long-range indirect exchange interaction using conduction carriers. Ferromagnetism in CeO_2 nanoparticles is an intriguing issue because bulk CeO_2 is not ferromagnetic but a non-magnetic, large band gap semiconductor. CeO_2 nanoparticles exhibit surprising RTFM, prompting much research. CeO_2 typically includes Ce^{4+} ions, but when oxygen vacancies occur (particularly in nanostructures), some Ce^{4+} ions are converted to Ce^{3+} to preserve charge neutrality [55]. Unpaired 4f electrons in Ce^{3+} ions can lead to localized magnetic moments. Ferromagnetic interactions can occur through bound magnetic polarons (BMPs): magnetic moments around oxygen vacancies can overlap and align, resulting in long-range magnetic ordering. Although, nanoparticles have high surface-to-volume ratio, hence surface defects are far more common than in bulk materials [56]. These surface imperfections can drastically change the electrical structure, allowing magnetic ordering. Doping with TM (such as Fe, Co, and Ni) or rare-earth elements can improve or alter magnetic characteristics. However, even undoped CeO_2 nanoparticles have displayed RTFM due to inherent defects The studies highlight the involvement of defects, hybridized states, and dopant in ferromagnetism in 4d-doped cerium oxide systems [57].

1.5.2. Super-Para magnetism in DMOs

Super-Para magnetism (SPM) occurs when ferromagnetic or Ferri-magnetic nanoparticles are sufficiently tiny (<30 nm) that thermal energy can randomly reverse their magnetization direction. These materials are highly magnetically susceptible and behave like paramagnets, but with substantially greater magnetic moments per particle. In DMOs, SPM behavior frequently occurs because of formation of magnetic clusters or secondary phases (for example, metallic Co in Co-doped ZnO), the host oxide or doped grains have a nano-scale size or the magnetic ions aggregate in places rather of being distributed uniformly. Instead of long-range ferromagnetic order, these magnetic clusters behave like single-domain particles, exhibiting super-paramagnetic properties. Although CeO_2 is essentially non-magnetic, its nano-scale form frequently exhibits SPM behavior, mainly due to surface defects, oxygen vacancies, and mixed valence states (Ce^{4+}/Ce^{3+}). This phenomenon is common in undoped or weakly doped CeO_2 nanoparticles prepared under certain conditions. CeO_2 nanoparticles, particularly those doped with Fe, Co, or Mn, exhibit super-paramagnetic properties at room temperature, with blocking temperatures of roughly 20 K [58]. The magnetism

of these nanoparticles is affected by their size and the presence of oxygen vacancies, which support magnetic interactions. Doping with transition metals such as Fe^{3+} greatly improves the magnetization of CeO_2 nanoparticles, with Fe-doped samples having the greatest magnetization values. Ce^{3+} ions and oxygen vacancies play an important role in mediating ferromagnetic interactions, which contributes to the observed super-paramagnetic behavior [59].

1.5.3. Various Theories to explain ferromagnetic behavior of undoped and 4d cation doped CeO_2 nanoparticles

Undoped CeO_2 nano powders exhibit modest ferromagnetism at room temperature attributed to oxygen vacancies and localized Ce^{3+} ions on the surface. The F-center exchange, double exchange interaction and BMP models are several models to explain how 4d TM doping enhances ferromagnetism by increasing oxygen vacancies, strengthening BMP coupling, and perhaps introducing novel orbital interactions.

1.5.3.1. Carrier Mediated Exchange (RKKY Model)

The RKKY model is an important idea for understanding indirect exchange interactions in magnetic materials, particularly DMSs and DMOs. The acronym RKKY stands for Ruderman-Kittel-Kasuya-Yosida. It addresses the indirect exchange interaction of localized magnetic moments (such as those from doped magnetic ions) in a metal or semiconductor via conduction electrons. In this model, magnetic ions are randomly distributed in a non-magnetic host material, such as CeO_2. These magnetic ions do not interact with one another, but instead interact via conduction electrons (free or weakly bound electrons in the material). These electrons "feel" the presence of a magnetic ion and become spin-polarized. This spin-polarization spreads in an oscillatory way and affects surrounding magnetic ions, causing them to align their spins in either ferromagnetic or anti-ferromagnetic orientation. If free carriers (for example, oxygen vacancies or doping) are present in DMOs, the RKKY model can assist explain long-range magnetic ordering between dilute magnetic ions. The strength of the RKKY interaction is strongly dependent on the distance between Ce ions. As the distance rises, the contact often diminishes, following a power-law pattern, which is critical for understanding magnetic ordering in nanoparticles. The RKKY coupling constant varies with temperature, indicating that ferromagnetic

interactions may persist even at high temperatures, which is relevant for applications in spintronics [60].

1.5.3.2. F-Centre Exchange (FCE) Interaction.

An F-center is an oxygen vacancy in an oxide lattice that holds an electron. Trapped electrons in magnetic oxides like CeO_2, ZnO, and TiO_2 facilitate magnetic coupling between non-magnetic or weakly magnetic ions. Oxygen vacancies arise in the oxide lattice, leaving behind two electrons. These electrons may localize at the vacancy site, generating an F-center. Charge compensation reduces nearby cations, such as Ce^{4+}, to Ce^{3+}. These Ce^{3+} ions exhibit localized magnetic moments ($4f^1$). The F-center (trapped electron) can overlap with the orbital of two nearby magnetic ions, such as Ce^{3+}, resulting in indirect exchange coupling. The intrinsic ferromagnetism in CeO_2 is believed to be explained by the FCE mechanism as nanocrystalline CeO_2 has a high number of oxygen vacancies and $Ce^{4+} \leftrightarrow Ce^{3+}$ transitions are frequently observed due to redox flexibility [61].

1.5.3.3. Bound Magnetic Polarons (BMP) Model

A magnetic polaron is a quasi-particle created when a charge carrier (e.g., electron or hole) is surrounded by a zone of aligned magnetic moments (usually from localized magnetic ions such as Mn^{2+} in diluted magnetic semiconductors). The carrier polarizes the spins of adjacent magnetic ions through exchange interactions. This forms a local ferromagnetic zone, which stabilizes the carrier. It's like a "bubble" of magnetic alignment that moves alongside the carrier. In recent years, extensive research has been conducted on the properties of a shallow donor electron paired with non-uniform spin polarization of localized 3d or 4f electrons. A bound magnetic Polarons (BMP) is the ultimate bound state with significant electrostatic and magnetic (s-d coupling) energy. Doping leads to an exchange interaction between oxygen vacancies and dopant ions. These electrons are coupled to a defect called an oxygen vacancy, which is housed in a hydrogenic orbital. In this case, hydrogenic electrons are obtained from a BMP by correlating with three-dimensional metal ions inside their orbits. Doping causes FM by exchange interactions between free charge carriers and spin of dopant ions, resulting in an exchange contact between oxygen vacancies and dopant ions. These interactions lead to the creation of BMPs. In the doped system, magnetic vacancies accept one electron to form an H-like orbit of limited radius 'r'.

The FM behavior with radius 'r' results from the interaction of doped magnetic ions with impurity electrons [62]. When the defect concentration is above the percolation threshold, the dopant ions form complexes groups through oxygen vacancy-mediated coupling. Bridging oxygen vacancies improves system stability and creates local magnetic Polarons, causing FM [63]. Figure 1.5 indicate that F centers use oxygen vacancies and interact with dopant ions to produce BMPs. Overlapping of these causes long-range FM ordering. In this way, this study emphasizes the importance of the BMP model and sheds light on the process behind dilute ferromagnetism.

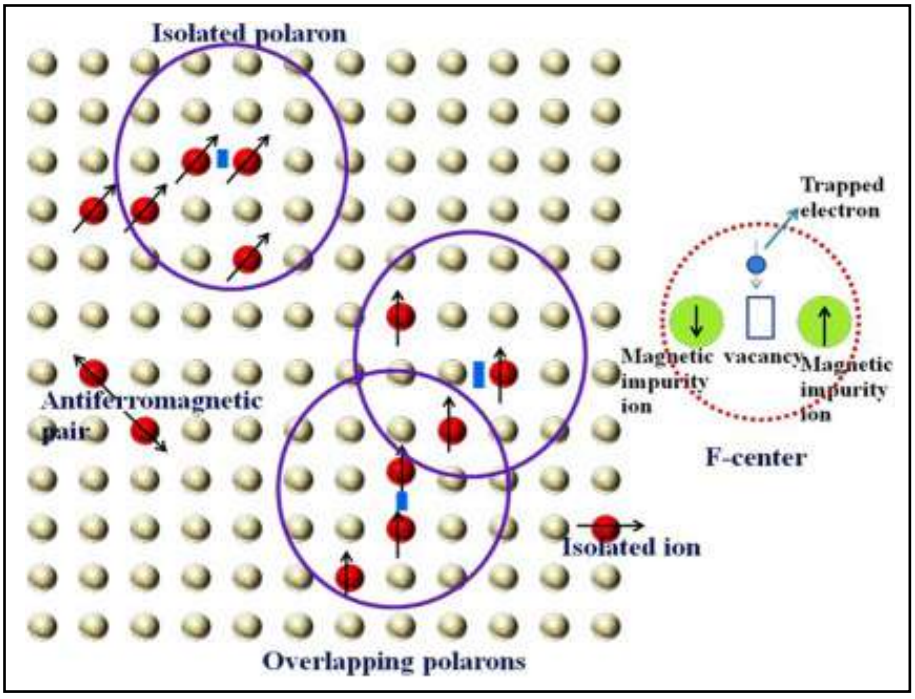

Figure 1.5: Schematic representation of bound magnetic polaron

1.5.4. Various Magnetization parameters

Magnetic parameters are physical parameters used to explain the magnetic behavior of materials. Here are some of the most frequent magnetic parameters, along with brief descriptions: Magnetic susceptibility (χ) is a dimensionless proportionality constant that determines a material's magnetization in response to a magnetic field. It is given by $\chi = M/H$, where M represents magnetization (A/m) and H represents the magnetic field strength (A/m). The magnetization is the vector field representing the density of permanent or induced magnetic dipole moments in a magnetic material. Magnetic flux density (B) refers to the quantity of magnetic flux per unit area perpendicular to the direction of magnetic flow. A constitutive relationship relates the

M-H and B-H loops: B equals μ_0 (M + H) in SI units [64, 65]. The saturation magnetization is the maximum magnetization occurs when all magnetic dipoles align in an external magnetic field.

1.5.5. Dependence of saturation magnetization on oxygen vacancies

The relation between saturation magnetization and oxygen vacancies is crucial in many magnetic materials, especially transition metal oxides. According to research, oxygen vacancies have a considerable impact on magnetic characteristics, especially saturation magnetization (Ms), via ferromagnetic and anti-ferromagnetic interactions [66]. Oxygen vacancies can have a major influence on saturation magnetization, particularly in oxide materials like transition metal oxide. Oxygen vacancies can reduce the oxidation state of neighboring transition metal ions. In CeO_2, oxygen vacancies can transform Ce^{4+} to Ce^{3+}. Mixed valence states (e.g., Ce^{4+}/Ce^{3+}) allow for double exchange interactions, boosting ferromagnetism and Ms. In non-magnetic materials like ZnO or TiO_2, oxygen vacancies can cause magnetism without the presence of magnetic ions. This is due to polarization of the conduction band or the formation of magnetic polarons, which increases saturation magnetization. For example, in Co-doped TiO_2, an optimum concentration of oxygen vacancies leads to a maximum Ms of 1.19 emu/g, but excessive vacancies can reduce magnetization due to anti-ferromagnetic interactions among Co^{2+} ions [67]. Excessive oxygen vacancies in certain materials can lead to disorder or anti-ferromagnetic interactions, reducing magnetization. This impact is nonlinear, with an optimal degree of vacancies for maximum magnetization.

1.5.6. Magnetic properties of 4d cation doped CeO_2 nanoparticles.

The magnetic characteristics of 4d cation doped CeO_2 nanoparticles have been intensively investigated, yielding important information about their ferromagnetic behavior and the effect of oxygen vacancies. Yttrium doping causes FM in CeO_2 nanoparticles, with Ms increasing up to a doping level of 9% before decreasing. The presence of Y^{3+} ions causes the formation of oxygen vacancies, which are necessary for improving magnetic characteristics. These voids promote charge delocalization, which contributes to the observed ferromagnetism [33]. ***Kumaran et al***. [68] reported that increasing Pd concentration from 3% to 5% reduces paramagnetic ordering. Both Pd-doped materials show non-saturating M-H curves at high magnetic fields,

demonstrating magneto-crystalline anisotropy. These findings reveal a weak paramagnetic ordering in the Pd-doped materials, with 5% Pd-doped CeO_2 exhibiting a preference of diamagnetic behavior over paramagnetic ordering. Silver doping can supply additional charge carriers and modify the electronic structure of CeO_2, potentially improving magnetic interactions using methods such as FCE and bound BMP models [69].

1.6. Applications of 4d cations doped CeO_2 nanoparticles

1.6.1. Photo-catalyst

The photo-catalytic uses of 4d cation-doped CeO_2 nanoparticles have received a lot of attention due to their increased efficacy in degrading organic contaminants and promoting chemical processes under light irradiation. Under UV irradiation, the charge separation process allows photo-generated electrons in semiconductors to migrate from the conduction band to the noble metal. The presence of noble metals slows electron-hole pair recombination in semiconductors, increasing photo-catalytic activity [70]. Several studies have shown that doping CeO_2 with 4d cations can increase its photo-catalytic characteristics by altering its electronic structure and producing oxygen vacancies, which provokes photo-catalytic activity. As reported by ***K. Negi et al.*** [71] in case of Ag/CeO_2 nano-crystal material, the photo-degradation of Rh B dye increases from 0.1 to 0.15 g of catalyst, but declines at 0.2 g. For complete photo-degradation of Rh B, the prepared Ag/CeO_2 catalyst should weigh 0.15 g. The UV-Vis spectra of deteriorated Rh B dye over 0.15 g of Ag/CeO_2 catalyst demonstrated complete degradation under UV light. According to ***A. Akbari et al.,*** [72] under visible light, Y-doped CeO_2 effectively degrades Rhodamine B solution for 6 hours because of the reduced band-gap value in the visible area, as confirmed by the UV-visible reflectance spectrum. Furthermore, because yttrium doped CeO_2 has a larger surface area than undoped CeO_2, visible light irradiation on its surface effectively creates electrons and holes through redox (reduction and oxidation) during the photo-catalytic reaction. The experimental results of ***S. Gnanam et al.*** [73] reported that the photo-catalytic activity of Cd^{2+} doped CeO_2 is higher than that of Pd^{2+} doped CeO_2, indicating that Cd^{2+} has a better degradation efficiency.

1.6.2. Electrochemical applications

Electrochemical properties refer to the numerous behaviors that materials display during redox reactions, which are determined by their structural and compositional characteristics. These properties are important in many applications, including energy storage, corrosion protection, and sensor technology. Because of their high specific capacitance and electro-active surface area, CeO_2 nanoparticles show promise for energy storage and electro-catalysis applications. A wide range of electrochemical methodologies have been used to investigate super-capacitors, including galvanostatic charge-discharge cycling, cyclic voltammetry (CV), and electrochemical impedance spectroscopy. The sections that follow provide the important discoveries about the electrochemical performance of CeO_2 nanoparticles when doped with 4d cation elements.

1.6.3. Supercapacitor Applications of 4d cation doped CeO_2 nanoparticles

The electrochemical characteristics of 4d cation-doped CeO_2 nanoparticles have been thoroughly investigated, demonstrating significant improvements in their performance for energy storage applications. Doping with elements like Ag, Y, and Cd has been demonstrated to improve CeO_2's structural integrity and electrochemical behavior, making it an attractive option for super-capacitors and other electrochemical devices. Recently, ***Arularasu et al.*** [74] found that the (CeO_2-Zr) electrodes showed a capacitance of 198 Fg^{-1} at a current density of 1 A/g and retained around 94.9% of their capacity after 3750 cycles. This suggests both strong reversibility and exceptional stability. A ternary Ag/CeO_2/rGO nanocomposites prepared by ***M. Vanitha et al.*** [75], reported to results in a high-specific capacitance electrode. The constructed ternary nano-composite had a specific capacitance of 710.42 Fg^{-1}. At a current density of 0.2 Ag^{-1}, the nano-composite's three components contribute significantly to its efficiency as a supercapacitor. The ternary Ag/CeO_2/rGO nano-composite has excellent recycling stability, making it a promising material for supercapacitor applications. Several key components determine a system's electrochemical properties, such as a supercapacitor or a battery. These attributes have an impact on the system's performance, efficiency, and applicability for specific applications. The primary components of electrochemical characteristics are:

1.6.3.1. Cyclic Voltammetry

The process involves oxidation and reduction reactions that produce distinct peaks in the current vs. voltage (I-V) curve, often known as a voltammogram [76]. The CV analysis of CeO_2 nanoparticles and their Zr-doped version has been conducted by ***Arularasu et al.*** [74] throughout a potential window of -0.5 to 0.8V at scan speeds ranging from 5 to 100 mVs^{-1}. This analysis provided substantial insights. The electrochemical behavior of these materials reveals redox peaks that highlight their pseudo-capacitive properties, principally due to cerium valence state transitions (Ce^{3+}/Ce^{4+}). According to ***Murugadas et al.*** [77], doping Ag with CeO_2 nanostructures enhances surface kinetics and electronic conductivity in the material. Ag and CeO_2 nanoparticles have a synergistic impact, resulting in increased capacitance in the CV of doped samples. This is due to the larger surface area and strong electrical conductivity of the nanoparticles. While the emphasis on 4d cation-doped CeO_2 nanoparticles is encouraging, it is required to consider the larger implications of doping and composite formation on the electrochemical properties of various nanostructures, as these factors can have a significant impact on performance outcomes in practical applications.

1.6.3.2. Galvanic Charging Discharging

The electrochemical properties of 4d cation doped CeO_2 nanoparticles, particularly during galvanic charging and discharging, show considerable improvements in performance measures such as specific capacitance and cycling stability. Doping with TM has been demonstrated to improve CeO_2's electrochemical performance, making it a suitable candidate for supercapacitor use. ***Murugadoss et al.*** [77] reported that doping Ag with CeO_2 nanostructures enhances surface kinetics and electronic conductivity in the material. Nanoparticles in doped samples exhibit increased capacitance in the GCD curve due to their larger surface area and strong electrical conductivity. Based on the GCD result, ***M. Sun et al.*** [78] reported that Zr-doped CeO_2 electrode has significantly higher capacity than pristine CeO_2, even at high current density of 10 A/g.

1.6.3.3. EIS

The electrochemical impedance spectroscopy (EIS) and Nyquist plot analysis of 4d cation-doped CeO_2 nanoparticles provide valuable information on their

electronic properties and charge transport mechanism. EIS offers information about the charge transfer resistance and capacitance of nanoparticles. The Nyquist plot often shows a semicircle at high frequencies, suggesting charge transfer resistance, and a straight line at low frequencies, representing Warburg impedance due to ion diffusion [79]. The diameter of the semicircle corresponds to the charge transfer resistance; smaller diameters imply increased conductivity due to efficient doping. The slope of the low-frequency line represents the diffusion behavior of ions, which is affected by the concentration of dopant and the associated defect structure. As reported by ***Matussin et al.*** [32] that significant reactions were observed with both 3% and 5% Pd-doped CeO_2 nanoparticles, particularly when exposed to visible light. Lower resistances from 3% and 5% Pd-CeO_2 indicate faster interfacial charge transfer. ***M. Vanitha et al.*** [75] reported that the Rct values for Ag/CeO_2/rGO, CeO_2/rGO, and CeO_2 were 95, 210, and 527 **Ω**, respectively. The lower electrolytic resistance of Ag/CeO_2/rGO ternary composite outperforms the CeO_2/rGO nano-composite due to its vertical domain parallel to the imaginary axis.

1.7. Main Objectives of the Research Work

The main objective of proposed research work is

- To investigate the structural properties of 4d transition elements doped CeO_2 nano-materials such as particle size, lattice-parameters, lattice spacing and surface morphology.
- To determine the optical properties of 4d transition elements doped CeO_2 nano materials such as absorption peaks, band gap energy and refractive index.
- To investigate the electronic structure properties of 4d transition elements doped CeO_2 like electronic and chemical state of given compound with defects.
- To investigate the magnetic properties of 4d transition elements doped CeO_2 like coercivity, saturation magnetization and remanence.

1.8. Discussion

DMS materials bridge the gap between magnetism and semiconductor physics, making them critical to the development of next-generation spintronics devices. They provide a technique to combine memory and logic, resulting in faster, more energy-

efficient electronics. Among these materials, CeO_2 is a multifunctional material with potential applications in green energy, environmental technology, nano-medicine, and next-generation electronics. Its distinct redox activity and nano-structuring potential put it at the center of various future technological developments. Doping CeO_2 with 4d cations creates oxygen vacancies, alters the electronic structure, and improves catalytic and photo-catalytic performance. These alterations make 4d-doped ceria an excellent choice for nano-electronic applications. The main purpose of this research work is to highlight the study on 4d cation-doped CeO_2 nanoparticles, focusing on improving or exploring functional properties relevant to our application (e.g., spintronics, LEDs, catalysis, super-capacitors etc).

1.9. Concluding Remarks

Although additional research on doped CeO_2 is needed to confirm that room-temperature ferromagnetic characteristics in the CeO_2 lattice are intrinsic. Meeting the world's energy demands necessitates the discovery and development of new electrode materials with higher energy and power density, as well as superior performance. There is still much work to be done to establish a correlation between the structural, optical, electronic, magnetic, and electrochemical properties of these samples, so we chose to tackle this task in the current thesis with 4d transition metal impurities in the CeO_2 lattice to study all properties as well as their application in spintronics, optoelectronics, and super-capacitors. Ce is the most important member of the lanthanide spectrum because to its non-toxic and environmentally friendly properties.

Chapter 2
Synthesis of Nanoparticles and Characterization Techniques

Chapter-2

Synthesis of Nanoparticles and Characterization Techniques

2.1. Introduction

Chemical synthesis, sample analysis, and result interpretation are all part of the Rare Earth and transition metal doped Cerium Oxide research. As a result, this chapter describes sample processing techniques, such as sample preparation and experimental methods. In materials science, “characterization” refers to the process of studying and comprehending material properties. Characterization techniques are critical for understanding material properties and behaviors in a variety of domains, including ceramics, nano-materials, and advanced materials such as graphene. These techniques allow researchers to evaluate mechanical, chemical, and structural properties, hence facilitating material creation and use. As a result, this chapter provides a summary of the various characterization techniques used in this study.

There are several methods for preparation of nanoparticles, each customized to a different material and application. Some common processes are hydrothermal [80], sol gel [81], sono-chemical [82], combustion [83], co-precipitation [84], micro-emulsion [85] and chemical vapor deposition. Among these methods, the coprecipitation process is frequently used for the synthesis of nanoparticles and materials because of its multiple applications. This approach allows for exact control over particle size, composition, and morphology, making it useful in a variety of applications. However, it requires careful reaction conditions to avoid agglomeration or unwanted phase formation. In this study, oxides nanoparticles are synthesized utilizing a co-precipitation method.

2.2. Preparation Technique: Co-Precipitation Method

The co-precipitation method is a well-known technique for synthesizing nanoparticles, particularly metal oxides, and it has unique advantages and challenges when compared to other synthesis methods. However, it frequently results in a broad size distribution, which might have an impact on nano-particles morphology and characteristics.

The procedure entails combining metal salt solutions, followed by the addition of a precipitating agent, usually in a basic solvent. Nucleation, proliferation, and

coagulation of particles are important mechanisms that might cause poly-disparity in size distribution.

Controlling parameters like pH and temperature allows for the control of particle properties, which influences their morphology and size. Figure 2.1 depicts a flow chart for each of the stages involved in the co-precipitation method.

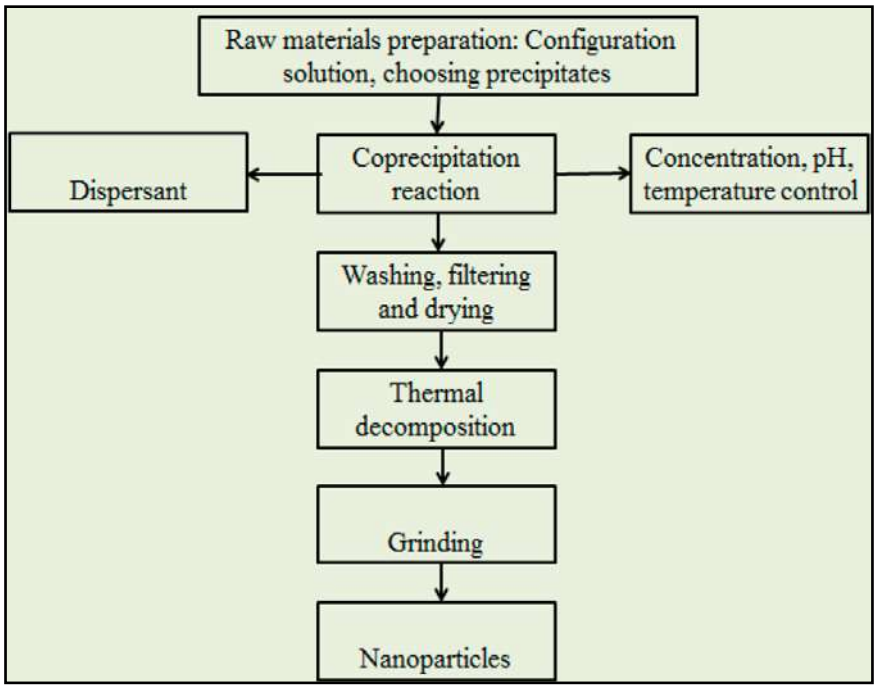

Figure 2.1: Flow chart of the preparation of the nanoparticles by the co-precipitation method

2.1.1. Co-precipitation Method

The co-precipitation method is a common process in materials science and chemistry for preparation of nanoparticles and mixed metal oxides or hydroxides. The following are the major steps in the co-precipitation method. Dissolve metal salts (such as nitrates, chlorides, or sulfates) in distilled or distilled water. This procedure ensures a uniform distribution of metal ions. Add a precipitating agent, such as NaOH or NH_4OH drop-wise to the metal ion solution while constantly stirring. Allow the precipitate to age for a set amount of time (4 hours), during which particle development, crystallization, and phase transitions may occur. Filtering, centrifuging, or decanting is used to separate the solid precipitate from the liquid phase. Wash the precipitate with distilled water (or ethanol) to eliminate any soluble contaminants, dry the cleaned precipitate in an oven (usually between 60 and 120°C) and then annealed

at 500°C. This method used the appropriate stoichiometry ratio of Alfa-Aesar's high purity chemicals, $Ce(NO_3)_3.6H_2O$, $AgNO_3$, $Y(NO_3)_3.6H_2O$ and $CdNO_3.4H_2O$ to yield $Ce_{1-x}Ag_xO_2$, $Ce_{1-x}Y_xO_2$ and $Ce_{1-x}Cd_xO_2$ nanoparticles. First, these compounds are methodically weighed using an accurate Percisa XB 220A balance with 0.0001 gm precision to determine their stoichiometry ratio as shown in figure 2.2.

Figure 2.2: Photograph of Precisa XB 220 A Analytical Balance

2.3. Characterization Techniques

This section gives an overview of the characterization techniques for undoped and transition metal doped CeO_2 nanoparticles. The following are major characterization techniques commonly employed in the field. X-ray Diffraction (XRD) is used for phase identification and crystallite size investigation, XRD is essential for understanding the structural characteristics of materials. Scanning Electron Microscopy (SEM) provides high-resolution pictures of sample surfaces that reveal topographical features. Transmission Electron Microscopy (TEM): allows for atomic-level imaging, which is essential for understanding material structure. Energy Dispersive X-ray Spectroscopy (EDX) is used to determine the elemental composition. UV-Vis NIR spectroscopy is important for identifying the optical band gap of materials because it allows for the examination of electronic transitions, which can reveal whether the band gap is direct or indirect. Raman Spectroscopy provides insights into molecular vibrations and can characterize materials such as ceramics and glasses, revealing structural and compositional information. Photoluminescence

Spectroscopy (PL) is an important tool for studying semiconductors' optical and electrical properties. It offers information on lattice defects, crystal structures, and carrier dynamics, making it extremely useful for material characterization. XPS determines chemical states and valence state. Two ways for determining the magnetic properties of nanoparticles are the vibration sample magnetometer (VSM) and the superconducting quantum interferometer device (SQUID). Understanding these characteristics is essential for applications like magnetic storage, MRI, and spintronics. Electrochemical study determines the material's energy and power density. While these methods are effective, they frequently require additional approaches to get a thorough understanding of material properties. This highlights the complexity of material characterization in research and industry.

2.4. X-Ray Diffractometer

The X-ray Diffractometer is an important tool in material science, used to identify and characterize crystalline solids. It works on the principle of X-ray diffraction, in which monochromatic X-rays (Cu Kα; 1.54 Å) interact with parallel crystal planes and scattered by the crystal lattice, resulting in a distinct diffraction pattern that gives structural information about the material. In this method, each lattice point in the parallel planes serves as a slit, and constructive interference produces sharp diffraction peaks in the graph (as shown in figure 2.3).

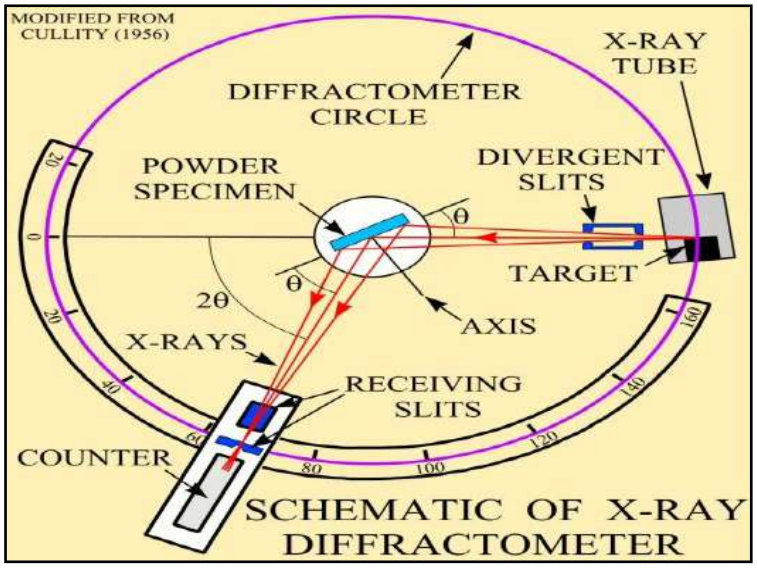

Figure 2.3: A Schematic Representation of Diffraction of X-Ray By crystallographic Plane (Bragg's Law)

2.4.1. Principle of XRD:

When X-rays with wavelengths equivalent to inter-atomic distances (0.15-0.4 nm) impact a crystal, they scatter in specified directions due to the periodic arrangement of atoms. This scattering produces constructive and destructive interference patterns, which can be used to determine crystal structure (figure 2.4). Constructive interference between dispersed rays arises when the difference in path length between two diffracted rays is an integral number of wavelengths. Bragg's law, also called Bragg's equation, states this situation mathematically as follows [86]:

$$2dsin\theta = n\lambda \quad \textbf{(2.1)}$$

Here, n is an integer, d is the interplanar distance, θ is the angle between the incident beam and the lattice planes, and λ is the X-ray wavelength. This approach allows for the determination of crystallographic structures and is critical for determining parameters such as the Crystallinity Index (CI) in materials. Misaligned samples can cause peak broadening and shifts in diffraction patterns, making it difficult to fulfill Bragg's Law. Overall, while Bragg's law is a fundamental principle of XRD, its implementation is impacted by a variety of experimental settings and theoretical considerations. The θ/2θ scan technique is extensively used to obtain diffraction patterns, allowing for both qualitative and quantitative investigation of minerals. Crystal phases are identified by examining the angles and intensities of diffraction spots. Overall, XRD is an important technique in materials research.

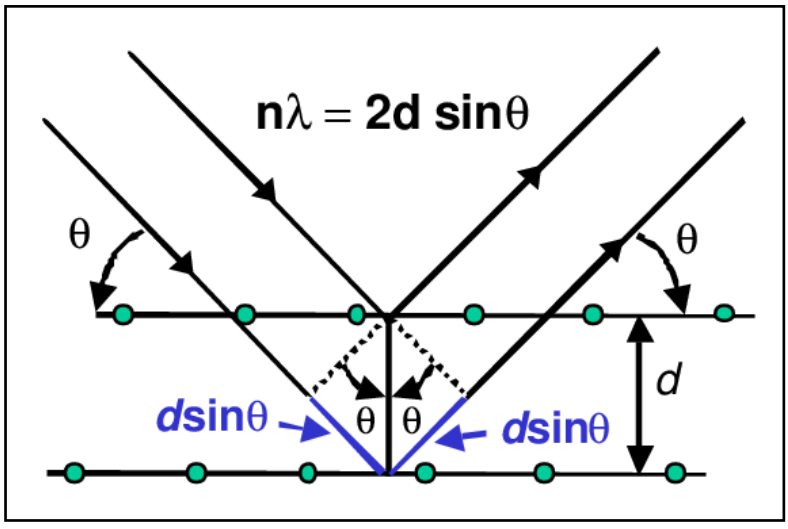

Figure 2.4: Bragg's diffraction

2.4.2. Instrumentation and Working:

The Brucker D8 Advance X-ray Diffractometer (figure 2.5) employs monochromatic Cu Kα radiation (λ = 1.54 Å) to produce XRD patterns for all samples. The X-ray source stayed stationary as the sample holder spun on its axis, and the detector followed suit. At room temperature, every sample's XRD patterns are recorded throughout the 2θ range of 10^o to 90^o, with a scanning speed of 0.05^o min^{-1} and a counting duration of 5 seconds each step. The XRD technique can determine crystallite size and microscopic strain using Debye Scherer's equation [87].

$$\boldsymbol{D = \frac{k\lambda}{\beta cos\theta}} \qquad \textbf{(2.2)}$$

The particle form factor (k) is 0.9, λ is the X-ray wavelength (1.54 Å), θ is the diffraction angle (in degrees), and β is the FWHM of the XRD peak (in radians). The calculated value of FWHM (β) is: $\beta = \sqrt{(\beta_m^2 - \beta_i^2)}$, where βm and βi represent measured and instrumental broadening, respectively. The formula for determining the lattice constant of the samples is: $a = d\sqrt{(h^2 + k^2 + l^2)}$, where d and a denote the interplanar distance (h k l) and the lattice constant, respectively.

Figure 2.5: Image of Brucker D8 Advance X-ray Diffractometer

The Williamson-Hall (W-H) equations are essential for assessing crystallite size and micro-strain in materials using X-ray diffraction. The Williamson-Hall technique demonstrated how the approximation equations for size broadening (β_l) and strain broadening (β_e) varied dramatically based on Bragg angle (θ) [88].

$$\boldsymbol{\beta_{tot} = \beta_e + \beta_L = C\varepsilon\, tan\theta + \frac{K\lambda}{Lcos\theta}} \quad \textbf{(2.3)}$$

$$\boldsymbol{\beta_{tot} cos\theta = C\varepsilon\, sin\theta + \frac{K\lambda}{L}} \quad \textbf{(2.4)}$$

When the above equation is compared to the equation of straight line:

$$\boldsymbol{y = mx + C} \quad \textbf{(2.5)}$$

The slope of the plot $\beta_{tot}\cos\theta$ versus $\sin\theta$ yields strain ($C\varepsilon$) and crystallite size (K/L) components is determined using the intercept. Figure 2.6 is an example of a Williamson-Hall plot.

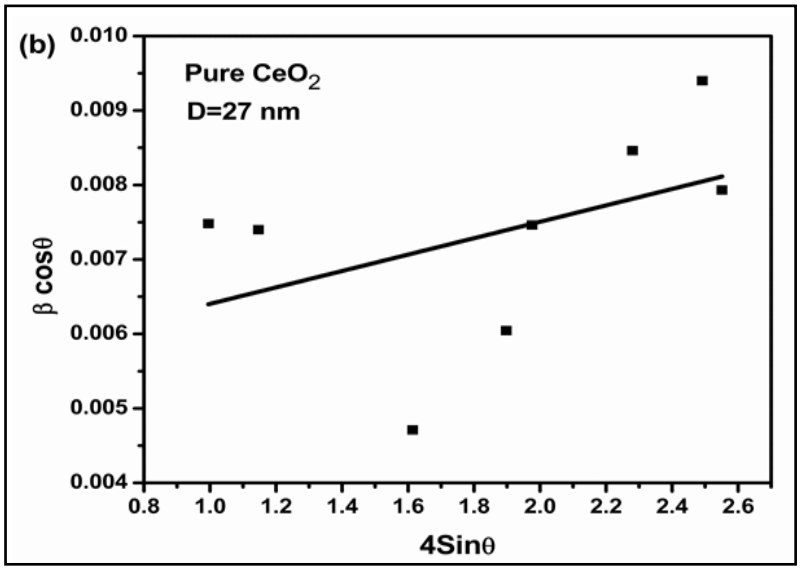

Figure 2.6: W-H plot of undoped CeO_2 nanoparticles

2.4.3. Rietveld Refinement:

Rietveld refinement is an important technique in crystallography that extracts detailed structural information from powder X-ray diffraction precise structural analysis in materials science and crystallography, enabling advances in a variety of applications. The well-known mono-crystalline diffraction approach is used to create best-fit criteria based on numerous R factors. The R factors include the Rp-profile, Rwp-weighted profile, R_b-Bragg factor, and others. This work employs the FULLPROOF software for Rietveld refinement [89]. The pseudo-Voigt function is used to fit parameters to a given data point. Volume, atomic functional sites, and Rf

factors are the refined properties obtained. This technique provides information on lattice parameters, strain, grain/particle size, dislocation density, and phase composition.

2.4.4. Information acquired from XRD:

XRD can determine the orientation and crystalline phase of a nanocrystalline material by examining its atomic and molecular structure. This technique provides information on lattice parameters, strain, grain/particle size, dislocation density, and phase composition.

2.5. Energy Dispersive X-ray Spectroscopy (EDX):

EDX is an important analytical technique for detecting the elemental composition of materials, especially in materials science and nanotechnology. EDX detects the characteristic X-rays generated by a sample when bombarded with high-energy electrons, allowing for both qualitative and quantitative study of elemental elements. The EDX setup is consists of four main parts: (1) a beam source, (2) an X-ray detector, (3) a pulse processor, and (4) an analyzer. X-rays are employed to convey the energy difference between the low- and high-energy shells. Recent advances in detector technology have substantially improved the throughput and resolution of EDX, allowing for quick analysis with precision down to 1% weight concentration. The approach is especially useful when paired with scanning electron microscopy (SEM), which provides great spatial resolution and the capacity to study nanoparticles. Furthermore, EDX can be adapted for use in low-energy electron microscopes, increasing its applicability.

Figure 2.7: Photograph of the TESCAN MIRA 3 FESEM Instrument Equipped with EDX

In this study, the quantitative analysis of undoped CeO_2 and Y, Ag- doped CeO_2 samples was performed using a TESCAN MIRA 3 FESEM equipped with an EDX system (figure 2.7) at Banasthali Vidyapith in Jaipur, India.

2.5.1. Information acquired from EDX:

EDX is used to identify trace elements in samples, such as gunshot residues and paint chips, while maintaining evidence integrity. Furthermore, EDX has been used in soil research to produce 2D chemical maps that disclose soil composition at high resolutions. The adaptability of EDX in these applications emphasizes its importance in both research and practical contexts.

2.6. Scanning Electron Microscope (SEM)

Scanning Electron Microscopy (SEM) is a sophisticated imaging technique that uses a concentrated electron beam to scan a specimen's surface, resulting in high-resolution images with an impressive depth of field [90]. SEM is particularly useful for characterizing materials, such as biological samples and electrochemical devices. The main components are an electron gun, which generates the electron beam, and several lenses, which concentrate the beam on the sample. Furthermore, modern techniques, such as surface height measurement, improve resolution and accuracy. The use of EDX enables elemental analysis, making SEM a powerful tool in materials science.

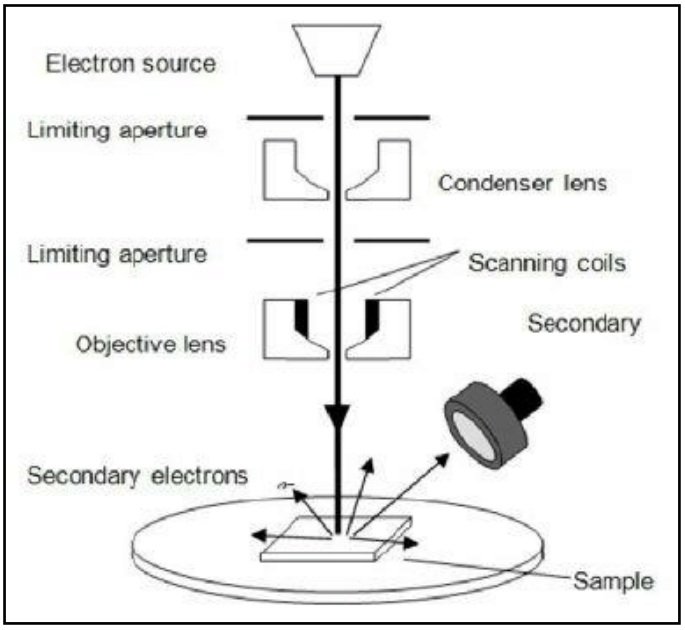

Figure 2.8: A schematic diagram of SEM

A schematic diagram of SEM (figure 2.8) shows that electrons and electromagnetic lenses are produced at the top of the column by tungsten filament lamps.

2.6.1. Information acquired from SEM:

The SEM operates in a vacuum environment to prevent electron scattering by air molecules, resulting in improved image quality. Key features include the detection of secondary and backscattered electrons, which provide information on the sample's surface morphology and composition.

2.7. Transmission Electron Microscope (TEM):

A Transmission Electron Microscope (TEM) is powerful imaging equipment that uses a beam of electrons to reveal the interior structure of specimens at the atomic or nano-scale. Unlike light microscopes, which are restricted by the wavelength of visible light, TEMs use the much shorter wavelength of electrons to attain significantly better resolution [91]. A high-energy electron beam—typically accelerated between 60 and 300 kilo electron volts (keV) is directed through an ultra-thin object, which is frequently less than 100 nanometers thick. TEM provides high-resolution viewing of nanoparticles, allowing for exact measurements of size, shape, and dispersion. For example, nanoparticles photographed via TEM are processed with software tools (ImageJ, Origin) to yield accurate size distributions. A schematic diagram of demonstrating working of TEM analysis is shown in figure 2.9.

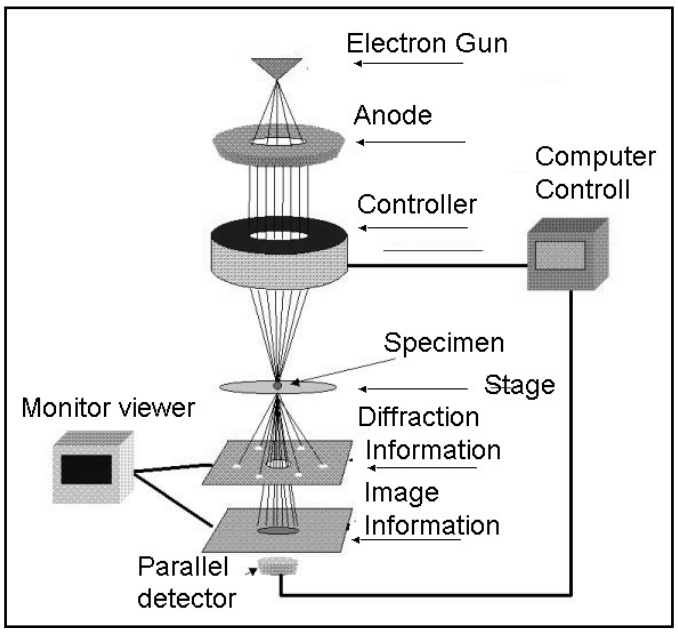

Figure 2.9: Schematic diagram demonstrating working of TEM

2.7.1. Information acquired from TEM:

Transmission Electron Microscopy (TEM) provides a lot of information about samples, particularly nanoparticles, by integrating imaging, diffraction, and spectroscopic techniques. Here is a breakdown of the insights TEM can offer:

- TEM generates high-resolution pictures (down to the sub-nanometer level), enabling exact studies of nano-particle form, size, and dispersion patterns.
- These contrast techniques make diverse sample features visible—diffraction contrast reveals crystalline areas, flaws, grain boundaries, and stacking faults, whereas mass/thickness contrast highlights dense regions.

The surface morphology, crystallinity, and average particle size of the samples were studied using a JEOL-JEM 2100 Plus TEM (figure 2.10) apparatus with an accelerating voltage of 200 kV. To prepare samples for TEM analysis, ultrasonically dispersed nano particles were applied to a typical holey carbon sheet set on a Cu grid. Further analysis of TEM images was done using ImageJ software.

Figure 2.10: Image of JEOL-JEM 2100 Plus TEM

2.8. Ultraviolet-Visible-Near Infrared (UV-Vis-NIR) Spectroscopy:

Recent advances in UV-Vis and NIR spectroscopy have greatly expanded their applications in a variety of sectors, including catalysis, agriculture, and environment monitoring. UV-Vis-NIR spectroscopy is a versatile analytical technique that is widely utilized in a variety of scientific domains due to its ability to deliver vital information about materials while avoiding harm. This approach works in the

ultraviolet to near-infrared wavelength range (usually 190-1100 nm) and is essential for identifying the chemical identity, concentration, and structural features of substances. The Lambert-Beer's law implies that the more molecules that can absorb light at a certain wavelength, the greater the amount of light absorbed. The Lambert-Beer's law is presented as follows [92]:

$$A = log\frac{I_0}{I} = \epsilon Cl \qquad (2.7)$$

In this equation, *A* indicates absorbance, I_0 is the intensity of light incident on the sample cell, I is the intensity of light leaving it, C is the molar concentration of the solute, L is the length of the sample cell (cm), and ϵ represents the molar absorptivity.

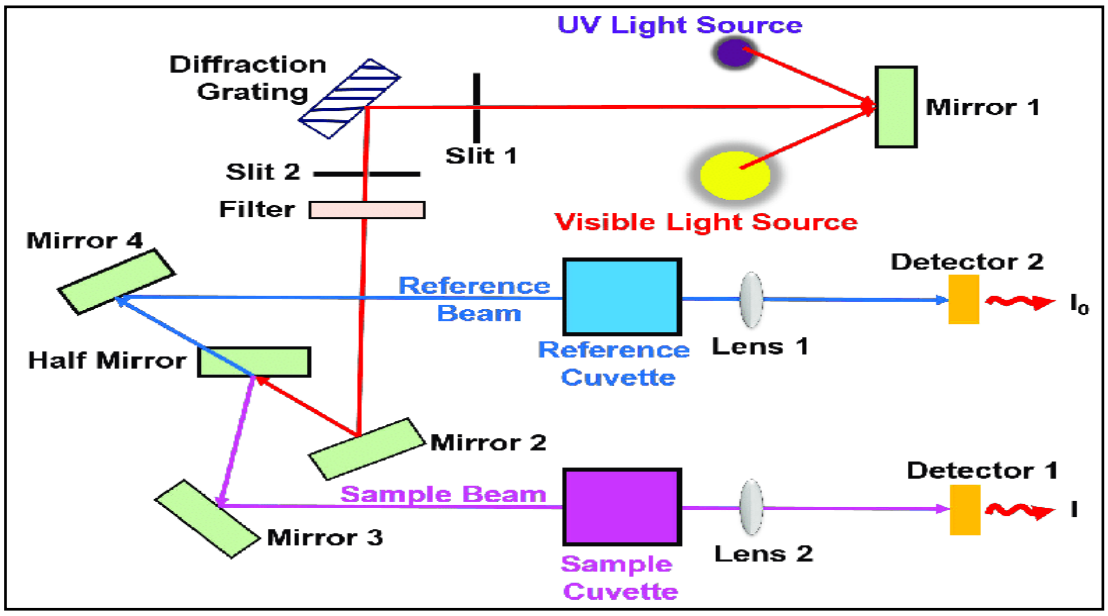

Figure 2.11: Schematic Representation of UV-Vis-NIR Spectrophotometer

UV-Vis-NIR spectroscopy is a versatile analytical technique that requires several critical components for its functioning. The required spectrum is typically emitted by a deuterium lamp for UV and a tungsten lamp for visible light as shown in figure 2.11. Sample holder holds the sample in place, ensuring a continuous light path and interaction with the source. Monochromator divides light into its constituent wavelengths, allowing for precise wavelength selection for analysis. Photomultiplier tubes, often known as CCDs, transform light into an electrical signal that can be measured. A half-mirrored device divides light from a monochromator source into two equal-intensity beams before it reaches the sample. When measuring UV

absorbance, the other bulb must be turned off, but when measuring visible light absorbance, the other lamp must be left on. In the current study, the optical absorption spectra of the sample at room temperature have been recorded using a Shimadzu UV-3600 Plus UV-Vis-NIR spectrophotometer with integrated clear cuvettes. The spectrometer has a maximum resolution of 0.1 nm and covers the wavelength range of 185 nm to 3300 nm, with slit width changes of 0.1 to 30 nm. The spectrophotometer has three detectors: InGaAs and PbS for the near infrared, and Photomultiplier tubes (PMTs) for the UV and visible ranges. As the machine scans the wavelengths, a solenoid-operated mirror automatically deflects light from either bulb.

The source comprises of a tungsten halogen lamp for wavelengths more than 375 nm and a deuterium discharge lamp for wavelengths less than that. The optical absorption spectra of the undoped and CeO_2 nano-particles samples are recorded between 200 and 1000 nm, with $BaSO_4$ serving as an internal reference. To find the peak position of the spectrum, use the spectrophotometer's peak-pick tool. There is about ±1 nm of measurement uncertainty. Although, the Shimadzu UV-3600 (figure 2.12) has vast capabilities, it is important to frequently inspect and calibrate the instrument to preserve accuracy, as external conditions might alter its performance over time.

Figure 2.12: Photograph of Shimadzu UV-3600 Plus Spectrophotometer

2.8.1. Information acquired from UV-Vis-NIR spectroscopy

UV spectroscopy evaluates materials' optical properties including the band gap energy, transmittance, reflectance, absorbance, and refractive index of the material which is important in materials science. It is also used in agricultural applications to examine the soil and plant nutrition levels.

2.9. Photoluminescence (PL)

PL spectroscopy is a versatile analytical technique for investigating the optical characteristics of diverse materials, particularly in semiconductor and photovoltaic applications. It includes the use of light to excite a sample, resulting in the emission of photons as the material returns to its ground state as shown in figure 2.13. Photo-exciton generation, dynamics, and decay require bound electron-hole pairs created by photon absorption. An Exciton is formed when an electron is excited from the valence band via photon to the conduction band, leaving a hole. Excitons have a high binding energy, particularly in low-temperature conditions, which allows them to exist as stable entities in semiconductors. Excitons eventually decay by radiative or non-radiative processes, with recombination being an important mechanism for light emission in devices such as OLEDs. Non-radiative reactions, such as triplet-triplet annihilation, can also occur and affect the efficacy of photo-catalytic materials.

2.9.1 Types of interaction:

- **Resonant Radiation:**

When a photo of a specific wavelength is absorbed, another photon of that wavelength is immediately emitted; the chemical substrate undergoes no significant internal energy changes between absorption and emission during this operation, which usually lasts 10^{-9} seconds or less.

- **Fluorescence:**

When the chemical substrate goes through internal energy transitions before relaxing to its ground state and emitting photons, some of the absorbed energy is lost, resulting in output light photons that have less energy than those absorbed. Fluorescence, with a short life of approximately 10^{-8} to 10^{-4} seconds, is the most well-known example.

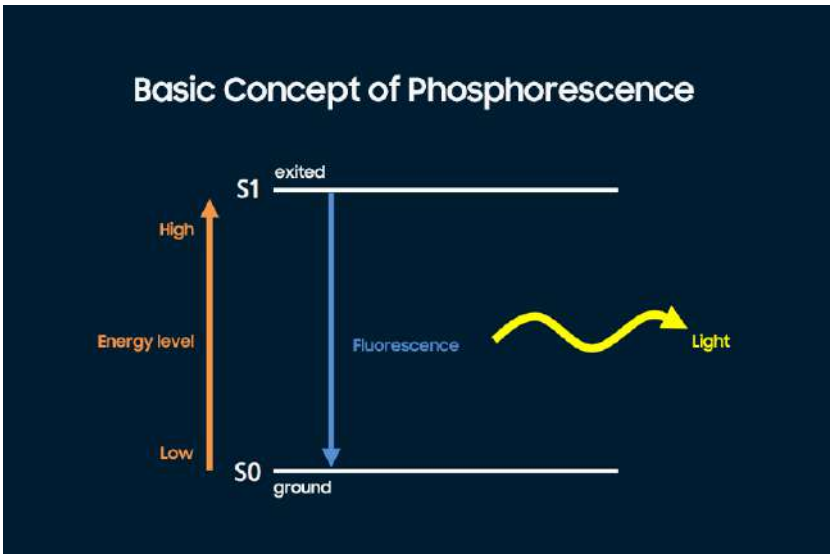

Figure 2.13: Diagram showing phosphorescence process

- **Phosphorescence:**

The absorbed energy enters a state with a different spin multiplicity, causing a radiation transition known as phosphorescence. Phosphorescence normally lasts between 10^{-4} and 10^{-2} seconds, substantially longer than fluorescence.

To limit scattered light that reaches the detector, a second monochromator is often placed 90 degrees distant from the incident light after the first monochromator selects an excitation wavelength. In most photoluminescent systems, chromophore aggregation frequently causes light emission quenching (L v CQ). However, there have been recent reports of luminogenic aggregation contributing positively to the light-emitting process rather than negatively. This "aggregated-induced emission" (AIE) offers a wide range of potential uses, especially in solid-state electronics. Thus, PL spectroscopy is a useful method for determining a substance's brightness.

2.9.2. Applications of PL

Photoluminescence (PL) has a wide range of applications that take advantage of its unique properties to provide novel solutions. This phenomenon, which causes materials to release light upon activation, is used in optoelectronic devices, urban infrastructure, and environmental monitoring, among other applications. Optoelectronics applications include photon up-conversion, which improves solar cell and LED efficiency by converting low-energy photons to higher-energy outputs.

- **Defect detection and impurity levels**: Even in pure semiconductors, localized defects (both native and impurities) can cause radiative transitions. PL energy and intensity can be used to pinpoint individual defects and quantify their concentration.
- **Material purity**: PL measurement assesses material purity and optical quality. The emission process of a material reveals the presence of defects. To determine material quality, calculate the proportion of radiative recombination. Non-radiative recombination is associated with more localized defects, which reduces material quality. These defects are damaging to device performance.
- **Determination of band gap**: Non-destructive band gap analysis is performed by analysing a semiconductor's PL spectrum variations. This approach quantifies the composition of semiconductor elements and material factors that impact device efficiency, such as solar cells.
- **Recombination**: The term "recombination" refers to radiation and non-radiative processes that occur in the band gap due to defects and interfacial areas. The photo excitation power and temperature impact the intensity of the PL, as demonstrated by the dominant recombination process.

2.9.3. Instrumentation and experimental technique

When a substance is illuminated with high-energy light, photons are absorbed and excitations occur. A beam with a wavelength near the sample's band gap energy illuminates it. The sample is positioned so that the reflected laser beam and PL emission face opposite directions. A fiber optic connection carries light to a spectrometer. To block incident laser light, place a filter in front of the fiber input. Different wavelengths diffract differently to the spectrometer's array of photo detectors, which determines the strength of each wavelength component. After analyzing the digital data, the computer may generate a PL spectrum. As light enters the detector, the spectrum displays the intensities of the various wavelengths.

2.9.4. Types of PL spectra

The underlying physical principles that produce various forms of photoluminescence (PL) spectra vary depending on material properties and excitation conditions. These mechanisms can be broadly classified into three major aspects: the

character of electronic transitions, the involvement of material structure, and the influence of external variables.

- **Emission spectrum**

The emission photoluminescence (PL) spectrum is an important part of material characterization, providing information about electronic states and imperfections. The emission monochromator chooses a wavelength based on peak values in the emission spectrum obtained during measurement. The excitation monochromator is also tested at wavelengths shorter than the emission. The resulting emission, which is just the excitation spectrum, is recorded. Because excited electrons are unstable, they return to their lower ground state via radiated radiation.

- **Excitation spectrum**

The excitation monochromator determines a certain wavelength (λe). This wavelength is often proportional to the host material's band gap. Excitation radiation is allowed to flow through the slit and onto the sample. The atoms in the sample undergo atomic transitions during the excitation process, resulting in the emission of radiation with a wavelength longer than the excitation wavelength. The resultant light flows through the emission monochromator, which detects wavelengths longer than the excitation wavelength. The sample transition probability may produce one or more emission maxima in the spectrum.

2.9.5. Luminescence parameter

The color chromaticity space developed by the Commission Internationals de L'Eclairage is the most used method (CIE) [93]. The color point is determined from the spectrum energy distribution of the emission and shown in a normalized two-dimensional coordinate diagram using the Commission Internationals de l'Eclairage (CIE) plot as shown in figure 2.14. The chromaticity coordinates are x, y, and z, which correspond to the color’s red, green, and blue, respectively. Color-matching functions (CMF) are calculated by combining three basic colors in a simulated patch and altering the lighting on the reference patch. The CMF gives the tristimulus values required to compare to a hypothetical equal-energy spectrum with equal energy at all wavelengths, yielding an illuminated E that is perceived as white.

- **The Correlated Color Temperature (CCT)**

The correlated color temperature (CCT) is the temperature required for a blackbody radiator to produce the same chromaticity as light. Lower color temperature light beams appear yellow-red, whereas higher temperature light beams appear bluer. Luminaries for general illumination will be placed around the CIE chromaticity diagram's blackbody center. The CCT can be determined using the formula given below [94]:

$$\boldsymbol{CCT = -437n^3 + 360n^2 - 6861n + 5514.31} \qquad \textbf{(2.8)}$$

Where $n = \frac{(x-x_e)}{(y-y_e)}$; xe and ye are chromaticity epicentres, they have values of 0.3320 and 0.1858, respectively.

- **Colour Purity**

Colour purity is proportional to the gap between the 1931 CIE point and the line's terminus. The colour saturation excitation purity is a well-defined expression. The dominating wavelength produces more saturated hues, whereas lower excitation purity results in less saturated colours like white.

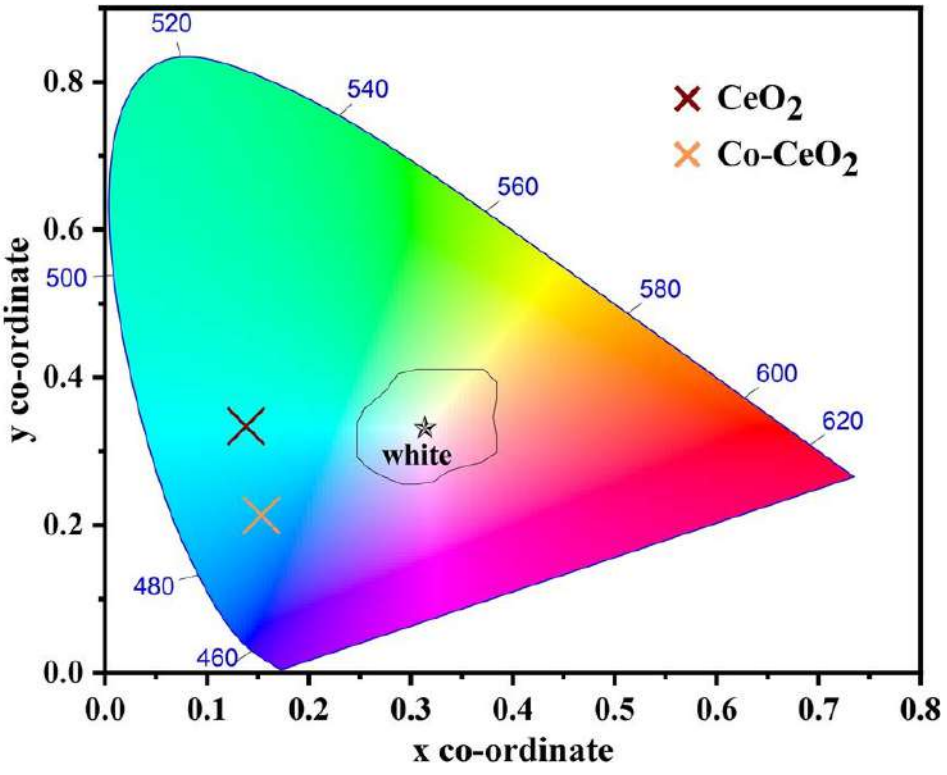

Figure 2.14: CIE plot of undoped and Co-doped CeO_2 nanoparticles

- **Dominant wavelength**

The dominant wavelength is the wavelength that a radiation source produces most frequently. To get the dominant wavelength, evaluate the light source's (x, y) colour coordinates and draw a line from one of the 1931 CIE white illuminations to the colour space's border. Color calculator software is used for determining color parameters, particularly those that analyze spectral data to calculate CCT, CRI, and other chromaticity-related parameters.

2.9.6. Information from PL

Photoluminescence (PL) spectra provide crucial information on material attributes such as impurity detection, structural changes, and device performance. The analysis of PL spectra can disclose information about the electronic and optical properties of materials, which possess variety of applications such as LED formation and solar cell performance. PL is particularly sensitive to impurities and lattice distortions, making it possible to check material quality. Spectral shifts can signal phase transitions in crystalline materials, with considerable intensity differences related to nanoparticles inclusions.

2.9.7. Specification of Model

In this research work, Horiba Jobin Yvon, LabRAM HR Evolution (figure 2.15) was used with the following specifications: Wavelength Range: He-Cd 325nm (30mW), Oxxius 532nm (100mW), and IPS Laser 785 nm(90mW); Detector Type: CCD, InGaAs (for NIR region); Spectral Range: 50 cm^{-1} to 4000 cm^{-1}

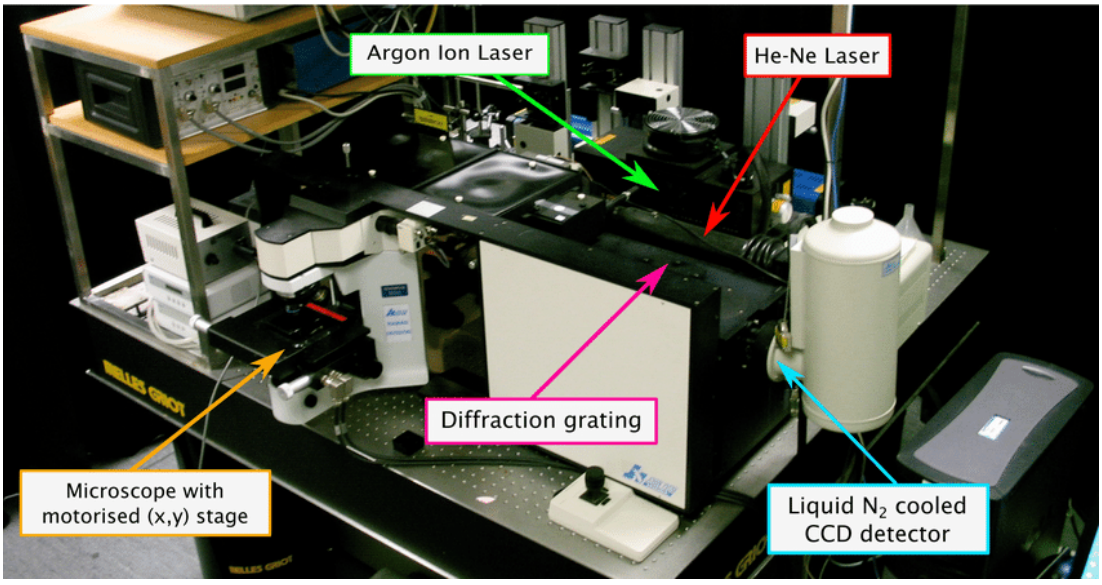

Figure 2.15: Photograph of Horiba-Jobin Yvon Labram HR800 spectrometer

2.10. X-ray photoelectron spectroscopy (XPS)

XPS is an important technique used in many scientific domains, including surface characterization and catalysis. It allows for the analysis of materials' electronic structures and chemical states, which provides information about their surface properties. The basic working principal of XPS is the photoelectric effect, which is a fundamental physics phenomenon that occurs when a material is subjected to high-frequency light (figure 2.16). If the X-ray photon's energy (E_{hv}) exceeds the electron's binding energy (E_{BE}), the excess energy is employed as the kinetic energy energy (E_{KE}) of the expelled photoelectrons. This is given as [95]:

$$\boldsymbol{E_{hv} = E_{KE} + E_{BE} + \phi_0} \qquad \textbf{(2.9)}$$

Where ϕ_0 is the material's work-function. The significance of the remaining symbols is explained above.

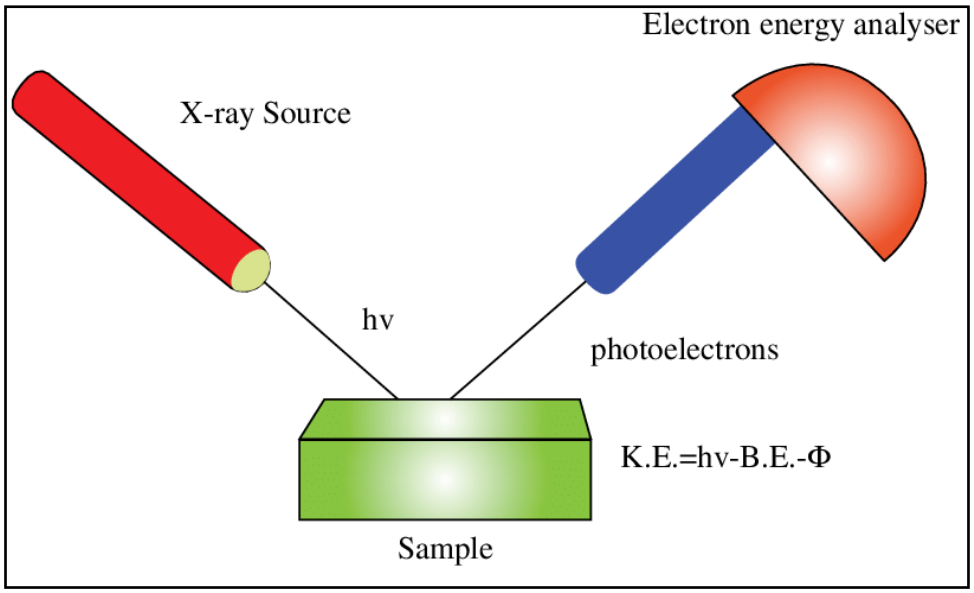

Figure 2.16: Schematic representation of working operation of XPS

The XPS spectrum is drawn by plotting kinetic energy against electron count. The quantity of that specific element depends directly to the number of electrons with a given kinetic energy, by measuring the kinetic energy of electron using XPS spectra, the binding energy of an electron can be calculated. The calculation of binding energy (BE) with X-ray photoelectron spectroscopy (XPS) entails examining the energy levels of core electrons in materials. XPS spectra show peaks that correspond to core-level electrons, with binding energies determined by the difference between photon energy and kinetic energy of emitted electrons. For example, in TiO_2 nanoparticles,

binding energies for Ti are discovered at 458.42 eV and 464.13 eV, validating expected electronic structures [96] to have chemical composition of various components in the sample. Ultra-high vacuum (UHV) conditions are required for XPS measurements. It is largely a surface method for studying the material's surface chemistry.

The XPS spectra are acquired in the analysis chamber with an ESCA+ Omicron Nanotechnology (Oxford apparatus, Germany) (figure 2.17) apparatus at a base pressure of 10^{-8} Torr. The X-ray source used mono-achromatized Al Kα (hv =1486.7 eV) radiation, and the binding energy scale is calibrated using the adsorbed hydrocarbon's C 1s line (hv = 284.6 eV) on the sample surface. The operating voltage and current of the instrument are set to 15 kV and 20 mA, respectively. The short scan pass energy is 20 eV, and the survey scan is 50 eV. Samples are collected in pellet form, wrapped in Cu tape, and degassed overnight in an XPS FEL room to reduce air contamination on the sample surface, as well as in the main sample chamber.

Figure 2.17: K-Alpha X-ray photoelectron spectrometer (Thermo Fisher SCIENTIFIC) XPS instrument

To remedy the charging issue, a 2 KeV charge neutralizer is added to the sample. The electron take-off angle, or angle between the analyzer and the source, is 90 degrees, and the measurements validated a resolution of around 0.60 eV using FWHM. The X-rays produced are allowed to fall on the sample placed on the sample stage. The electron collecting lens, electron detector system, and electron energy

analyzer are utilized to determine the kinetic energy of the ejected electrons and count those with a specific kinetic energy. This investigation is carried out in an ultra-high vacuum to prevent electron energy loss from interactions with residual gas molecules.

2.10.1. Information acquired from XPS

XPS identifies the components present on the material's surface (usually the top 5-10 nm). It determines the atomic proportion of each element (excluding H and He) and detects the oxidation state of elements, such as Ce^{3+} vs Ce^{4+} in CeO_2 and Fe^{2+} vs Fe^{3+}. It provides information about electron density and bonding environment. Because XPS is surface-sensitive, it can differentiate between surface-enriched and bulk compositions. It is effective for assessing surface coatings, adsorbed species, and surface-modified nanoparticles It also detects undesirable materials or surface contamination (such as adventitious carbon and chlorine residues). Provides information on the valence band structure, which is useful for semiconductors.

2.11. SQUID -VSM

SQUID magnetometer is highly sensitive and can detect magnetic fields as low as 10^{-14} Tesla. It works on the principle that when an external magnetic field is supplied, it alters the magnetic flux across the loop. Because of flux quantization, the SQUID modifies the current in the loop to retain discrete flux values. SQUID displays RTFM caused by oxygen vacancies or Ce^{3+} ions in doped CeO_2, while Vibrating Sample Magnetometer (VSM) is a device used to test the magnetic characteristics of materials, particularly magnetization (M) as a function of the applied magnetic field (H) or temperature (T). VSM confirms magnetic hysteresis loops but may overlook weak signals with low doping. If both exhibit consistent hysteresis, coercivity, or magnetic ordering tendencies, it enhances the magnetic interpretation. It's working is based on Faraday's law of induction [97]. A magnetic sample is mechanically vibrated (typically vertically) within a homogeneous magnetic field. This vibration alters the magnetic flux in neighboring pickup coils. In doped CeO_2 nanoparticles, the increase in Ms and Hc after doping suggests induced ferromagnetism. The origin of ferromagnetism could be due to oxygen vacancies caused by charge imbalance. Mixed valence states ($Ce^{4+} \rightarrow Ce^{3+}$). Dopant ions with adjacent oxygen vacancies align spins, forming bound magnetic polarons (BMP). A greater coercive (Hc) field

denotes magnetic ordering stability, but a higher saturation magnetization (Ms) indicates stronger interaction among localized magnetic moments. The VSM is an instrument used to detect solid samples' magnetic moments, which are the most fundamental properties in magnetism. If the sample is subjected to sinusoidal motion as well, an electrical signal will be induced in appropriately situated stationary pick-coils. This signal at the vibration frequency is proportional to the magnetic moment, vibration amplitude, and frequency. In this study, magnetic measurements of materials were taken at room temperature with a VSM-Lake shore, Model-7410 series (figure 2.18) at the Institute Computer Centre (IIC), Indian Institute of Technology (IIT) in Roorkee.

2.11.1. Information acquired from SQUID-VSM:

The SQUID-VSM is a high-sensitivity hybrid instrument that combines SQUID sensitivity with VSM flexibility, allowing for the measurement of extremely weak magnetic signals as well as traditional magnetic characterization. SQUID-VSM detects very small magnetic signals ($\sim 10^{-8}$ to 10^{-11} emu), which is required for weakly magnetic materials such as doped CeO_2, DMS, superconductors, or single nanoparticle. This device measures M-H and M-T curves and provides data on magnetic moment, Ms, magnetic susceptibility (χ), coercively, retentively, and magnetic behavior.

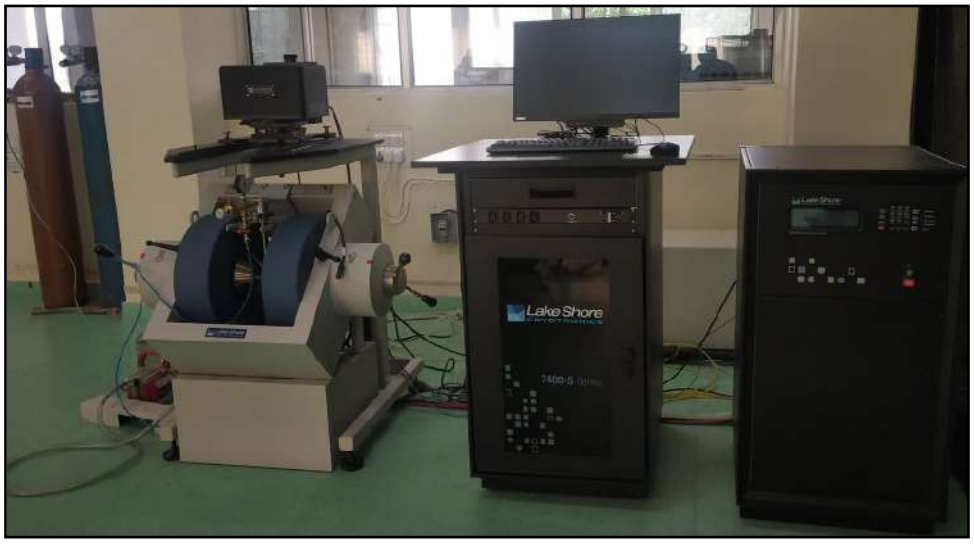

Figure 2.18: Schematic diagram of VSM-Lake shore, Model-7410

2.12. Photo-catalytic activity

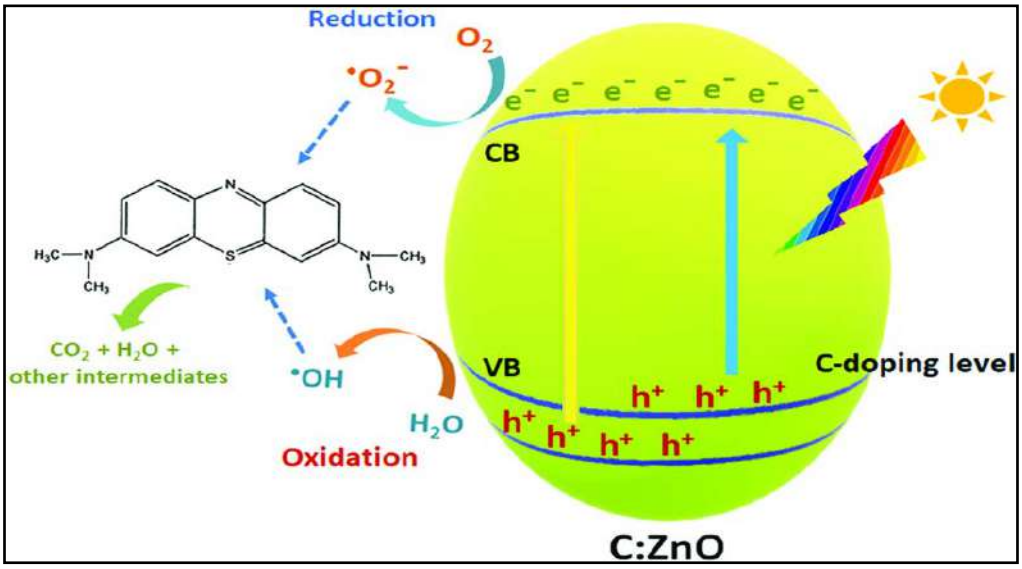

Figure 2.19: Mechanism of photo-catalytic degradation of MB dye by C:ZnO nanostructures exposed to visible light

Photo-catalytic activity refers to a material's ability to accelerate a photoreaction in the presence of light, which is commonly used for environmental remediation and energy generation. Photo catalytic activity under visible light irradiation has received a lot of interest for its potential in environmental remediation. The mechanism of photo-catalytic degradation of MB dye by C:ZnO nanostructures exposed to visible light is shown in figure 2.19.

The photo-catalytic activity of CeO_2 and Y-doped CeO_2 is studied utilizing the methylene Blue (MB) dye degradation method. UV-Vis light from a mercury lamp (250W, ~200-600 nm) is utilized to photo-catalyze the degradation of 150 ml aqueous solution (10-5M or 10 ppm) of MB dye. The catalyst employed is 30 mg undoped CeO_2 and Y-doped CeO_2 nanoparticles. To reach adsorption/desorption equilibrium between the substances and the catalyst, the catalyst-added MB dye solution is agitated for an hour in a dark environment using a magnetic stirrer. After that, the dye solution is exposed to UV-visible light, and 20ml of MB solution is collected every 30 minutes to evaluate the degradation kinetics. The following formula calculates the efficiency of degradation (η) of MB [98].

$$\boldsymbol{n = \frac{C_0 - C}{C_0} \times 100} \qquad \textbf{(2.10)}$$

C_0 and C are the initial and residual MB solution concentrations, respectively.

2.12.1. Information acquired from Photo-catalytic activity:

In analytical techniques, such as fluorescence and infrared spectroscopy, photo-catalytic mechanism improves understanding of reactive oxygen species. While photo-catalytic techniques show promise in degrading pollutants, the byproducts generated during these reactions may represent environmental hazards, demanding further investigations on their toxicity.

2.13. Electrochemical Characterization Techniques

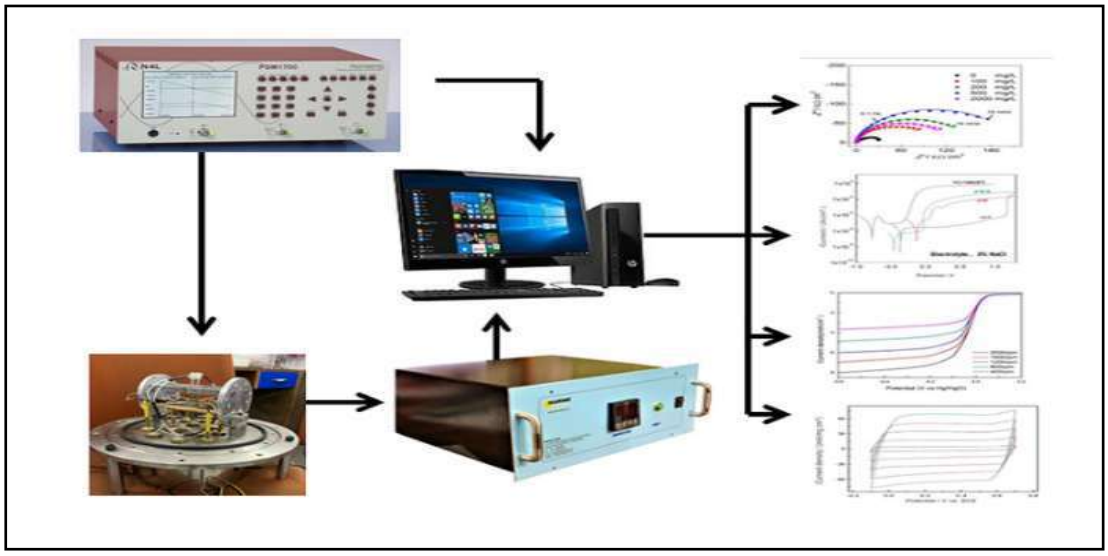

Figure 2.20: Photograph of electro-chemical analyzer

Electrochemical analysis comprises a wide range of techniques and applications that are critical for understanding charge transfer mechanisms, creating biosensors, and improving diagnostic approaches. An image of electro-chemical analyzer is shown in figure 2.20. The following sections focus on major features of electrochemical analysis.

- **Cyclic Voltammetry:**

CV is most often used in electrochemical technique for measuring an analyte's current response as a function of applied voltage. This technique is very useful for examining redox reactions, determining electrochemical properties, and investigating various chemical processes. CV's adaptability allows it to be employed in a variety of domains, including environmental analysis, energy storage, and sensor creation.

- **Principle of Cyclic Voltammetry:**

CV entails sweeping the potential of a working electrode and measuring the resulting current, giving insights on redox potentials and reaction kinetics. The voltammogram offers information about the electrochemical behavior, including stability and charge transfer mechanism.

- **Working of Cyclic Voltammetry:**

The measurements are taken using a conventional three-electrode setup, that entails performing two cyclic potential scans in opposite directions between the working and reference electrodes while monitoring the current change across the working electrode. To make a voltammogram, plot the current flowing through the working electrode versus its potential. An ideal capacitor has a rectangular shape because capacitance (C) remains constant at a scan rate. Pseudo-capacitive activity is frequently characterized by sharp peaks at specific voltage windows. The redox peak occurs when a cell stores energy via electron transport. A voltammogram with multiple peaks will be shown for materials with varying valence states. Using the limited region of the CV curve in cyclic voltammetry, the electrochemical-specific capacitance can be estimated using the formula [99]:

$$\boldsymbol{C = \frac{1}{2mVk}\int_{v^-}^{v^+} I(v)dV} \qquad \textbf{(2.10)}$$

This equation indicates that the specific capacitance of materials is inversely related to scan rate due to the considerable internal resistance that occurs in a short period of time with a high scan rate. Furthermore, the number of active sites involved in redox processes affects oscillations in specific capacitance values.

- **Galvanic Charge Discharge method**

Galvanic charging and discharging in super-capacitors use electrochemical processes to increase energy storage and efficiency. Galvanic charging and discharging in super-capacitors use electrochemical processes to increase energy storage and efficiency. This approach can considerably improve the performance of super-capacitors, especially in solar energy and hybrid systems. The next sections go over the mechanisms and advantages of galvanic processes in super-capacitors. GCD investigations involve recording the cell voltage over time while charging or discharging the cell with a steady current. GCD curves measure electrode capacitance

at varying current density (A/g). Because of the observed asymmetry and nonlinearity of the electrode's discharge response, the specific capacitance is calculated using the equation below [100].

$$C_{GCD} = \frac{2E}{m(\Delta V)^2} \quad \textbf{(2.11)}$$

Where C_{GCD} stands for specific capacitance (F/g), E and m represent the energy and mass of the active material, respectively. The discharge potential window is represented as ΔV.

The following formula can be used to calculate critical profitability factors such as a supercapacitor's specific power density and specific energy density [101]:

$$E = \frac{1}{2} C V_{max}^2 \quad \textbf{(2.12)}$$

and

$$P = \frac{E}{t} \quad \textbf{(2.13)}$$

Where total integration refers to the integral area of the discharged curve, I is the current density, and t is the discharge duration. Durability testing is critical for real-world supercapacitor applications; for this purpose, 2100 charge-discharge cycles at a current density of 1 A/g was conducted.

- **Impedance Spectroscopy**

Impedance spectroscopy (IS) is a versatile analytical technique that investigates the electrical characteristics of materials and biological systems. It works by passing an alternating current through a sample and measuring the voltage those results, allowing you to characterize material qualities including conductivity, permittivity, and charge mobility. This approach has acquired popularity in several domains, including microbiology, materials science, and biomedical engineering. The next sections discuss its applications and relevance. When a specific combination of resistors and capacitors is used at an electrode contact, an electrochemical reaction occurs. The system's impedance is determined by applying a sinusoidal voltage of moderate amplitude to the cell electrodes and watching the current response. The responsive current (ΔI(ω)) and sinusoidal potential to be applied are provided as [102]:

$$\Delta I(\omega) = \Delta I e^{i(\omega t + \phi)} \quad \textbf{(2.14)}$$

where symbols carry their standard meanings. Electrochemical impedance is calculated using the following formula:

$$\boldsymbol{Z(\omega) = \frac{\Delta V}{\Delta I} = |Z(\omega)|e^{-i\phi} = Z' + iZ''} \quad \textbf{(2.15)}$$

$$\textbf{phase Angle } \boldsymbol{\phi} = \left(\frac{Z''}{Z'}\right) \quad \textbf{(2.16)}$$

The symbols Z′ and Z″ are real and imaginary parts of the complex impedance.

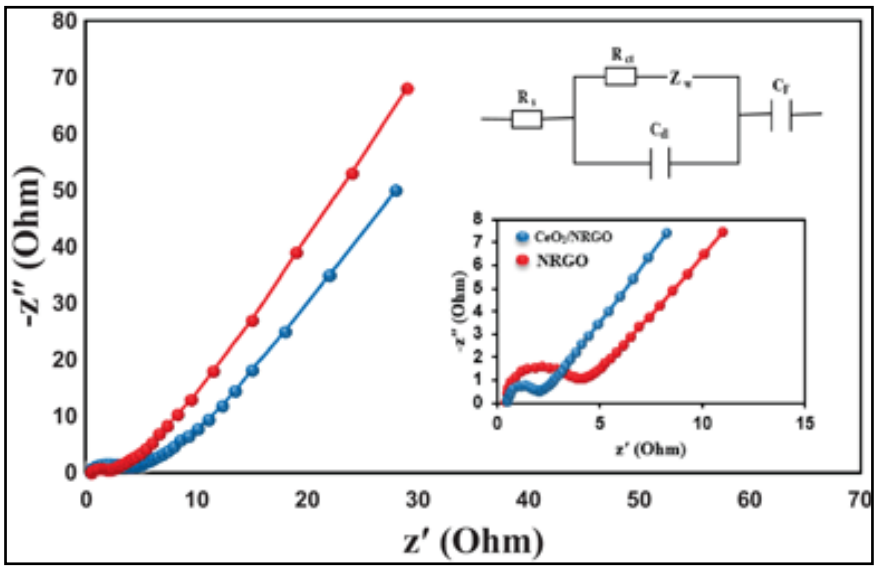

Figure 2.21: Nyquist impedance plots of NRGO and CeO_2/NRGO nanocomposites

The Nyquist plots show the relationship between imaginary impedance (-Z″) and real impedance (Z′) (figure 2.21), while the Bode plot represents phase shift and absolute impedance |Z| as angular frequency. The EIS instrument's impedance responses characterize the equivalent circuit, which includes components such as solution resistance (R_S), charge-transfer resistance (R_{ct}), constant phase element (CPE), and Warburg impedance (W). The resistance (R_{ct}), caused by the faradic reaction at high frequencies, is proportional to the semicircle diameter. The Warburg resistance (W) is the low-frequency slope of a linear curve that accounts for the frequency-dependent diffusion of ions into the electrode surface [103]. CPE and Q values are used to represent imperfectly homogenous surfaces or non-ideal cells. The constant phase element (CPE or Q) is used when dealing with imperfect or non-ideal cells. The CPE parameter 'N' is used to determine the electrode material quality (N=1, 0, and 0.5). These properties are determined by modeling or fitting impedance spectra using a comparable circuit and analyzing EIS data (EC). Depending on the shape of

the EIS spectrum, the resistors (R), conductors (L), and capacitors (C) that comprise the EC model are frequently connected in series or parallel.

2.13.1 Information acquired from the Electrochemical Characterization method:

Electrochemical analysis includes several approaches that provide useful information in a variety of sectors, including environmental monitoring, food safety, and medical diagnostics. It measures the voltage of electrochemical cells to determine ion concentrations. Voltammetry analyzes current as a function of applied voltage, making it valuable for detecting trace metals in food and environmental samples. Impedancemetry assesses a system's impedance, providing insights on material qualities and reactions. Overall, we have seen that CeO_2 nanoparticles can tackle crucial challenges in healthcare, energy, the environment, and industry due to their redox activity, surface reactivity, biocompatibility, and customizable nanostructure. This makes them an important material for developing innovative and sustainable technology.

Chapter 3
Study of Structural, Optical, Photoluminescence, Electronic Structure and Photo-catalytic Activity of Y-Doped CeO_2 Nanoparticles

Chapter-3

Study of Structural, Optical, Photoluminescence, Electronic Structure and Photo-catalytic activity Properties of Y-Doped CeO_2 Nanoparticles

ABSTRACT

The exceptional characteristics of CeO_2 and $Ce_{1-x}Y_xO_2$ (x = 0.03, 0.05 and 0.07) nanoparticles were reported in the chapter supporting that Y^{3+} replaces Ce^{3+}/Ce^{4+} leads to oxygen vacancies formation. The results of XRD measurements revealed FCC structure of decreased crystallite size of CeO_2 with improved crystallinity. To investigate the surface morphology, HRTEM and SAED patterns were performed. EDX analyses were undertaken to discuss the elemental and compositional characteristics. The absorption spectra using UV-Vis-NIR spectroscopy were analyzed and red shifted absorbance was found to enhance with decreasing band gap values for increased Y doping. The Photoluminescence spectra depicted various emissions representing the development of various defects and oxygen vacancy with incorporation of Y content in the lattice with CCT values below 4000 K to be classified as warm yellow light for indoor applications. The development of oxygen vacancies in the CeO_2 lattice was further supported by XPS measurements for core levels Ce 3d, O 1s and Y 3d. Furthermore, the XPS measurements also reported the valence states of elements, Ce with 3+ and 4+, Y with 3+ and O with 2- along with charged oxygen vacancies. The photo-catalytic analysis revealed that Y-doped CeO_2 nanoparticles show better degradation using a variety of characterization. The degradation mechanism that illustrates the impact of oxygen vacancies created by Y-doping on the photo-degradation process has been proposed in this chapter. The detailed outcomes of present study suggested the use of Y-doped CeO_2 nanoparticles in optoelectronics, spintronics devices and photocatalyst applications.

3.1 Introduction

Recently, there has been a huge surge in attention in ceria-based nanoparticles from both basic scientific and business perspectives [104]. Researchers are also working eagerly for developing photocatalytic materials that possess lower band gap.

Some metal oxide semiconductors materials show poor response under visible light but exert better photo-catalytic activity under UV radiations such as CeO_2 which can be utilized as a UV filter in cosmetics, sunscreen, and glass polishing agents [37]. Its superior performance attributes to high oxygen-storage capacity. Because of prominent high capacity to store oxygen (OSC) of ceria, numerous investigations have shown that the material can be utilized as a supporting agent in variety of catalysts [105]. It is a reducible oxide, and at high temperatures, ceria can develop oxygen vacancies [106]. For every V_o, this mechanism fallouts in the reduction of $Ce^{4+} \rightarrow Ce^{3+}$cation; depending on the circumstances, this reduction may be reversible [107, 108]. Generally, it is expected that doping with lower valent cation is essential to create oxygen vacancies. Therefore, doping of suitable ions with lower vacancy into host material results into a hybrid composite with modified properties and distorted lattice. Since oxygen vacancies may function as centers for the capture of electrons-holes and can hold onto photogenerated electrons or holes triggered by visible or UV radiations. More oxygen vacancies can successfully prevent electron-hole pair recombination, improving photo-catalytic activity [109]. Therefore, TM as a result may be introduced in such case, which might significantly shorten the duration of electron-hole recombination and increase the efficiency in the photo-catalytic process of the system [110]. The band-gap shift and trap state generation caused by TM doping make it important for luminescence as well. As reported by ***Sharma et al.*** [111,112] that doping and co-doping in the host lattice can change the photo-catalytic activity by multiple times. According to them, due to generation of the ideal quantity of O-vacancies, the (Y, Zn) co-doped CeO_2 samples exhibit improved photo-catalytic activity compared to Y-doped and Zn-doped CeO_2 samples. The effect of concentration can be correlated with the generation of defects structures. It is generally expected that a material microstructure governs its property. To acquire a thorough knowledge of the dopant's atomic-level effects on host (CeO_2) material, numerous researches have focused on the precise analysis of microstructures. A possible explanation is provided by the dopant cations interacting strongly with corresponding oxygen vacancies. Due to rise in the dopant concentration, formation of clusters takes place which reduces the carrier's mobility and consequently decrease in electrical conductivity [113]. A considerable increase in the defect formation has

been addressed by ***Patil et al.*** [114] in case of lanthanum doped CeO_2. Doping CeO_2 with alio-valent or iso-valent metal cations can modify its structural, optical, photoluminescence, electronic structure, and photo-catalytic properties for enhanced functional applications. Yttrium (Y^{3+}) is a highly effective dopant due to its comparable ionic radius and ability to cause lattice distortions and oxygen vacancies, which greatly impact material behavior [115]. The formation of oxygen vacancies in the initial structure of CeO_2 when it is doped with a trivalent element, such as Yttrium, to counteract the effective negatively charge caused by the replacement of Y^{3+} for Ce^{4+}. Consequently, a distortion is created in the Y-doped CeO_2 cubic matrix. ***Atribak et al.*** [116] have reported the advantageous Y-doping effect on ceria's activity in soot combustion. ***She et al.*** [117] investigated the impact of adding Y (0.5 wt%) to a CuO/CeO_2 catalyst on its activity in the water–gas shift, considering the large amount of yttrium sources. ***Nolan et al.*** [118] have reported that Yttrium doping into CeO_2 possess a positive anion vacancy formation owing to its ionic radius nearly equal to that of Ce^{4+} ion. Introducing trivalent cation into CeO_2 lattice fallouts in the formation of Ce^{3+} state with an oxygen hole as these trivalent cations could easily mixed into CeO_2 lattice and forms a stable ternary compound. It has been addressed by ***C. Sun et al.*** [51] that promotion of yttrium tailored the various properties and enhances the catalytic performance of CeO_2 in the Ni catalysts. Such study suggests that doping ceria with trivalent dopant strongly affects the defects formation and possesses wide range of applications as shown in figure 3.1. A vast study has been devoted experimentally to establishing the relationship between these defects. In this research, we examine the characteristics of yttrium-doped cerium oxide nanoparticles and nano-ceramics to investigate their surface morphology, electronic structure properties for their potential in opto-electronics, luminescence device materials and spintronics applications. Furthermore, doping in CeO_2 improves photocatalytic activity, enabling effective pollutant decomposition and solar-powered hydrogen generation [119, 120]. The transfer and separation of photogenerated charge carriers (e^- and h^+) is one of the key elements affecting photo-catalytic activity. The large concentration of defect sites shown by the enhanced Urbach energy helps prolong the carriers' lifetime of charge separation. This efficient charge separation and transfer contribute to enhanced photo-catalytic performance [120].

This chapter reveals the synthesis, structural analysis, and characterization of Y-doped CeO_2 nanoparticles. The goal is to understand how yttrium inclusion affects physical properties and their potential for multifunctional applications. For this study, undoped CeO_2 and $Ce_{1-x}Y_xO_2$ (x = 0.03, 0.05 and 0.07) nanoparticles are synthesized by the simple microwave-aided co-precipitation method. Investigating structural traits such crystalline quality, strain, size and degree of disorder is done using X-ray diffraction (XRD). With varying doping concentration, the effect of Y doping on the surface morphology has been studied using a different type of methods, including energy-dispersive X-ray spectroscopy (EDX) and transmission electron microscopy (TEM). The optical characteristics of undoped CeO_2 and Y-doped CeO_2 nanoparticles have been done employing UV-Vis -NIR and photoluminescence (PL) spectroscopy. The correlation has also been established between the measured visible PL spectra, which offers important details regarding structural disorder and its microscopic behavior. Finally, we tried to investigate how V_o and Ce^{3+} defects, which are existing in both undoped and yttrium-doped CeO_2 nanoparticles, are affected by doping concentration. After considering the impact of doping, pH, and oxygen vacancy production on the photo-catalytic efficiency of Y-doped CeO_2 nanoparticles, a potential mechanism has been put forth.

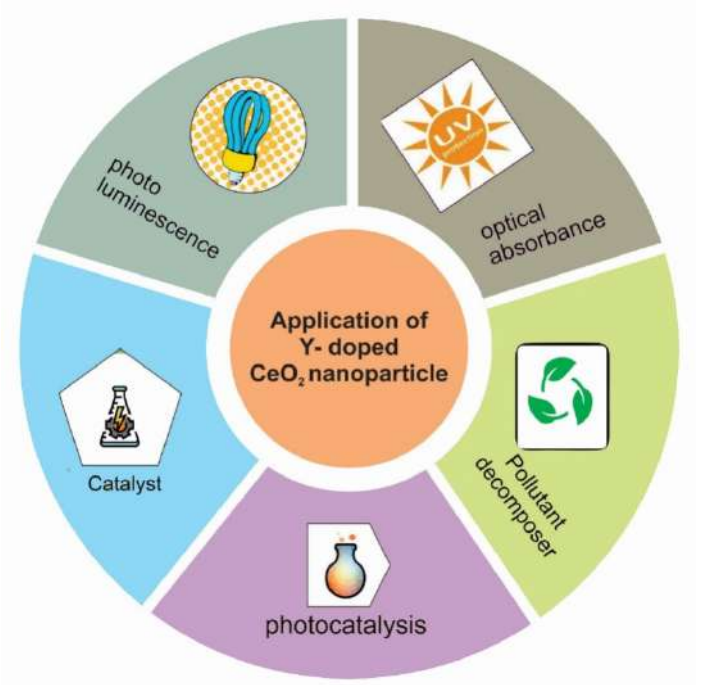

Figure 3.1: Pictorial representation of various applications of Y-doped CeO_2 nanoparticles

3.2. Experimental details

3.2.1. Material preparation

Cerium (IV) Ammonium Nitrate $(NH_4)_2Ce(NO_3)_6$ (Alpha Aeser 99.9%), Yttrium (III) Nitrate Hepta-hydrate ($Y(NO_3)_3.6H_2O$) (Alpha Aeser 99.9%) and NH_4OH (30 % solution) chemicals were used during the synthesis of the nanoparticles. The undoped CeO_2 and $Ce_{1-x}Y_xO_2$ samples were synthesized using coprecipitation route of synthesis [121]. The proper stoichiometric ratio of $(NH_4)_2Ce(NO_3)_6$ and $Y(NO_3)_3.6H_2O$ was employed to synthesizing $Ce_{1-x}Y_xO_2$ nanoparticles. Precursor solutions of $(NH_4)_2Ce(NO_3)_6$ and $Y(NO_3)_3.6H_2O$ were first made in distilled water using magnetic stirring at a speed of 600 rpm, until the pH was about 8, using 30% NH_4OH solution as a reducing agent, then stirred for roughly 4 hours. Further obtained light-yellow precipitate was strained and cleaned with distilled water to be sintered about 6 hours in the muffle furnace at 500 °C temperature. The following chemical reaction (as shown in equation-3.1) can be used to synthesize these nanoparticles.

$$\mathbf{(1-x)\,[(NH_4)_2Ce(NO_3)_6] + x[Y(NO_3)_3.6H_2O] + 3NH_4OH \Rightarrow Ce_{1-x}Y_xO_2 + gases\uparrow} \qquad \mathbf{(3.1)}$$

3.2.2. Nanoparticles characterization:

The structural properties were characterised using X-Ray Diffractometer of make BrukerD8 Advance with Cu Kα (λ =1.5406 Å) radiation in the 2θ range of 20°-90°. The samples' surface morphology, crystallinity and the average particle size were examined using a JEOL-JEM 2100 Plus make TEM instrument operating at 200 kV accelerating voltage. Ultra sonicated nano powders were dispersed on a conventional holey carbon film mounted on a Cu grid to prepare TEM samples. Further analysis of TEM images was taken using Image-J software for the distribution of particle size for 120 particles. Using a Shimadzu UV-3600 Plus spectrophotometer, UV-Vis-NIR absorption spectra in the wavelength range of 200-800 nm were acquired to explore the optical characteristics. The photoluminescence spectra were recorded in the wavelength range 350-580 nm with spectro-fluoromax of HORIBA and using an excitation wavelength of 325 nm. The XPS measurement were taken on Thermo-scientific make Model no. NEXSA surface analysis, with a micro-focused X-ray (400μm) having monochromatic Al-Kα source of 1486.6 eV energy and pass energy 20 eV calibrated to binding energy of C 1s line (hν = 284.6 eV) of adsorbed hydrocarbon at the sample surface with analysis chamber at 10^{-9} Torr base pressure. The photo-catalytic activity has been performed using mercury lamp (250 W) with

wavelength range 200-600 nm and 10-5 M Methylene Blue (MB) solution is used as organic solvent. The initial and degraded dye concentrations were measured using UV-Vis spectroscopy (Shimadzu UV-2600).

3.3. Result and discussions

3.3.1. Surface characterization of nanoparticles

The XRD pattern of CeO_2 nanoparticles with varying concentration of Y (x = 0.03, 0.05, 0.07) is shown in figure 3.2. To determine the crystalline phases and calculate the crystallite sizes, XRD analysis has been done. As the figure indicates the peaks so observed correspond to the (111), (200), (220), (311), (222), (400), (331), and (420) are well indexed to single phase cubic fluorite structure of CeO_2. The space group is Fm3m and identified using standard JCPDS card no. (81-0792) [34]. The presence of no other peak related to impurity over the entire range of doping confirms that Y has well incorporated into CeO_2 lattice and partially substituting Ce ions, rather than forming oxide related phase. Based on the XRD patterns, it can be observed that when the concentration of Y-doping in CeO_2 nanoparticles increases, there is increase in lattice parameters.

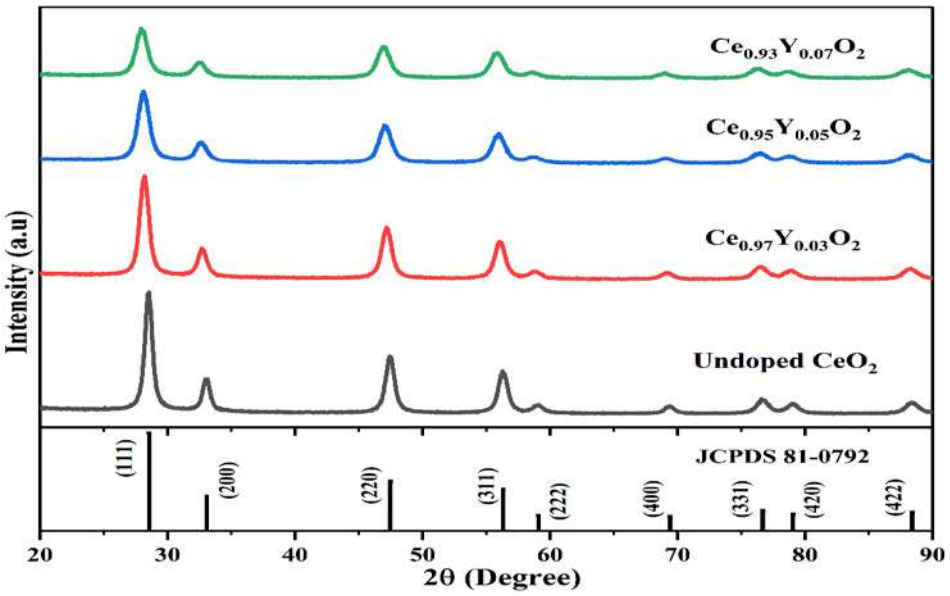

Figure 3.2: The XRD pattern of undoped CeO_2 and $Ce_{1-x}Y_xO_2$ nanoparticles samples

The rise in lattice parameters of the as-prepared nanoparticles samples could be explained by the entry and of yttrium-ions, which have ionic radii greater than Ce-ions, in the CeO_2 lattice. The XRD pattern also elaborated that the highest peak

position corresponding to (111) plane obviously shows peaks-shifting towards a lower angle with introducing Y doping [122]. This demonstrates the expansion in the crystal lattice with the entry of Y into CeO_2 crystal structure. With a rise in lattice parameter with Y doping, the peaks shifted towards the lower angle side, which is explained by Bragg diffraction equation [123]. Yet, it is also seen that as the doping of Y doping concentration is increased, all peaks gradually broadened with fall in the intensity, showing that incorporation of foreign cations reduces the crystallinity of the sample. The broadening of the peaks suggests that the reduction in the crystallite sizes. The crystallite size (D) has been obtained using Scherrer's equation [121] as 13 nm for undoped CeO_2, 11 nm for x = 0.03, 9 nm for x = 0.05 and x = 0.07 as shown in Table 3.1. Even while the reduction in crystallite size led to CeO_2 crystal lattice expansion. The concentration of dopants influences how much the crystal lattice will expand or compress. Nanoparticles may experience strain because of crystal imperfections and deformation. Examining Table 3.1, the values of strain show that Y-doped CeO_2 nanoparticles are under tensile strain. Some theoretical research has shown that tensile strain favors the creation of oxygen over compressive strain [124].

Table 3.1: The calculated value of FWHM, lattice parameter (a), micro strain (ϵ) and crystallite size (D) obtained through Scherer's equation, W-H plot, SSP method and TEM analysis for undoped CeO_2 and $Ce_{1-x}Y_xO_2$ nanoparticles samples

Samples	D (nm)			Average particle size (TEM analysis) (nm)	d spacing (nm)	a (Å)	Micro strain ϵ x10^{-4}	
	Scherer's equation	W-H plot	SSP method				(W-H plot)	Scherer's equation
Undoped CeO_2	13	16	15	18	0.311	5.42	10.7	26.19
$Ce_{0.97}Y_{0.03}O_2$	11	12	12	14	0.315	5.48	5.26	30.87
$Ce_{0.95}Y_{0.05}O_2$	9	10	10	12	0.316	5.49	6.78	38.67
$Ce_{0.93}Y_{0.07}O_2$	9	10	10	12	0.317	5.52	11.00	39.86

The prevalence of oxygen vacancies in doped CeO_2 samples, which may be attributed to the bonding length and strength between the surface O and Ce atoms, can thus be directly related to the higher value of tensile strain in Y-doped CeO_2 samples [125]. Lattice strain behaviour that has been observed suggests that all Y ions have replaced all of Ce ions in the CeO_2 host matrix. Consequently, high oxygen vacancies are created due to entry of Y into the CeO_2 lattice, which causes the substitution of small Ce^{4+} (0.97 Å) cations by larger Y cations (1.019 Å), thus enlarging the crystal lattice [126, 127]. Since the XRD diffraction peaks of nanoparticles are often wide and broad, it becomes difficult to resolve them separately [128]. Therefore, XRD by itself cannot completely rule out the formation of the oxide phase. The Rietveld refinement of the diffraction peaks has been carried out using the FULLPROF program. Figure 3.3 displays the Rietveld fits of experimental XRD pattern of the synthesized undoped CeO_2 and Y-doped CeO_2 nanoparticles.

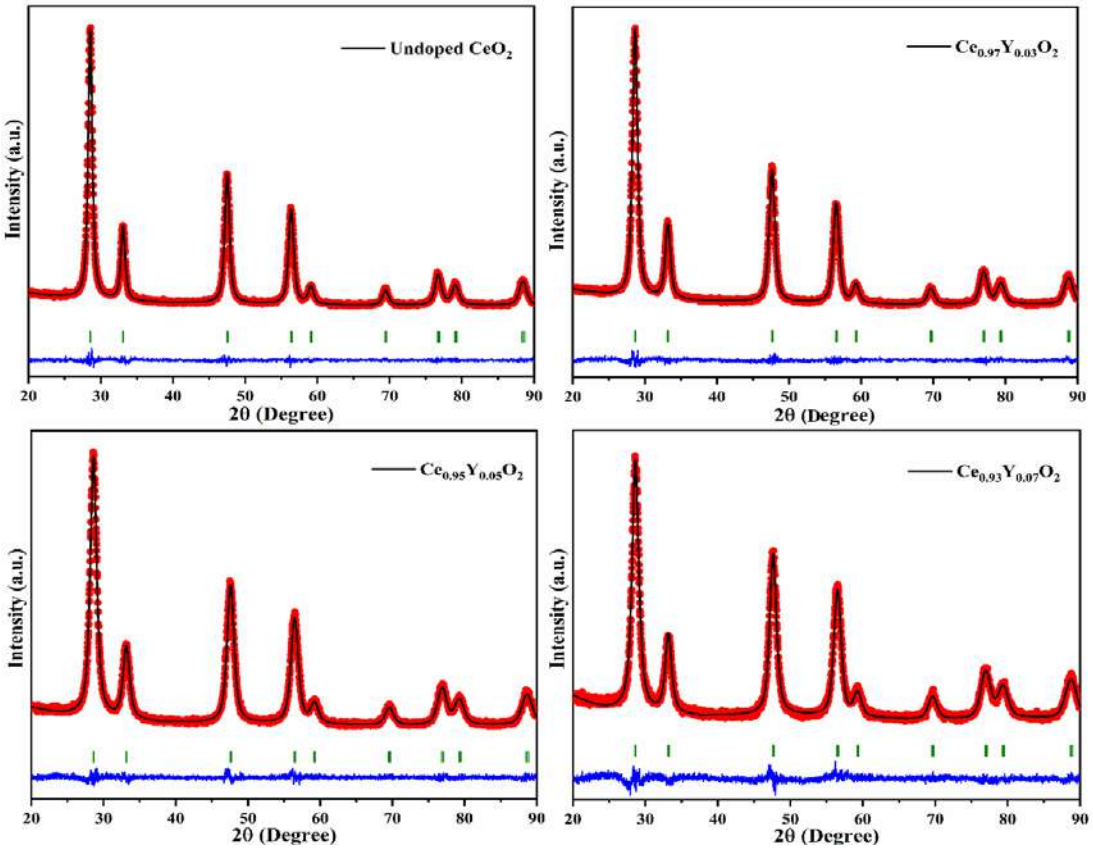

Figure 3.3: Rietveld refined and fitted curve of undoped CeO_2 and $Ce_{1-x}Y_xO_2$ nanoparticles samples at 300 K. Dotted (solid) lines represent the observed (calculated) profiles. The short vertical lines signify Bragg reflections. The difference plot is shown by the lower curve.

The corresponding lattice parameters, goodness of fit (χ^2), R_p, R_{wp}, R_{exp}, R_{Bragg}, and cell density are listed in Table 3.2. The experimentally estimated and Rietveld derived XRD patterns showed an acceptable match, as indicated by the χ^2 values.

Table 3.2: Structural data and refinement parameters for undoped CeO_2 and $Ce_{1-x}Y_xO_2$ nanoparticles samples

Samples	a (Å)	Volume $(Å)^3$	χ^2	R_p	R_{wp}	R_{exp}	R_{Bragg}	Cell density (gm/cm^3)
Undoped CeO_2	5.4145	158.73	1.190	8.88	8.82	8.09	1.56	7.123
$Ce_{0.97}Y_{0.03}O_2$	5.3991	157.38	1.575	10.2	10.1	8.05	1.77	7.025
$Ce_{0.95}Y_{0.05}O_2$	5.4047	157.87	1.123	9.14	9.16	8.64	1.16	7.090
$Ce_{0.93}Y_{0.07}O_2$	5.3998	157.44	1.880	13.9	13.3	9.68	2.96	6.940

3.3.1.1. Williamson-Hall (W-H) and Size-Strain Plot (SSP):

Considering an isotropic property of the material, the W-H equation can be simply used to determine the crystallite size [129, 130]. However, a better assessment "size strain plot" (SSP), where precision is typically lower can be considered for determination of D [131, 50]. As shown in figure 3.4(a), 3.4(b) the y-intercept root yields the strain and the crystallite size is obtained from the slope of the linearly fitted data. Table 3.1 provides an overview of the findings from the Scherrer equation, W-H plot and SSP model. The values of D derived from all above-mentioned methods are closer, whereas the obtained results for x = 0.05 and x = 0.07 concentration are the same, suggesting to control the doping concentration after x = 0.05. This is because if Y concentration is increased above x = 0.05, some of yttrium ions will replace Ce^{4+}/Ce^{3+}ions and some will remain on the surface. The nanocrystals in this procedure only take in the amount of dopant ions that are permissible by thermodynamics and excess number of dopants ions are eliminated from the interior surface, and prevent the growth of the nanocrystals. As a result, agglomeration of Y ions at the surface of CeO_2 crystal lattice takes place. Therefore, in this case x = 0.05 can be considered as an optimal doping concentration.

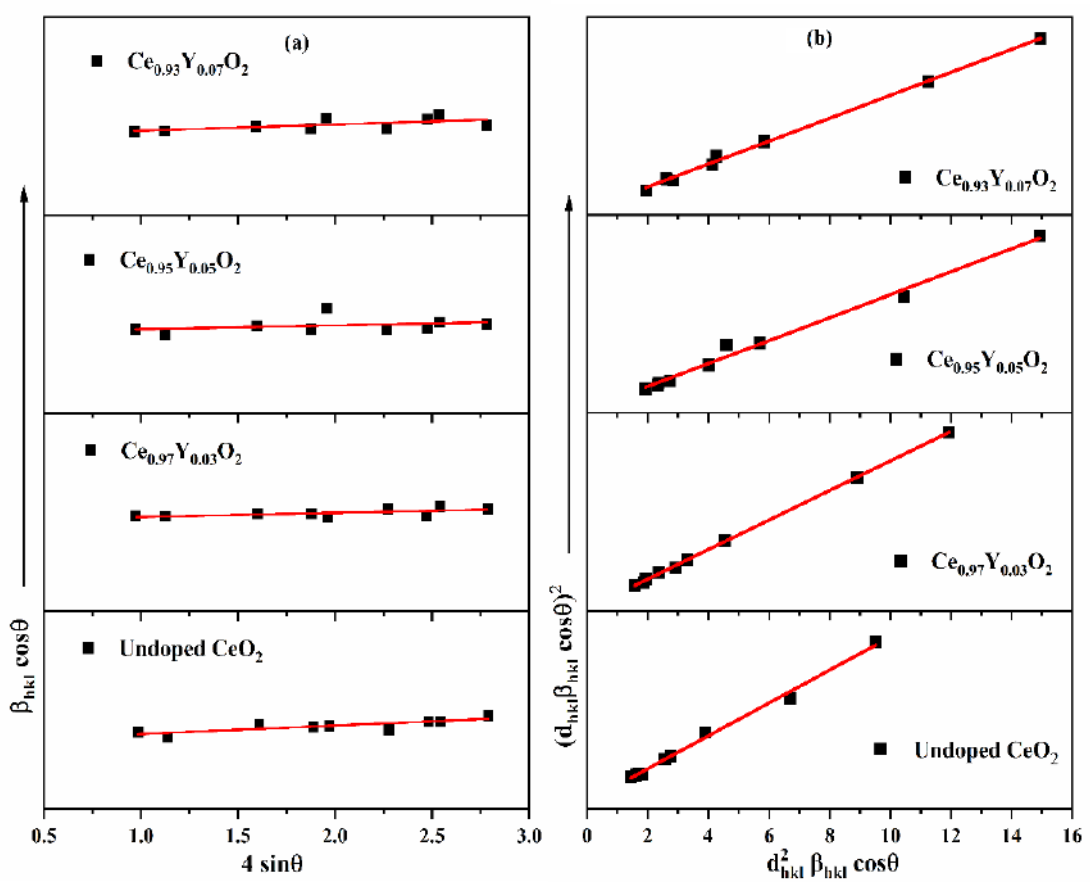

Figure 3.4: (a)W-H plots of $\beta_{hkl}cos\theta$ Vs 4sinθ (b) SSP of $(d_{hkl}\beta cos\theta)^2$ Vs. $d^2\beta_{hkl}cos\theta$ of undoped CeO_2 and $Ce_{1-x}Y_xO_2$ nanoparticles samples

3.3.2. Surface Morphology:

3.3.2.1. Energy Dispersive X-ray Spectroscopy (EDX):

In Figure 3.5, EDX of CeO_2 prepared through co-precipitate method of synthesis is depicted, confirming the presence of Ce, O and Y in terms of weight percentage. To ascertain the chemical constitution and purity of the synthesised CeO_2 nanoparticles, the investigation has been done using EDX. The EDX of the prepared samples reveal peaks of cerium, oxygen, and yttrium with no impurities (figure 3.5). This demonstrated that the samples contained the elements in the proper ratios for stoichiometry. Based on its wt% and at%, the findings of the EDX examination clearly showed the composition Ce, O and Y elements as shown in Table 3.3. The presence of C is associated with the carbon tape that supports the grid.

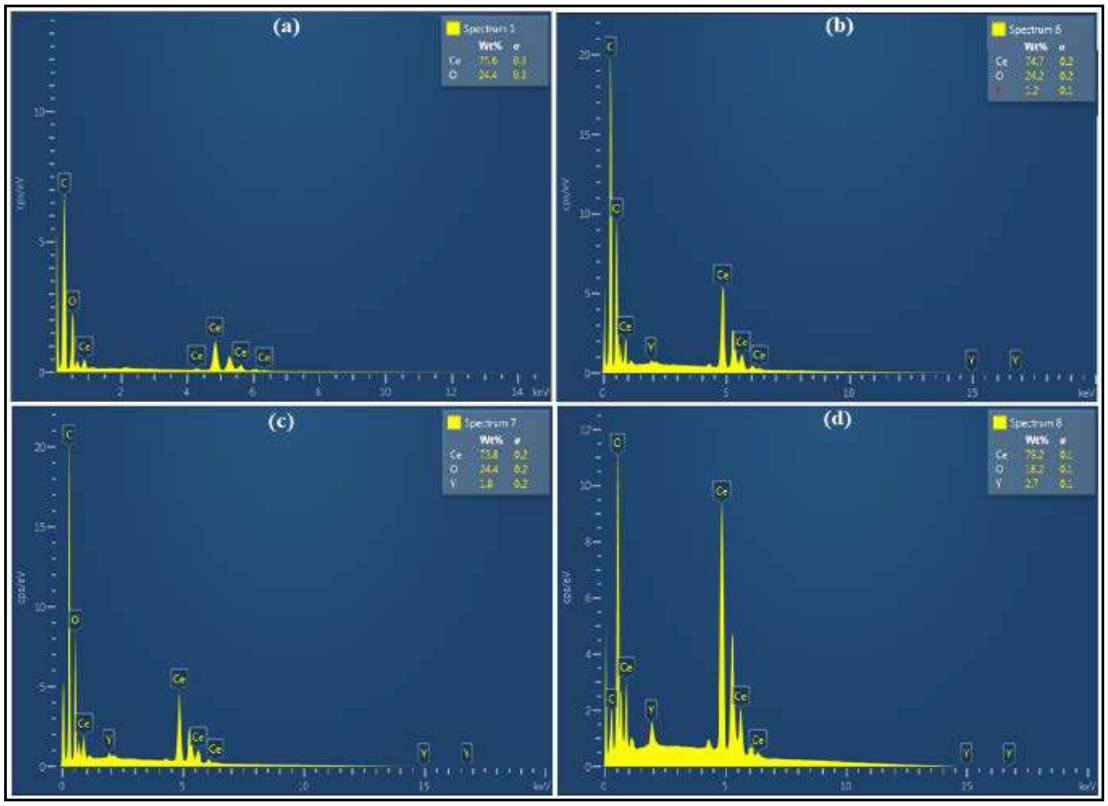

Figure 3.5: EDX spectra of (a) undoped CeO_2, (b) $Ce_{0.97}Y_{0.03}O_2$, (c) $Ce_{0.95}Y_{0.05}O_2$ and (d) $Ce_{0.93}Y_{0.07}O_2$ nanoparticles samples

Table 3.3: Analysis of the elemental composition of undoped CeO_2 and $Ce_{1-x}Y_xO_2$ nanoparticles samples

Elements	**Undoped CeO_2**		**$Ce_{0.97}Y_{0.03}O_2$**		**$Ce_{0.95}Y_{0.05}O_2$**		**$Ce_{0.93}Y_{0.07}O_2$**	
	wt (%)	at. (%)	wt (%)	at. (%)	wt (%)	at. (%)	wt (%)	at. (%)
Ce	75.6	26.13	74.7	25.88	73.8	25.41	79.2	32.61
O	24.4	73.86	24.2	73.45	24.4	73.60	18.2	65.63
Y	-	-	1.2	0.65	1.8	0.97	2.7	1.75

3.3.2.2. TEM analysis

Using transmission electron microscopy, we additionally analyse our materials' surface morphology, microstructure, and the particle size of the nanoparticles [132]. With the help of ImageJ software, the average diameters of $Ce_{1-x}Y_xO_2$ samples are determined to be 18, 14, 12, and 12 nm for x values = 0.00, 0.03, 0.05, and 0.07, respectively (TEM images, figure 3.6 inset) and tabulated in Table 3.1.The obtained size is consistent with the results of XRD measurement where the

average particle size for x = 0.05 and 0.07 concentration are again the same which validate our conclusion that higher doping concentration results in smaller particle size of Y-doped CeO_2 nanoparticles, but after optimal doping (x = 0.05) in our case, the particle size does not change effectively. For Y-doped CeO_2 nanoparticles, the histogram showing particle-size distribution (displayed in the inset of figure 6) demonstrates that the distribution of particle size is rather fine in the range of 12-18 nm. Additionally, information regarding the impurity phases related to Y, in doped CeO_2 nanoparticles is interpreted using HRTEM and SAED analysis.

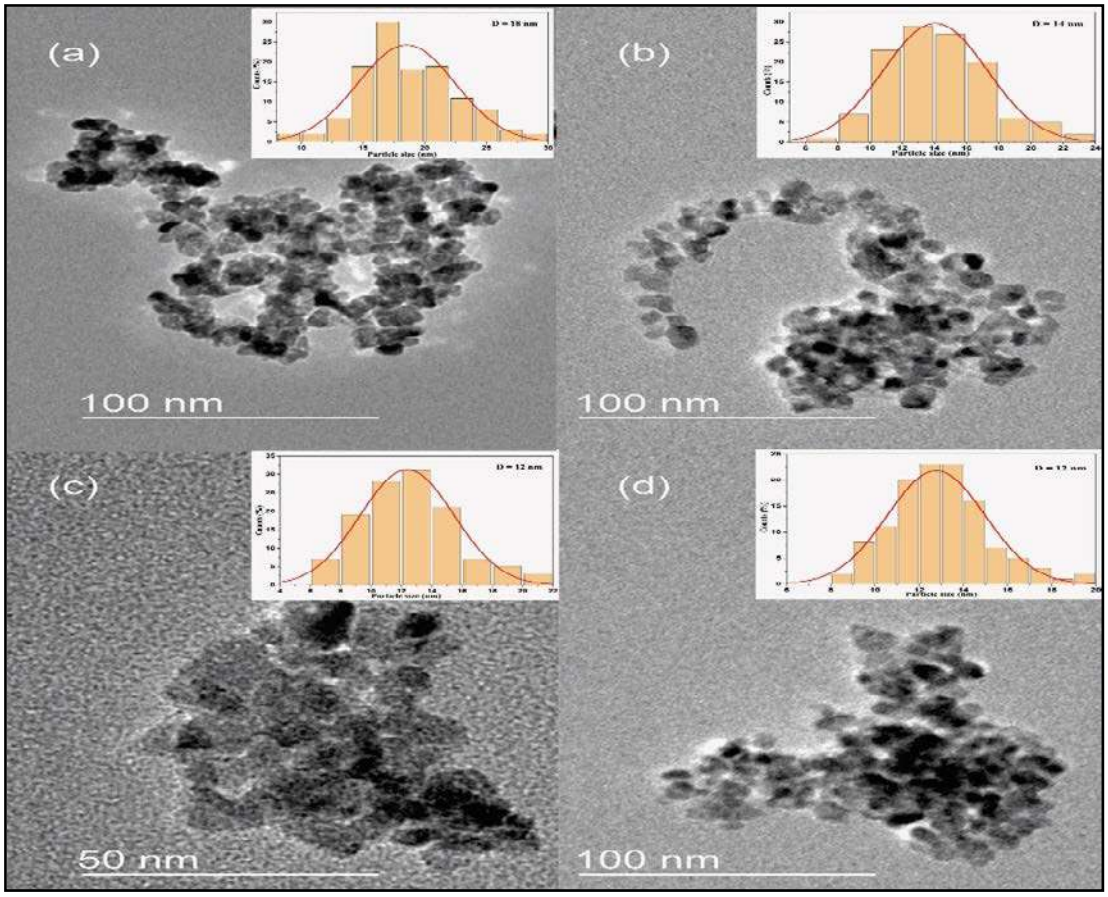

Figure 3.6: TEM images of (a) undoped CeO_2, (b) $Ce_{0.97}Y_{0.03}O_2$, (c) $Ce_{0.95}Y_{0.05}O_2$ and (d) $Ce_{0.93}Y_{0.07}O_2$ nanoparticles. An inset histogram graph displays the corresponding particle size of the samples

The lattice fringes in the HRTEM pictures are well-orientated as shown in figure 3.7 and majority of them are separated by about 0.31 nm. Furthermore, the SAED pattern of undoped CeO_2 and Y-doped CeO_2 samples are displayed in inset of Figure 3.7. Four broad rings can be seen in the SAED pattern, and they may correspond to the (111), (200), (220), and (311) planes. Every sample's diffraction

rings closely resemble the XRD pattern, and when the concentration of Y ions rise, the diffraction rings widen, signifying the samples' diminishing crystalline nature and decrease in particle size [121]. The optical band gap energy is also influenced by the fluency of Y ions in CeO_2 nanoparticles; this is covered in more detail using UV-Vis-NIR spectroscopy in the following section.

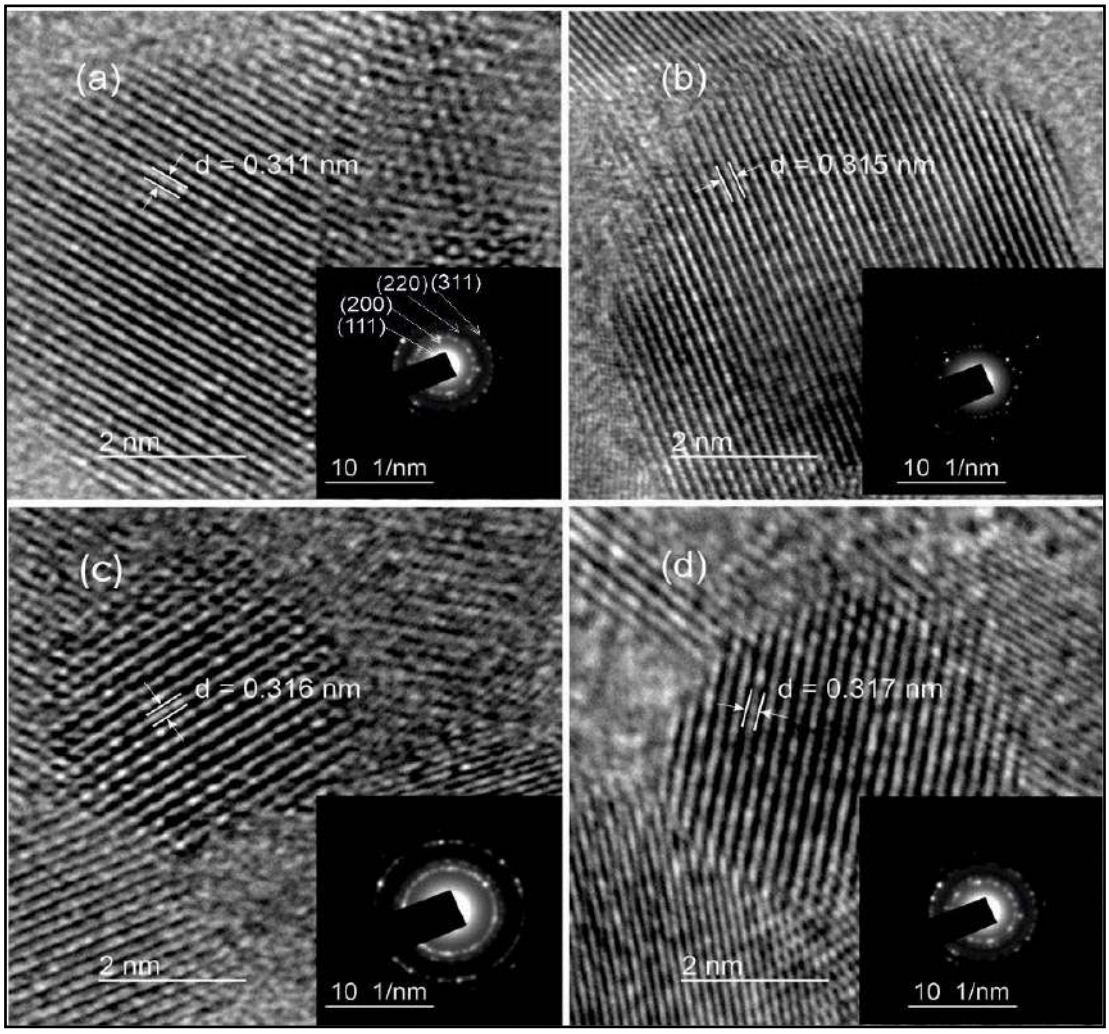

Figure 3.7: HRTEM images of Y doped CeO_2 nanoparticles with d spacing corresponding to (111) plane: (a) Undoped CeO_2, (b) $Ce_{0.97}Y_{0.03}O_2$, (c) $Ce_{0.95}Y_{0.05}O_2$ and (d) $Ce_{0.93}Y_{0.07}O_2$ nanoparticles and the inset graph shows their corresponding SAED images

3.3.3. Absorption spectroscopy

The absorption spectra of undoped CeO_2 and $Ce_{1-x}Y_xO_2$ nanoparticles as determined using UV-visible absorption spectroscopy is depicted in figure 3.8 (a), which shows that band edge absorption have undergone considerable alterations.

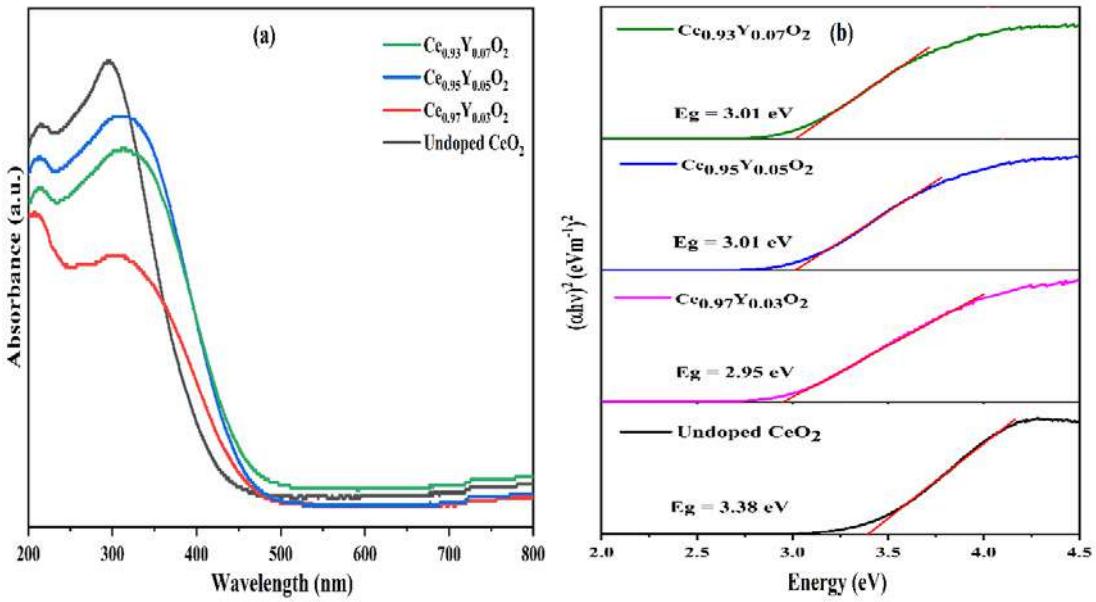

Figure 3.8: (a) UV-Vis optical absorbance spectra, (b) Tauc's plot of $(\alpha h\nu)^2$ versus photon energy (eV) of undoped CeO_2 and $Ce_{1-x}Y_xO_2$ nanoparticles samples

To further explain that how Yttrium-doping affects the optical characteristics of the host material, the Tauc's relation have been considered to determine band gap energies (E_g) [133]. The value of E_g have been derived by extending the linear portion of the photon energy curve to the energy axis (figure3.8 (b)). Table 3.4 summarizes the calculated value of E_g using Tauc's plot, energy equation method and derivation method. From Tauc's plot, the estimated E_g for undoped CeO_2 nanoparticles is measured to be 3.38 eV, which gradually decreases to 2.95 eV with entry of yttrium (x = 0.03), indicating that incorporation of yttrium ions exhibits the potential to strongly modify the optical properties of CeO_2 nanoparticles. As seen in figure 3.8 (a), red shift is observed for the absorption peaks because of the formation of smaller size nanoparticles [134, 135]. The band gap, however, is once more widened at higher Y content (x = 0.05, 0.07). Band gap expansion at this concentration is correlated with the Burstein-Moss (BM) effect [136,137].

Even though the crystallite size is smaller for x = 0.03 as well, the BM effect cannot occur because the carrier concentration is insufficient to overcome the critical density concentration. As a result, the persistence of band gap narrowing continues up to x = 0.03. However, at x = 0.05 doping concentration, the crystallite size drops to 9 nm and therefore the band gap energy will widen because of the carriers being more restricted in the small particle size. Band gap is thereby widened by both carrier

confinement and the BM effect at higher doping (x = 0.05, 0.07) concentration. As a result, for a given band gap, there is an optimal doping. Additionally, the value of energy band gap has also been derived using energy equation method and derivation method, each method yields a different numerical result but has a similar pattern of variance in the E_g as shown in Table 3.4.

Table 3.4: Various optical parameters for undoped CeO_2 and $Ce_{1-x}Y_xO_2$ nanoparticles samples

Samples	E_g (eV)			E_u (eV)	n
	Tauc's formula	Energy equation method	Derivation method		
Undoped CeO_2	3.38	3.53	3.54	0.1386	2.3016
$Ce_{0.97}Y_{0.03}O_2$	2.95	3.08	3.07	0.2054	2.4106
$Ce_{0.95}Y_{0.05}O_2$	3.01	3.12	3.12	0.1659	2.3943
$Ce_{0.93}Y_{0.07}O_2$	3.01	3.10	3.10	0.1682	2.3943

The Urbach (E_u) represents the spectral variation at the absorption edge [138]. Plotting logarithm of absorption coefficient versus hν curve yields E_u, as seen in figure 3.9. Table-3.4 provides a summary of calculated values of E_u. As it can be seen, the Y^{3+} substitution (x = 0.03) in CeO_2 lattice enhances the E_u value. This shows an increase in structural disorder and the role of defects in localised states of the band gap [139]. Further as we go on higher doping concentration (x = 0.05, 0.07), the E_u decreases again. This shows that optical band gap modifies the Urbach energy reversely. An important optical property of the material is the refractive index (n), whose variation significantly affect the optical properties for many applications [140,141]. The estimated refractive index for the prepared samples is shown in Table 3.4. The value of n for undoped CeO_2 is found to be 2.0316 but as Y ion is incorporated into CeO_2 sample (x = 0.03), the value of n increases which further decreases for x = 0.05 and 0.07. Table 3.4 shows that variations in Urbach energy and refractive indices exhibit similar patterns with varying Y ion concentration. We predicted a non-systematic variation in the E_g values as a function of Y doping. This proof establishes that the defects brought on by the Y content strongly affect the optical properties of the CeO_2 nanoparticles.

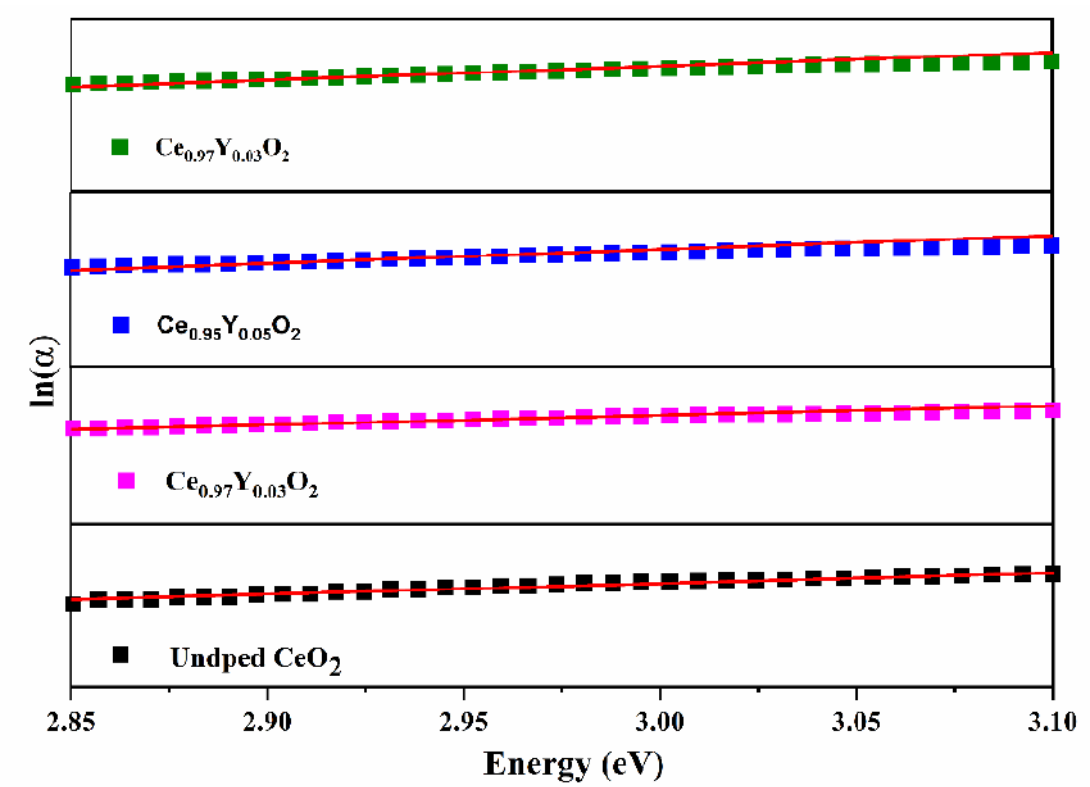

Figure 3.9: lnα versus hν for undoped CeO_2 and $Ce_{1-x}Y_xO_2$ nanoparticles samples.

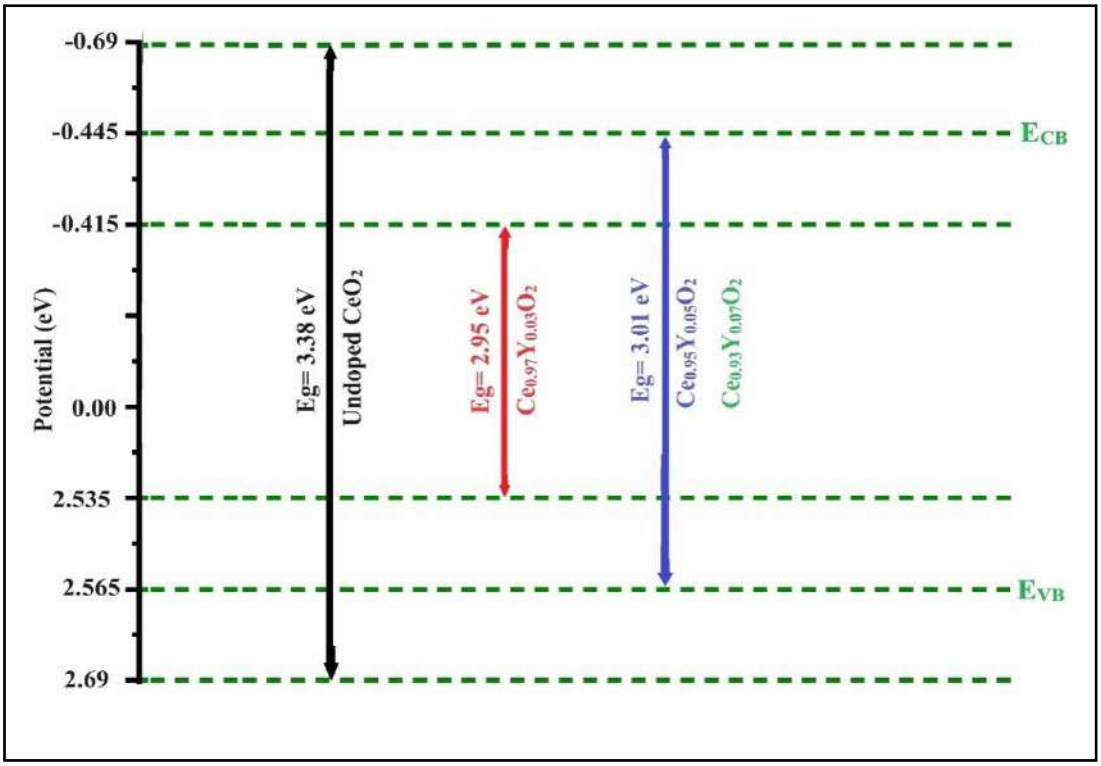

Figure 3.10: Energy band diagram of undoped CeO_2 and$Ce_{1-x}Y_xO_2$ nanoparticles samples

The Mullikan electro negativity formula [61] can be used to further establish the generation of defects with introducing yttrium ions, which is also likewise shown in the UV-Vis band gap measurement. This helps us to better understand the mechanism of electron and hole separation. The relative change in the energy positions of the VB and CB caused by the entry of yttrium into CeO_2 lattice is depicted in figure 3.10, The conduction band is located 3.38 eV above the Fermi level indicating that the predicted band gap matches the experimental value of 3.38 eV for undoped CeO_2 nanoparticles as shown in figure 3.10. The findings validate that the absorption peaks of Y-doped CeO_2 nanoparticles are most probably originated due to intra-bands formation and the absorption maxima is red shifted towards higher wavelength with variation in band gap owing to the BM effect at higher doping concentration.

3.3.4. Photoluminescence Spectroscopy

The PL spectrum excited under 325 nm for undoped CeO_2 and Y-doped CeO_2 samples with in wavelength range 350-580 nm is shown in figure 3.11.

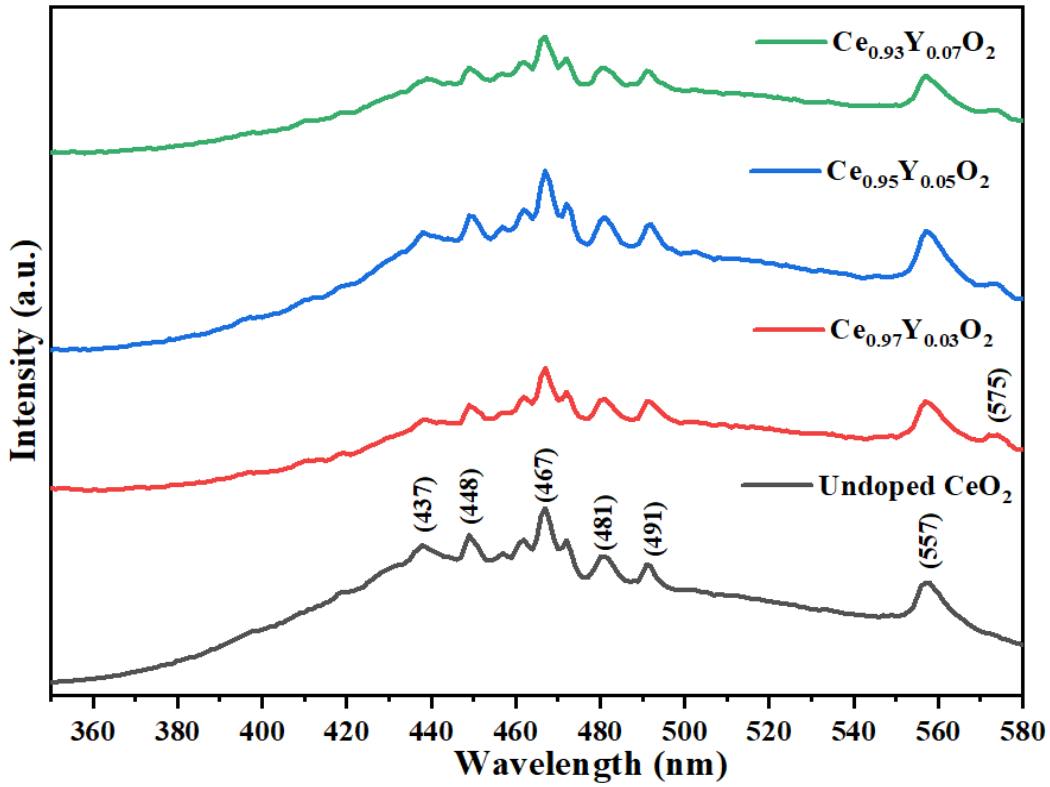

Figure 3.11: The PL spectra of undoped CeO_2 and $Ce_{1-x}Y_xO_2$ nanoparticles samples

The observed emission peaks are the outcomes of the radiative recombination of electrons-holes [89]. According to the findings from the literatures [142], the emission band of CeO_2 samples between 400 and 500 nm arises due to transition from one defect level to another in the Ce 4f to O 2p level. The visible spectra between 400 – 500 nm corresponds to the photogenerated hole and the electron filling the oxygen vacancy undergoing radiative recombination. A band of seven peaks has been detected in the PL spectra that are centred at 437, 448, 467, 481, 491 and 557 nm. Blue emission has peaks around 437 and 448 nm, while blue green emission has peaks around 467, 481, and 491 nm. The green emission is responsible for the peak visible at 557 nm. The near-band exitonic recombination is responsible for emission band peak observed at 437 nm. According to ***Meng et al.*** [143], emission peak at 445-500 nm could attribute to the transitions from various defects levels to the O 2p band. A blue emission band at 448 nm, which may be related to the oxygen vacancies. A sharp peak location at 467-469 nm is accountable for the features of the traps existing in the nanoparticles [144] whereas; in view to ***Wang et al.*** [145] the emission peak at 467 nm is caused by numerous beneficial defects. ***Kwok et al.*** [146] found that an emission peak around 481 nm is arisen by the transition from the ionised oxygen vacancies state to the valence band. There is a blue PL emission peak 491 nm that results from electron decay from the CB to the acceptor band. Oxygen interstitial (Oi) can also cause the formation of this zone as reported by ***Kavita et al.*** [147]. Green radiation in the 500–560 nm range is attributed to local oxygen vacancies defects where; the oxygen vacancy leaves four unbound electrons and weakly bonded Ce ion electrons in the unit cell. These electrons produce a donor energy range that is near to and lower than CB. In the PL spectra of Y-doped CeO_2 samples, not a shift in the defect emission position, but the appearance of and Y-related emission peak, has been noted Interestingly, the spectrum of undoped CeO_2 does not show the peak at 575 nm, which is present in the Y-doped sample. Y ions themselves may be responsible for this rise. The existence of a significant number of defects linked to the Y content, can alter PL emission. The Y content is crucial to the PL because it induces defects and material disarray when it is present.

Since both undoped $CeO_2$and Y-doped samples shows band to band excitation peak within the wavelength range 360 to 580 nm. Considering that the position of the peaks does not differ noticeably in undoped and doped samples except the appearance of peak at 575 nm which is observed only for Y-doped samples. The oxygen defect

levels below the Ce 4f level in the mid band gap of CeO_2 extend nearly up to 3 eV from the valence band. Since, all the excitation peaks fall inside this energy range, so these peaks can be associated with the oxygen vacancies. The presence of various energy levels of oxygen vacancies in the CeO_2 nanoparticles is evident from the appearance of these excitation peaks [136]. Therefore, it is evident from PL spectra that oxygen vacancies, which serve as effective centre for the capture of excited electron, are primarily responsible for these visible emission peaks. By recombining with the valence band or trapped hole, the excitation energy is held there and then released to dopants or directly radiated as light.

The colour parameters related to the prepared undoped and Y-doped CeO_2 samples are identified to comprehend their usefulness in the light emitting diodes (LEDs). In a two-dimensional colour system established by the Commission Internationale de' Eclairge (CIE) in 1931, the emitted colours of undoped and Y-doped CeO_2 are displayed as (x, y) points. The name of this colour space is CIE (x, y) 1931 [148]. To accurately determine colour parameters like dominant wavelength, CRI, CCT and colour purity, the CIE plot can be used. Table 3.5 contains the calculated colorimetric values (x, y) of undoped CeO_2 and Y-doped CeO_2 samples. The horseshoe diagram in a CIE plot as shown in figure 3.12 contains all the colours that are visible and have a set of (x, y) coordinates. According to the NTSE system, the CIE colour coordinates of Y-doped and undoped CeO_2 nanoparticles are close to yellow point region (CIE standard Illuminant C), indicating that colorimetric coordinates (x, y) lie in the yellow region, showing the richness of yellow colour emission. The calculated magnitude of dominant is provided in Table 3.5 and ranging from 575-582 nm, corresponding to yellow emission.

Table 3.5: Various colour parameters for undoped CeO_2 and $Ce_{1-x}Y_xO_2$ nanoparticles samples

Samples	X	y	λ_d (nm)	Purity (%)	CCT	CRI
Undoped CeO_2	0.4026	0.4133	576.3	44.9	3729	89
$Ce_{0.97}Y_{0.03}O_2$	0.3953	0.3750	583.0	31.2	3600	95
$Ce_{0.95}Y_{0.05}O_2$	0.4028	0.3896	580.7	37.8	3547	93
$Ce_{0.93}Y_{0.07}O_2$	0.4014	0.3867	581.1	36.5	3554	93

As a result, the samples can be utilized as a yellow phosphor in applications involving solid state illumination [149,150]. When discussing x-y chromaticity, purity (also known as saturation) refers to how "pure" or monochromatic a colour is at a specific brightness [151]. With higher excitation purity, pure colours appear more saturated and vice-versa [149]. Table 3.5 shows that both undoped and Y-doped samples have calculated purity values below 50%, meaning that these samples exhibit less saturation of yellow colour.

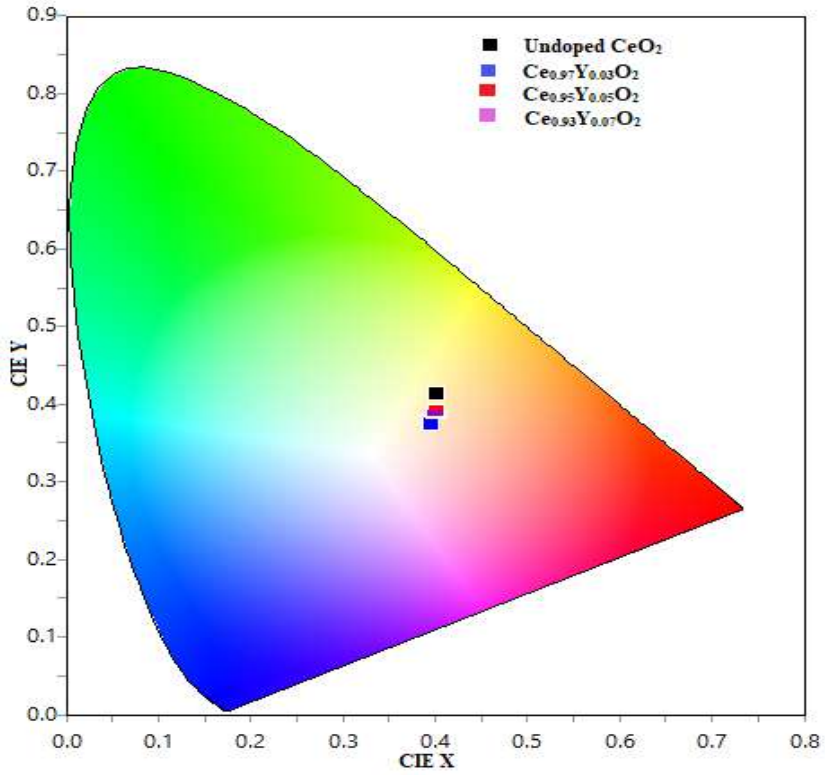

Figure 3.12: The CIE- plot of undoped CeO_2 and $Ce_{1-x}Y_xO_2$ nanoparticles samples.

Technically, the CCT parameter is employed to produce various kinds of commercial atmospheres as it represents the warmth of a light source [152]. As demonstrated in Table 3.5, the CCT values of the prepared samples in our case is below 4000 K, which falls under the category of warm light sources with wide range of applications at indoor site. These samples are useful for lighting office spaces where CCT (3000–4000K) is typically appropriate, hospitals where CCT (3500–4000K) is better for setting a fresh, alert atmosphere, and schools and universities where CCT range (3500–400K) is more preferred for creating an energising

atmosphere. Using a mathematical method, the colour-rendering index (CRI) measures how well the capacity of a light source to make colours visible to human vision in comparison to the standard light sources [148]. As the Table 3.5 indicates the value of CRI for Y-doped CeO_2 samples is more than compared to undoped CeO_2. Such results show that doping CeO_2 with the elements such as Y can effectively enhance the optical as well as photoluminescence characteristics. The obtained results from Table 3.5 shows that all the colour parameters for x = 0.05 and 0.07 concentration is almost the same, which is consistent with the outcomes of XRD, TEM and absorption spectroscopy where the parameters such as average particle size, E_g, n and E_u are obtained to be similar for x = 0.05 and 0.07 concentration.

3.3.5. X-Ray Photoelectron Spectroscopy (XPS) Measurement

3.3.5.1. XPS spectra of Ce 3d

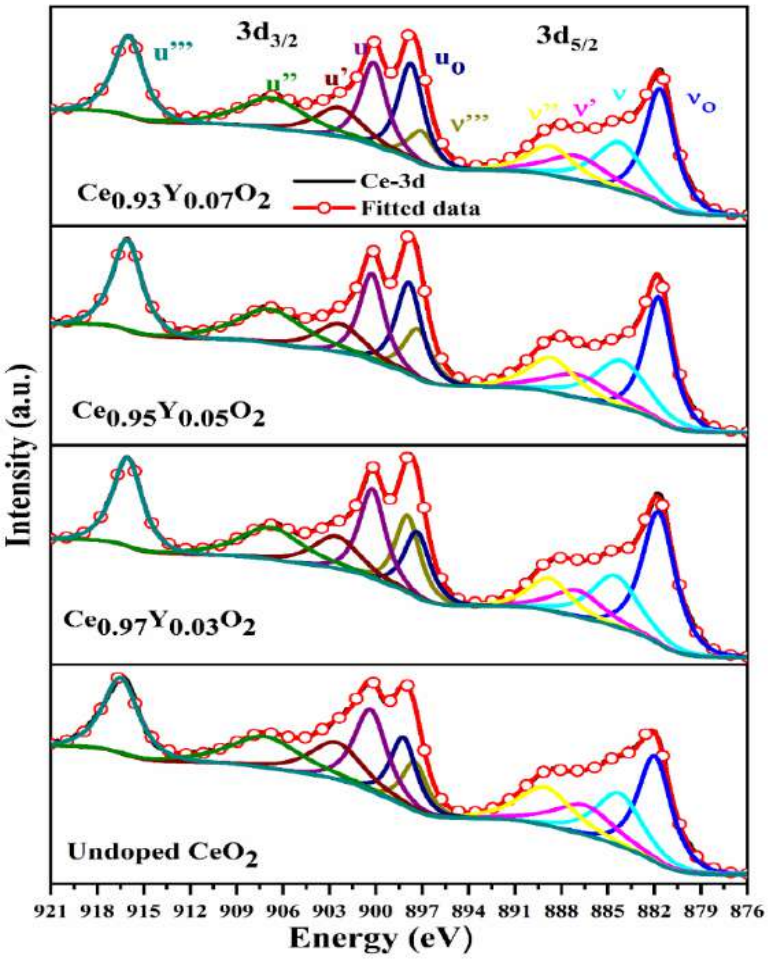

Figure 3.13: The deconvoluted peak of Ce 3d profile of undoped CeO_2 and $Ce_{1-x}Y_xO_2$ nanoparticles samples

The CeO_2 nanoparticles have been characterized using XPS of Ce 3d, O 1s and Y 3d core level before and after yttrium doping. The Ce 3d core level XPS spectra of $Ce_{1-x}Y_xO_2$ samples are shown in figure 3.12. The C 1s peak (binding energy (BE) = 284.6 eV) has been taken as a reference point to adjust all BE for the charge shift [153]. Figure 3.13 illustrates how Ce 3d core level spectra in the BE range 876-921 eV have been deconvoluted using Gaussian fitting. The final-state occupancy of the Ce 4f level in Ce 3d XPS core-level spectra is often characterized by complicated but distinctive characteristics [154]. Based on the previous studies [155], there are following classifications for the Ce 3d spectrum: the peaks denoted by u and v are caused by the corresponding $3d_{3/2}$ and $3d_{5/2}$spin-orbit states, respectively. The principal photoemission from Ce^{4+} is what causes the u‴/v‴ doublet to exist. The transfer of electrons from fulfilled O 2p orbital to an unfilled Ce 4f orbital results in the u/v and u″/v″ doublets, which are shakedown characteristics.

Ce^{3+} cation photoemission is responsible for the u′/v′ doublet. In general, these deconvoluted Ce 3d core-level spectra can be classified into ten peaks, six of which are structures formed by Ce^{4+} ions and four of which are formed by Ce^{3+} ions. The peaks labelled v_o, v′, u_o, and u′ are typical Ce^{3+} peaks, whereas the remaining six peaks labelled v, v″, v‴, u, u″, and u‴ are typical Ce^{4+} peaks (figure 3.13) [156].

Table 3.6: Assignments of the Ce 3d XPS peaks and the concentration of Ce^{3+} and Ce^{4+} ions along with their ratio for undoped CeO_2 and $Ce_{1-x}Y_xO_2$ nanoparticles samples

Samples	$3d_{5/2}$ [in eV]						$3d_{3/2}$ [in eV]				Ce^{3+} (%)	Ce^{4+} (%)	$\frac{Ce^{3+}}{Ce^{4+}}$
	v_o	V	v’	v”	v”’	u_o	u	u’	u’’	u’’’			
Undoped CeO_2	881.96	884.25	886.53	889.03	897.47	898.20	900.33	902.54	907.11	916.42	40.60	59.39	0.68
$Ce_{0.97}Y_{0.03}O_2$	881.70	884.51	886.97	888.78	897.31	897.93	900.21	902.58	906.75	916.03	42.45	57.54	0.73
$Ce_{0.95}Y_{0.05}O_2$	881.71	884.09	886.94	888.65	897.31	897.85	900.24	902.33	906.81	916.06	44.84	55.15	0.81
$Ce_{0.93}Y_{0.07}O_2$	881.62	884.24	886.98	888.73	897.73	897.73	900.38	902.38	906.70	915.97	44.14	55.85	0.79

Table 3.6 lists all peak positions for "u" and "v" for undoped CeO_2 and $Ce_{1-x}Y_xO_2$ samples. The total concentration of Ce^{3+} and Ce^{4+} ions present in the samples is determined by the equation as per the reference [157]. Table 3.6 summarizes the concentration of Ce^{3+} and Ce^{4+} ions, which demonstrates that on increasing doping concentrations (x = 0.03, 0.05), the concentration of Ce^{3+} ions gradually rise because of the lower radii Ce^{4+} ions being replaced by bigger radii Y^{3+} ions in CeO_2 nanoparticles, to retain charge neutrality. The presence of Ce^{3+} corresponds to the formation of oxygen vacancies or Ce_2O_3 phase. At x = 0.07, not much difference in the concentration of Ce^{3+} ions have been observed in compare to x = 0.05, which again suggest to control the limit of doping concentration after x = 0.05. According to the XPS analysis, the occurrence of Ce^{3+} and Ce^{4+} ions have been detected in all the samples, and the increase in the Ce^{3+} concentration attributes to the more defects and/or an amorphous phase of Ce_2O_3, so formed.

3.3.5.2. XPS spectra of O1s

Figure 3.14 displays the O 1s spectra for undoped CeO_2 and $Ce_{1-x}Y_xO_2$ samples. The concentration of O^{2-} ions for all samples is calculated using the deconvoluted three-peak asymmetrical O 1s core level spectrum. The BE range of the spectrum is 526-540 eV. Peaks with BE of (528.80, 529.50 and 531.60) eV in the O1s represents oxygen lattice (O_L), oxygen vacancies peak (O_v) and O_C associated with the Ce^{3+} ions (Ce^{3+} -hydroxide and Ce^{3+}-oxide), observed in CeO_2 nanoparticles respectively [158,143].

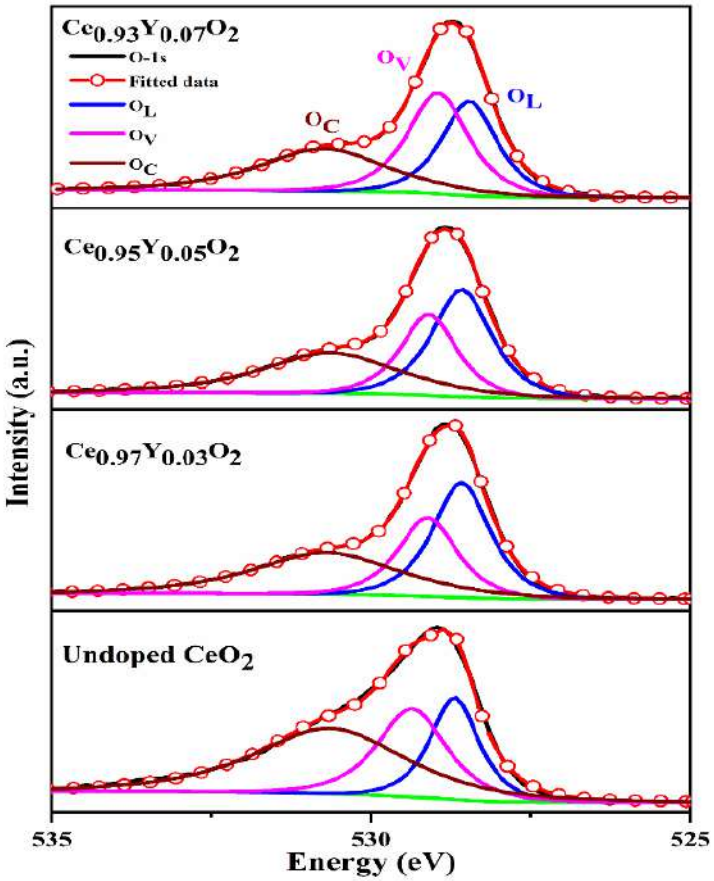

Figure 3.14: The deconvoluted core level spectra of the O 1s profile for undoped CeO_2 and $Ce_{1-x}Y_xO_2$ nanoparticles samples

The quantitative analysis of the O_L and O_v peaks demonstrates that the formation of oxygen vacancies on the surface and found to vary when the Y concentration in the CeO_2 nanoparticles changes. Additionally, the O 1s electron is more closely bound to the Ce^{3+} than Ce^{4+} oxidation state [130]. Therefore, the change in the formation of oxygen vacancies may also be related to the change in the transition state of $Ce^{4+} \rightarrow Ce^{3+}$ ions brought on by the incorporation of yttrium ions in the CeO_2 nanoparticles. The total oxygen concentration of the samples is equal to the sum of the oxygen required to completely oxidize both oxidation state: Ce^{3+} and Ce^{4+} to form Ce_2O_3 and CeO_2. After that, considering the stoichiometry, which is 1.5 for Ce_2O_3 and 2 for CeO_2 respectively. The concentration of Ce^{3+} and Ce^{4+} ions as shown in Table 3.7 may now be used to establish the stoichiometric ratio of the oxygen to the sum of Ce^{3+} and Ce^{4+} ions using the equation as per the reference [159].The actual stoichiometry x′, which do not account for the theoretical stoichiometry of the totally oxidized forms, namely Ce_2O_3 and CeO_2, respectively, are thought to be much closer

to reality [160,161]. Table 3.7 shows how Yttrium concentration affects the stoichiometry obtained by x and x' for all the prepared nanoparticles samples. In most cases, x > x, with magnitude of x <2 (nearly 1.5), if CeO_2 is oxygen deficient. Because of the maximum oxygen storage in the lattice for both oxides' forms, Ce_2O_3 and CeO_2, x' cannot exceed x. The values of the theoretical stoichiometric parameter x, for the prepared samples are found to be less than 2. The deficiency of the lattice oxygen influences the creation of oxygen vacancies [162]. The calculated stoichiometric ratio of oxygen to cerium has greater value of x in compare to x' for all the samples, suggesting that part of Ce^{3+} is consumed in the formation of Ce_2O_3, along with the generation of oxygen vacancies [163]. Therefore, an increase in Ce^{3+} ions occur simultaneously with the promotion of these oxygen vacancies.

The study of XPS revealed the creation of oxygen vacancies and Ce_2O_3, present in the CeO_2 deposits in this work, although XRD only revealed CeO_2. Considering this, the Ce_2O_3 phase is amorphous in nature [159].

Table 3.7: Individual O 1s peak XPS binding energies and stoichiometry ratio x and x' for undoped CeO_2 and $Ce_{1-x}Y_xO_2$ nanoparticles samples

Samples	O_L [eV]	O_V [eV]	O_C [eV]	% O_L	% O_V	X	x'
Undoped CeO_2	528.69	529.35	530.63	44.81	55.19	1.79	1.48
$Ce_{0.97}$ $Y_{0.03}O_2$	528.58	529.11	530.69	58.85	41.14	1.78	1.69
$Ce_{0.95}$ $Y_{0.05}O_2$	528.57	529.09	530.62	58.53	41.46	1.77	1.64
$Ce_{0.93}$ $Y_{0.07}O_2$	528.45	528.95	530.72	45.98	54.01	1.78	1.68

3.3.5.3.XPS spectra of Y 3d:

Table 3.8: XPS binding energy peak position of Y 3d of $Ce_{1-x}Y_xO_2$ nanoparticles samples

Samples	$Y3d_{5/2}$ [eV]	$Y3d_{3/2}$ [eV]
$Ce_{0.97}$ $Y_{0.03}O_2$	156.47	158.58
$Ce_{0.95}$ $Y_{0.05}O_2$	156.58	158.60
$Ce_{0.93}Y_{0.07}O_2$	158.42	158.34

The Y-doped samples exhibit a doublet for 3d state which have been detected in the XPS spectra as shown in figure 3.15. These two peaks existing at binding energy range 156-157 eV and 158-159 eV corresponds to $Y3d_{5/2}$ and $Y3d_{3/2}$ respectively, as shown in Table 3.8 [164].

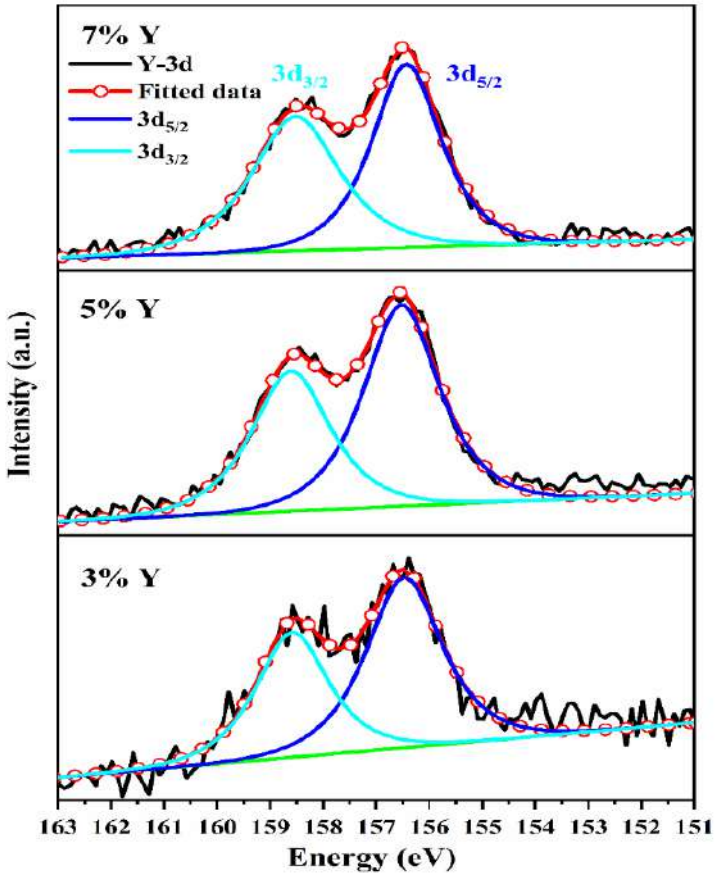

Figure 3.15: Y 3d core level spectra of $Ce_{1-x}Y_xO_2$ nanoparticles samples.

The XPS analysis conclude that doping of Y give rise to generation of more defects and oxygen vacancies in CeO_2 nanoparticles**.** Using XPS, it has also been shown that for Y-doped samples, the concentration of Ce^{3+} has risen as the doping concentration of Y has increased. However, after an optimal doping concentration (x = 0.05), no significant effect is observed due to presence of optimal level of Ce^{3+} ions and oxygen vacancies.

3.3.6. Photocatalytic activity

The photo-catalytic activity of CeO_2 and Y-doped CeO_2 are investigated using the methylene Blue (MB) dye degradation. For this purpose, UV-Vis light of mercury lamp (250W, ~200-600 nm) is used for photo-catalytic degradation of 150 ml aqueous

solution (10^{-5}M or 10 ppm) of MB dye using 30 mg undoped CeO_2 and Y-doped CeO_2 nanoparticles as catalyst. To achieve adsorption/desorption equilibrium between the substances and catalyst, the catalyst-added MB dye solution is stirred for an hour in a dark atmosphere using a magnetic stirrer. After that, dye solution is exposed to UV-visible light and in every 30 min time interval 20ml MB solution is collected for study of degradation kinetic. The following formula is used to get the efficiency of degradation (η) of MB [98]:

$$\boldsymbol{n = \frac{C_0 - C}{C_0} \times 100\%} \qquad \textbf{(3.2)}$$

Here, $\boldsymbol{C_0}$ and $\boldsymbol{C}$ are the initial and leftover MB solution concentrations, respectively. The photocatalytic activity of CeO_2 is enhanced by doping concentration of Y in CeO_2 nanoparticles. MO solution is showing a comparable change of 39%, 42%, 47% and 54% in its concentration with uses of undoped CeO_2, and as photo-catalyst, respectively. This outcome demonstrates the improvement in photoinduced activities with Y concentration increment, which obey undoped CeO_2 < $Ce_{0.97}Y_{0.03}O_2$ < $Ce_{0.95}Y_{0.05}O_2$ < $Ce_{0.93}Y_{0.07}O_2$ orders and $3.2x10^{-3}min^{-1}$, $3.6x10^{-3}$ min^{-1}, $4.2x10^{-3}$ $min^{-1}$and $5.1x10^{-3}$ min^{-1} are the calculated reaction rate value for them. Whole calculation is based on the pseudo-first-order kinetic equation (i.e. $\ln(\mathbf{C/C_0}) = \boldsymbol{k}t$). Reaction rate constant (***k***) for $Ce_{0.93}Y_{0.07}O_2$is ~1.5 times higher than the undoped CeO_2 rate constant. It draws attention to the fact that Y-doped CeO_2 has higher photocatalytic activity than undoped CeO_2.The chemical and pollutant oxidation processes caused by photosynthesis are described in the following reactions:

$$\mathbf{h\nu + CeO_2/Y\text{-}CeO_2 \rightarrow h^+ (VB) + e^- (CB)} \qquad \textbf{(3.3.i)}$$

$$\mathbf{h^+ + H_2O \rightarrow H^+ + OH^-} \qquad \textbf{(3.3.ii)}$$

$$\mathbf{h^+ + OH^- \rightarrow OH^\bullet} \qquad \textbf{(3.3.iii)}$$

$$\mathbf{e^- + O_2 \rightarrow O_2^\bullet} \qquad \textbf{(3.3.iv)}$$

$$\mathbf{2e^- + O_2 + H_2O \rightarrow H_2O_2} \qquad \textbf{(3.3.v)}$$

$$\mathbf{e^- + H_2O_2 \rightarrow OH^\bullet + OH^-} \qquad \textbf{(3.3.vi)}$$

$$\textbf{Organic pollutant} + \mathbf{OH^\bullet + O_2 \rightarrow H_2O + CO_2} + \textbf{other degraded molecules.} \qquad \textbf{(3.3.vii)}$$

This enhanced photocatalytic phenomenon may be attributed to many factors such as Y-doped content in CeO_2 nanoparticles, improved defect density or oxygen vacancies, wide surface area, broad optical absorption spectra, reduced band gap, and high electron-hole separation time [119, 120, 98]. Y-doped CeO_2 and undoped CeO_2

nanosheets undergo electron-hole pair production during a photocatalytic reduction activity when they are subjected to UV-Vis light exposure. The enhanced light harvesting ability of Y-doped CeO_2 is a significant contributor to its high photocatalytic efficiency. With a large bandgap of around 3.3 to 3.5 eV and a short Urbach tail, pure CeO_2 absorbs light exclusively in the UV range ($\lambda < 370$ nm), with very low absorption from the visible range. Nevertheless, when the Y-dopant proportion rises, CeO_2 exhibits a decreasing band gap and an increased Urbach energy [98, 165].

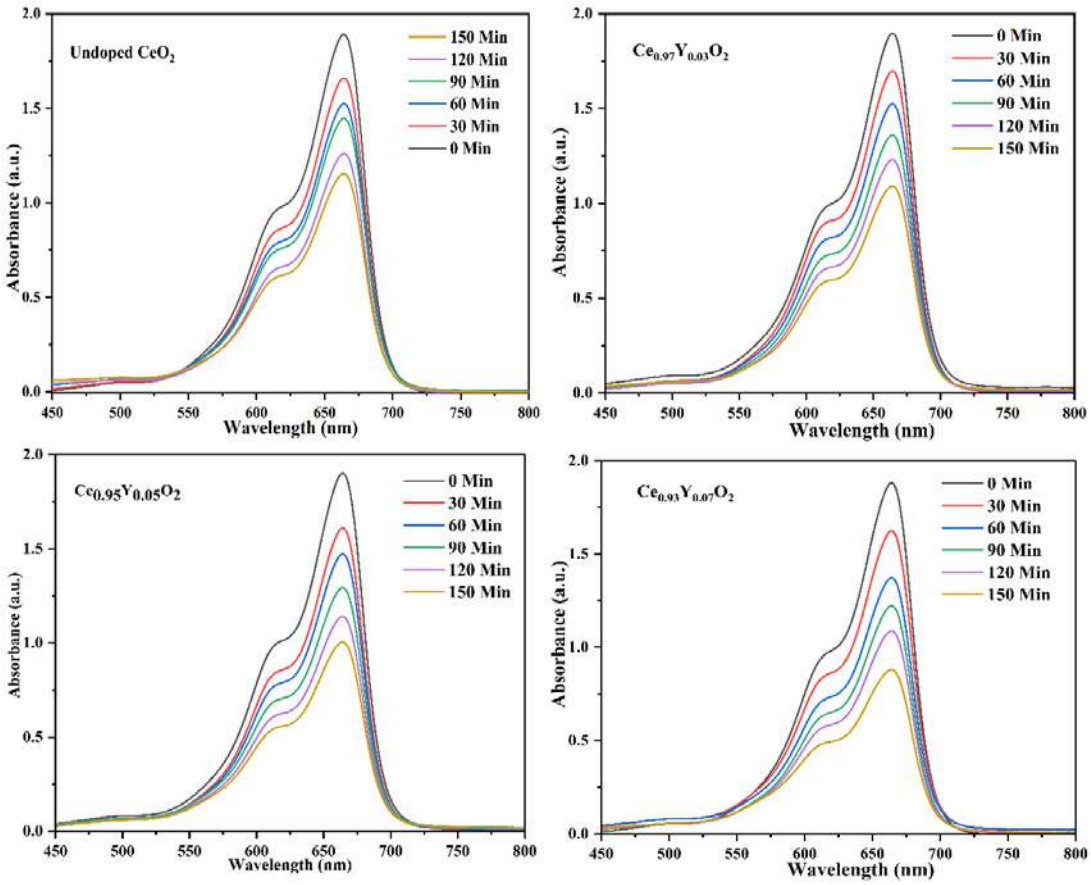

Figure 3.16: UV-Vis absorption spectra of photocatalytic reduction for varying time in presence of different catalyst (a) Undoped CeO_2, (b) $Ce_{0.97}Y_{0.03}O_2$, (c) $Ce_{0.95}Y_{0.05}O_2$ and (d) $Ce_{0.93}Y_{0.07}O_2$.

Therefore, in comparison to undoped CeO_2, it offers a greater absorption in the UV-visible range. As a result of the photocatalytic activity being carried out using a mercury UV-Vis lamp (250W, 200-600nm range). UV-Vis absorption spectra of photo-catalytic reduction for varying time in presence of different catalyst (a)

Undoped CeO_2 (b) $Ce_{0.97}Y_{0.03}O_2$, (c) $Ce_{0.95}Y_{0.05}O_2$and (d) $Ce_{0.93}Y_{0.07}O_2$ are shown in figure 3.16. The absorption range of the spectra increased as the bandgap narrowed with increasing Y dopant. A decrease in the bandgap enhances photo-catalytic activity by enabling low-energy photons to participate in photo-induced reduction. Secondly, a high defect density leads to an improvement in the Urbach tail.

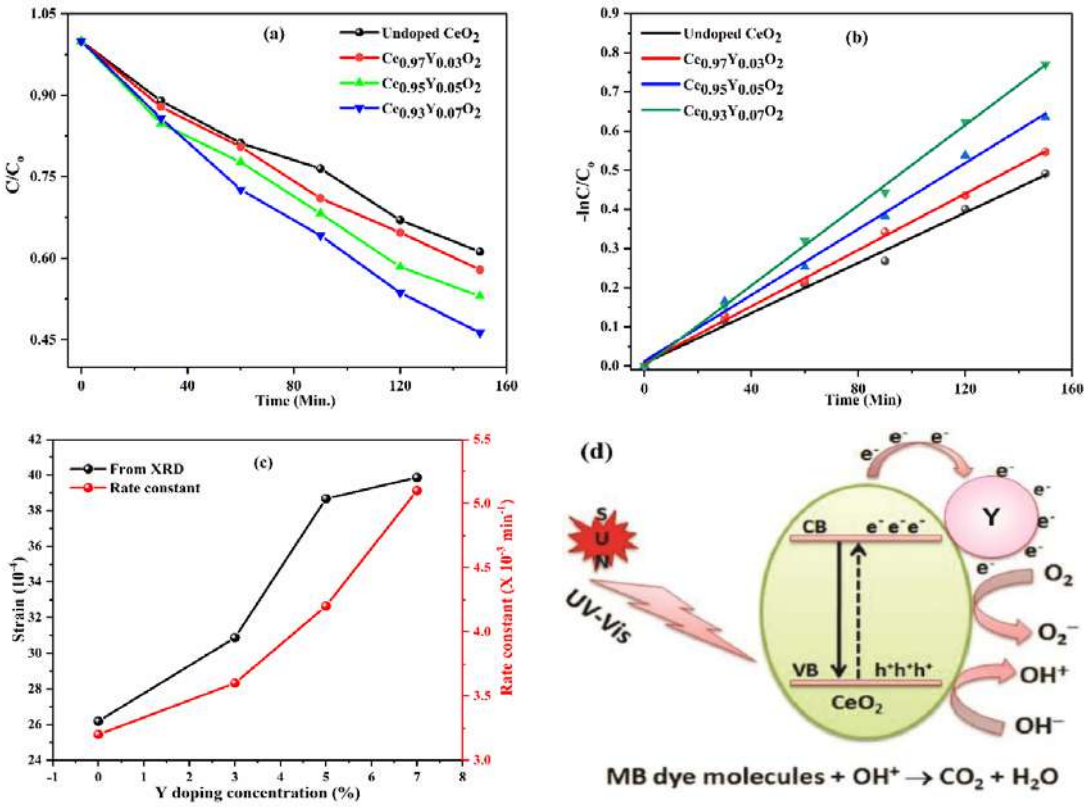

Figure 3.17: (a) Concentration variation of MB after photocatalytic oxidation, (b) Photocatalytic reaction kinetics of MB, (c) Rate constant and strain variation with doping concentration and (d) Schematic diagram of undoped CeO_2 and Y-doped CeO_2 photocatalytic activity.

The high density of states close to the conduction band edge is caused by these defects, which also enable the valance band electron to be stimulated by a photon with somewhat lower energy. These defects offer places of stimulating electron trapping, assisting in extending the period of electron hole pair recombination [165]. Therefore, the long charge separation time of Y-doped CeO_2 makes it an extremely effective photocatalyst, encouraging improvements in the rate of photo-catalytic reduction. The concentration variation of MB after photocatalytic oxidation and photocatalytic reaction kinetics is shown in figure 3.17(a) and (b) respectively, whereas, figure

3.17(c) represents the rate constant and strain variation with doping concentration. Y demonstrated the behavior of a sensitizer to absorb visible light when it is doped with CeO_2. As a result, CeO_2's excited electrons transfer to the transition metal Y's conduction band, where they produce a similar number of holes in the valance band [165]. Figure 3.17(d) provides a schematic representation of the process involved in the improvement of the photo-catalytic activity of both undoped and Y-doped CeO_2. For Y doped CeO_2, the holes that have formed in the valance band shift to the O-Y-O energy level, his causes Y-doped CeO_2 to be working far better photo-catalytically. As shown in figure 3.17(c), lattice strain and photocatalytic rate constant showing a similar trend with doping concentration.

It can be summarized that the number of oxygen vacancies and generation of defects are found to increase by Y-doping. The occurrence of strain and structural distortion has been revealed by the XRD measurement. The results from HRTEM image shows that Y-doped samples comprised of many small particles which are spherical in shape and having particle size below 20 nm. The successful incorporation of Y^{3+} ions is additionally supported by UV-Vis spectroscopy which shows that the absorption peaks arises due to electronic transition of Y in the crystalline environment of CeO_2.The lowering of the optical band gap after Y-doping is due to presence of defects related to Y present in the mid of the gap.However, the BM effect is responsible for the rise of the band gap at the optimal concentration of Y. The CeO_2 nanoparticles' oxygen defects are also visible in the PL spectra. Therefore, by adding Y dopant concentration, the oxygen vacancies concentration in CeO_2 may be raised, making it an effective oxygen storage material. The XPS analysis suggests that concentration of Ce^{3+} first rises as Y content is increased. It is demonstrated that x = 0.05 dopant concentration corresponds to the maximum Ce^{3+}. But as the amount of Y rises above x = 0.05, no variation has been found. Thus, the present work shows that the defect structure in Y-doped cerium is highly dependent on the doping concentration. Our results convincingly demonstrate a random distribution of Y^{3+} along with oxygen vacancies complex at lower doping. However, our findings showed that Y^{3+} tends to aggregate at the surface of CeO_2 accompanied by oxygen vacancies and Ce^{3+} ions at higher doping. This result can be explained that lattice strain can modify the surface energy and reactivity of photocatalytic materials. Strained surfaces may exhibit higher reactivity, providing more active sites for photo-catalytic

reactions. Also, a crystal's strain can cause defects to develop, such as oxygen vacancies and these voids may serve as active sites. Change in the electrical band structure can result in modifications to the band gap caused by strain inside the crystal lattice [166]. By increasing visible light absorption, a narrower band gap can raise photo-catalytic efficiency. In summary, these circumstances improve the electron hole pair separation time, activate a wide range of spectra for photocatalytic reduction of organic pollutants, and increase porosity and surface area for photochemical reactivity.

Adding yttrium to the CeO_2 lattice changes its structure and electronic environment by partially substituting Ce^{4+} ions. This substitution changes not only the crystallite size and lattice strain, but also the oxygen vacancy content, which is crucial for improving structural, optical, and photo-catalytic responses. The inclusion of Y^{3+} stimulates lattice relaxation and oxygen defects development due to its lower valence state and slightly different ionic radius than Ce^{4+}. Y-doped CeO_2 nanoparticles exhibit better redox activity, reduced band gap, enhanced photoluminescence, electronic structure at ambient temperature, and improved surface morphology. This makes them excellent for photo-catalysis, environmental remediation, and optical devices.

3.4. Conclusion

The co-precipitation route synthesized $CeO_2$and Y-doped CeO_2 nanoparticles are investigated in this chapter for structural, morphological, optical, XPS, luminescence properties and their photocatalytic activity. The crystallite size of these single-phase nanoparticles is measured within the range 18-9 nm by XRD and TEM analysis with better crystalline nature. According to HRTEM images, the inter-planer distance for (111) plane changes significantly for different doping concentration. We have seen variations in magnitude of refractive index and E_g values with varied concentrations of Y^{3+} ions in CeO_2 from the analysis of the UV-Vis-NIR spectroscopy. Incorporating Y^{3+} ions into CeO_2 nanoparticles lowers the refractive index, which improves UV protection. Increases in Eu values at higher doping concentration support the introduction of defects and new inter band states within the band gap. The obtained CCT for the doped samples examined using PL spectra indicates the wide application of these samples with yellow luminescence. The core level Ce 3d, O1s, and Y 3d XPS spectra have also been obtained and thoroughly examined to govern the

electronic structure properties of these nanoparticles. The XPS investigation reports the incorporation of the Y^{3+} ions in the lattice, the transition of the oxidation state: $Ce^{+4} \rightarrow Ce^{3+}$ ions, and formation of oxygen vacancy states by the creation of defects or an amorphous phase of Ce_2O_3. According to photo-catalytic results, 7% Y dopedCeO_2 is showing almost 1.5 times higher photocatalytic reduction rate constant than undoped CeO_2. Reason behind this higher photocatalytic reduction of organic pollutant might be synergistic effect of photogenerated high electron hole pair concentration and $OH^{\bullet}$ radicals generated in catalytic reaction. Y doped CeO_2 nanoparticles are an excellent catalyst driven by UV-Vis light and can eliminate organic pollutants from aqueous solutions.

Chapter 4
Study of Structural, Optical, Photoluminescence, Electronic Structure and Electrochemical Properties of Ag-Doped CeO_2 Nanoparticles

Chapter-4

Study of Structural, Optical, Photoluminescence, Electronic Structure and Electrochemical Properties of Ag-Doped CeO_2 Nanoparticles

Abstract

The structure and functional properties of materials can be significantly influenced by the synthesis of nanoparticles. This chapter presents undoped CeO_2 and Ag doped CeO_2 nanoparticles with different concentration of Ag (x = 0.03, 0.05 and 0.07), prepared using a simple coprecipitation route of synthesis. The prepared nanoparticles have been characterized via X-ray diffraction (XRD), UV-Vis NIR spectroscopy, photoluminescence (PL), X-ray photoelectron spectroscopy (XPS) and electrochemical analysis. The XRD measurement infers the improvement in the crystalline nature with Ag-doping and crystallite size between 13-9 nm. The absorption spectra reflect the red shifting of the absorption peaks along with the narrowing of band gap with rise in the Ag concentration. To ascertain the defects and excitation wavelength, PL measurement has been performed. High color rendering index (CRI) of the prepared samples showed good luminescence with white light emission. The development of oxygen vacancies upon Ag doping is further confirmed by XPS measurement. In addition, the XPS measurements revealed the charged oxygen vacancies as well as the valence states of Ce with 3+ and 4+, Ag with 1+, and O with 2-. The CV test verified that in 2 M KOH electrolyte solution, the 5% Ag-doped CeO_2 nanoparticles had the maximum specific capacitance (C_{SP}) value of 363.44 F/g at scan rate of 10mV/s the best cycle stability (retaining 93.90% after 2100 cycles). It was discovered that the 5% Ag-doped CeO_2 nanoparticles had an energy density of 125.08 Wh/kg and a power density of 652.48 W/kg. An excellent super capacitive performance of Ag doping in CeO_2 could be used as a unique electrode material to develop high-efficiency and durable energy storage devices and resulted in the enrichment of electrochemical properties of these nano-materials. Cyclic voltammetry (CV) results are consistent with electrochemical impedance spectroscopy, indicating good voltammetry and impedance spectroscopy performance of Ag-doped CeO_2 nanoparticles. These nano-materials are also better alternatives for solid state electrolyte for fuel cells, UV blockers, photo-catalyst, and many other applications.

4.1. Introduction

In this modern world, the need for electrical power is rising so fast as the capacity to deliver a significant amount of electric power quickly becomes crucial with the rise of electrically powered devices and electric motors. Similarly, there is a growing trend in automobiles to recover power when braking. This necessitates the use of storage devices with rapid charging times and a big capacity to hold the energy generated during braking. These prerequisites bring to the imminence of supercapacitor. The supercapacitor is placed somewhere in between storage batteries and commercial capacitors [100]. An additional draw of supercapacitor is their extended cycle life and environmentally friendly design. The electric double layer capacitor (EDLC) used in supercapacitor was initially made of carbonaceous materials, which offer low resistance, and a long cycle. Yet, the double layer area limits the energy density of the EDLC [167]. Due to this limitation, researchers are now looking for substitute materials for pseudocapacitors, which store charge using Faradic redox processes [168,169]. In pseudocapacitors, rare earth (RE) oxides, polymers, and transition metal oxides are the most common materials used. Due to their multi-oxidation state stability and enhanced ionic conductivity, transition metal and RE oxides are thought to be the best options [170]. The potential of RE oxides in supercapacitor applications has recently attracted a lot of attention. Our investigation into preparation cerium oxide nanoparticles via co-precipitation method have resulted into very favorable outcomes. Cerium oxide is the preferred material because of its appealing valence states, high theoretical capacitance, affordability, and environmental friendliness. Also, CeO_2 can be used as a supercapacitor because of their electrochemical properties in different electrolytes and when paired with other materials [171, 172]. CeO_2 can store and release oxygen at low temperatures owing to its FCC structure, which produces cations with varying oxidation levels between Ce^{3+} and Ce^{4+}. The redox cycle between $Ce^{3+} \rightarrow Ce^{4+}$, is known as the oxygen storage capacity (OSC) [105]. Therefore, CeO_2 has been employed as a stable catalytic material for redox reactions [173]. It is a semiconductor with an indirect optical band-gap 2.9-3.2 eV, great efficiency, thermal stability, and exceptional unique properties such as oxygen diffusion rates, quick reaction kinetics, the material can be applied in the thermo-chemical industry [174, 175]. The leading properties of CeO_2 nanoparticles, such as high oxygen ion conductivity, high specific capacitance, high refractive index, and non-toxicity, have resulted into their various applications,

including supercapacitor [176], solar cells [177], photo- catalysis [178] and solid-oxide fuel cells [79]. Many studies revealed that addition of other material to the CeO_2 structure to enhance the materials' properties and increase its applications. Doping approach on CeO_2 nanostructures has been directed towards the oxidation reactions that convert Ce^{4+} to Ce^{3+}. Doping metal ions with valances <4+ may increase the mixed conductivity of CeO_2 nanoparticles. TM ions are widely recognized as appropriate options for industrial use due to their affordability, stability, and excellent catalysis [77] for various applications as depicted in the figure 4.1. Integrating TMs as dopant in ceria crystal lattices improves oxygen vacancy mobility, redox performance, specific surface area, lattice defects, and synergistic effects. Impurities in the ceria crystal lattice boost ionic mobility, leading to increased conductivity and ion release. CeO_2 lattice mobility of ionic species varies based on dopant type, quantity, and concentration. Dopant ions can significantly increase the number of ionic compounds in a lattice, leading to increased electro-oxidation of redox species characteristics. [180, 181]. Noble metals like Ag and Au have been loaded onto CeO_2, in addition to doping, and found to improve its catalytic performance [53]. According to ***Ma et al.*** [182], Ag-modified CeO_2 enhances visible light absorption and is a promising approach for developing photo catalysts that react with visible light. ***Haghighatzadeh et al.*** [183] identified that Ag-doped CeO_2 possess the potential for nonlinear optical materials.

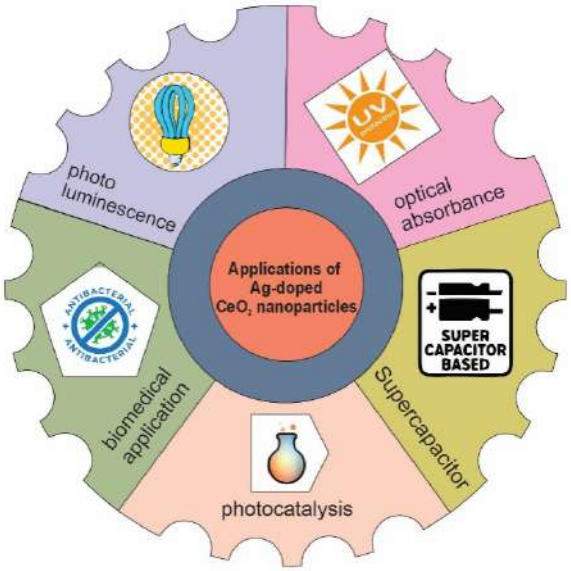

Figure 4.1: Pictorial representation of various possible applications of the Ag-doped CeO_2 nanoparticles

In the chapter, silver has been chosen as a suitable dopant to the CeO_2 because of the following reasons. First, it is anticipated that the conductivity and the transport ionic kinetics of the electrode material will be enhanced by the addition of high-quality conductive material to the low-dimensional form of metal oxide. Second, because of its several oxidation states (Ag^{+}, Ag^{2+}, Ag^{3+}) and exceptional electrical conductivity, silver and its oxides are becoming more fascinating materials [184]. The addition of Ag nanoparticles in CeO_2 considerably improves their performance in supercapacitor applications. Research suggests that Ag-doped CeO_2 has outstanding electrochemical characteristics, making it a suitable contender for energy storage devices. The structural integrity of Ag-doped CeO_2 is preserved, with Ag nano-clusters improving the structure and lowering charge transfer resistance.

Recent studies have demonstrated how incorporation of Ag to metal oxides can improve their electrochemical as well luminescence properties. ***G. Murugadoss et al.*** [77] reported that at constant current densities of 3 A/g, Ag doped CeO_2 nanoparticles assisted in reaching the high specific capacitance (C_{sp}) of 456 F/g. ***Vanitha et al.*** [75] found that Ag nano-crystal-incorporated CeO_2/Grapheme nanocomposites had the maximum capacitance of 710 F/g at 0.2 A/g.

This manuscript presents a simple co-precipitation method to study structural, optical, electronic structure characteristics and electrochemical behavior of Ag doped CeO_2 nanoparticles. Such investigation rules out how the Ag-doping concentration affects the various properties of host material. X-ray diffraction (XRD), UV-visible absorption and photoluminescence spectroscopy were used to study the crystal structure and optical characteristics. The optical properties evaluate its applicability for light emitting diodes in industrial and commercial purpose. The XPS measurement undertaken to study the electronic structure property explains the valence state of Ce, O and Ag as well as the oxygen vacancies and related defects. Electrochemical characteristics were assessed using cyclic voltammetry (CV) and impedance spectroscopy. We used co-precipitation to synthesize ceria nanoparticles, which is simple, eco-friendly, low-cost, and easy to process. Further, the electrochemical analysis of the prepared samples reveals the variation in the C_{SP} with fluency of Ag dopant ions. The exploration of Ag-doped CeO_2 nanoparticles-based electrodes could lead to the development of industrial electrodes that can accommodate different capacitance requirements for a range of energy storage uses.

4.2. Experimental details

4.2.1. Method of preparation

All the chemicals were acquired from Alpha Aeser, including ammonia (NH_4OH), silver nitrate ($AgNO_3$) with 99% purity, and cerium (IV) nitrate hexahydrate $(NH_4)_2Ce(NO_3)_6$ with 99.9% purity. Using the coprecipitation process, undoped $CeO_2$and $Ce_{1-x}Ag_xO_2$ (x = 0.00, 0.03, 0.05, and 0.07) [CAO3, CAO5, CAO7] nanoparticles were produced using stoichiometrically calculated ratio of the chemicals indicated above. $AgNO_3$ with different concentration of x dissolved in distilled water of 100 ml, for each solution. Further, using NH_4OH as the reducing agent the pH of every solution was brought to 10. These mixtures were agitated for 4 hours at 50°C using a magnetic stirrer. Further, after drying each sample in an oven for 12 hours at 90°C, the dried samples were annealed for 5 hours at 500°C in an electric furnace to produce pale yellow powdered undoped and Ag-doped CeO_2 (CAO) nanoparticles.

4.2.2. Nanoparticles characterization

The diffraction patterns were taken using BrukerD8 Advance X-Ray Diffractometer to analyse the crystal structures of the as-synthesised samples. Cu Kα radiation (λ = 1.5406 Å) was used for XRD measurements in the 2θ range of $20° \leq 2\theta \leq 90°$. The optical absorption spectra in the wavelength range 200–800 nm was obtained using a Shimadzu UV-3600 Plus spectrophotometer. The PL spectra were carried out in the wavelength range 350–580 nm with an exciting wavelength of 325 nm on spectro-fluoromax of HORIBA. Thermo-scientific made Model No. NEXSA surface analysis was used for the XPS measurement using 400μm micro-focused X-ray with a monochromatic Al-Kα source [Energy = 1486.6 eV] with 20 eV pass energy. The XPS spectra were calibrated to the binding energy of the C 1s core line (hv = 284.6 eV), where the experimental chamber was set at a base pressure of better than 10^{-9}torr. The prepared undoped CeO_2 and CAO nanoparticles were also electrochemically analyzed using a three-electrode setup and an electrochemical analyzer/galvanostat (PGSTAT302). Using activated carbon and PVFA, the working electrodes were made from $CeO_2$and CAO samples at various concentration of Ag. All electrochemical measurement was carried out in an electrolyte that contained 2 M KOH, where the Pt wire and an Ag/AgCl electrode were considered as the reference and counter electrodes, respectively. The cyclic voltammetry (CV) measurements were made in the potential range of -0.5 to 0.8V, scanning at a rate of 10–160 mV/s.

Studies on galvanostatic charge-discharge (GCD) was conducted at different current densities ranging from 0.6 A/g to 5 A/g, within a potential range of -0.5 to 0.8V.

4.3. Result and discussions

4.3.1. Surface characterization of nanoparticles

To determine the structural parameters of the synthesized nanoparticles, an XRD pattern in the 20–90° range was obtained, which validated the FCC structure of CeO_2 in each sample as evidenced by JCPDS Files (81- 0792) [185] and illustrated in figure 4.2. The absence of the diffraction peak related to the dopant (like Ag_2O) indicated that the Ag had been successfully doped into the CeO_2 lattice. In both undoped and Ag-doped CeO_2, no additional peaks are observed, showing the exceptional purity of the synthesised samples. According to figure 4.2, strong diffraction peaks showed the well-crystalline nature of CAO nanoparticles. Using Scherer formula [186], the average crystallite size of CAO nanoparticles is determined. The crystallite size variation with Ag doping is shown in Table 4.1.

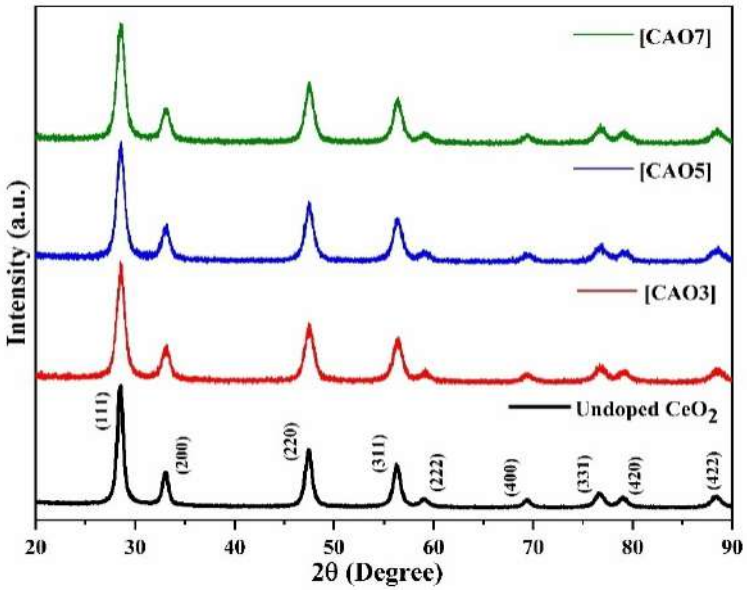

Figure 4.2: The XRD pattern of undoped CeO_2 and CAO nanoparticles samples

The crystallite sizes of the nanoparticles are reduced for CAO nanoparticles; this could be due to varying metal dopant' ionic radii of Ce^{3+} (1.02 Å) and Ag^{+} (1.015 Å) [77]. A primary factor in the lattice distortion is the concentration of Ce^{4+} ions, which falls with increase in Ce^{3+} ions as the foreign metal ions are incorporated in the CeO_2 lattice. A reduction in crystallite size with doping signifies a suppression of

crystal growth formation. The grain boundary in CeO_2 consists of these non-stoichiometrically oxygen defects and Ce^{3+} ions. Noticeably, the maximum crystallite size among the doped samples is obtained for CAO5 sample. This is because some Ag ions will replace Ce^{4+}/Ce^{3+}ions and some will remain on the surface if the Ag concentration is raised above x = 0.05. Through this process, excess dopant ions are removed from the internal surface of the nanoparticles, preventing them from growing, and the nanoparticles only absorb the quantity of dopant ions that are permitted by thermodynamics. Consequently, Ag ions aggregate near the surface of the CeO_2 crystal lattice. Therefore, the optimal doping concentration in this instance would be x = 0.05.

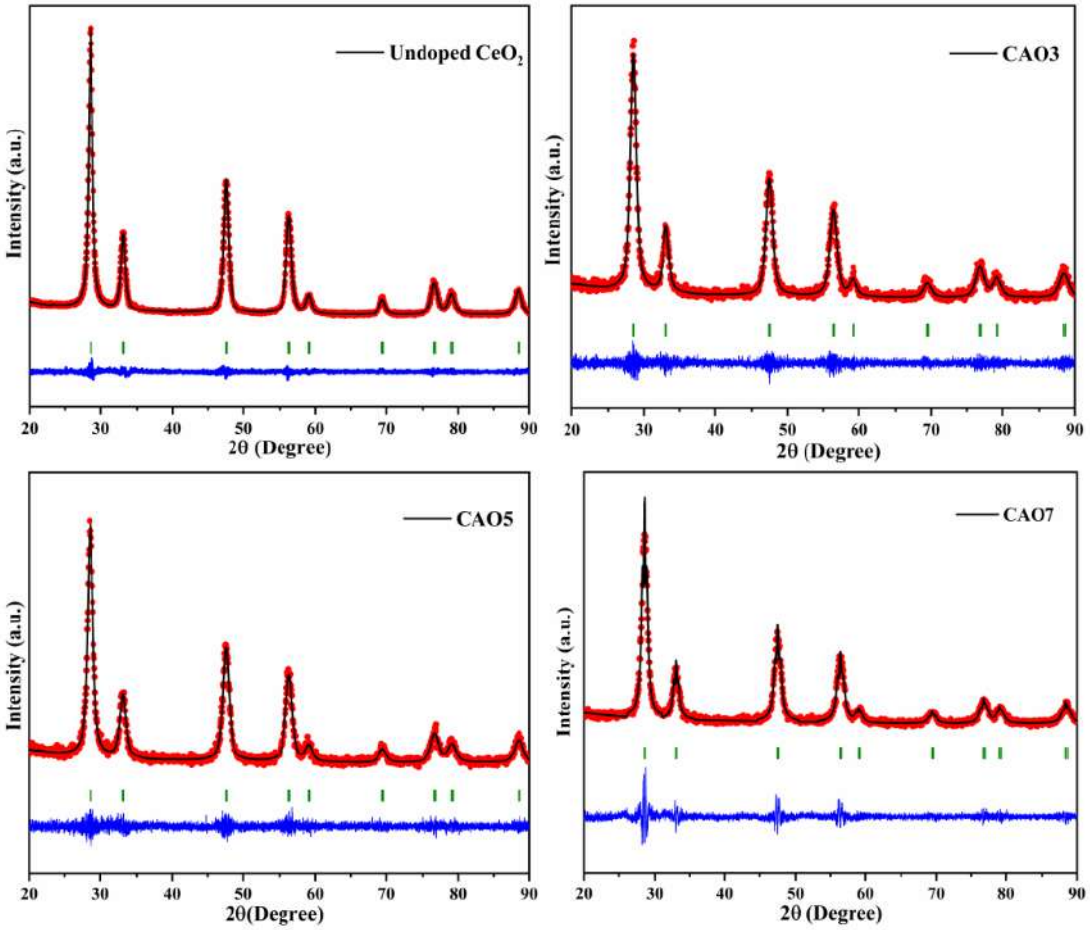

Figure 4.3: Rietveld refined fitted curve of undoped CeO_2 and CAO nanoparticles samples at 300 K. Solid, dot-filled lines depict the observed (calculated) profiles. Bragg reflections are indicated by the brief vertical marks. The difference plot is shown on the lower curve

An important feature that contributes significantly to the XRD peak's broadening is the strain [50]. The value of strain for all the prepared samples determined using Scherer's formula is provided in Table 4.1. As we can see from Table 4.1, the lattice strain increases as the Ag content increases. In undoped CeO_2, oxygen defects and Ce^{3+} are the primary causes of the lattice strain. In addition to grain boundary defects, the replacement of slightly bigger Ag^{+} (1.15 Å) ions on Ce^{4+} (0.97 Å) results in high magnitude of lattice strain in the CAO samples. To maintain charge neutrality, Ag doping creates oxygen vacancies in the lattice due to a discrepancy in the radii of the two ions. The increased value of strain in the CAO samples is also ascribed to these oxygen vacancies in the lattice sites [124]. The FULLPROF program has been used to do the Riveted refinement of the diffraction peaks. The prepared undoped CeO_2 and CAO nanoparticles' Rietveld fits of the experimental XRD pattern are shown in figure 4.3. Table 4.1 contains the relevant lattice parameters, goodness of fit (χ^2), R_p, R_{wp}, R_{exp}, R_{Bragg}, and cell density. The values of χ^2 suggest that there is a satisfactory match between the XRD patterns obtained by Rietveld and experimentally assessed.

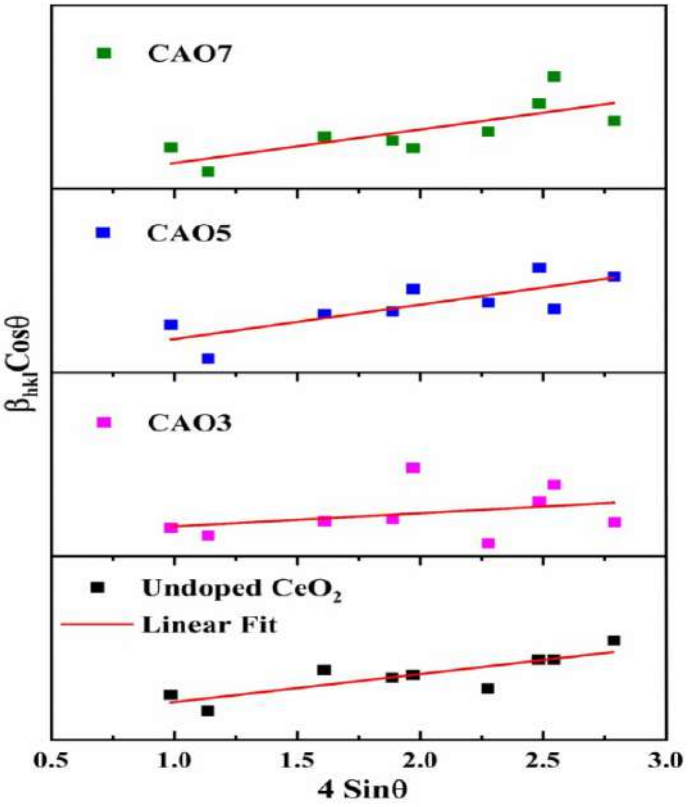

Figure 4.4: W-H plot to calculate the crystallite size and strain of undoped CeO_2 and CAO nanoparticles samples

Another approach for determining the crystallite size and lattice strain is Williamson-Hall (W-H) [61] plot. The W-H plot for the undoped $CeO_2$and CAO nanoparticles is depicted in figure 4.4. The obtained results using this method are also provided in Table 4.1, which correspond favorably with the outcomes of Scherer's equation.

Table 4.1: Various structural parameters determined by using Scherer's equation and W-H plot and Rietveld analysis

Samples		**Undoped CeO_2**	**CAO3**	**CAO5**	**CAO7**
Crystallite Size(nm)	**Scherer equation**	13.00	9.33	9.68	9.56
	W-H plot	16.56	10.52	11.30	10.91
Micro strain ϵ x10^{-4}	**Scherer equation**	26.19	37.54	35.93	36.92
	W-H plot	10.7	9.38	10.7	9.29
Lattice parameter (Å)		5.4145	5.4105	5.4111	5.4115
Volume $(Å)^3$		158.73	158.38	158.50	158.47
R_p, R_{wp}, R_{exp}, χ^2		8.88,8.82,8.09, 1.19	16.9,19.2, 18.9, 1.027	17.5, 20.0, 19.2, 1.082	17.4,19.5, 15.61, 15.67

4.3.2 Absorption spectra

The absorption spectra of all CAO nanoparticles in the wavelength range 200 nm to 800 nm are depicted in figure 4.5(a). According to this figure, all CAO samples exhibit their absorption peak below 400 nm and the optical band gap (E_g) of these prepared samples is determined using Tauc's relation [187]. Figure 4.5(b) is the plot between $(\alpha h\nu)^2$ versus photon energy hν and the extrapolation of the linear curve is used to determine the E_g. Table 4.2 lists the calculated E_g values for all CAO samples. Table 4.2 shows how doping with Ag causes the Eg values to gradually decline. One possible explanation for the decrease in E_g could be the impurity defect level brought about by the doping of metals ions [136]. More number of photons in the higher wavelength range will be absorbed when metal ions such as Ag are doped in CeO_2.

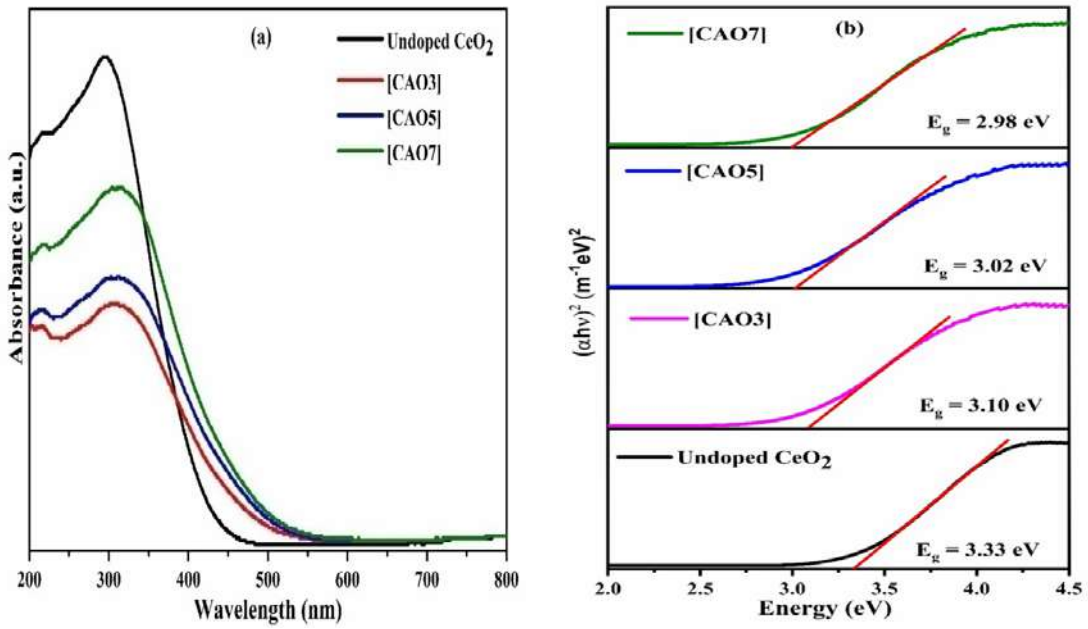

Figure 4.5: (a) The absorption spectra and (b) Tauc's plot of undoped CeO_2 and CAO nanoparticles samples

This will result in an extension of the visible light's usefulness range, which enhances the optical properties of doped CeO_2 nanoparticles significantly [77]. The reduction in E_g is also associated with increase in Ce^{3+} ion concentration due to doping of foreign Ag cations. The investigation reports that Ce^{3+}ions present at grain boundaries results in a decrease in E_g and red shifting of the absorption edge in CeO_2 nanoparticles. The presence of Ce^{3+} and oxygen vacancies led to the formation of localized band gap states and the oxygen released during the reaction is required to maintain the charge equilibrium [188]. Higher doping concentrations of TMs ions in $CeO_2$are observed to exhibit a similar red-shift. Consequently, the change of the two ionic states of the cerium ion and generation of defects level brought about by the doping of Ag ions result in the band gap narrowing of the synthesized CAO nanoparticles. The findings of the optical properties demonstrated how important it is for metal ions to be incorporated into the CeO_2 lattice [53].

Based on Urbach rule, optical absorption near the basic absorption edge in crystals with disturbed order regions is exponential in relation to the energy of the absorbed radiation. The band gap transition energy from the fundamental absorption edge to the tail states confined close to the absorption edge defines Urbach energy (E_U). Defects in the crystal structure manifest these localized states [160]. Thus, E_U

may be understood as a crystal lattice disorder parameter, measured by the inverse of the slope of the graphical representation of equation as per the ref. [189] (as shown in figure 4.6).

The calculated E_U values are showing an increasing trend, starting at 0.2733 eV for undoped CeO_2 and going up to 0.5139 eV, 0.5579 and 0.5702 eV for CAO3, CAO5 and CAO7 respectively as shown in Table 4.2. The rise in the E_U is well related with the rise in Ce^{3+} ions with increase in Ag content. The findings indicate that Ce^{3+} may have had an important role in the formation of oxygen vacancies or other defects that resulted in the crystalline lattice's disorderness.

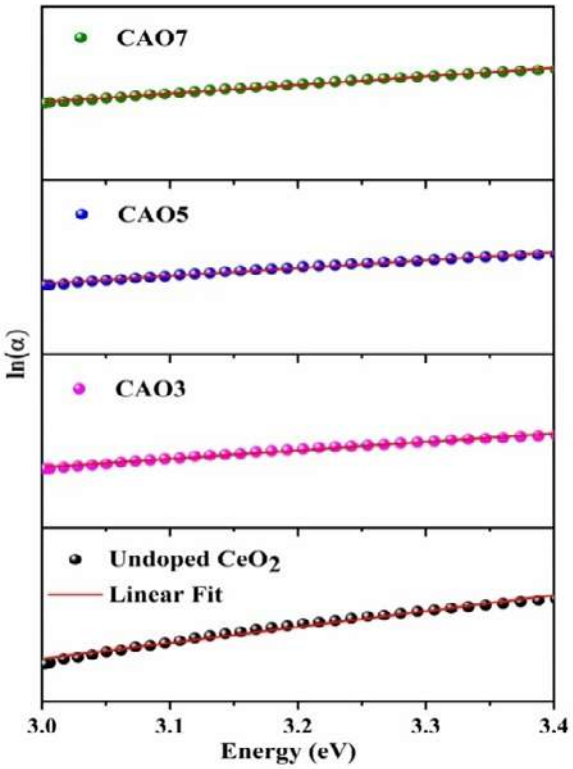

Figure 4.6: lnα vs. photon energy for undoped CeO_2 and CAO nanoparticles samples

Table 4.2: Various optical parameters for undoped CeO_2 and CAO nanoparticles

Samples	E_g (eV)	E_u (eV)	n
Undoped CeO_2	3.33	0.2733	2.3134
CAO3	3.10	0.5139	2.3706
CAO5	3.02	0.5579	2.3917
CAO7	2.98	0.5702	2.40284

Refractive index (n) is another optical characteristic used in many different applications. Changes in the refractive index can result from modifications to the electronic band structure as the nanoparticles getting smaller. The value of n has been calculated using the formula as per the ref. [138] and tabulated in Table 4.2. A rise in the n value can be observed from Table 4.2 with rise in Ag content. A material's optical characteristics are altered by raising its refractive index since it changes the optical density. Applications ranging from optoelectronics devices to lens design can benefit from these modifications.

In addition to reducing the band-gap, defect states cause electrical transitions that are aided by phonons. Ag substitution in CeO_2 results in lattice deformation and the reduction of Ce^{4+} to Ce^{3+} because of the different crystal radius and lower charge of Ag relative to Ce^{4+}. This raises the concentration of oxygen vacancies, which significantly alters CeO_2's band structure. These alterations result in the creation of localized states and the spatial distribution of band structure, which opens the door to the potential for various electronic transitions, which can be further detected by PL spectra.

4.3.3. Photoluminescence (PL) Spectroscopy

Figure 4.7 displayed the PL characteristics of CAO nanoparticles with excitation wavelength of 325 nm. The PL emission spectrum has been measured between 360 and 580 nm. The prepared CAO nanoparticles exhibit UV emission below 400 nm, which arises from the interstitial oxygen and Ce defect locations [190]. UV emission is also associated to the recombination of charge carriers through the exciton-exciton collision phenomenon. There exists strong PL emission from violet to orange regions, although the blue- green region showed the strongest emission between 450-500 nm. In addition to the strong emission, a few shoulder peaks caused by surface-related defects can be seen in the blue region (~438 nm). The emission band peak at 438 nm is related by near-band exitonic recombination. The emission peak at 445–500 nm may be related to transitions from different defect levels to the O 2p band, according to ***Meng et al.*** [143]. The remaining peaks at 450, 467, 481 and 492 nm are caused by dislocation or oxygen. Local oxygen vacancies defects, in which the oxygen vacancies leave four unbound electrons and weakly bonded Ce ion electrons in the unit cell, are responsible for the green emission

detected in the 500–560 nm range. The donor energy range produced by these electrons is close to and below CB [147]. The emission peaks of undoped CeO_2 and CAO nanoparticles are nearly similar. Crystal structural disorder is the cause of the weak spectra at the orange region (573 nm). Ag dopant ions have thus caused a notable alteration in the visible emission band, confirming that additional defects are created by the Ag ions.

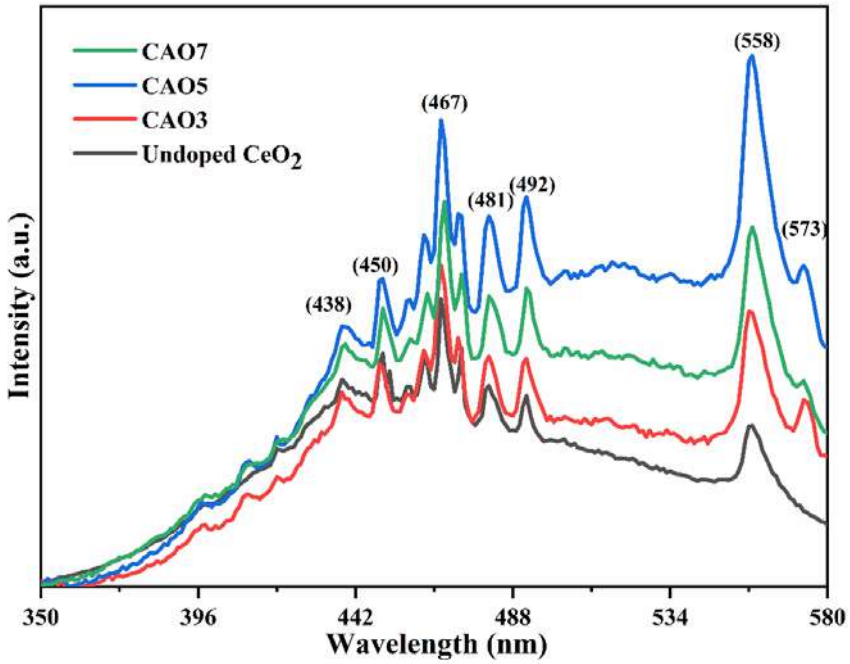

Figure 4.7: The PL spectra of undoped CeO_2 and CAO nanoparticles samples at exciting wavelength of 325 nm

Thus, it is evident by PL spectra that these defects could be the cause of the development of several states inside the band-gap, which would lead to various non-radiative decay processes, which appear to intensify as substitution occurs, suggesting that Ag ions play a significant role in the substituted lattice, which raises the population of oxygen vacancies and causes the $Ce^{4+} \rightarrow Ce^{3+}$conversion [191]. Furthermore, multi-phonon processes are generated by structural distortion and strain in the lattice, as confirmed by the XRD analysis. This lowers the band gap by reflecting in the structure properties.

It is shown that both undoped CeO_2 and CAO samples exhibit band-to-band excitation peaks in the 360–580 nm wavelength range considering that undoped and Ag-doped samples do not significantly differ. The excitation peaks can all be related

to the oxygen vacancies as they are all located within this energy range. The occurrence of these excitation peaks indicates the different defects levels of oxygen vacancies in the CeO_2 nanoparticles. Therefore, the presence of oxygen vacancies and defects are clearly visible in the PL spectra. The relationship between PL and electrochemical characteristics in CeO_2 nanoparticles is heavily influenced by structural defects, particularly oxygen vacancies, and the synthesis methods used. This correlation is critical for optimizing their use in photo-catalysis and energy storage.

The PL visible light emission spectra have been investigated using the CIE 1931 chromaticity coordinates to determine colour coordinates [89]. The CIE 1931 chromaticity diagram is displayed in X–Y space in figure 4.8. The points on the horseshoe diagram represent the colour emitted by the undoped CeO_2 and CAO nanoparticles. It is evident that the point colours are not found at the CIE chromaticity diagram's boundaries, indicating that the light being emitted is not pure but rather a mixture of hues. These colour coordinates of the undoped CeO_2 and CAO nanoparticles, respectively, X, Y = "0.36, 0.40", "0.36, 0.37", "0.37, 0.38"and "0.37, 0.38" with a little shift with Ag dopant concentration increases. These coordinates correspond to white colour, which is the combination of red, blue, and green colour produced by the dopant ions activated the white luminescence [147]. The good performance of the prepared samples is a crucial component of a high-quality white light-emitting diode (LED). There are following parameters that describe the quality of the illumination sources: Correlated Colour Temperature (CCT), CIE colour-rendering index (CRI), dominant wavelength (λ_d) and purity. CCT value is derived using CIE coordinates to determine technological applicability. Lamps with a CCT rating < 3200 K are regarded as "warm," while lamps with a CCT rating > 4000 K as "cool" [39]. The CCT coordinates for CAO nanoparticles are determined to be above 4000 K, as shown in Table 4.1. As a result, the prepared samples are beneficial for cool appearance.

However, it is difficult to design white LEDs with CCT tuneable consist of high CRI values [192]. For the prepared nanoparticles, the CRI values are above 90 as shown in Table 4.3. Therefore, these samples are beneficial especially for widespread use in indoor illumination applications with cool enough CCT of about 4000 K and a

high enough CRI of about 90. The wavelength of light that is most frequently emitted is known as the dominant wavelength (λ_d). A mixture of white light with saturated light of a specific dominant might be thought of as the CIE (x, y) coordinates of a light source. The calculated values of λ_d are provided in Table 4.3.

Table 4.3: The CIE colour parameters x, y, λ_d, colour purity, CRI and CCT values for undoped CeO_2 and CAO nanoparticles

Samples	x	y	CCT (K)	λ_d (nm)	Purity	CRI
Undoped CeO_2	0.3644	0.4079	4611	568.1	31.8	84
CAO3	0.3608	0.3738	4556	573.4	20.8	94
CAO5	0.3758	0.3796	4148	577.0	26.7	95
CAO7	0.3725	0.3857	4279	574.5	27.6	93

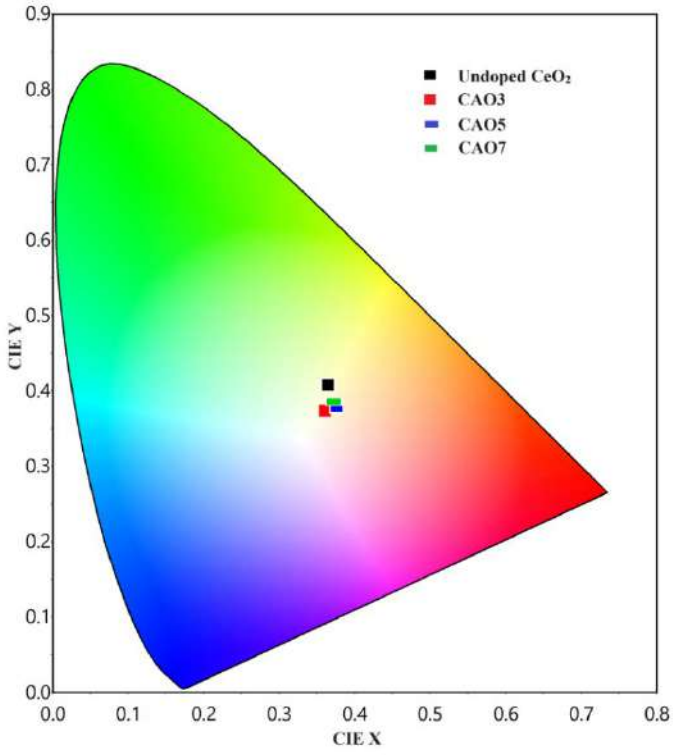

Figure 4.8: The CIE plot of undoped CeO_2 and CAO nanoparticles samples

The numerical measurement of saturation of colour is the excitation purity. More intense or pure colours of the λ_d observed, the higher the excitation purity. The calculated value of excitation purity is tabulated in Table 4.3. Table 4.3 demonstrates

that the CAO nanoparticles samples have estimated purity values below 50%, indicating that the colour saturation of these samples is not much high [151]. As revealed by our XRD measurement, the crystallize size of CeO_2 nanoparticles reduced upon Ag doping which enhance surface to volume ratio, and therefore increases number of surface states and surface ions. Additionally, as particle size is reduced, the electron and hole wave functions overlap, potentially increasing the probability of their recombination. When electron-hole pairs form inside of Nanoparticles and are close to one another, recombination is more likely to occur and luminescence efficiency can be increased [89].

4.3.4 X-Ray Photoelectron Spectroscopy (XPS) Measurement

4.3.4.1 XPS spectra of Ce 3d

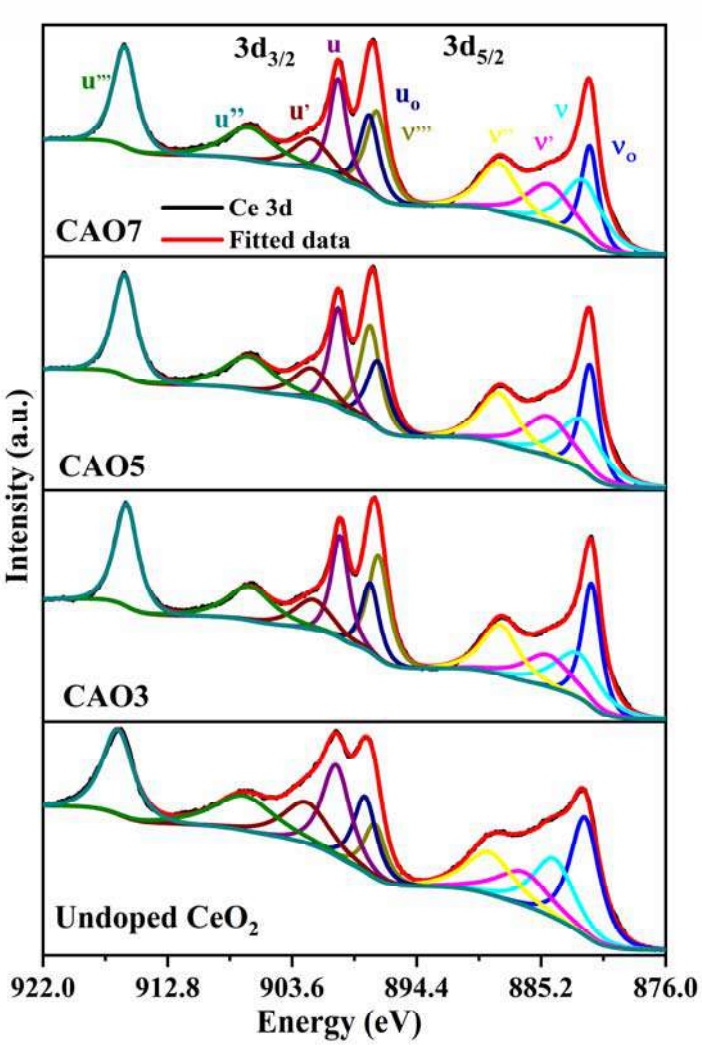

Figure 4.9: Ce 3d spectrum of undoped CeO_2 and CAO nanoparticles samples

Using the XPS survey spectra for undoped $CeO_2$and CAO nanoparticles respectively, the existence of Ce, O and Ag on the surface has been depicted. Figure 4.9 displays the Ce3d core level XPS spectra of undoped $CeO_2$and CAO nanoparticles samples. In order to correct all BE for the charge shift, the C 1s peak (binding energy (BE) = 284.6 eV) has been used as a reference point [153, 155], To correct all BE for the charge shift, the C 1s peak (binding energy (BE = 284.6 eV) has been used as a reference point. Gaussian fitting has been used to deconvolute Ce 3d core level spectra in the BE range 876-922 eV, as shown in figure 4.9. The spin-orbit split of $3d_{3/2}$ and $3d_{5/2}$ is represented by multiple doublets (u and v) in the Ce 3d spectrum. The Gaussian function fit of the Ce3d spectrum indicated the presence of Ce^{3+} and Ce^{4+}. According to figure 4.10, the peaks designated v_o, v′, u_o, and u′ suggest the existence of Ce^{3+} states, whereas the peaks named v, v″, v‴, u, u″, and u‴ indicate the presence of Ce^{4+}states. The BE peak positions for "u" and "v" for the undoped CeO_2 and CAO nanoparticles samples are listed in Table 4.4.

Using the following formula as per the ref. [53], the relative concentration of Ce^{3+} in each of the synthesized samples has been determined. As Table 4.4 indicates that as the Ag cations are doped in CeO_2, the Ce^{3+}/Ce^{4+} ratio rises. It reached its maximum for CAO5 sample (Ce^{3+}/Ce^{4+} = 0.81) because the concentration of Ce^{3+} and the oxygen vacancies formation energy increased when Ag ions took the position of Ce^{3+} in the CeO_2 lattice. On the other hand, for CAO7 sample, the Ce^{3+}/Ce^{4+} ratio slightly dropped. Due to the interaction between Ag and CeO_2, it is assumed that the Ag particles that did not replace Ce in the CeO_2 lattice may have changed Ce^{3+} into Ce^{4}[193].

Table-4.4: Binding energies (eV) of various GL30 components of Ce 3d XPS spectra of undoped CeO_2 and CAO nanoparticles

Samples	$3d_{5/2}$ [in eV]						$3d_{3/2}$ [in eV]				Ce^{3+} (%)	Ce^{4+} (%)	$\frac{Ce^{3+}}{Ce^{4+}}$
	v_o	V	v’	v”	v”’	u_o	u	u’	u’’	u’’’			
Undoped CeO_2	881.96	884.25	886.53	889.03	897.47	898.20	900.33	902.54	907.11	916.42	40.60	59.39	0.68
CAO3	881.47	882.48	884.71	888.20	897.21	897.81	900.05	902.03	906.68	915.82	34.44	65.55	0.72
CAO5	881.60	882.20	884.66	888.30	897.26	897.82	900.18	902.17	906.76	915.96	38.05	61.94	0.81
CAO7	881.59	882.03	884.64	888.29	897.33	897.88	900.18	902.17	906.76	915.97	34.17	65.82	0.71

4.3.4.2 XPS spectra of O1s

The O 1s spectra of the undoped CeO_2 and CAO nanoparticles samples are shown in figure 4.10. The deconvoluted three-peak asymmetrical O 1s core level spectrum in BE range is used to calculate the concentration of O^{2-} ions in all samples. The O 1s spectra consist of three major peaks at 528, 529 and 531 eV. The Lattice oxygen (O_L) is responsible for the peak at 528 eV, while oxygen vacancy is responsible for the peak around 529 eV. Defect oxides or surface hydroxyl groups could be the cause of the third peak at 531 eV [158, 194]. The concentration of O_L and Ov can be obtained through the quantification of O 1s spectra, are shown in Table V, indicating that Ag doping will result in an increase in oxygen vacancies content. The increase in oxygen vacancies and Ce^{3+} are further confirmed by XPS analysis.

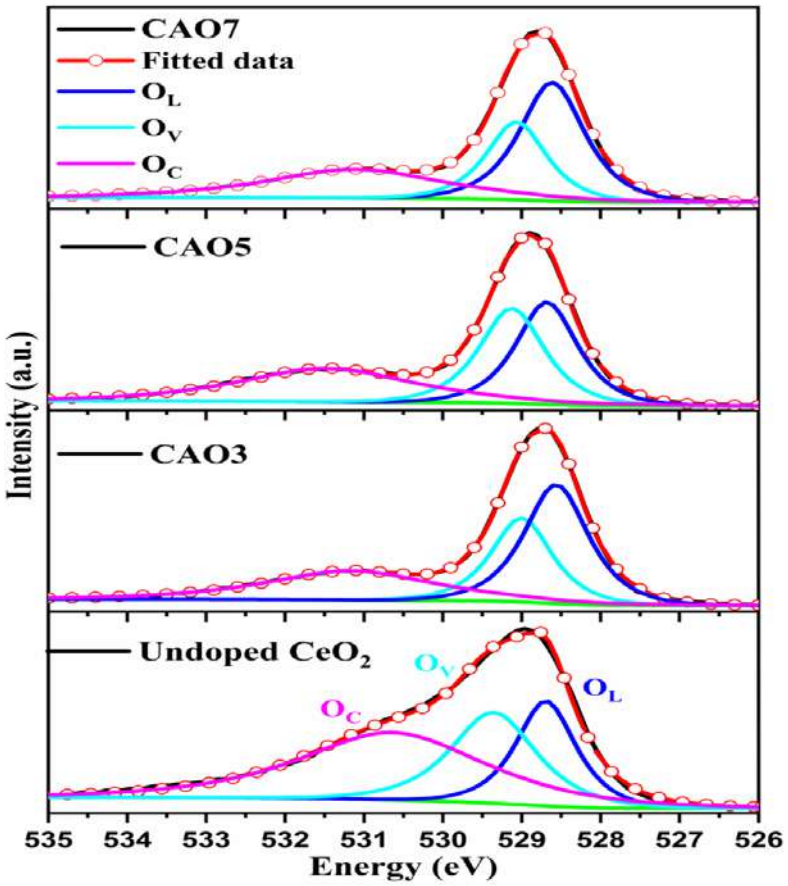

Figure 4.10: O 1s spectra of undoped $CeO_2$and CAO nanoparticles samples

XPS analysis further validated the improved Ag-CeO_2 interaction (Table 4.5). Because Ag doping in CeO_2 lattice enhanced oxygen vacancies formation, the Ce^{3+}/Ce^{4+} ratio increases when Ag concentration is doped in small amount. The

maximum concentration of V_o has been obtained for CAO5 sample. Conversely, when Ag is added in excess (in case of CAO7), the Ce^{3+}/Ce^{4+} ratio along with oxygen vacancies concentration dropped. Therefore, it could be crucial to ascertain whether Ag has replaced Ce^{3+} in the CeO_2 lattice in terms of the Ce^{3+}/Ce^{4+} ratio, which results an optimal concentration of Ag that enhanced the Ce^{3+}/Ce^{4+} ratio and the oxygen vacancies ratio.

Table 4.5: Binding energies (eV) of various GL30 components of O 1s XPS spectra of undoped CeO_2 and CAO nanoparticles samples

Samples	O_L [eV]	O_V [eV]	O_C [eV]	% O_L	% O_V
Undoped CeO_2	528.69	529.35	530.63	44.81	55.19
CAO3	528.56	528.99	531.16	42.84	57.15
CAO5	528.67	529.12	531.47	40.56	59.43
CAO7	528.61	529.06	531.10	42.29	57.70

4.3.4.3. XPS spectra of Ag 3p and 3d

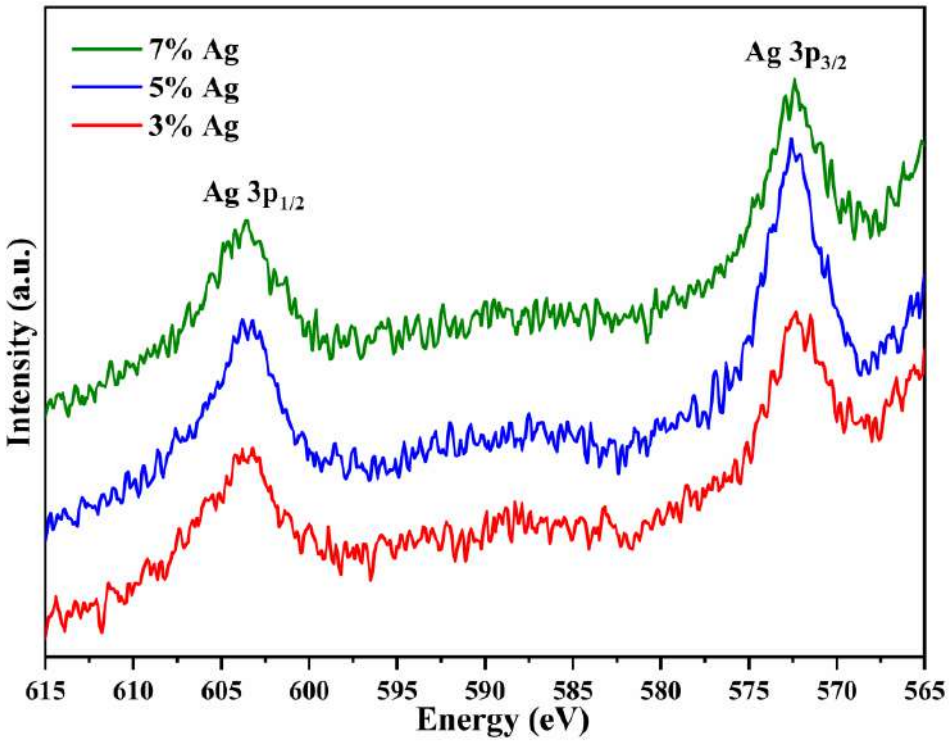

Figure 4.11: XPS binding energy peak position of Ag 3p of CAO nanoparticles samples

The XPS spectra of Ag 3p and 3d profile for all CAO nanoparticles is shown by figure 4.11 and figure 4.12 respectively. Figure 4.11 reveals the two Ag $3p_{3/2}$ and $3p_{1/2}$ state, located at ~572.52 eV and ~ 603.83 eV respectively, whereas figure 4.12 represents Ag $3d_{5/2}$ and $3d_{3/2}$ state positioned at ~367.7 eV and ~ 373.7 eV respectively. Both the figures suggest the monovalent state of Ag, which agrees well with previously reported papers [195].

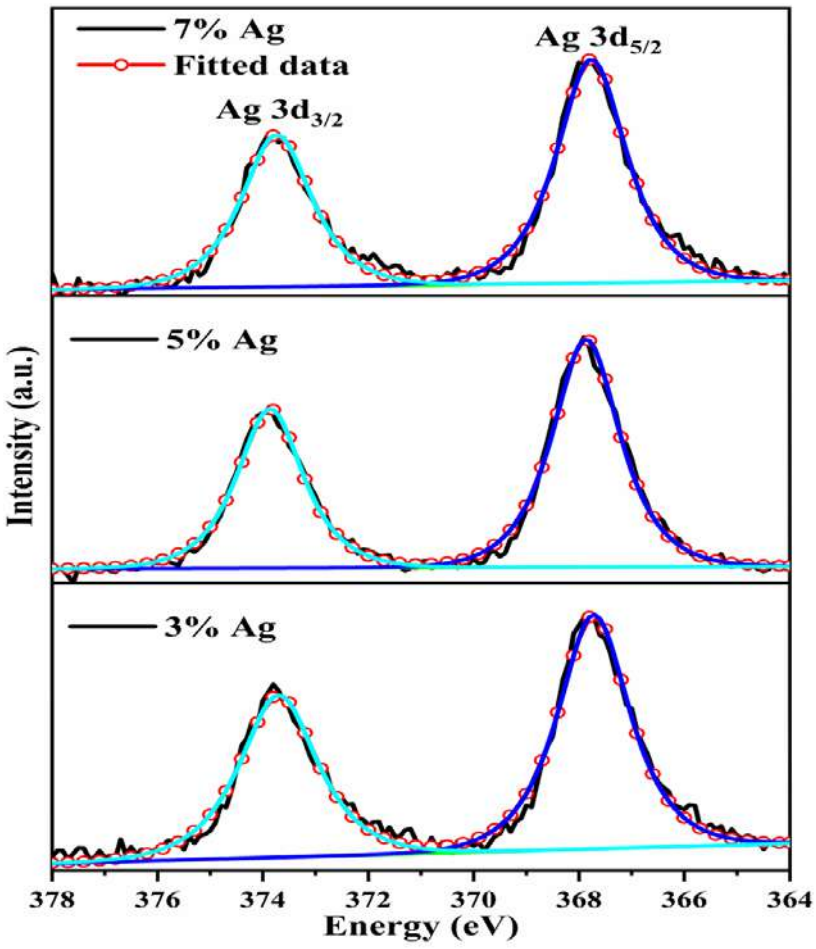

Figure 4.12: XPS binding energy peak position of Ag 3d of CAO nanoparticles samples

4.3.5 Electrochemical properties

The prepared undoped CeO_2 and CAO nanoparticles are subjected to cyclic voltammetry (CV), galvanic charged-discharge (GCD), and electrochemical impedance spectroscopy (EIS), analysis to investigate its electrochemical behavior. CV and GCD analysis are performed in 2 M KOH within the potential window of 1.3 V and different current density to assess the capacity of the constructed electrode.

Figure 4.13(a) displays the CV measurements of the prepared electrodes at the potential window of 1.3 V. The CV curve of the CAO5 sample at different scan rates ranging from 10-160 mV/s is shown in figure 4.13(b). This interval yields the best performances of the nanoparticles because it has a higher occupied surface area than other potentials [77]. Undoped CeO_2 and CAO nanoparticles exhibit a rectangular curve as shown in figure 4.13(a). It is significant to note that the rectangular shape characteristic of the CV curves demonstrates the electrodes' excellent pseudo-capacitive function [196]. It has been noted that at a scan rate of 10 mV/s, all electrodes show the highest C_{SP} value, which decreases as the scan rate increases to 160 mV/s. Figure 4.13(a) shows that, in comparison to the other electrodes, the CAO5 electrode has the largest area under the curve, indicating the strongest capacitive reaction. The following relation is used to determine the C_{SP} values [99].

$$\boldsymbol{C_{SP} = \frac{1}{2mVk}\int_{v^-}^{v^+} I(v)dV} \qquad \textbf{(4.1)}$$

In this relation, m (g) stands for mass of the active material, k (V/s) for scan rate, and I (A) for discharge current. Utilizing the CV curve at a scan rate of 10 mV/s, the values of C_{sp} of undoped CeO_2, CAO3, CAO5 and CAO7 electrodes are 120.68 F/g, 185.56 F/g, 363.44 F/g and 247.44 F/g, respectively.

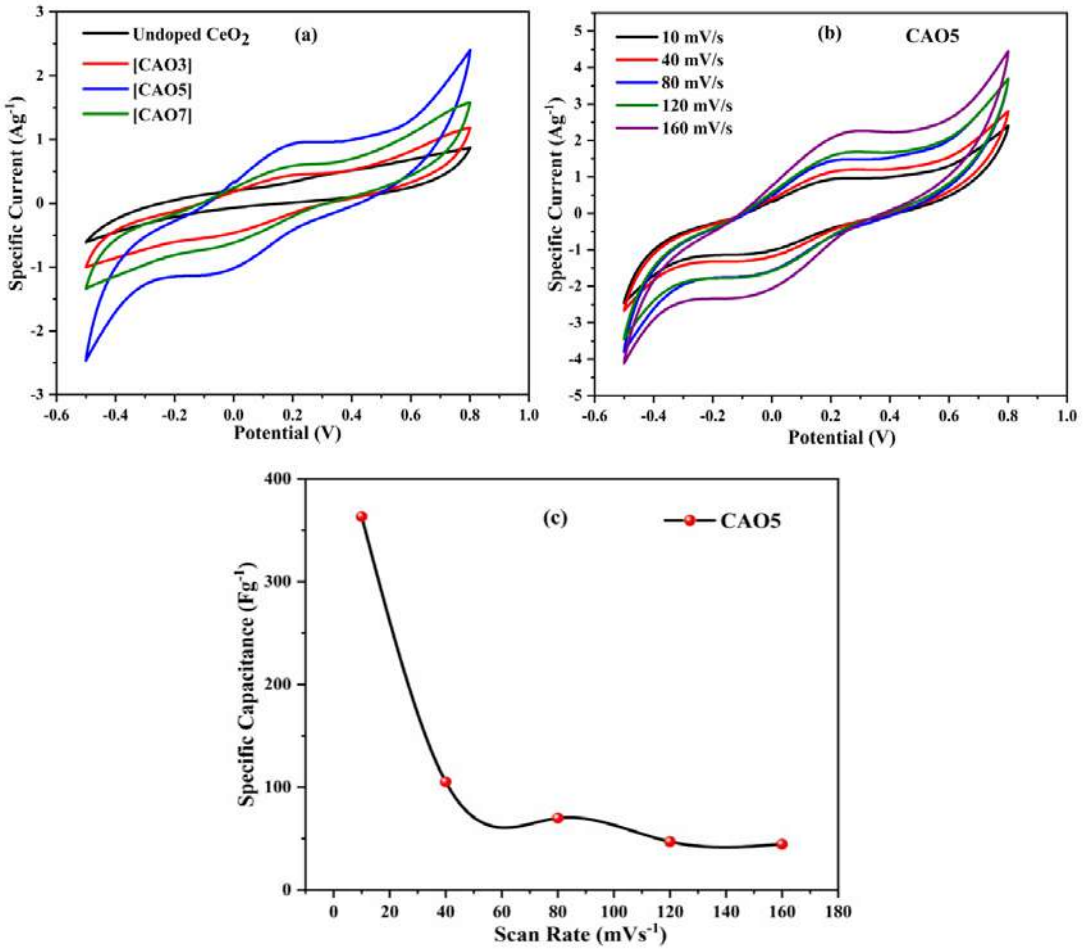

Figure 4.13: (a) CV curves of undoped CeO_2 and CAO nanoparticles samples with a scan rate of 10 mV/s in 2 M KOH, (b) CV curves at of CAO5 nanoparticles sample at various scan rates (10, 40, 80, 120 and 160 mV/s) and (c) C_{sp} variation for CAO5 nanoparticles sample at varying scan rates

The CV curves of CAO nanoparticles exhibit significantly higher capacitance in compared to undoped CeO_2. It is to be noted that CAO5 based electrode exhibiting the better performance among the other CAO based electrodes. The C_{SP} variation with scan rate of CAO5 sample is shown in figure 4.13(c). Furthermore, it is also discovered that increase in scan rate from 10 mV/s to 160 mV/s leads to fall in C_{SP} of the CAO5 electrode (figure 4.13(c)) from 363.44 F/g to 44.56 F/g. The combined effects of Ag and small-size CeO_2 nanostructures are responsible for the electrochemical richness of CAO5. Introducing Ag into a small-size CeO_2 nanostructure improves the material's electronic conductivity and produces effective surface kinetics [197, 198]. Therefore, Ag-doped CeO_2 nanoparticles results in improved electronic conductivity and effective surface dynamics.

Galvanostatic charge-discharge (GCD) study is used to analysis the extent of discharge capacitance using potential window of 1.3 V to determine the beneficial electrochemical activity of the prepared electrode [174]. Using this method, slow-charge and fast-discharge experiments are performed in 2 M KOH at different current densities ranging from 0.6 to 5 A/g (0.6, 0.8, 1, 2, 3 and 5 A/g). To characterize the electrochemical (EC) behavior of the prepared electrodes, the GCD performance of undoped CeO_2 and CAO nanoparticles as electrodes is measured at different current density from 0.6 to 5 A/g. Figure 4.14(a) shows the GCD curves of undoped CeO_2 and CAO nanoparticles electrodes at current density 0.6 A/g and the GCD curve of CAO5 nanoparticles electrode at different current density ranging from 0.6 to 5 A/g is shown in figure 4.14(b).

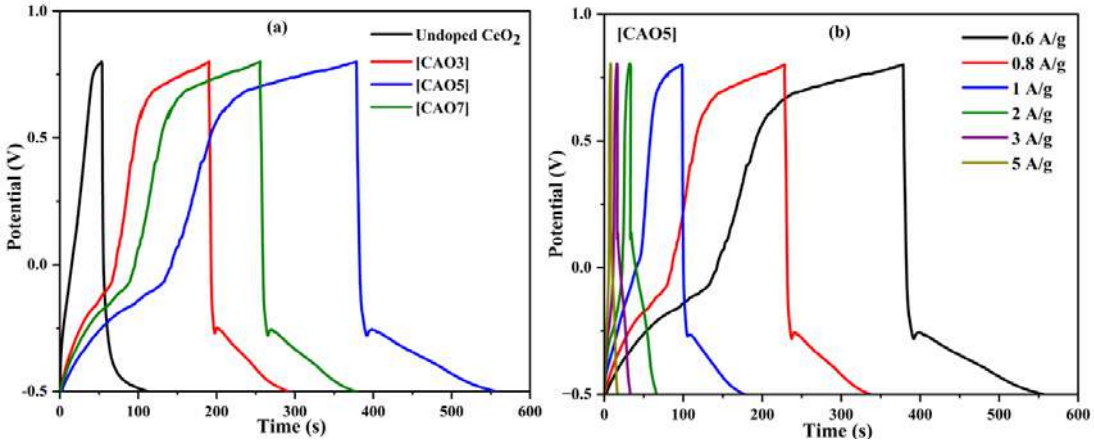

Figure 4.14: (a) GCD curve for undoped and CAO nanoparticles samples at current density of 0.6 A/g and (b) GCD curves of CAO5 nanoparticles sample at various current density

The pseudo-capacitive behavior of the undoped $CeO_2$and CAO electrode resulted in symmetric non-triangular morphologies in the GCD curves, which displayed the plateau at a similar voltage seen in the CV curves [198]. The C_{sp} has been determined using [100]:

$$C_{sp} = \frac{I\Delta t}{m\Delta v} \qquad (4.2)$$

Where, all the parameters are discussed above except Δt which is the discharging time (s). The C_{sp} values at current density 0.6 A/g of the undoped CeO_2, CAO3, CAO5 and CAO7 samples are 105.92, 250.52, 353.92 and 336.72 F/g respectively.

It is to be noticed that specific capacitance rises together with the Ag concentration (x = 0.05) as in CAO5, as figure 4.14(a) illustrates the sample with the highest. C_{sp} of 353.92 F/g at current density of 0.6 A/g is CAO5. On the other hand, when the Ag content is too high, as in CAO7, the structural breakdown and self-aggregation ions cause the C_{sp} to drop. Higher solution resistance (Rs) caused by excessive self-aggregation of Ag can lower the capacitance output.

The EIS analysis is a principal approach utilized to investigate the basic characteristics of electrode materials used in supercapacitor [199]. The Nyquist plot of all the prepared samples is shown in figure 4.15, which displays nearly identical profiles. Interestingly, there are two distinct zones in the Nyquist plot.

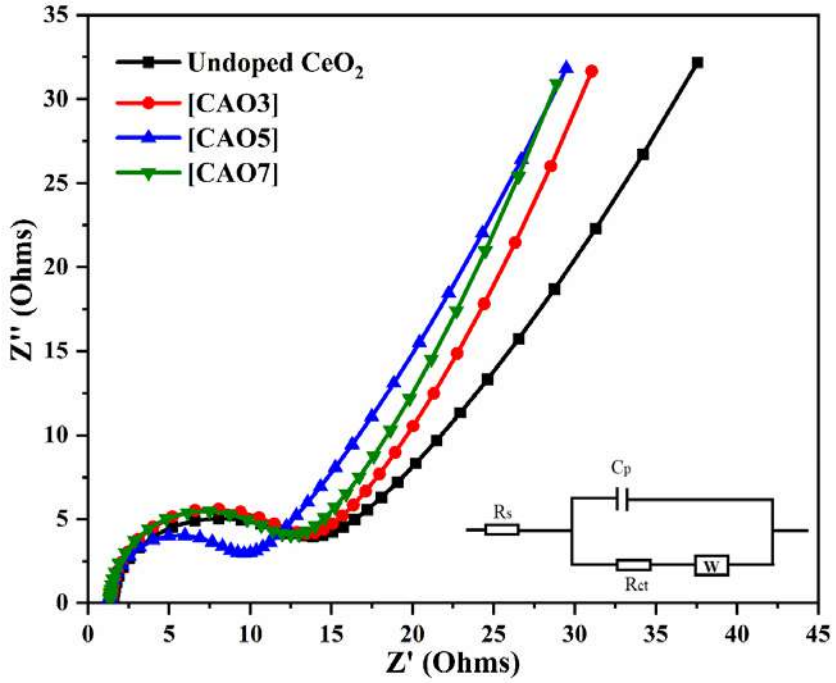

Figure 4.15: Nyquist plot of undoped CeO_2 and CAO nanoparticles samples along with an equivalent circuit

The Nyquist plots in figure 4.15 includes Rs (electrolyte resistance), Rct (charge-transfer resistance), W (Warburg component), and C_P (specific capacitance). The Rs signify the resistance between the electrolyte, electrode, and current collector. The charge transfer resistance (R_{ct}) is responsible for the semi-circle in the high frequency areas, whereas EDLC is responsible for the straight in the low frequency regions. The R_{ct} and solution (electrolyte) resistance (R_s) of electrochemical reactions are calculated using the first and second intercepts with the actual impedance axis (x

axis) [200]. The calculated value of R_{ct} for the undoped CeO_2 and CAO samples are 11.18, 11.27, 7.80 and 10.69 & respectively. Such resultssuggest that R_{ct} value is found to decrease with increasing Ag^+ cation doping, indicating that the inclusion of Ag^+ cation in CeO_2 electrodes improves charge transfer capability. These results reflects that the R_{ct} of CAO5 electrode is lower than that of other samples for CAO electrodes, which could be explained by the structure enabling effective access of electrolyte ions to the CeO_2 and Ag surfaces. The lower R_{ct} values of the material further suggested that it had less resistance and helped to maintain exceptional stability throughout the electrochemical measurement. Therefore, the lower R_{ct} of CAO electrode is crucial to their usability in supercapacitor [77]. The charge-discharge measurement can be further used to calculate the specific electrical energy density (E) stored in an ideal symmetric EDLC and the specific power density (P) using the following equation [101, 201].

$$\boldsymbol{E = \frac{1}{2} C V_{max}^2} \qquad \textbf{(4.3)}$$

$$\boldsymbol{p = \frac{E}{\Delta t}} \qquad \textbf{(4.4)}$$

Where, all the parameters are having their usual meanings. The values obtained from various cells are given in terms of P and E with the unit of (KW/kg) and (Wh/kg), respectively.

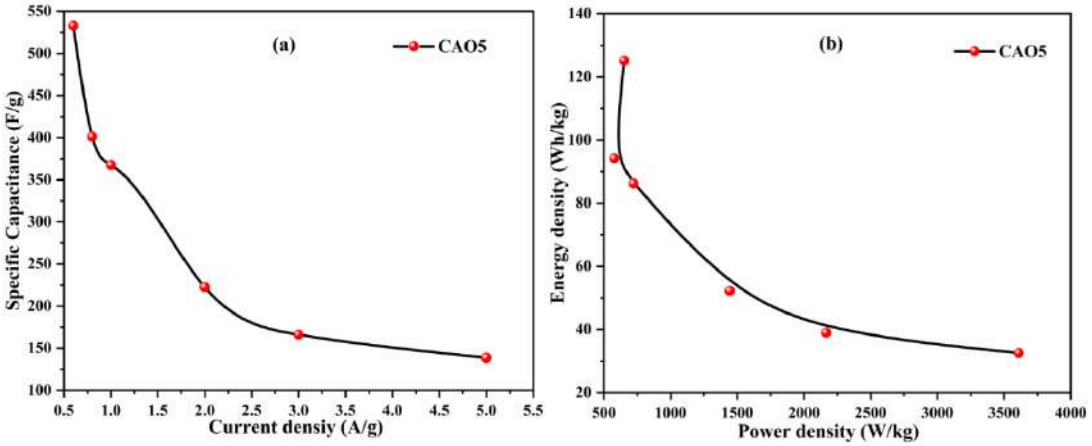

Figure 4.16: (a) Variation of C_{sp} with different current density for CAO5 nanoparticles, (b) Ragone plot (energy density verses power density) of corresponding nanoparticles

Since E is directly proportional to the capacitance and the square of the maximum potential. Therefore, a rise in capacitance can directly result in a rise in

energy density of the supercapacitor. The power density of supercapacitor is determined by energy per unit of time. An increase in the electrode's surface area can also aid in achieving capacitance, which increases energy density. The plot between E and P also known as the Ragone plot depict the characteristics of supercapacitor. Figure 4.16(a) represents the C_{SP} variation with different current density and figure 4.16(b) represents the E verses P curve for all the prepared samples. At a current density of 0.6 A/g, the CAO5 sample exhibit E=125.08 Wh/kg and P = of 652.48 W/kg. Consequently, all of the samples perform quite well overall, with the CAO5 showing maximum E and P than the other samples. With a high conducting Ag doping into CeO_2 nanostructure, the maximum energy density of the CeO_2-based nanostructure electrode in the present study is achieved. Supercapacitor performance is enhanced by the Ag doping concentration since it raises electronic conductivity as much as possible [202].

The cycling efficiency of CAO5 samples is displayed in figure 4.17 for 2100 cycles at current density of 1 A/g. Even yet, C_{SP} exhibits a little fall of 6. 09 %after 2100 cycles, suggesting that there has not been a significant decline. Because of the surface and interfacial characteristics, the structural properties of nanoparticles enhanced the C_{SP} and cyclic stability for supercapacitor application.

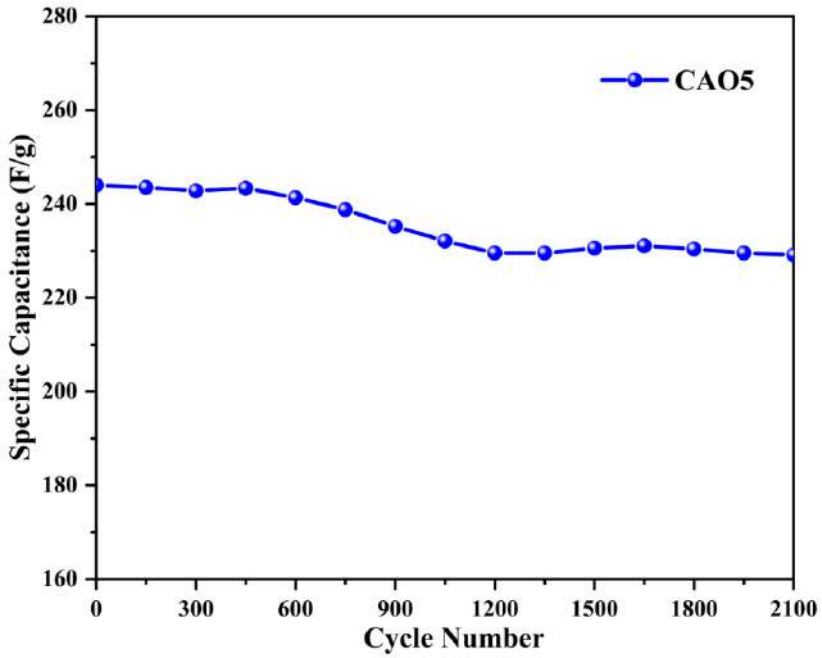

Figure 4.17: Cyclic performance of CAO5 electrode for 2100 cycles at current density of 1 A/g

The presence of oxygen vacancies and defects as detected by our UV and PL measurement could alter the surface's chemical composition. The increase in the oxygen vacancies has been confirmed by our XPS analysis. Oxygen defect sites which provide big reaction sites and rapid ion intercalation, improve electrical conductivity. The generation of oxygen vacancies can promote the diffusion of charge carriers and enhance the amount of electro-active surface area that is in contact with the electrolyte. Therefore, oxygen vacancies are responsible for the electrochemically active sites to be created. The enhanced EC performance of CAO nanoparticles results from the beneficial interaction between Ag and CeO_2, which additionally improves the electrical conductivity. The exceptional performance of CAO5 is intended to be used for the formation of the energy storage devices. After the overall analysis, the maximum capacitance of was found 363.44 F/g at scan rate of 10 mV/s. This appropriate design may become the high-performance electrodes used in supercapacitor applications.

Silver doping improves the electrochemical performance of CeO_2 nanoparticles, making them appropriate for energy storage, catalysis, and sensing applications. The Ce^{3+}/Ce^{4+} reversible redox pair is responsible for the increased redox peaks observed during cyclic voltammetry (CV). Ag facilitates the $Ce^{4+} \rightarrow Ce^{3+}$ redox transition, improving oxygen storage and release properties in catalysts and fuel cells. The EIS measurement shows reduced charge transfer resistance (Rct) in Ag-doped CeO_2 and increase ion diffusion and surface reactivity. Doping with Ag enhances CeO_2 nanoparticles' electrochemical activity by improving redox behavior, charge transfer, and conductivity. Ag-CeO_2 exhibits intriguing features for fuel cells, electrochemical sensors, supercapacitor, and catalysis.

4.4. Conclusion

The co-precipitation method found to be an efficient in synthesizing the Ag-doped CeO_2 nanoparticles. The prepared samples have a cubic CeO_2-type crystal structure in space group Fm-3m and are phase-pure. The Rietveld method yielded an average crystallite size estimate of 9-13 nm. Owing to a substantial charge transfer from O^{2-} to Ce^{4+} ions, both undoped and CAO samples exhibit significant light absorption in the near-ultraviolet region and therefore may find application such as UV absorber. Due to the existence of defects states in the mid band gap, the effective

band gap of CAO nanoparticles has decreased and causes the red shift of the absorption peaks. Additionally, oxygen defects in the CeO_2 nanoparticles are shown by PL spectra. Therefore, by introducing Ag dopant, the oxygen vacancies concentration in CeO_2 can be raised.

The interplay between PL and electrochemical characteristics in CeO_2 nanoparticles is predominantly determined by structural defects, emphasizing the need of tailored techniques for specific applications. However, it is important to note that severe defects may result in non-radiative recombination, thereby affecting the PL and electrochemical responses. The CIE diagram of CAO samples indicates a white color emission, making CAO nanoparticles appropriate for use in white light applications. The comparatively high CRI values suggest that they are suitable to be used in white LED devices. Using XPS, it has been determined thatCe^{3+}/Ce^{4+}ratio has increased as the doping concentration has increased. But the concentration ratio has dropped on higher doping concentration. Based on the Ce 3d XPS profiles, the ratio Ce^{3+}/Ce^{4+}which indicates the amount of oxygen vacancies, showed a similar trend to electrochemical properties. It follows that using the optimum concentration of Ag is important as doping with excess concentration (more than 5%) reduces the number of oxygen vacancies and the performance of electrochemical characteristics. The highest specific capacitance of all the samples is 363.44 F/g for CAO5 sample. At a current density of 0.6 A/g, the maximum value of E and P of CAO5 sample are 125.08 Wh/kg and 652.48 W/kg, respectively. The low contact resistance and excellent electrical conductivity of CAO5 electrode combined with its high-rate performance made it very attractive for real-world applications. Additionally, it is discovered that CAO5 electrode with 2100 cycle cyclic times exhibits a very slight 6.09% decline in super capacitance value. These results suggest that the CAO sample is a material that can be used in electrochemical supercapacitor applications. Therefore, this work offers up new possibilities for the development of supercapacitor electrode materials as well as other low-cost electrochemical energy storage devices.

Chapter 5
Study of Structural, Optical, Electronic Structure and Magnetic Properties of Cd-Doped CeO_2 Nanoparticles

Chapter-5

Study of Structural, Optical, Electronic Structure and Magnetic Properties of Cd-Doped CeO_2 Nanoparticles

ABSTRACT

This study employs a novel co-precipitation approach to synthesize Cd-doped CeO_2 nanoparticles and analyzes their structural, optical, electronic structure and magnetic properties. X-ray diffraction (XRD) and electron transmission microscopy (TEM) indicate cubic fcc structures and spherical symmetry with diameter ranging 6-12 nm respectively. UV-Vis spectroscopy unveiled a red-shift in the absorption edge and lower band gap decreased from 3.39 eV to 2.98 eV with increasing Cd concentration, ranging from (x = 0.00 to 0.09), indicating increased visible light absorption. XPS measurements for core levels Ce 3d, O 1s, and Cd 3p and 3d provided additional evidence for the development of oxygen vacancies in the CeO_2 lattice. Furthermore, the XPS measurements revealed the valence states of elements such as Ce (3+ and 4+), Cd (2+), and O (2-), as well as charged oxygen vacancies. Magnetic experiments revealed improved characteristics in Cd doped CeO_2, switching to RTFM behavior. Therefore, such findings revealing that Cd doping can customize CeO_2 nanoparticles for several applications, including optical and spintronics.

5.1. Introduction

There is a high demand for novel technologies to prepare and measure the properties of nano-material-related devices. Nano-particles are just revolutionary in the development of new technologies in a variety of scientific and industrial sectors. Their distinct size-dependent property, including as high surface area, quantum effects, and improved reactivity, enable new functions that bulk materials cannot provide. If dilute magnetic semiconductors (DMS) are integrated into nanoparticles, it could combine the benefits of nano-scale materials with the spin-dependent features of magnetic dopants, resulting in multifunctional materials for next-generation electronics [203]. These materials are essential for spintronics, quantum devices, sophisticated sensors, and multifunctional nanocomposites, bridging the gap between traditional semiconductors and magnetic materials at the nano-scale [204, 205]. For successful spintronics applications, DMS materials require strong magnetization,

which is achieved by incorporating magnetic components into the semiconducting matrix. Over the years, DMS research has focused on semiconductors with wide band gap energy (Eg) such as zinc oxide, GaAs, TiO_2, and CeO_2. These materials exhibit ferromagnetism at room temperature (RTFM) when doped with some foreign impurity such transition metals [206]. Transition metal-doped semiconductors have gained popularity for their prospective applications, including UV detectors, LEDs, and highly sensitive chemical sensors [207-209]. In this context, Cerium Oxide (CeO_2) nanoparticles have drawn a great attention owing to its unique properties making them important for promoting new technologies [210]. CeO_2 nanoparticles have strong catalytic activity in chemical processes due to their high mobility and oxygen storage capacity, particularly with cerium, which can be easily switch from $Ce^{4+} \rightarrow Ce^{3+}$ [105, 211]. It is best source to noble metal catalysts used for eliminating exhaust gases [212, 213]. CeO_2 nanoparticles have numerous applications, including optoelectronics, solid oxide fuel cells, UV absorber [214, 215], oxygen gas sensors [216, 217], photo-catalysis [218] and for anti-bacterial activity [219, 220] and as solid oxide fuel cell (SOFC) [221]. Various synthesis processes have been used to synthesize CeO_2 nanoparticles under controlled conditions. The chemical co-precipitation method is superior to other methods for the synthesis of large-surface metal oxides due to its improved homogeneity, regulated stoichiometry, high-purity powders, and lower temperature requirements [222]. Doping is a typical method for modifying material properties. More recently, studies have concentrated on improving the various properties of rare-earth metal oxide nanoparticles by adding dopant. To develop highly luminous nanoparticles, tiny amounts of transition metal elements can be injected as dopant. Transition metal ions, including Fe, Mn, Ti, Pd, and Co, have been found to enhance the optical property and photo-catalytic response of CeO_2 nanoparticles. ***Kumar et al.*** [223] developed a reusable and efficient Zr-doped CeO_2 catalyst with nanostructures. ***Saranya, et al.*** [224] discovered Co-doped ceria nanoparticles exhibited photo-catalytic activity under UV and visible light exposure. ***T. Shittu et al.*** [225] reported that doping of Nb improves CeO_2 properties by narrowing the Eg and altering the electronic structure. XRD studies show the creation of additional Nb peaks at high doping. ***P. Rajkumar et al.*** [68] observed a significant shift toward longer wavelengths through UV-Vis absorption spectra show, particularly in the red region. Also, the controlled Pd doping has the potential to modify CeO_2's optical properties, as seen by a significant decrease in Eg energy with increasing Pd

concentration. ***Alla et al.*** [226] demonstrated the ferromagnetism in Fe-doped CeO_2 nano-rods at ambient temperature, with the maximum saturation magnetization (Ms) of 0.80 Am^{-4}/kg. ***Song et al.*** [227] observed RTFM when Y^{3+} and Co^{2+} ions were combined with CeO_2 nanoparticles. CeO_2 nanoparticles containing transition metal elements can exhibit good ferromagnetic activity at normal temperature, according to these edicts. CeO_2 nanoparticles doped with transition metals like Fe have shown improved ferromagnetic characteristics. Previous literature explained the origin of ferromagnetism using various models including F-centre exchange interaction, charge transfer mechanism, and bound magnetic polaron model [228, 61, 229, 130, 41, 230].

According to recent study, Cd-doped CeO_2 nanoparticles also exhibit the RTFM. This phenomenon is ascribed to the development of Ov and structural distortions caused by Cd^{+} ions substituting Ce^{4+} in the CeO_2 lattice [231]. Also, Cd doped CeO_2 nanoparticles have unique properties that make them useful in a variety of sectors, including photo-catalysis and biological applications. The addition of Cd to CeO_2 alters its various properties, making it a popular research interest. The optical Eg of Cd-doped CeO_2 films varies from 3.23 to 3.52 eV, showing promise for photo-catalytic use. These nanoparticles exhibit strong photo-catalytic activity, especially in the breakdown of contaminants such as Methyl Orange, demonstrating their efficiency in environmental remediation [232]. Doping with Cd can also reduce the valency state of Ce ions, favouring the formation of Ce^{3+} ions, which improves electronic conductivity and modifies the electronic band structure [233]. While Cd doping improves the characteristics of CeO_2 nanoparticles, concern about more toxicity in biological systems persist, demanding additional study into safe uses. This chapter employed simple co-precipitation method to prepare Cd-doped CeO_2 nanoparticles. This is a simple method for synthesis of low-cost nanoparticles. XRD, TEM, UV-Vis spectroscopy, XPS and VSM were used to analyse Cd doped CeO_2 in details.

5.2. Experimental details

5.2.1. Method of preparation

Using Co-precipitation route of synthesis, undoped and Cd-doped CeO_2 (CCdO) nanoparticles were prepared with different concentration of Cd (x = 0.00 0.03, 0.06 and 0.09). Alpha Aeser provided all the chemicals, including ammonia

(NH_4OH), cadmium nitrate tetra-hydrate ($CdNO_3.4H_2O$) (99.99% purity), and cerium (IV) nitrate hexahydrate $(NH_4)_2Ce(NO_3)_6$ (99.9% purity). $Ce_{1-x}Cd_xO_2$ nanoparticles were synthesized with the stoichiometrically predicted ratio of the chemicals listed above. The experiment involves 100 mL of distilled water to dissolve $(NH_4)_2Ce(NO_3)_6$ along with 50 mL of $CdNO_3.4H_2O$ with varying x concentrations. Furthermore, using NH_4OH as a precipitate agent, the pH of the solution was maintained to 10. Continuous stirring for 4 hours at 50°C with a magnetic stirrer regulates particle size and shape and guarantees even precipitate dispersion. Filtration was used to separate the precipitate that forms. After that, it is repeatedly cleaned with ethanol and distilled water to get rid of any remaining ions or contaminants. The cleaned precipitate is usually dried for 12 hours at a moderate temperature (90°C) in an oven. To produce yellow precipitate, the dry powder is annealed in a furnace for five hours at high temperatures (500°C).

5.2.2. Nanoparticles characterization:

The Bruker D8 Advance X-Ray Diffractometer was used to analyze the crystal structures of the synthesized samples. Cu Kα radiation (λ = 1.5406 Å) was used for XRD measurements in the 2θ range of $20° \leq 2\theta \leq 90°$. To measure TEM, samples were dispersed in ethanol using ultrasonic and 10 µl of the solution was manually dropped on a grid. The grids were then let to air dry. The grids from the prepared samples were imaged using an FEI Tecnai t20 TEM system at both low and high magnifications. The particle size and surface morphology of the prepared nanoparticles were determined using Image-J software. A Shimadzu UV-3600 Plus spectrophotometer was used to obtain optical absorption spectra in the wavelength range 200-800 nm. The XPS measurement was performed using Thermoscientific's Model No. NEXSA surface analysis. The experiment utilized a 400µm micro-focused X-ray with a monochromatic Al-Kα source, yielding energy of 1486.6 eV. The pass energy of 20 eV was calibrated to the binding energy of the C 1s line (hv = 284.6 eV) of adsorbed hydrocarbon on the sample surface, and the analysis chamber was set to 10-9 Torr. In this study, magnetic measurements of materials were taken at room temperature with magnetic field range -0.5 T to +0.5 T using VSM-Lake shore, Model-7410 series

5.3 Result and Discussion

5.3.1 XRD

Figure 5.1 represents the XRD patterns of Cd doped CeO_2 nanoparticles. The diffraction peaks of all the samples indicate a fcc structure, which matches data from JCPDS (81-0792). No impurity peaks are identified in any of the prepared nanoparticles [234]. The Cd-doped CeO_2 nanoparticles show no extra impurity peaks, confirming their high purity and absence of the bulk transition metal phase [224]. Adding, Cd dopant to the CeO_2 nanoparticles results in a slight broadening of the peak intensity. The inclusion of Cd reduces the maximum intensity of the peaks. Ce^{3+} ions have larger ionic radius (1.1 Å) than Cd ions (0.97 Å) [235].

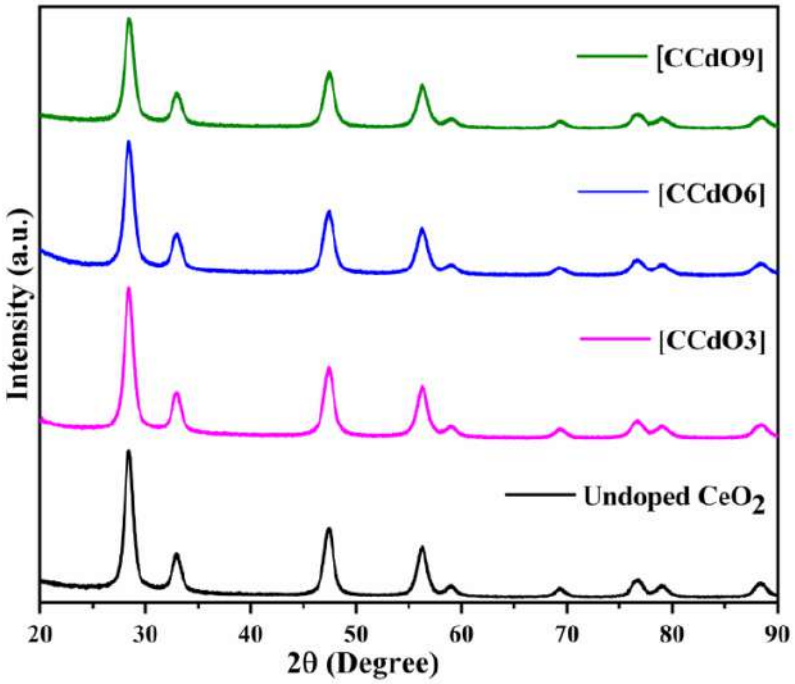

Figure 5.1: XRD pattern of CCdO nanoparticles samples

As doping levels increase, doping ions occupy intermediary sites. The crystallite size (D) of the nanoparticles is calculated from Scherer's equation [236]. Table 5.1 demonstrates that the CCdO samples have a lower crystallite size value than the undoped CeO_2. The smaller crystallite size in Cd-doped CeO_2 nanoparticles can be due to some reason, the most important of which are structural alterations and defect creation during the doping process. Doping introduces oxygen vacancy and other defects within the crystal lattice, resulting in a reduced crystallite size. For example, the introduction of dopant like Fe and Cu in CeO_2 leads in reduced particle sizes by creating defect states that are responsible for smaller crystallite size [123].

The presence of dopant can affect the local coordination of oxygen around the dopant atoms, perhaps contributing to size reduction [99].

Table 5.1: Various structural parameters obtained from Rietveld refinement, crystallite size from Scherer's equation, average particle size from TEM, band gap and refractive index of CCdO nanoparticles

Samples $Ce_{1-x}Cd_xO_2$		**X =0.00**	**X =0.03**	**X =0.06**	**X =0.09**
Lattice Parameter *a*(Å)		5.4096	5.4058	5.4076	5.4081
Unit Cell Volume V(Å^3)		158.30	157.97	158.13	158.17
R_p, R_{wp}, R_{exp}, χ^2		8.36, 8.85, 6.91, 1.64	6.68, 7.45, 6.25, 1.42	14.4, 14.2, 6.72, 4.44	7.15, 7.80, 4.04, 1.22
R_{Bragg}		1.53	0.78	1.31	0.81
Density (g/cm^3)		7.11	7.06	6.96	7.03
Crystallite size (D) (nm)		5.57	5.41	5.25	4.62
Average Particle size (TEM) (nm)		11.15	9.69	7.47	6.10
Band-gap energy (eV)		3.39	3.06	3.00	2.97
Refractive index (n)	**Moss's relation**	2.30	2.36	2.37	2.37
	Ravindra's relation	1.90	2.18	2.22	2.24
	Reddy's relation	2.67	2.75	2.76	2.77

Incorporating Cd reduces the crystallite size, indicating the effect of doping with grain growth [237]. This provides information defects and other structural parameters. Since, the XRD peaks are generally wide and broad, which makes it challenging to resolve them separately. The FULLPROF program is therefore used to perform Rietveld refining on the diffraction peaks which depict the formation of any oxide's form [238]. Figure 5.2 shows the Rietveld fits to the experimental XRD patterns of the CCdO nanoparticles. Rietveld refinement is a strong technique for obtaining precise crystallographic information from XRD data. Applying it to Cd-doped CeO_2 nanoparticles allow for quantitative analysis of doping-induced structural changes. Nanoparticles. It provides quantitative insights into how Cd doping modifies the crystal structure, size, strain, and potential defect formation in the CeO_2 lattice—information not easily extracted from raw XRD data alone. The various parameters such as goodness of fit indicator (Rp, Rw, Rexp, χ^2) are provided in Table 5.1.

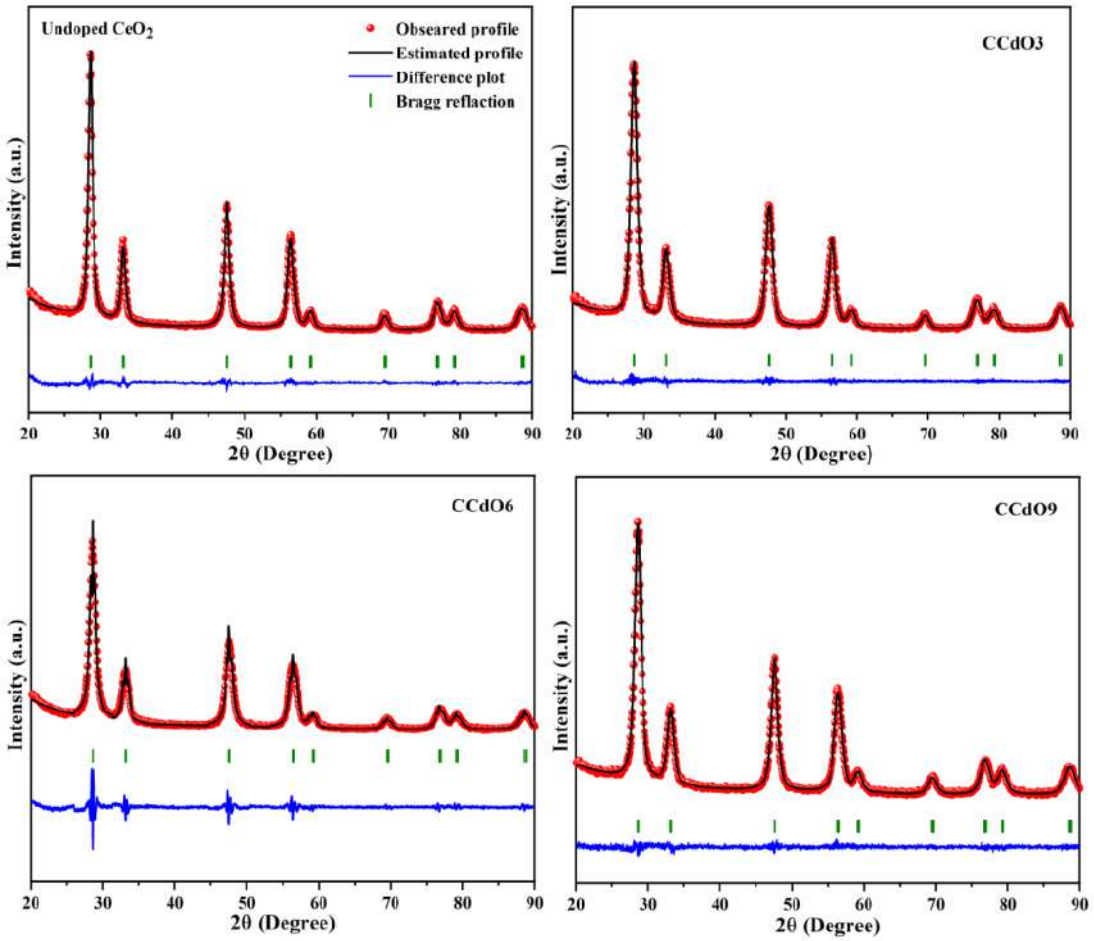

Figure 5.2: Rietveld refined and fitted curves for undoped CCdO nanoparticles samples. The short vertical lines indicate Bragg reflections. The difference plot is represented by the lower curve

However, raw XRD data has a limited precision. Rietveld refinement improves on this by fitting a calculated pattern to an experimental XRD pattern using a least-squares technique, allowing for the extraction of revised parameters. Rietveld refining of XRD data is necessary for accurate structural characterization of Cd-doped CeO_2 nanoparticles. It provides quantitative insights into how Cd doping modifies the crystal structure, size, strain, and potential defect formation in the CeO_2 lattice—information not easily extracted from raw XRD data alone. The findings of XRD analysis show minor modification to the CeO_2 matrix when divalent Cd ions substitute Ce ions, while maintaining charge neutrality. The substitution of process causes modest variations in XRD patterns, indicating lattice alterations. The peak intensity and position variation show that Cd has been effectively incorporated into the CeO_2 structure. Subtle structural changes can significantly affect material

properties, particularly optical and electronic structural properties. The Scherer formula is used to evaluate the XRD data such as material's crystalline structure and our goal of this work is to determine empirically which form this "simple" formula must be applied in to provide results that are consistent with more complex techniques like TEM. Therefore, to visualize the microstructure and information about the crystal structure at a core level, these nanoparticles are subjected to TEM analysis [239].

5.3.2. Transmission Electron Microscope (TEM):

TEM study of Cd-doped CeO_2 nanoparticles reveals their structural and morphological properties. Figure 3 depicts the TEM images of CCdO nanoparticles confirming that the particles in the Cd-doped CeO_2 samples are well-dispersed and spherical/elliptical in shape. The inset of figure 5.3 displays the histogram depicting the size measurements of 50 randomly picked particles. Fitting with a log normal curve yields a mean diameter of 6-12 nm. The images show small, homogenous particles with average diameters or particle size of 11.15, 9.69, 7.47 and 6.10 nm, consistent with XRD results as shown in Table 5.1.

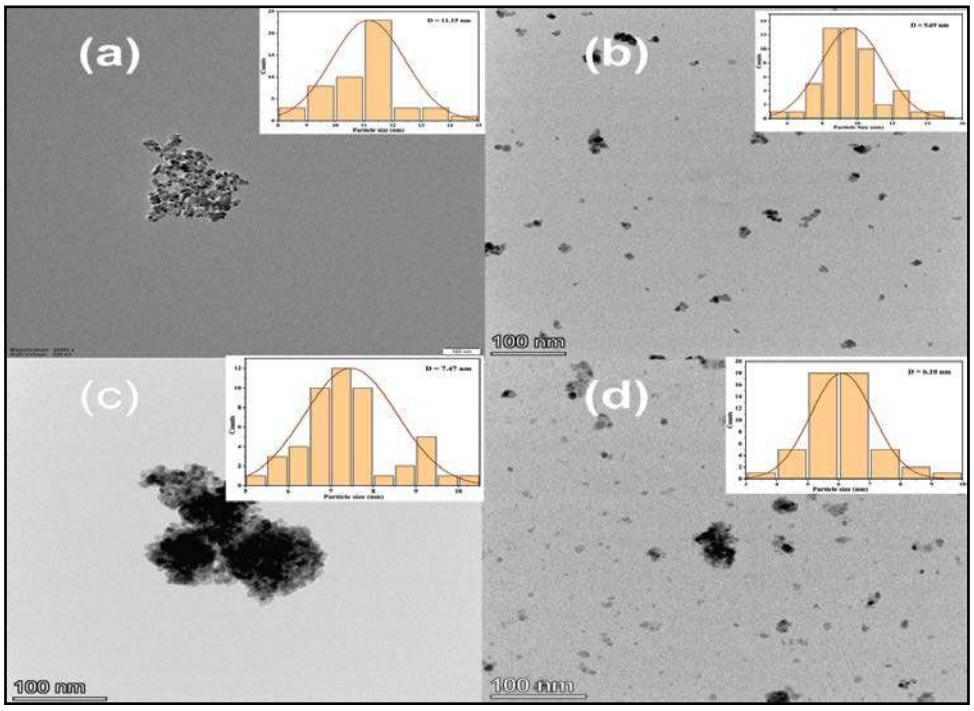

Figure 5.3: TEM images of (a) undoped CeO_2, (b) CCdO3, (c) CCdO6 and (d) CCdO9 nanoparticles samples. The samples' corresponding particle sizes are shown in an inset histogram

The Selected Area Electron Diffraction (SAED) patterns for CCdO nanoparticles are shown in the figure 5.4. The reflected planes from the SAED show a ring pattern that matches the fcc structure of CeO_2. The broadening of diffraction rings indicates tiny particles with high crystallinity [240]. The presence of Cd lowers particle size in CeO_2, indicating that the dopant regulates grain growth. Correlating TEM with optical absorption spectra (UV-Vis) enables a greater knowledge of how the size, shape, and structure of Cd-doped CeO_2 nanoparticles affect their optical properties, particularly Eg energy. TEM provides structural insights that have a direct impact on how nano-particles interact with light, influencing band gap, light absorption, and emission behavior. Thus, TEM data is important for interpreting and justifying patterns in optical measurements.

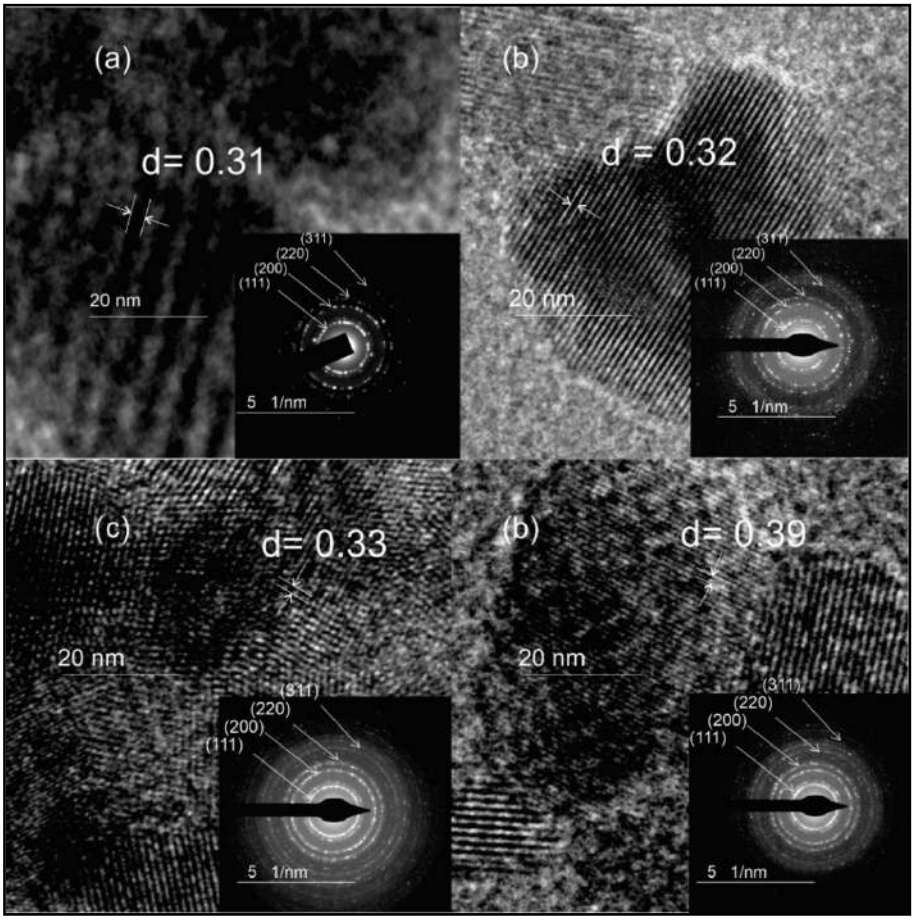

Figure 5.4: TEM images of CCdO nanoparticles samples with d spacing corresponding to (111) plane: (a) Undoped CeO_2, (b) CCdO3, (c) CCdO6 and (d) CCdO9 nanoparticles and the inset graph shows their corresponding SAED images

5.3.3. Optical Absorption Spectra

UV-Vis spectroscopy is a popular analytical method that gauges a substance's ability to absorb or transmit UV and visible light. N the present study, samples are measured for absorbance at room temperature throughout a wavelength range of 200-800 nm. Figure 5.5 (a) shows the UV-Vis absorption spectra of CCdO nanoparticles. The prepared samples exhibit a prominent absorbance band below 400 nm (UV region). An absorption band in this region is attributed to the charge transfer transition from O^{2-} in O 2p to Ce^{4+} in Ce 4f [241]. These findings support the presence of Ce^{3+} ions, as well as the formation of oxygen vacancies in CCdO nanoparticles [242].

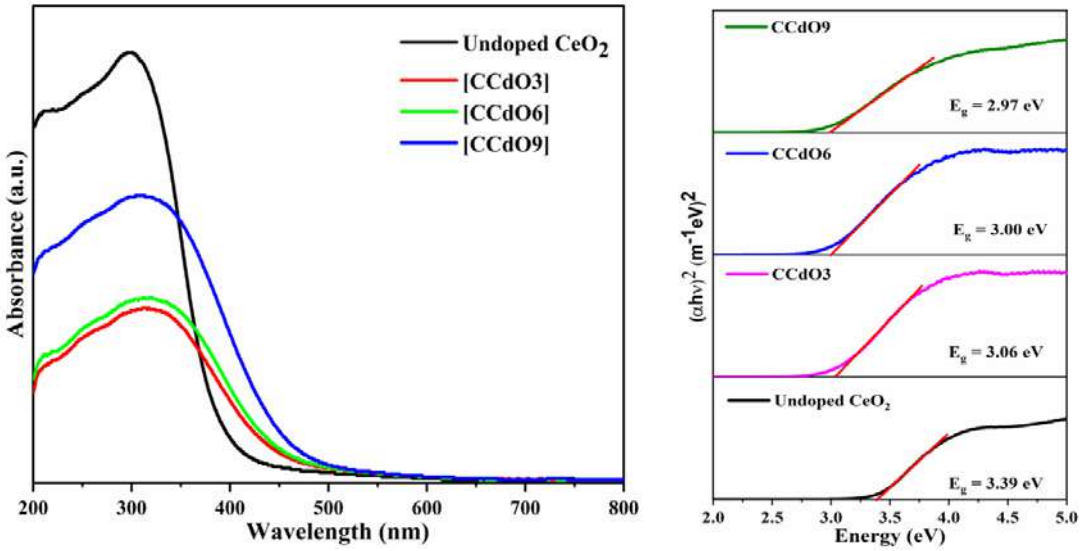

Figure 5.5: (a) Optical absorption spectra, (b) Tauc's plot of CCdO nanoparticles samples

UV-Vis absorption peaks represent particle band-gaps. Nnanoparticle's ' basic absorption causes electron excitation from their valance. The Tauc' relation can be used to determine a material's optical Eg using absorption spectra in which the direct Eg energy is determined by extrapolating the linear sections of the curves to zero absorption [46]. Extrapolating a straight line from the band edge to the intersection with the hυ axis yields the Eg energy as shown in figure 5(b). Table 5.1 displays the Eg energy of undoped and CCdO nanoparticles. The Eg energy values for CCdO samples are 3.39, 3.06, 3.00 and 2.98 eV respectively. Doped ceria nanoparticles exhibit red-shifted band gap values and higher concentrations of doped CeO_2 nanoparticles result in a smaller band gap. The substitution of Cd ions leads to a

narrower band gap. This adds electron states into CeO_2's band gap, resulting in a new lowest unoccupied molecular orbital. ***Yue et al.*** [243] found that doping reduces the Eg of CeO_2, creating oxygen vacancies that promote the generation of Ce^{3+} from Ce^{4+}. Cd -doped CeO_2 nanoparticles exhibit a reduction in band gap, promoting the development of oxygen vacancies. According to ***Kumari et al.*** [244], the incorporation of dopant also causes oxygen vacancies, which contribute to the development of extra energy levels inside the band gap, facilitating electron transitions and decreasing the total band gap. The optical energy gap or the absorption edge, and refractive index are the two most intriguing and essential characteristics of a semiconductor. As a result, numerous efforts have been made to discover more relations between these characteristics from a fundamental interest as well as a tool for technology. Moss, for the first time successfully organized an empirical relationship between the refractive index and band gap which as follows [245]:

$$\boldsymbol{n^4 E_g = K} \qquad \textbf{(5.1)}$$

Where, K is constant which is equal to 95, n and Eg are the refractive index and energy Eg (in eV) respectively. The main drawback of this relationship is that it lacks the uniqueness of such a constant (K), even though it has been verified for a large variety of semiconductor systems. Another linear relationship between these two parameters has been suggested by ***Ravindra et al***. [246], which is as:

$$\boldsymbol{n = 4.084 - 0.62 E_g} \qquad \textbf{(5.2)}$$

Another empirical relation between Eg and n is given by ***Reddy et al.*** [247] as:

$$\mathbf{n = \sqrt{\frac{12.417}{\sqrt{E_g} - 0.365}}} \qquad \textbf{(5.3)}$$

Eq. (5.3) is a simple alteration of the Moss relation. The calculated values of the refractive index by all above three formulas and are summarized in Table 5.1, which reflects the increase in value of n with rise in Cd doping. These materials with high refractive index result in strong light-matter interactions, which is particularly advantageous for optical devices such as solar cells and photo-detectors. Therefore, the lowering of the Eg in Cd-doped CeO_2 nanoparticles can be attributed to several relatable variables, the most important of which are structural changes and electronic

state modifications caused by doping. This effect is important for improving the electronic properties of these materials. Since, UV-Vis reveals about what is occurring to the band structure (Eg narrowing) but XPS reveals why the defects such as oxygen vacancies are generated due to incorporation of Cd ions into CeO_2 lattice. In this way, XPS supports the origin of the modification in the optical properties observed in UV-Vis. These studies provide a comprehensive understanding of how Cd doping affects the electronic and optical properties of CeO_2 nanoparticles.

5.3.4. Electronic Structural Properties (XPS):

5.3.4.1. XPS of Ce 3d core level

Further XPS research revealed more information on the electronic structure and surface composition of CCdO nanoparticles. The addition of Cd ions in the ceria lattice can also affect the transformation of Ce^{3+} to Ce^{4+}. XPS is used to analyze changes in the valence chemistry and binding energy of constituent elements. The XPS spectra have been charge-corrected for the C(1s) peak at 284.6 eV [248]. Figure 5.6 displays the XPS spectra of deconvoluted core level Ce 3d spectrum of CCdO nanoparticles. The spectra showed no peaks for elements other than Ce, O, and Cd. The Ce 3d spectrum show multiplet peaks for Ce^{3+} and Ce^{4+} spin-orbit doublets. The deconvoluted Ce 3d spectrum is complex due to the presence of Ce in 3+ and 4+ oxidation states and multiple d-splitting. The peaks u‴, u″, u, and v‴, v″, v represent the $3d_{3/2}$ and $3d_{5/2}$ final states of Ce^{4+}. u‴ and v‴ are the final states of Ce $3d^9O2p^6Ce\ 4f^0$, whereas u_o, u', v_o and v' are a combination of Ce $3d^9O2p^5Ce\ 4f^1$ and $Ce3d^9O2p^4Ce\ 4f^2$ states. u' and v' are $3d_{3/2}$ and $3d_{5/2}$ for Ce^{3+} final states, resulting from the com of $Ce3d^9O\ 2p^5Ce4f^2$ and $Ce3d^9O2p^6Ce4f$ [249]. The interaction between Ce 4f and Ce 3d results in electron transfer from O 2p to Ce 4f orbitals and decrease in Ce 3d binding energy. The core hole drags the Ce 4f level to a lower energy state. The relative concentration of Ce^{3+} and Ce^{4+} $[Ce^{3+}]/[Ce^{3+} + Ce^{4+}]$ is estimated using the integrated areas (Ai) of the respective peaks [250]. Table 5.2 summarizes the individual peak areas, binding energies, and Ce^{3+} concentrations. Increasing Cd doping from 3 to 9 % resulted in an increase in Ce^{3+} concentration.

Table 5.2: Binding energies (eV) of several GL30 components in the Ce 3d XPS spectra of CCdO samples

Samples	$3d_{5/2}$ (eV)					$3d_{3/2}$ (eV)					Ce^{+3} %	Ce^{+4} %	Ce^{+3}/Ce^{+4}
	V_0 Ce^{3+}	V Ce^{4+}	V' Ce^{3+}	V'' Ce^{4+}	V'' Ce^{4+}	U_0 Ce^{3+}	U Ce^{4+}	U' Ce^{3+}	U'' Ce^{4+}	U'' Ce^{4+}			
Undoped CeO_2	882.00	883.45	885.80	888.75	898.12	900.65	903.23	906.85	908.36	916.50	36.91	63.09	58.50
CCdO3	881.77	883.14	885.13	888.45	897.61	898.28	900.36	902.57	906.89	916.13	37.86	62.13	60.93
CCdO5	881.70	884.18	886.15	888.47	897.44	898.13	900.24	902.55	906.82	916.01	38.73	61.26	63.22
CCdO7	881.87	883.72	885.69	888.54	897.52	898.21	900.44	902.60	906.99	916.20	39.75	60.24	65.98

Table 5.2 shows small amount of Ce^{3+} coexists with Ce^{4+} in CCdO nanoparticles. Fitting curves and calculating $Ce^{3+}/(Ce^{3+} + Ce^{4+})$ yields a significantly increase in Ce^{3+} to Ce^{4+} ratio. Ultra-high Ce^{3+} ratios is proportional to the number of oxygen vacancies in nanoparticles, as Ce^{3+} abundance often correlates with oxygen vacancies. XPS can detect both Ce^{4+} and Ce^{3+} oxidation states. An increasing ratio of Ce^{3+} to Ce^{4+} indicates a larger concentration of oxygen vacancies, as the reduction from Ce^{4+} to Ce^{3+} is generally associated with the loss of oxygen atoms from the lattice. Further, this result is confirmed by the XPS analysis of the O 1s region of the prepared samples.

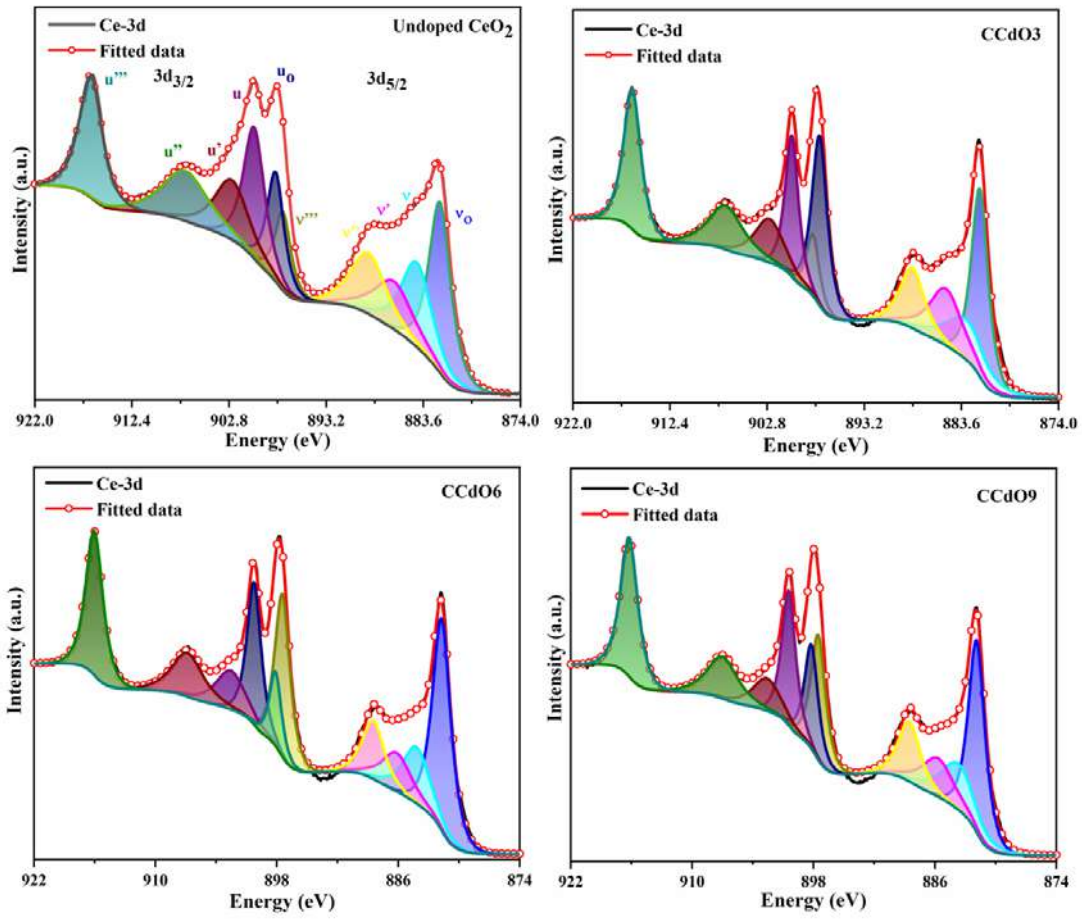

Figure 5.6: The deconvoluted peak of the Ce 3d profile of CCdO nanoparticles samples

5.3.4.2 XPS of O 1s

To better examine the behavior of oxygen vacancies, the core level O 1s XPS plot of CCdO nanoparticles is displayed in figure 5.7. By deconvoluting the O 1s spectra, the present oxygen species have been identified. Three separate components

comprise of well Gaussian fitted O 1s (O_L, O_V, and O_C). O–Ce–O bonds are responsible for the O_L peak, which arises at ~528 eV and corresponds to lattice oxygen, while the peak arises at ~529 eV is brought on by oxygen ions in areas with low oxygen concentrations (Ov). Because of surface imperfections, Cd-doped CeO_2 exhibits a high binding energy that is centered at ~530 eV and many oxygen vacancies in the lattice crystal indicating the existence of –OH groups on the sample surfaces [49]. The concentration of O_L and Ov can be derived by quantifying O 1s spectra, as indicated in Table 5.3.

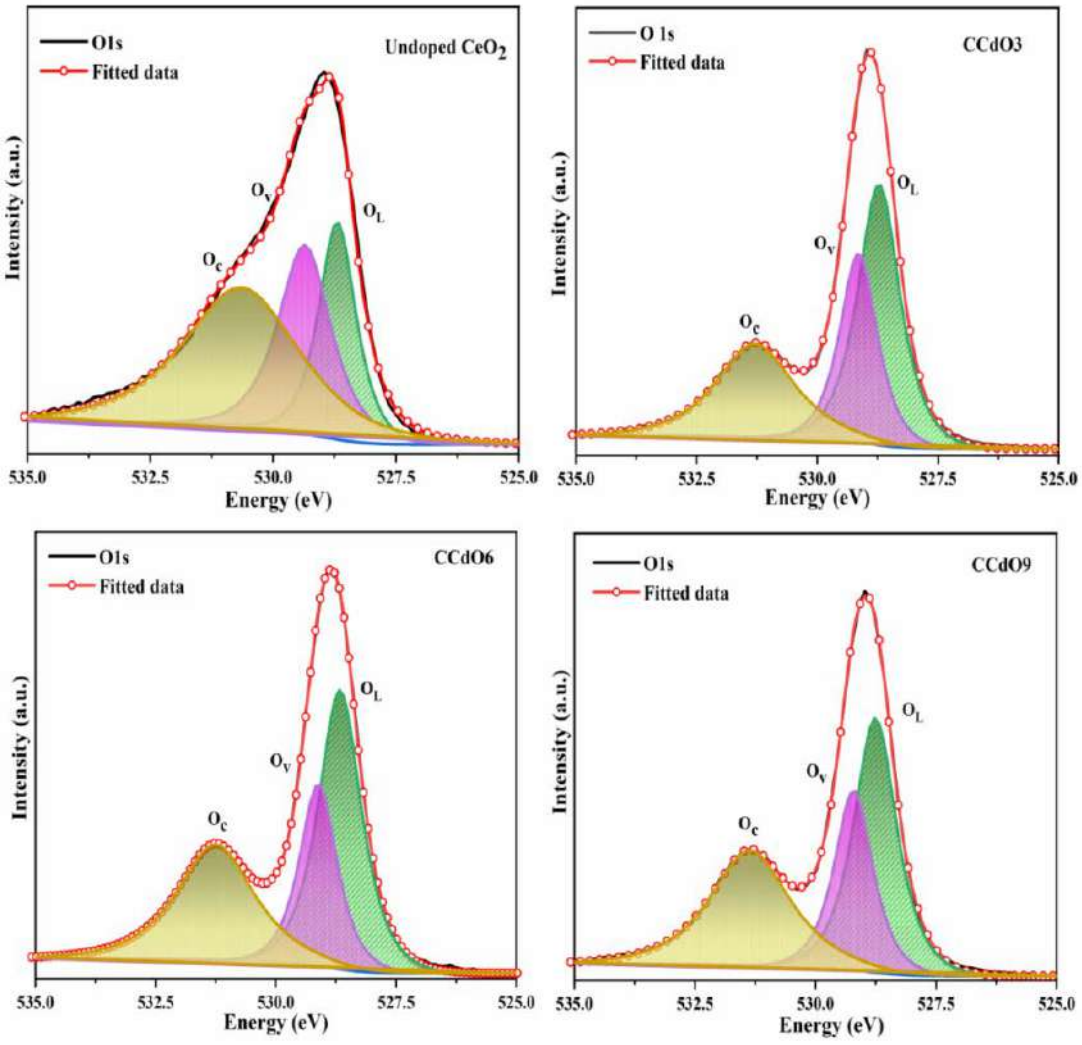

Figure 5.7: The deconvoluted core level spectra of the O 1s profile for CCdO nanoparticles samples

Table 5.3: Binding energies (eV) of several GL30 components in the O 1s XPS spectra of CCdO nanoparticles samples

Samples	O_L [eV]	O_V [eV]	O_C [eV]	% O_L	% O_V
Undoped CeO_2	528.70	529.40	530.69	44.83	55.17
CCdO3	528.72	529.14	531.28	63.91	36.08
CCdO6	528.66	529.11	531.25	61.27	38.72
CCdO9	528.76	529.20	531.35	60.93	39.06

The peak denoted by oxygen vacancies related to adsorbed and weakly bonded oxygen species, while Oc with the maximum binding energy attributed to hydroxide or adsorbed water on the catalyst surface. Both peaks confirm the presence of surface oxygen vacancies in CCdO samples. The weakest peak at ~528 eV, was attributed to lattice oxygen in attached CeO_2 nano-crystals. Surface adsorbed oxygen is typically more reactive than lattice oxygen in oxidation processes because to its increased mobility [251].

5.3.4.3 XPS of Cd

Figure 8 displays the XPS spectrum of Cd. The Cd characteristics include the main Cd $3p_{3/2}$ (~617eV), Cd $3p_{1/2}$ (~651 eV) as well as $3d_{5/2}$ (~404 eV) and $3d_{3/2}$ (~411 eV) spin-orbit components, manifesting Cadmium in Cd^{2+} state. As predicted by Figure 5.8(a) and 5.8(b), CdO nanoparticles exhibit prominent peaks corresponding to (Cd $3p_{3/2,}$ $3p_{1/2}$) and (Cd $3d_{5/2}$, Cd $3d_{3/2}$) which well matched with the published result of XPS spectra of Cd [252,253]. The binding energy peak position of Cd 3p and Cd 3d are provided in Table 5.4.

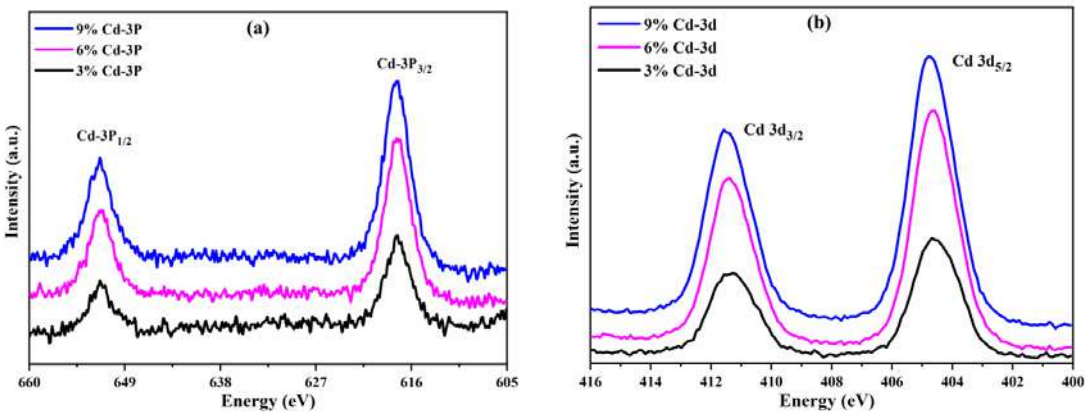

Figure 5.8: (a) The core level spectra of Cd 3p and (b) Cd 3d of CCdO nanoparticles samples

Table 5.4: Binding energy peak position of core level spectra Cd 3p and Cd 3d of CCdO nanoparticles samples

Samples	Cd $3p_{1/2}$ [eV]	Cd $3d_{3/2}$ [eV]	$3d_{3/2}$ [eV]	Cd $3d_{5/2}$ [eV]
CCdO3	651.76	617.60	411.29	404.53
CCdO6	651.78	617.61	411.33	404.58
CCdO9	651.87	617.71	411.41	404.65

Therefore, it can be concluded that substituting Cd^{2+} ions into the CeO_2 lattice might cause lattice distortions due to their differing ionic radius from Ce^{4+}. This substitution can help to produce oxygen vacancies and keep the charge neutral. Incorporating Cd into CeO_2 nanoparticles affects the creation of Ov, which are crucial for the material's electronic properties. Therefore, oxygen vacancies are not merely structural defects, but active mediators of magnetism in Cd-doped CeO_2 nanoparticles, causing ferromagnetism which is further discussed in the next section.

5.3.5 Magnetic properties (VSM)

To investigate the magnetic properties of CCdO nanoparticles at room temperature, VSM has been used which analyzes the various magnetic characteristics of nanoparticles, including TM-doped CeO_2 particles. Although there is insufficient VSM data on Cd-doped CeO_2 nanoparticles, investigations on related systems can provide insights. Also, the patterns observed in other doped systems show that Cd doping may cause or increase ferromagnetic behavior in CeO_2 nanoparticles. The

injection of Cd^{2+} ions may create oxygen vacancies, which promote magnetic interactions. However, experimental research is required to corroborate these effects and understand the exact magnetic properties conferred by Cd doping. The room-temperature M-H curve for all samples is displayed in figure 5.9, which depicts that all samples exhibit weak ferromagnetism (FM) at normal temperature. The figure shows that CCdO nano-particle samples are soft ferromagnetic materials, with saturated M-H curves and a small hysteresis region. This FM behavior has already been described by previously studies. As reported by ***Ge et al.*** [254] oxygen vacancies produce localized states that polarize the f electrons of cerium ions, causing ferromagnetism. Vacancies on the surface of nanoparticles contribute more strongly to magnetism than those in the bulk, raising the overall magnetic moment. According to ***Tarui et al.*** [255] the presence of oxygen vacancies is a key factor in the ferromagnetism of CeO_2 nanoparticles, which can be generated by doping with transition metals or manipulating the oxidation states of CeO_2 may also improve the magnetic properties. Such results show a complex interplay of factors influencing ferromagnetism in these materials.

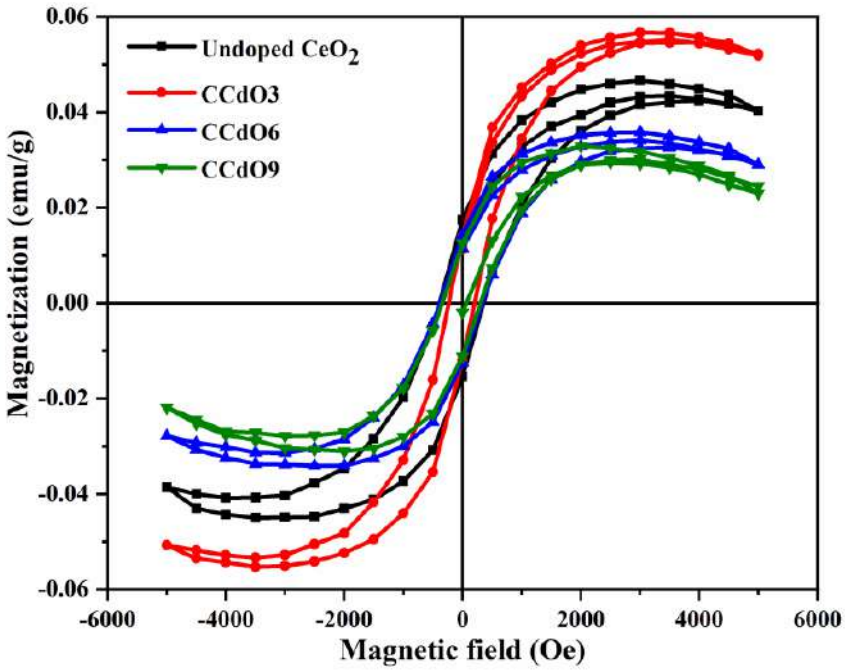

Figure 5.9: Room temperature M-H curves for CCdO nanoparticles samples

The Langevin function is important for analyzing the magnetic behavior of materials with a high-spin system. It explains how magnetic materials' magnetization

changes in response to applied magnetic fields. To extract the ferromagnetic component, all samples are fitted with the Langevin function L(x) as shown in figure 5.10.

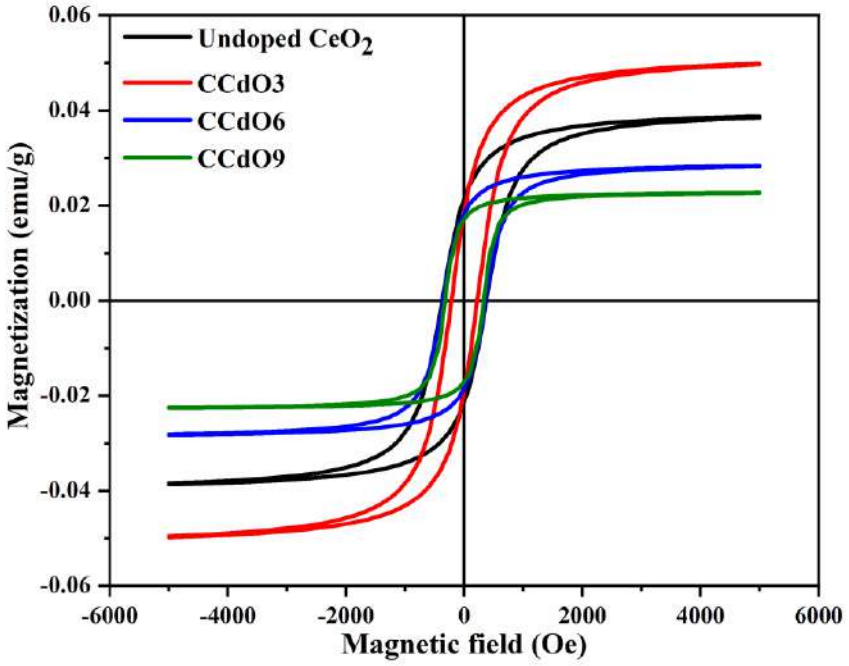

Figure 5.10: Langevin equation fitted M-H curves of CCdO nanoparticles samples

Table 5.5 displays the measured values for magnetic parameters including saturation magnetization (M_S), remanent magnetization (M_R), and coercively (H_C), magnetic susceptibility (χ), Squareness Ratio (SQR), Anisotropy Constant (K) and magnetic moment (n_B) obtained from the analysis of magnetic curves (figure 5.9 and figure 5.10). Table 5.5 shows that Ms value of undoped CeO_2 sample is 0.0402 emu/g, but increases to 0.0518 emu/g as Cd^{2+} ions are added, while the value of Hc decreases from 372.8 Oe to 218.93 Oe. A decrease in H_C reduces magnetic and electric losses, while increasing M_S leads to higher spin current generation and attributed to increased crystallinity and reduced spin disorder on nano-particle surfaces. Therefore, such findings predict the potential use of these materials in spintronics. The relationship of Ms and Hc in our case is further verified by the following Brown's equation [256]:

$$H_c = \frac{2K}{\mu_0 M_S} \qquad \textbf{(5.4)}$$

where, K is anisotropy constant. Magneto-crystalline anisotropy in ferromagnetic materials results from the interaction of electron spins with the crystal lattice, which

occurs predominantly through spin-orbit coupling. This interaction makes some crystallographic directions energetically advantageous for magnetization. The calculated anisotropy constant (K) using the above relation (equation 5.4) is summarized in Table 5.5.

Table 5.5: Various magnetic parameters of CCdO nanoparticles samples

Sample	M_S **(emu/g)**	M_R **(emu/g)**	H_C **(Oe)**	χ **(emu/g-Oe)×10^{-5}**	**SQR**	K **(erg/gm)**	n_B (μ_B) **× 10^{-3}**
Undoped CeO_2	0.0402	0.0165	372.8	0.90	0.5339	15.611	1.23
CCdO3	0.0518	0.0130	218.93	1.18	0.3721	11.813	1.58
CCdO6	0.0290	0.0133	361.07	0.67	0.6428	10.471	0.85
CCdO9	0.0229	0.0119	324.9	0.52	0.7554	7.750	0.69

The squareness ratio (SQR) is another magnetic parameter used to determine a material's magnetic hardness, which is its resistance to demagnetization. The SQR is defined as the ration between Mr and Ms. SQR equals Mr/Ms [257]. This ratio is calculated using the hysteresis loop. The SQR shows how "square" the hysteresis loop is, which reflects the material's magnetic hardness. According to literature, SQR greater than 0.5, indicates a strong magnetic orientation and increased resistance to demagnetization, which is typical of hard magnetic materials. SQR < 0.5 indicates a multi-domain structure with decreased magnetic hardness, prevalent in soft magnetic materials [258]. In our case, Table 5.5 shows that the prepared samples are single domain structures. A higher SQR is preferable for greater data retention since it shows that the material retains its magnetization more effectively when the external field is withdrawn. As a result, studying the SQR from the hysteresis loop allows one to evaluate a material's magnetic hardness, which is essential for applications that require stable and persistent magnetization [259].

To investigate magnetic properties further, the magnetic moment (n_B) in units of Bohr magneton (μ_B) from hysteresis curve is yielded from using the following equation, which gives information about the strength and presence of magnetism in a material [260].

$$n_B = \frac{(M_{wt} \times M_S)}{5585} \qquad \textbf{(5.5)}$$

Here, M_{wt} stands for molecular weights of specific composition. CeO_2 in its bulk form is regarded as non-magnetic due to the occupied 4f shell of Ce^{4+} [213]. However, these materials show the emergence of some kind of magnetic response which could by arises due to defects such as oxygen vacancies [261]. As our findings show that calculated magnetic moment (n_B) for undoped CeO_2 is 1.23×10^{-3} μ_B. This very tiny magnetic moment suggests weak magnetism for CeO_2 nanoparticles which increases upon Cd doping and attributed to the crystal lattice defects. This result reflects that the exchange interaction between oxygen vacancies and electron spin moment causes some cerium ions to deviate from Ce^{4+} to Ce^{3+} state, which is key mechanism in understanding the magnetic behaviour of defect-induced material like CeO_2

Table 5.5 shows that the variation in magnetic parameters do not vary consistently with Cd-ion doping, as expected based on our earlier XRD, TEM, UV-Vis and XPS experiments. RTFM behavior in synthesized samples is not so strong; according to calculated values Ms. Such findings demonstrate that the magnetic behavior is strictly reliant on the concentration of Cd^{2+} ions. As shown in Table 5.5, RTFM may be initially improved by lower Cd concentrations, but Cd with higher doping may cause secondary phases or defect saturation, which could lessen magnetism. Overall, because of the improved RTFM of Cd-doped CeO_2 in compare to undoped CeO_2 can be used in spintronics devices, which take advantage of electrons' charge and spin.

The addition of Cd to CeO_2 nanoparticles affects their structural, optical, electronic and magnetic characteristics. A thorough investigation employing techniques such as XRD, TEM, UV-Vis spectroscopy, XPS and VSM sheds light on these changes. Cd doping causes a minor shift in the diffraction peaks of CeO_2, showing lattice distortion due to the substitution of Ce^{4+} ions with Cd^{2+} ions. The average crystallite size decreases as Cd content increases, indicating that Cd incorporation lowers grain growth. TEM images show that Cd-doped CeO_2 nanoparticles have a spherical shape and a homogeneous size distribution. The particle size measured by TEM confirms the crystallite size calculated from XRD data, verifying the nano-scale dimensions of the prepared particles. According to UV-Vis spectroscopy, due mostly to caused structural defects and charge compensation effects, Cd doping dramatically changes the optical characteristics of CeO_2

nanoparticles by decreasing the band gap, moving the absorption edge (red shift), and increasing visible light absorption. XPS analysis shows the existence of Ce^{3+} and Ce^{4+} oxidation states, confirming the presence of oxygen vacancies from Cd doping. The Cd 3d spectra show peaks for Cd^{2+}, indicating effective incorporation of Cd into the CeO_2 lattice. The increase in oxygen vacancies improves the electronic characteristics of the nanoparticles. The investigation from VSM measurement shows that Cd-doped CeO_2 nanoparticles display RTFM. The Ms increases with Cd concentration until an appropriate doping level (3%) is reached, at which point it declines, potentially due to the formation of non-magnetic secondary phases or Cd ion clusters. The observed ferromagnetism is attributed to exchange interactions between oxygen vacancies and cerium's mixed valence states. The structural distortion and reduced particle size (XRD and TEM) increases surface area, which influences optical absorption (UV-Vis). Increased oxygen vacancies and changed electronic structure (XPS) contribute to a narrower Eg (UV-Vis) and high value of refractive index and ferromagnetism (VSM). Cd doping enhances the multifunctional characteristics of CeO_2 nanoparticles, enabling applications in photo-catalysis, spintronics, and optoelectronics.

5.4. Conclusion

Cadmium doping in CeO_2 nanoparticles has been widely explored to improve their structural, optical, and magnetic properties for diverse applications. This is a complete summary and conclusion based on this study findings. Cd-doped CeO_2 nanoparticles prepared by co-precipitation have a cubic fluorite structure and an average size of about 5 nm. Cd doping affects grain growth and decreases particle size, which can increase surface area and reactivity or in other words Cd doping does not affect the fcc structure of CeO_2, but does reduce crystallite size. TEM analysis shows that Cd-doped CeO_2 nanoparticles have spherical morphologies with diameters ranging from 6-12 nm. Cd doping reduces the average grain size relative to undoped CeO_2, suggesting that it slows grain expansion during synthesis. SAED patterns confirm its crystalline structure, with clear diffraction rings corresponding to the fluorite phase. Incorporating Cd^{2+} ions into CeO_2 lattice, results in localized energy levels within the band gap. These defect states enable electronic transitions at lower energies, hence decreasing the band gap. The substitution of Ce^{4+} with Cd^{2+} upsets the charge balance, creating oxygen vacancies. These vacancies introduce new energy levels and change the electronic structure, resulting in narrowing of band gap. The Ce

3d XPS spectra show a mixed oxidation state of Ce^{3+} and Ce^{4+}. Ce^{3+} is commonly related with oxygen vacancies in the lattice. The higher ratio of Ce^{3+} to Ce^{4+} in Cd-doped samples indicates that Cd doping stimulates the creation of oxygen vacancies, potentially improving the material's electronic structure. Cd 3p and 3d XPS spectra typically show two notable peaks corresponding to (Cd $3p_{3/2,}$ $3p_{1/2}$) and (Cd $3d_{5/2}$, Cd $3d_{3/2}$) indicating Cd^{2+} oxidation states. These peaks confirm Cd's effective integration into the CeO_2 lattice, either displacing Ce sites or occupying interstitial sites. VSM study of Cd-doped CeO_2 nanoparticles shows improved magnetic behavior compared to undoped CeO_2. Undoped CeO_2 has weak ferromagnetic behavior due to its electronic configuration of 4f shell and intrinsic defects. However, adding Cd ions causes RTFM or enhances magnetic susceptibility, depending on the doping concentration. The increased magnetism can be ascribed to create by Cd doping, resulting in localized magnetic moments and charge imbalances and lattice distortions promote magnetic exchange interactions. Mixed valence states (Ce^{3+}/Ce^{4+}) produce defect-induced magnetism. Cd doping improves the magnetic response of CeO_2 nanoparticles, making them suitable for spintronics and magnetic semiconductor applications.

Chapter 6
Conclusion and Future Scope

Chapter 6

Conclusion and Future Scope

6.1 Conclusion of the Research work

Transition metal (TM)-doped CeO_2 nanoparticles have attracted a lot of interest because of their improved characteristics, which make them appropriate for use in spintronics, photo-catalysis, and supercapacitor applications. The reversible Ce^{3+}/Ce^{4+} transition gives CeO_2 its inherent redox capacity, making it a viable material for energy storage. Its poor electrical conductivity presents difficulties, though. It has been demonstrated that doping with TM like Ag improves electrochemical performance, which in turn improves capacitance and cycling stability. The band gap of CeO_2 can be reduced via TM doping, enabling improved photo-catalytic activity and absorption of visible light. Doping with metals such as Yttrium has been found to introduce 3d orbital states within the band gap, allowing for increased visible spectrum light absorption and generation of more oxygen vacancies which encourages reactive sites and enhanced organic pollutant breakdown in the presence of light. The size, shape, surface area, crystallinity, and functional performance of CeO_2 nanoparticles are all greatly influenced by the synthesis process. The structural and functional characteristics of CeO_2 nanoparticles are directly impacted by the process of synthesis selected. The intended application determines which approach is best. In this research work, a simple, economical, and fast chemical co-precipitation method is used to synthesize 4d cations (Y, Ag and Cd) doped CeO_2 at various concentrations. The obtained samples were analyzed to determine their structural, optical, and magnetic properties. Ag-doped CeO_2 nanoparticles were then subjected to electrochemical investigation. Finally, we investigated the different properties of these 4d cation doped CeO_2 nanoparticles.

XRD study of 4d cations doped CeO_2 nanoparticles revealed a face-centered cubic fluorite (Fm-3m) structure with no secondary phases. The average crystallite size was determined using Scherer's equation, which reflected the well-integration of dopant ions (Y, Ag and Cd) in the lattice of CeO_2 nanoparticles and was discovered to change the smaller Ce^{4+} (0.097 nm) ions into larger Ce^{3+} ions (0.114 nm). A decrease in crystallite size and lattice parameter following TM doping indicates accumulation

of lattice strain (tensile because of ionic radius mismatch). Various structural parameters, such as crystallite size, lattice parameter, and lattice strain, were calculated to investigate the change in structural properties following dopant addition (Y, Ag and Cd). Slight shifting in (111) d-spacing are confirmed by a sample calculation using Bragg's law. Trends in strain align with the contraction or expansion of the lattice. The crystallite size and lattice strain were also determined using the W-H plot, and the findings were remarkably similar with those obtained using Scherer's equation. More oxygen vacancies are associated with higher strain, and these vacancies are frequently related to improved catalytic, magnetic, or electrochemical characteristics. An effective method for obtaining comprehensive crystallographic and micro-structural details from powder diffraction data is Rietveld refinement. The Rietveld fitted curve reflects that doping of 4d cations (Y^{3+}, Ag^{+} and Cd^{2+}) preserves the fluorite ($Fm\bar{3}m$) cubic phase without the presence of secondary phases. Such XRD-derived structural data are essential for establishing a correlation with spintronics, photo-catalysis, or supercapacitor performance.

To determine the elemental composition, EDX spectra of 4d cation doped CeO_2 were obtained. The inclusion of (Y^{3+}) in accordance with the correct stoichiometry ratio was demonstrated using EDX. In a similar vein, the proper stoichiometry ratio of cerium (Ce) and oxygen (O) was found in these prepared samples. The TEM, HRTEM, and SAED patterns validate the spherical morphology of undoped and Y and Cd-doped samples. TEM images indicate that Y and Cd-doped CeO_2 nanoparticles had average crystalline sizes of 12-18 nm and 5-11 nm respectively. The CeO_2 nano-lattice contains dopant ions Y resulting in well-arranged crystalline particles as shown in HRTEM and SAED images. The d-spacing ~0.31 nm for CeO_2 (111) has been be measured directly, and their shift with doping has been observed. The particle size of Y and Cd-doped CeO_2 decreased, which is consistent with a reduced lattice caused by smaller Y^{3+} and Cd^{2+} ions replacing Ce^{4+}. High crystallinity of the samples has been observed by lattice fringes with great contrast.

The optical absorption spectra revealed that the refractive index and band gap energy of all samples altered in the UV-Vis-NIR spectra, showing the incorporation of dopant ions (Y^{3+}, Ag^{+} and Cd^{2+}) into CeO_2 nanoparticles. The band gap energy of CeO_2 nanoparticles decreased as the fluency of dopant ions increased. Impurity levels

in the CeO_2 band structure may be arises by oxygen vacancies between the O 2p and Ce 4f states. These oxygen vacancy states capture the excited electrons, lowering the band gap energy of the CeO_2 nanoparticles doped with (Y^{3+}, Ag^{+} and Cd^{2+}). The red shift of the absorption edge indicates that dopant cations were well incorporated in the CeO_2 sample. The inclusion of dopant ions (Y^{3+}, Ag^{+} and Cd^{2+}) in CeO_2 lattice has generated defects and oxygen vacancies, as determined by the calculation of Urbach energy and refractive index. The band-gap of CeO_2 is reduced by Y doping from roughly 3.38 eV to 2.95 eV, which moves absorption into the visible light spectrum and increases photo-catalytic activity. Finally, it was discovered that the host CeO_2-based DMS compound, which has good optical performance, could have its optical band gap energy modified by changing the concentration of dopant ions. The XRD findings validated the concept that defects caused by doping enhance Urbach energy.

The PL spectra of (Y^{3+}, Ag^{+}) doped CeO_2 nanoparticles have been used to confirm the presence of various defects and structure disorderness. The PL spectra show a variety of peaks that correspond to different causes, including transitions from different energy levels and valence changes. The prepared nanoparticles emission color was assessed using the 1931 CIE (Commission International de L'Eclairage) standard. Higher CCT and CRI values for all doped nanoparticles evaluated using PL spectra indicate that they are better suited for emitting different colors light sources. Ag decorating frequently improves CRI and CCT by shifting emission toward the white-light region. Chromaticity graphs for Y-doped CeO_2, on the other hand, exhibit a peak shift into the yellow region, which is suitable for LED and display applications.

The XPS analysis of samples of undoped and (Y^{3+}, Ag^{+} and Cd^{2+}) doped CeO_2 nanoparticles revealed information regarding the elements' oxidation states and chemical compositions. The core level Ce 3d XPS spectra for and (Y^{3+}, Ag^{+} and Cd^{2+}) doped CeO_2 nanoparticles samples revealed the existence of Ce-ions in both the Ce^{4+} and Ce^{3+} oxidation states. XPS analysis revealed the samples' composition of cations, as well as their enhanced oxygen vacancy content in comparison to total oxygen concentration. These factors have resulted in a large number of oxygen vacancies at the surface, indicating long-range ferromagnetic ordering. The O 1s XPS spectra indicate the lattice oxygen contribution, oxygen vacancies, surface hydroxyl groups, and other carbonate species, as well as fluctuations in the concentration of dopant ions

(Y^{3+}, Ag^{+} and Cd^{2+}) in the CeO_2 nanoparticles sample. The addition of (Y^{3+}, Ag^{+} and Cd^{2+}) ions, as well as the development of oxygen vacancies in doped CeO_2 nanoparticles affected the relative concentration ratio (Ce^{3+}/Ce^{4+}) for Ce^{3+} ions. The Ce^{3+} ion concentration increased significantly, as seen by the Ce 3d XPS spectra, and the oxygen vacancies increased as a result of the Ce_2O_3 phase formation in 4d cation-doped CeO_2 samples, which was not evident in the XRD patterns.

The undoped, Cd-doped CeO_2 nanoparticles samples were magnetically measured at room temperature as a function of the applied magnetic field in the -5 T to +5 T range using the VSM system. In contrast to the diamagnetic response of bulk CeO_2, the M–H curve at room temperature frequently exhibits weak ferromagnetic (FM) behavior. Here, the ferromagnetic ordering of the CeO_2 nano-lattice is improved by the incorporation of Cd-ions into the CeO_2 lattice and this behavior was explained on the basis of exchange interaction between oxygen vacancies and electron charge spin. The value of M_s and M_r were observed to be frequently raised by increasing doping until they reach a saturation threshold, after which further dopant ions may pair anti-ferromagnetically or decrease the creation of oxygen vacancies.

The photo-catalytic analysis of Y doped CeO_2 samples revealed that at higher doping levels, Y^{3+} aggregates at the CeO_2 surface, accompanied by oxygen vacancy and Ce^{3+} ions. This observation can be explained by the fact that lattice strain alters the surface energy and reactivity of photo-catalytic materials. Strained surfaces may have increased reactivity, resulting in more active sites for photo-catalytic processes. Furthermore, a crystal's strain can induce defects to form, such as oxygen vacancies, and these vacancies can function as active sites. Strain inside the crystal lattice can produce changes in the electronic band structure, resulting in band gap variations. A narrower band gap can improve photo-catalytic effectiveness by increasing visible light absorption.

The redox reaction of cerium oxide, along with the high surface area and conductivity of Ag, results in a high specific capacitance. This is why Ag-doped CeO_2 nanoparticles are employed as supercapacitor electrodes. When their electrochemical properties are investigated, Ag doped CeO_2 nanoparticles perform well as electrode materials, with a significant specific capacitance reported. When compared to other

doped nanoparticles, the CV results revealed that CAO5 (Ag = 5 %) nanoparticles had the highest specific capacitance. According to the results of this work, electrodes made of binary Ag-doped CeO_2 nanoparticles have a larger specific capacitance than that of undoped CeO_2. As a result, Ag-doped CeO_2 clearly has the potential to be a useful electrode material in the electronic field.

Previous discussions have highlighted the intriguing structural, optical, magnetic, electronic structure and electrochemical properties of 4d cations (Y^{3+}, Ag^{+} and Cd^{2+})-doped CeO_2 nanoparticles prepared via co-precipitation. The findings indicate that the prepared undoped and 4d cations (Y^{3+}, Ag^{+} and Cd^{2+}) -doped CeO_2 nanoparticles have potential applications in optoelectronics, spintronics, LEDs, and super capacitors as storage devices.

6.2 Scope for Future Work

Dilute magnetic semiconductors have a wide range of potential applications in the future, especially in spintronics, quantum computing, and magnetic memory technologies. To fully utilise DMS materials, it will be essential to overcome obstacles pertaining to Curie temperature, carrier mobility, and fabrication techniques as material science advances. DMS materials are essential for quantum technologies and next-generation electronics because of their magnetic qualities and semiconductor behaviour. The present study is all about the investigation of the various properties of undoped and doped CeO_2 based DMS nanoparticles with varying dopant concentrations to synthesize smaller particle sized nanoparticles. Furthermore, we have also carefully examined the structural, optical, electrical, magnetic, and electrochemical properties of the undoped and TM-doped CeO_2 samples using a variety of characterisation techniques. The study highlights the potential applications of transition metal-doped CeO_2, a highly promising field in materials research, particularly for environmental, energy storage, electronics, and catalysis. This thesis attempts to advance knowledge of TM-doped CeO_2-based DMS materials and their nanostructures. Nonetheless, the area can always be developed further. As a result, a dedicated future effort in this direction is required. We propose the following additional research work to be completed in future:

- **Determination of electronic structure property using XAS**: We can use XAS to analysis our samples in order to gather more detailed information about the electronic structure property. With bulk sensitivity, in-situ adaptability, and the capacity to quantify oxidation states, coordination environments, and vacant orbitals, XAS unlocks atom-specific structural, electronic, and catalytic dynamics, moving beyond the only surface-sensitive chemical state that XPS can detect. When it comes to multi-technique characterization, it is an effective approach. At Elletra Italy, ESRF, and other sites, we want to submit a beam time proposal for these measurements.
- **Probing the photo-catalytic activity:** There is great potential for solving environmental and energy issues with the incorporation of DMS materials in photo-catalytic applications. Realizing the full potential of DMS-based photo-catalysts in a variety of industries will depend heavily on ongoing research targeted at enhancing efficiency, stability, and scalability.
- **Investigating several synthesis techniques for TM-doped CeO_2 nanoparticles with variable structural and optical properties:** The optimal synthesis techniques for the materials' tuneable structural and optical characteristics can be developed with the help of an understanding of the mechanism and effects of defect development in TM-doped CeO_2 nanoparticles.
- **Looking for ways to combine different nano-materials, such as M-xene, RGO, and other carbon-based materials, to take use of their unique properties**: More research should be done on our current periodic table, which has many elements, to find unusual materials and learn the basics of physics.
- **Performing electrochemical properties:** Since TM-doped CeO_2 nanoparticles have been shown to perform well in super-capacitors. Therefore, we would like to examine these samples' dielectric properties, impedance, and batteries.

In conclusion, TM doping in CeO_2 nanoparticles modifies their electronic and structural characteristics, increasing their potential for a range of cutting-edge applications including gas sensing, catalysis, photo-catalysis, electronics, spintronics, energy, and biomedicine. Their tunable electronic and defect properties make them versatile materials suitable for next-generation technology. These materials' performance in energy storage, ecological remediation, and spin-based electronics is being improved by ongoing study.

Summary

Summary

Recently, researchers are interested in semiconducting materials (DMS) for their prospective uses in optoelectronics, magneto-electronics, and spintronics. DMS involves substituting a percentage of the host semiconductor's atoms with transition metals or non-metals that can add localized magnetic moments. DMS retains both semiconducting and magnetic characteristics, including paramagnetic, ferromagnetic, and anti-ferromagnetic, unlike typical semiconductors. To construct DMS compounds, transition metals or rare-earth elements has been employed as magnetic dopant in the host semiconductor. CeO_2 is an excellent DMS compound for spintronics applications due to its versatility and smaller band gap following nano-scale doping with rare earth metals. There are further industrial applications for it. CeO_2 has received attention as a promising material due to its high exciton binding energy, huge direct band gap, and defect-related optical and magnetic characteristics. Several different concentrations were employed to study the defects in undoped CeO_2.

4d cation-doped CeO_2 nanoparticles have superior physical, chemical, and catalytic characteristics compared to undoped CeO_2. Therefore, this study provides an overview of why this doping is important, particularly in scientific and industrial settings. CeO_2 is well-known for its capacity to store and release oxygen through the Ce^{4+}/Ce^{3+} redox reaction. When doped with 4d transition metal cations (e.g. Zr^{4+}, Mo^{6+}, Nb^{5+}, Ru^{4+}), it improves oxygen vacancy formation, oxygen ion mobility and faster redox cycling ($Ce^{4+} \rightarrow Ce^{3+}$). This increases its effectiveness in applications such as: three-way catalysts in automobile exhaust systems, solid oxide fuel cells (SOFCs) and chemical looping reactions. Doping with 4d cations can alter the band-gap and electronic structure of CeO_2. Doping improves charge carrier mobility, positions of the valence and conduction bands and photo-catalytic activity, particularly under visible light. Doping with 4d cation is particularly beneficial in Photo-catalysis (such as water splitting and pollutant degradation) and Solar energy harvesting. Transition metal doped CeO_2 systems, such as (Y^{3+}, Ag^{+} and Cd^{2+})-, have received a lot of attention for their usage in emission displays and super-capacitors.

The main purpose of this research is to determine how 4d transition elements alter the structure, optical, electronic structure and magnetic properties of CeO_2

nanoparticles X-ray diffraction was used to explore how doping impacts the structure of CeO_2. HRTEM was used to determine the surface morphology. UV-Vis-NIR and photoluminescence spectroscopy are used to identify defects. X-ray photoelectron spectroscopy was utilized to determine the valence state. Electrochemical properties were analyzed using electrochemical analyzer. It has been reported in the previous section that how doping of 4d cations in CeO_2 nanoparticles prepared via co-precipitation improves their structure, optical, and electronic structure properties. Based on the findings, it is possible to deduce that these nanoparticles have applications in spintronics, optoelectronic devices such as LEDs, photo-catalysis and energy storage devices such as super-capacitors. The six chapters of the thesis cover the following topics:

Chapter 1:

The first chapter provides an overview of spintronics and spintronics materials, focusing on their magnetic properties. This section provides a basic overview of DMS, which are widely used in spintronics devices. Several theoretical ideas and methods have been presented to explain the genesis of room temperature ferromagnetism in DMS materials. Nano-materials as metal oxide semiconductors can be synthesized using various methods, resulting in high-quality nanoparticles. The structure of CeO_2, its physical properties, and related defects have been described. In the last, this chapter concludes with a survey of literature on how doping affects the physical properties including structural, morphological, optical, electronic structure, magnetic, and electrochemical properties of undoped CeO_2 and doped CeO_2 nanoparticles.

Chapter 2:

The second chapter provides a brief explanation of the various synthesis method and characterisation techniques used in this study to examine the different characteristics of undoped and doped CeO_2 nanoparticles. The co-precipitation route of synthesis for the preparation of both undoped and doped CeO_2 nanoparticles has generated a lot of discussion. This chapter layout the detailed information of characterization techniques such as X-ray diffraction (XRD), Rietveld Refinement analysis, Energy Dispersive X-ray Spectroscopy (EDX), Ultraviolet-Visible-Near Infrared (UV-Vis-NIR) Spectroscopy, Surface-Enhanced Raman Spectroscopy

(SERS), X-ray Photoelectron Spectroscopy (XPS), Superconducting Quantum Interference Device-Vibrating Sample Magnetometer (SQUID-VSM), and electrochemical analyser. These techniques are just a few of the experimental methods used for characterisation of the samples used in this method.

Chapter 3:

In this chapter undoped and Y-doped CeO_2 [$Ce_{1-x}Y_xO_2$] (x = 0.00, 0.03, 0.05 and 0.07) nanoparticles prepared by the co-precipitation method are examined for their structural, morphological, optical, XPS, luminescence, and photo-catalytic characteristics. According to XRD and TEM studies, these single-phase nanoparticles have a better crystalline nature and a crystallite size between 18 and 9 nm. The inter-planer distance for the (111) plane varies considerably depending on the doping concentration, as shown by HRTEM images. The investigation of the UV-Vis-NIR spectroscopy has shown us that different concentrations of Y^{3+} ions in CeO_2 have caused differences in the magnitude of the refractive index and Eg values. The wide application of these materials with yellow luminescence is indicated by the obtained CCT for the doped samples analysed using PL spectra. According to the XPS analysis, the Y^{3+} ions have been incorporated into the lattice, the oxidation state has changed from Ce^{4+} to Ce^{3+} ions, and oxygen vacancy states have been formed by the generation of defects or an amorphous phase of Ce_2O_3.The photo-catalytic reduction rate constant of 7% Y doped CeO_2 is nearly 1.5 times higher than that of undoped CeO2, based on photo-catalytic results. The synergistic effect of photo-generated high electron hole pair concentration and OH● radicals generated in the catalytic reaction may be the cause of this increased photo-catalytic reduction of organic pollutants. Y-doped CeO_2 nanoparticles may remove organic contaminants from aqueous solutions and are a great catalyst when activated by UV-Vis light. Because of their structural flexibility, Y-doped nanoparticles are suitable for a wide range of applications due to their stability and catalytic activity.

Chapter 4:

In this chapter, undoped and Ag-doped CeO_2[$Ce_{1-x}Ag_xO_2$] (x = 0.00, 0.03, 0.05 and 0.07) nanoparticles are synthesised efficiently using the co-precipitation method; the resulting samples are phase-pure and have a cubic CeO_2-type crystal structure in space group Fm-3m; the Rietveld approach yields an average crystallite size estimate

of 9-13 nm. Both the undoped and Ag-doped samples exhibit significant light absorption in the near-ultraviolet region due to a substantial charge transfer from O^{2-} to Ce^{4+} ions, which may find use as a UV absorber. Ag-doped CeO_2 nanoparticles are suitable for usage in white light applications since their CIE diagram shows a white colour emission. The Ce^{3+}/Ce^{4+} ratio has been found to have grown in tandem with the doping concentration by the observed by XPS. However, as the doping concentration increased, the concentration ratio decreased. The ratio Ce^{3+}/Ce^{4+}, which represents the amount of oxygen vacancies, displayed a pattern that was comparable to electrochemical properties. Because doping with an excess concentration (more than 5%) lowers the number of oxygen and the performance of electrochemical characteristics, it follows that utilising the optimal concentration of Ag is crucial. The CAO5 sample has the highest specific capacitance of any sample, measuring 363.44 F/g. The maximum values of energy density and power density for the CAO5 sample are 125.08 Wh/kg and 652.48 W/kg, respectively, at a current density of 0.6 A/g. The CAO5 electrode's high-rate performance, low contact resistance, and superior electrical conductivity made it a particularly appealing option for practical uses. Furthermore, a very minor 6.09% decrease in the super-capacitance value is found for the CAO5 electrode with 2100 cycle cyclic durations. According to these findings, the CAO sample may find usage in electrochemical supercapacitor applications.

Chapter 5:

In this chapter Cd-doped CeO_2 nanoparticles [$Ce_{1-x}Cd_xO_2$] (x = 0.00, 0.03, 0.06 and 0.09) nanoparticles synthesised using the co-precipitation method reports that doping reduces particle size while increasing oxygen vacancies, which is useful for a variety of applications. XRD and TEM reveal the formation of nanoparticles ranging in size from 4 to 12 nm, as well as a cubic fcc structure. Cd-doped CeO_2 has a lower band-gap energy compared to undoped CeO_2 (from 3.39 to 2.96 eV), implying better absorption of visible light. The Ce 3d XPS spectra show a mixture of Ce^{4+} and Ce^{3+} oxidation states. The higher ratio of Ce^{3+} to Ce^{4+} in Cd-doped samples indicates that Cd doping stimulates the creation of oxygen vacancies, potentially improving the material's electronic structure. Cd 3p and 3d XPS typically show two notable peaks (Cd $3p_{3/2,}$ $3p_{1/2}$) and (Cd $3d_{5/2}$, Cd $3d_{3/2}$) indicating Cd^{2+} oxidation states. However, depending on the doping concentration, the addition of Cd ions either increases magnetic susceptibility or results in RTFM. Oxygen vacancies produced by Cd

doping is responsible for the enhanced magnetism; it causes localized magnetic moments, charge imbalances, and lattice distortions that encourage magnetic exchange interactions. Defect-induced magnetism is produced by mixed valence states (Ce^{3+}/Ce^{4+}). CeO_2 nanoparticles can be used in spintronics and magnetic semiconductor applications because Cd doping enhances their magnetic responsiveness.

Chapter 6:

To highlight the new findings on the structural, optical, electronic structure, magnetic, and electro-chemical properties of 4d cations-doped CeO_2 nanoparticles for their potential applications in various field, the sixth chapter provides a chapter-by-chapter summary of the entire work along with significant conclusions from the current thesis work. The chapter concludes with a discussion of potential avenues for future research and how they might affect the thesis work.

Bibliography

Bibliography

1. R. Yu, Q. Lin, S. F. Leung & Z. Fan; **Nano Energy,** 1(1), 57-72, **(2012)**.
2. R. Nagarajan; **Nanoparticles: Building Blocks for Nanotechnology**, **(2008)**.
3. V. J. Mohanraj & Y. J. T. J. O. P. R. Chen; **Tropical Journal of Pharmaceutical Research**, 5(1), 561-573, **(2006)**.
4. Y. Wu, Y. Cui, L. Huynh, C. J Barrelet, D. C Bell & C. M. Lieber; **Nano letters**, 4(3), 433-436, **(2004)**.
5. M. K Jain; **World Scientific, (1991)**.
6. T. Dietl; **Journal of Applied Physics**, 103(7), **(2008)**.
7. S. J. Pearton, W. H Heo, M. Ivill, D. P. Norton & T. Steiner; **Semiconductor Science and Technology**, 19(10), R59, **(2004)**.
8. M. T. Tegegne; **World Journal of Applied Physics**, 10(4), 1-10, **(2022)**.
9. A. A. Kaufman, R. O. Hansen & R. L. Kleinberg; **Methods in Geochemistry and Geophysics**, 42, 207-254, **(2008)**.
10. Q. Chen & H. Wang; **Journal of Alloys and Compounds**, 846, 156394, **(2020)**.
11. K. Sato, P. H. Dederichs & H. Katayama-Yoshida; **Hyperfine interactions**, 160, 57-65, **(2005)**.
12. R. S. Sukumar, M. M. Rao & A. G. Krishna; **Recent Advances in Material Sciences**, 627-635, **(2019)**.
13. X. Fu, P. Li, X. Chen, Y. Ma, R. Wang, W. Ji & Z. Zhang; **Journal of Zhejiang University-SCIENCE B**, 25(5), 361-388, **(2024)**.
14. L. S. Jairam, A. Chandrashekar, T. N. Prabhu, S. B. Kotha, M. S. Girish, I. M. Devraj & K. Prashantha; **Journal of Rare Earths**, 41(11), 1645-1661, **(2023)**.
15. S. P. Lochab, D. Kanjilal, N. Salah, S. S. Habib, J. Lochab, R. Ranjan & A. Pandey; **Journal of Applied Physics**, 104(3), **(2008)**.
16. J. Lee, J. P. Ahn & S. W. Kim; **Journal of Nano-Science and Nanotechnology**, 10(1), 130-134, **(2010)**.

17. S. Kumar, G. W. Kim, B. H. Koo, S. K. Sharma, M. Knobel, H. Chung & C. G. Lee. **Journal of Nano-Science and Nanotechnology**, 11(1), 555-559, **(2011)**.

18. P. Estevenon, L. Amidani, S. Bauters, C. Tamain, M. Bodensteiner, F. Meurer & K. O Kvashnina; **Chemistry of Materials**, 35(4), 1723-1734, **(2023)**.

19. N. Fifere, A. Airinei, M. Asandulesa, A. Rotaru, E. L. Ursu & F. Doroftei,. **International Journal of Molecular Sciences**, 23(22), 13883, **(2022)**.

20. S. A. Abdulsattar; **Medical Journal of Babylon**, 21(2), 235-239, **(2024)**.

21. Z. Wu, L. Guo, H. Li, Q. Yang, Q. Li & H. Zhu;. **Materials Science and Engineering: A**, 286(1), 179-182, **(2000)**.

22. T. Ungár & G. Tichy; **Physica Status Solidi (a)**, 171(2), 425-434, **(1999)**.

23. S. Mustapha, M. M. Ndamitso, A. S. Abdulkareem, J. O. Tijani, D. T. Shuaib, A. K. Mohammed & A. Sumaila; **Nanoscience and Nanotechnology**, 10(4), 045013 **(2019)**.

24. V. D. Mote, Y. Purushotham & B. N. Dole; **Journal of Theoretical and Applied Physics,** 6, 1-8, **(2012)**.

25. A. K. Zak, W. A. Majid, M. E. Abrishami & R. Yousefi; **Solid State Sciences**, 13(1), 251-256, **(2011)**.

26. M. Dave, S. Kumar, B. Dalela, P. A. Alvi, S. S.Sharma, D. M. Phase & S. Dalela; **Vacuum**, 180, 109537, **(2020)**.

27. E. Raudonyte-Svirbutaviciene, L. Mikoliunaite, A. Drabavicius, R. Juskenas, S. Sakirzanovas, T. Jüstel & A. Katelnikovas; **RSC Advances**, 6(108), 107065-107074, **(2016)**.

28. M. R. Ansari, & K. R. Peta; **Opportunities and Challenges,** (pp. 49-55), **(2022)**.

29. G. Jayakumar, A. A. Irudayaraj & A. D. Raj; **Mechanics, Materials Science & Engineering Journal**, 9(1), **(2017)**.

30. N. Xu, J. Ma, Q. Liu, W. Han & Z. Shan; **Tribology Letters**, 70, 1-10, **(2022)**.

31. S. Srivastava & N. K. Pandey; **Materials Proceedings**, 14(1), 26, **(2023)**.

32. R. Munirathnam, L. Seenappa, H. C. S. Manjunatha, Y. S. Vidya, K. N. Sridhar, S. Manjunath & N. Nagaiah; **Radiation Protection Dosimetry,** 199(20), 2513-2519, **(2023)**.

33. S. N. Matussin, F. Khan, M. H. Harunsani, Y. M. Kim & M. M. Khan; **Catalysts**, 13(1), 96, **(2023)**.

34. W. Lee, S. Y. Chen, Y. S. Chen, C. L. Dong, H. J. Lin, C. T. Chen & A. Gloter; **The Journal of Physical Chemistry C**, 118(45), 26359-26367, **(2014)**.

35. A. A. Atran, J. S. Algethami, H. H. Hegazy & M. S. Hamdy; **Optik**, 308, 171818, **(2024)**.

36. V. Prokopiuk, A. Onishchenko, S. Yefimova, P. Maksimchuk, V. Seminko, O. Nakonechna, & A. Tkachenko; **Nanomaterials: Applications & Properties,** (NAP) (pp. NRA07-1), **(2022)**.

37. Z. Li, L. Tong, Y. Ma & L. Zhao; **Ceramics International**, 50(11), 20431-20440, **(2024)**.

38. A. M. Ibrahim; **Applied Physics** A, 127(12), 947, **(2021)**.

39. R. N. Bharathi, & S. Sankar; **Superlattices and Microstructures**, 123, 37-51, **(2018).**

40. T. Guo, J. Du & J. Li; **Journal of Materials Science**, 51, 10917-10925 **(2016)**.

41. E. Swatsitang, S. Phokha, S. Hunpratub, & S. Maensiri; **Physica B: Condensed Matter**, *485*, 14-20, **(2016)**.

42. B. Xu, Q. Zhang, S. Yuan, M. Zhang & T. Ohno, **Applied Catalysis B: Environmental**, 183, 361-370, **(2016)**.

43. D. Van Dao, T. T. Nguyen, H. Y. Song, J. K. Yang, T. W. Kim, Y. T. Yu & I. H. Lee; **Materials & Design**, 159, 186-194, **(2018)**.

44. H. Tan, Y. Cai, G. Liang, P. Aprea & S. Hao; **Arabian Journal of Chemistry**, 17(1), 105496, **(2024)**.

45. A. L. Chibac-Scutaru, V. Podasca, I. A. Dascalu, & V. Melinte; **Nanomaterials**, 12(9), 1402, **(2022)**.

46. B. Choudhury, P. Chetri, & A. Choudhury; **RSC advances**, 4(9), 4663-4671, **(2014)**.

47. K. Kumari, R. N. Aljawfi, Y. S. Katharria, S. Dwivedi, K. H. Chae, R. Kumar & S. Kumar; **Journal of Electron Spectroscopy and Related Phenomena**, 235, 29-39, **(2019)**.

48. D. C. Amaral, M. Assis, L. S. R. Rocha, E. Longo, C. M. Aldao, P. M. Desimone & F. Moura; **Ceramics International**, 50(9), 16532-16539, **(2024)**.

49. R. Suresh, V. Ponnuswamy, & R. Mariappan; **Applied Surface Science,** 273, 457-464, **(2013)**.

50. S. Soni, N. Chouhan, R. K. Meena, S. Kumar, B. Dalela, M. Mishra & S. Dalela; **Global Challenges**, 3(5), 1800090, **(2019)**.

51. C. Sun, P. Beaunier, V. La Parola, L. F. Liotta & P. Da Costa;, **ACS Applied Nano Material** 3(12), 12355-12368, **(2020)**.

52. W. Zhang, X. Wang, J. Wu, X. Wang, X. Lv, G. Liu & Z. Zhang; **Applied Surface Science**, 602, 154303, **(2022)**.

53. M. Mittal, A. Gupta & O. P. Pandey; **Solar Energy**, 165, 206-216, **(2018)**.

54. E. Varga, P. Pusztai, A. Oszkó, K. Baán, A. Erdőhelyi, Z. Kónya & J. Kiss; **Langmuir**, 32(11), 2761-2770, **(2016).**

55. J. M. D. Coey; **Current Opinion in Solid State and Materials Science**, 10(2), 83-92, **(2006)**.

56. S. Chahal, L. Phor, A. Kumar, S. Duhan & P. Kumar; **In Defect-Induced Magnetism in Oxide Semiconductors,** (pp. 529-546), **(2023)**.

57. S. Phokha, E. Swatsitang, S. & Maensiri; **Electronic Materials Letters**, 11, 1012-1020, **(2015).**

58. P. Jantachum, S. Utara, S. Hunpratub, N. Chanlek, P. Kidkhunthod & S Phokha; **Radiation Physics and Chemistry**, 208, 110920, **(2023)**.

59. M. Coey, K. Ackland, M. Venkatesan & S. Sen; **Nature Physics**, 12(7), 694-699, **(2016)**.

60. M. A. Majidi, A. Bupu, & A. D. Fauzi; **Physica B: Condensed Matter**, 526, 172-176, **(2017)**.

61. N. S. Leel, M. Kiran, M. K. Kumawat, P. A. Alvi, V. S. Vats, D. Patidar & S. Dalela; **Journal of Luminescence**, 263, 119981, **(2023).**

62. C. Song, F. Zeng, K. W. Geng, X. J. Liu, F. Pan, B. He & W. S. Yan; **Physical Review B—Condensed Matter and Materials Physics,** 76(4), 045215, **(2007).**

63. P. Kaur, S Chalotra, H. Kaur, A. Kandasami & D. P. Singh; **Applied Surface Science Advances**, *5*, 100100, **(2021)**.

64. K. Cho; Journal of Physics: **Condensed Matter,** 20(17), 175202, **(2008)**.

65. A. G. Kolhatkar, A. C. Jamison, D. Litvinov, R. C. Willson & T. R. Lee; **International Journal of Molecular Sciences,** 14(8), 15977-16009, **(2013).**

66. S. Y. Chen, C. H. Tsai, M. Z. Huang, D. C.Yan, T. W. Huang, A. Gloter, & C. L. Dong; **The Journal of Physical Chemistry C**, 116(15), 8707-8713, **(2012)**.

67. W. Huang, R. Lin, W. Chen, Y. Wang & Zhang; **Journal of Semiconductors**, 42(7), 072501, **(2021).**

68. P. Rajkumar, S. Selvaraj, & S. M. GP; **Physical Chemistry Research**, 12(2), 407-417, **(2024)**.

69. A. A. Ansari, J. P. Labis, M. Alam, S. M. Ramay, N. Ahmed & A. Mahmood; **Analytical Letters**, 50(8), 1360-1371, **(2017)**.

70. A. Bumajdad, & M. Madkour; **Physical Chemistry Chemical Physics**, 16(16), 7146-7158, **(2014)**.

71. K. Negi, A. Umar, M. S. Chauhan & M. S. Akhtar; **Ceramics International,** 45**(**16), 20509-20517, (**2019)**.

72. A. Akbari-Fakhrabadi, R. Saravanan, M. Jamshidijam, R. V. Mangalaraja & M. A.Gracia; **Journal of Saudi Chemical Society**, 19(5), 505-510, **(2015)**.

73. S. Gnanam & V. Rajendran; **Journal of Alloys and Compounds**, 735, 1854-1862, **(2018)**.

74. M. V. Arularasu, T. V. Rajendran, B. Arkook, M. Harb & K. Kaviyarasu; **Microscopy Research and Technique**, 88(3), 621-630, **(2025)**.

75. M. Vanitha, P. Cao & N. Balasubramanian; **Journal of Alloys and Compounds**, 644, 534-544, **(2015)**.

76. P. Daubinger, J. Kieninger, T. Unmüssig & G. A. Urban, **Physical Chemistry Chemical Physics**, 16(18), 8392-8399, **(2014)**.

77. G. Murugadoss, J. Ma, X. Ning & M. R. Kumar**, Inorganic Chemistry Communications**, 109, 107577, **(2019).**

78. M. Sun, Z. Li, H. Li, Z. Wu, W. Shen & Y. Q. Fu, **Electrochimica Acta**, 331, 135366, **(2020)**.

79. P. J. Gracie, & D. Geetha; **Physica Scripta**, 99(10), 105954, **(2024)**.

80. Y. C. Zhou, & M. N. Rahaman; **Journal of Materials Research**, 8(7), 1680-1686, **(1993)**.

81. M. Alifanti, B. Baps, N. Blangenois, J. Naud, P. Grange & B. Delmon; **Chemistry of Materials**, 15(2), 395-403, **(2003)**.

82. C. Y. Jimmy, L. Zhang & J. Lin**; Journal of Colloid and Interface Science**, 260(1), 240-243 **(2003)**.

83. S. Ekambaram & K. C. Patil; **Journal of Materials Chemistry**, 5(6), 905-908, **(1995)**.

84. N. Uekawa, M. Ueta, Y. J. Wu & K. Kakegawa; **Chemistry Letters**, 31(8), 854-855, **(2002)**.

85. J. S. Lee, J. S. Lee & S. C. Choi, **Materials Letters**, 59(2-3), 395-398, **(2005)**.

86. A. Ali, Y. W. Chiang & R. M. Santos, **Minerals**, 12(2), 205, **(2022)**.

87. S. Fatimah, R. Ragadhita, D. F. Al Husaeni & A. B Nandiyanto; **Journal of Science and Engineering**, 2(1), 65-76, **(2022)**.

88. G. H. Al-Hazmi, M. G. El-Desouky & A. A. El-Bindary. Synthesis; **Bulletin of the Chemical Society of Ethiopia**, 36(4), 815-829 **(2022)**.

89. J. Malleshappa, H. Nagabhushana, B. D. Prasad, S. C. Sharma, Y. S. Vidya & K. S. Anantharaju, **Optik**, 127(2), 855-861, **(2016)**.

90. T. Ohkubo, H. Sepehri-Amin, T. T. Sasaki & K. Hono; **Microscopy**, 63(suppl_1), i6-i7, **(2014)**.

91. S. N. N. M. Makhtar, N. K. Abd Hamed & M. A. H. bin Hamdan; **Advanced Ceramics for Photo-catalytic Membranes** (pp. 221-238), **(2024).**

92. R. Raghavan & J. C. Joseph, **Cosmic rays**, 1020(10), 12, (**2013)**.

93. P. M. Lewis, D. Hebbar, K. S. Choudhari, & S. D. Kulkarni; **Materials Science in Semiconductor Processing**, 138, 106284, **(2022)**.

94. D. A. Hakeem, J. W. Pi, S. W. Kim & K. Park; **Inorganic Chemistry Frontiers**, 5(6), 1336-1345, **(2018)**.

95. J. Güémez, & M. Fiolhais; **American Journal of Physics,** 86(11), 825-830, **(2018)**.

96. F. K. M. Alosfur, N. J. Ridha, M. H. H. Jumali, & S. Radiman; **Nanotechnology**, 29(14), 145707, **(2018)**.

97. W. Burgei, M. J. Pechan, & H. Jaeger; **American Journal of Physics**, 71(8), 825-828, **(2003)**.

98. S. E. George, M. George, J. Alex, L.K. Joy, A. Aravind, D. Sajan, A. Thakur, S. Hussain, and G. Vinitha; **Ceramics International**, 46(9), 13932-13940, **(2020)**.

99. S. Kumar, F. Ahmed, N. Ahmad, N. M. Shaalan, R. Kumar, A. Alshoaibi, & K. Kumari; **Materials,** 15(12), 4119, **(2022)**.

100. B. K. Saikia, S. M. Benoy, M. Bora, J. Tamuly, M. Pandey, & D. Bhattacharya; **Fuel**, 282, 118796, **(2020)**.

101. S. Sonsupap, N. Chanlek, P. Kidkhunthod, T. Sinprachim, & S. Maensiri; **Journal of Electronic Materials**, 51(6), 2933-2948, **(2022)**.

102. M. Grossi, & B. Riccò; **Journal of sensors and sensor systems,** 6(2), 303-325, **(2017)**.

103. J. Huang, Z. Li, B. Y. Liaw & J. Zhang; **Journal of Power Sources**, 309, 82-98, **(2016)**.

104. A. Othman, A. Gowda, D. Andreescu, M. H. Hassan, S. V. Babu, J. Seo & S. Andreescu; **Materials Horizons**, 11(14), 3213-3266, **(2024)**.

105. S. Y. Ahn, W. J. Jang, J. O. Shim, B. H. Jeon & H. S. Roh; **Catalysis Reviews**, 66(4), 1316-1399, **(2024)**.

106. M. Kim, G. Park, K. Jo & H. Lee; **Materials Today Chemistry**, 29, 101440, **(2023)**.

107. H. Teng, L. Qi, G. Jian, Y. Li, Q. Yang & H. Lin; **Ceramics International, (2025)**.

108. O. Bezkrovnyi, M. Szymczak, L. Marciniak, V. Seminko, P. Kraszkiewicz, M. Małecka & I. Matolinova; **The Journal of Physical Chemistry C,** 129(3), 1724-1732, **(2025)**.

109. B. Liu, Z. Yan, T. Xu, C. Li, R. Gao, H. Hao & J. Bai; **Chemical Engineering Journal**, 442, 136226, **(2022)**.

110. K. Dubey, S. Dubey, V. Sahu, A. Modi, J. Bamne, F. Z. Haque & N. K. Gaur;. **Materials Science and Engineering: B**, 288, 116154, **(2023)**.

111. P. K. Sharma & O. P. Pandey; **Solid State Sciences**, 126, 106846, **(2022)**.

112. P. K. Sharma & O. P. Pandey; **Journal of Materials Science: Materials in Electronics**, 33(14), 11281-11307, **(2022)**.

113. Z. P. Li, T. Mori, F. Ye, D. R. Ou, J. Zou & J. Drennan; **Microscopy and Microanalysis**, 17(1), 49-53, **(2011)**.

114. S. Patil, S. Seal, Y. Guo, A. Schulte & J. Norwood; **Applied Physics Letters**, 88(24), 243110, **(2006)**.

115. H. A. Aleksandrov, I. Z. Koleva, K. M. Neyman, T. T. Tabakova & G. N. Vayssilov, **RSC advances**, 8(59), 33728-33741, **(2018)**.

116. I. Atribak, A. Bueno-López & A. García-García; **Journal of Molecular Catalysis A: Chemical**, 300(1-2), 103-110, **(2009)**.

117. S. Yusheng, L. Lei, Z. Yingying, L. I. N. Xingyi, Q. Zheng & W. E. I. Kemei; **Journal of Rare Earths,** 27(3), 411-417, **(2009).**

118. M. Nolan; **The Journal of Physical Chemistry C**, 115(14), 6671-6681, **(2011)**.

119. S. N. Matussin, F. Khan, M. H. Harunsani, Y. M. Kim & M. M. Khan; **ACS omega**, 8(13) 11868-11879, **(2023)**.

120. A. D. Liyanage, S. D. Perera, K. Tan, Y. Chabal and K. J. Balkus; **Jr. ACS Catalysis**, 4(2) 577-584, **(2014)**.

121. S. Soni, S. Kumar, B. Dalela, S. Kumar, P. A. Alvi & S. Dalela; **Journal of Alloys and Compounds**, 752, 520-531, **(2018)**.

122. P. Kumar, P. Kumar, A. Kumar, I. Sulania, F. Chand & K. Asokan, **RSC advances**, 7(15), 9160-9168, **(2017)**.

123. A. Monshi, M. R. Foroughi & M. R. Monshi; **World Journal of Nano Science and Engineering**, 2(3), 154-160, **(2012)**.

124. D. Ma, Z. Lu, Y. Tang, T. Li, Z. Tang & Z. Yang; **Physics Letters A**, 378(34), 2570-2575, **(2014)**.

125. M. Nolan, V. S. Verdugo & H. Metiu; **Surface Science**, 602(16), 2734-2742, **(2008)**.

126. B. Xu, Q. Zhang, S. Yuan, M. Zhang, & T. Ohno; **Applied Catalysis B: Environmental**, 164, 120-127, **(2015)**.

127. L. Truffault, M. T. Ta, T. Devers, K. Konstantinov, V. Harel, C. Simmonard & J. P. Blondeau; **Materials Research Bulletin**, 45(5), 527-535, **(2010)**.

128. A. A. Ansari, J. Labis, M. Alam, S. M. Ramay, N. Ahmad & A. Mahmood; **Journal of the Chinese Chemical Society**, 62(10), 925-932, **(2015)**.

129. S. B. Dangi, N.S. Leel, A. M. Quraishi, S. Z. Hashmi, S. Kumar, S. Dalela, & P. A. Alvi, **Optical Materials**, 148,114965, **(2024)**.

130. N. S. Leel, S. Kumar, P. A. Alvi, B. Dalela, A. Sharma, S. Kumar, &S. Dalela; **Journal of Magnetism and Magnetic Materials**, 603,172233, **(2024)**.

131. A. K. Zak, W. A. Majid, M. E. Abrishami & R. Yousefi; **Solid State Sciences,** 13(1), 251-256 **(2011)**.

132. M. A. Tagliente & M. Massaro; **Nuclear Instruments and Methods in Physics Research Section B: Beam Interactions with Materials and Atoms,** 266(7), 1055-1061, **(2008)**.

133. F. Abbas, T. Jan, J. Iqbal, I. Ahmad, M. S. H. Naqvi & M. Malik, **Applied Surface Science,** 357, 931-936, **(2015)**.

134. P. Patsalas, S. Logothetidis, L. Sygellou, S. Kennou; **Phys. Rev. B** 68,035104, **(2003)**.

135. A. H. Morshed, M. E. Moussa, S. M. Bedair, R. Leonard, S. X. Liu & N. El-Masry; **Applied Physics Letters,** 70(13), 1647-1649, **(1997)**.

136. B. Choudhury & A. Choudhury, "**Current Applied Physics,** 13(1), 217-223, **(2013)**.

137. I. Hamberg, C. G. Granqvist, K. F. Berggren, B. E. Sernelius & L. Engström, **Physical Review B**, 30(6), 3240, **(1984)**.

138. J. Arya, N. S. Leel, A. Singh, A. M. Quraishi, S. Z. Hashmi, S. Kumar, &P. A. Alvi; **Physica Status Solidi (a)**, *221*(4), 2300742**, (2024)**.

139. P. Pandey, R. Kurchania & F. Z. Haque; **Optik,** 126(21), 3310-3315, **(2015)**.

140. M. Kahouli, A. Barhoumi, A. Bouzid, A. Al-Hajry& S. Guermazi; **Superlattices and Microstructures**, 85, 7-23, **(2015)**.

141. P. Nagaraju, Y. V. Kumar, M. R. Reddy, C. V. Reddy, V. R. Reddy, D. M. Phase & I. I. UGC-DAE-CSR, **Int. J. Sci. Eng. Res,** 5(3), 185-190, **(2014)**.

142. E. Zhang, C. J. Brabec & M. Kato; **Journal of Physics D: Applied Physics**, 57(30), 305104, **(2024)**.

143. F. Meng, L. Wang & J. Cui; **Journal of Alloys and Compounds**, 556, 102-108, **(2013)**.

144. S. Gnanam, & V. Rajendran, **Journal of Sol-Gel Science and Technology**, 58, 62-69, **(2011)**.

145. G. Wang, Q. Mu, T. Chen, & Y. Wang; **Journal of Alloys and Compounds**, 493(1-2), 202-207, **(2010)**.

146. W. M. Kwok, A. B. Djurišić, Y. H. Leung, W. K. Chan & D. L. Phillips; **Applied Physics Letters**, 87(22), 223111, **(2005)**.

147. K. Kumari, R. N. Aljawfi, A. K. Chawla, R. Kumar, P. A. Alvi, A. Alshoaibi& S. Kumar; **Ceramics International**, 46(6), 7482-7488, **(2020)**.

148. M. Kiran, N. S. Leel, B. Dalela, M. A. Khan, A. Bhargava, D. Lovevanshi, & S. Dalela;. **Journal of Electronic Materials**, 1-13, 0361-5235, **(2024)**.

149. K. M. Sandeep, S. Bhat & S. M. Dharmaprakash; **Journal of Physics and Chemistry of Solids**, 104, 36-44, **(2017)**.

150. A. K. Vishwakarma, K. Jha, M. Jayasimhadr, A. S. Rao, K. Jang, B. Sivaiah & D. Haranath; **Journal of Alloys and Compounds**, 622, 97-101, **(2015)**.

151. J. Sahu, S. Kumar, V. S. Vats, P. A. Alvi, B. Dalela, S. Kumar & S. Dalela; **Journal of Luminescence**, 243, 118673, **(2022)**.

152. J. S. B. Valencia, F. E. L. Giraldo & J. F. V. Bonilla; **Symposium of Signals, Images and Artificial Vision-2013: STSIVA-**(pp. 1-6), **(2013)**.

153. X. Ma, P. Lu & P. Wu; **Journal of Alloys and Compounds**, 734, 22-28, **(2018)**.

154. D. R. Mullins, S. H. Overbury & D. R. Huntley; **Surface Science**, 409(2), 307-319, **(1998)**.

155. A. K. Sinha & K. Suzuki; **The Journal of Physical Chemistry B**, 109(5), 1708-1714, **(2005)**.

156. P. Luches, F. Pagliuca, S. Valeri & F. Boscherini; **The Journal of Physical Chemistry C,** 117(2), 1030-1036**, (2013).**

157. F. Pagliuca, P. Luches & S. Valeri; **Surface Science**, 607, 164-169, **(2013)**.

158. N. S. Leel, M. Kiran, P. A. Alvi, B. Dalela, S. Kumar, & S. Dalela; **Ceramics International**, , 0272-8842, **(2023)**.

159. M. Khan, S. A. Ansari, D. Pradhan, D. H. Han, J. Lee & M. H. Cho, **Industrial & Engineering Chemistry Research**, 53(23), 9754-9763, **(2014)**.

160. N. Fifere, A. Airinei, M. Dobromir, L. Sacarescu & S. I. Dunca; **Nanomaterials**, 11(10), 2596, **(2021)**.

161. L. Wang & F. Meng; **Materials Research Bulletin**, 48(9), 3492-3498, **(2013)**.

162. P. Venkataswamy, K. N. Rao, D. Jampaiah & B. M. Reddy; **Applied Catalysis B: Environmental**, 162, 122-132 **(2015)**.

163. J. Zhang, H. Wong, D. Yu, K. Kakushima & H. Iwai; **AIP Advances**, 4(11), 117117, **(2014)**.

164. W. Kallel, S. Bouattour, L. V. Ferreira & A. B. do Rego; **Materials Chemistry and Physics**, 114(1), 304-308, **(2009)**.

165. K. J. Archana, A. C. Preetha & K. Balasubramanian; **Optical Materials,** 127 112245, **(2022)**.

166. S. Liang, X. Liu, Z. Zhong, B. Han, X. Zhong, W. Chen, K. Song, H. Deng & Z. Lin; **Nano Research**, 14, 2558-2567, **(2021)**.

167. A. Bothe & A. Balducci; **Journal of Power Sources**, 548, 232090, **(2022)**.

168. M. G. Ashritha & K. Hareesh; **In Smart Supercapacitors,** (pp. 179-198), **(2023).**

169. M. E Şahin, F. Blaabjerg & A. Sangwongwanich; **Energies**, 15(3), 674, **(2022)**.

170. S. Arunachalam, B. Kirubasankar, D. Pan, H. Liu, C. Yan, Z. Guo & S. Angaiah; **Green Energy & Environment**, 5(3), 259-273, **(2020)**.

171. J. Zimou, M. Oubakalla, N. Ait Labyad, Z. Barbouch, E. Laghchim, K. Fareh & M. Addou, **Journal of Energy Storage**, 109, 115162, **(2025)**.

172. R. Munirathnam, R. F. SM, S. Manjunatha, H. C. Manjunatha, Y. S. Vidya, K. N. Sridhar & S. Krishnaveni; **Journal of Science: Advanced Materials and Devices**, 8(2), 100551, **(2023)**.

173. Y. Xu, L. Gao, Q. Hou, P. Wu, Y. Zhou & Z. Ding; **Molecules**, 28(16), 6005, **(2023)**.

174. A. J. Khan, M. Hanif, M. S. Javed, S. Hussain, W. Zhong, M. Saleem, & Z. Liu; **Journal of Electroanalytical Chemistry**, 865, 114158, **(2020)**.

175. R. B. Wexler, E. B. Stechel & E. A. Carter; **Solar Fuels**, 1-63, **(2023)**.

176. H. Xie, L. Mao & J. Mao; **Chemical Engineering Journal**, 421, 127826, **(2021)**.

177. N. Ahmad, A. Umar, R. Kumar, & M. Alam; **Ceramics International,** 42(10), 11562-11567, **(2016)**.

178. K. Salimi; **Colloids and Surfaces A: Physicochemical and Engineering Aspects**, 599, 124908, **(2020)**.

179. Y. Jing, P. Lund, M. I. Asghar, F. Li, B. Zhu, B. Wang & L. Fan; **Ceramics International,** 46(18), 29290-29296, **(2020)**.

180. A. A. Ansari, & M. Alam; **Journal of Materials Science: Materials in Electronics**, 32(10), 13897-13905, **(2021)**.

181. A. A. Ansari, & M. Alam; **Journal of Materials Science: Materials in Electronics**, 32(18), 23266-23274, **(2021)**.

182. R. Ma, S. Zhang, T. Wen, P. Gu, L. Li, G. Zhao & X. Wang; **Catalysis Today,** 335, 20-30, **(2019)**.

183. A. Haghighatzadeh; **Optics & Laser Technology**, 126, 106114, **(2020)**.

184. N. L. Yong, A. Ahmad & A. W. Mohammad; **Int. J. Sci. Eng. Res**, 4(4), **(2013)**.

185. S. Shi, M. Hossu, R. Hall, & W. Chen; **Journal of Materials Chemistry**, 22(44), 23461-23467, (**2012)**.

186. T. Ates; **Journal of the Australian Ceramic Society**, 57(2), 615-623, **(2021)**.

187. S. B. Dangi, N. S. Leel, A. M. Quraishi, S. Z. Hashmi, S. Kumar, S. Dalela & P. A. Alvi; **Optical Materials**, 148, 114965, **(2024)**.

188. K. Rajesh, P. Sakthivel, A. Santhanam, & J. Venugobal; **Optik,** 216,164800, **(2020)**.

189. V. Dhayal, N. S. Leel, P. M. Z. Hasan, R. Darwesh, A. M. Quraishi, S. Z. Hashmi & P. A. Alvi; **Shysica Status Solidi (a)**, 2300894, **(2024)**.

190. R. N. Bharathi, & S. Sankar; **Journal of Materials Science: Materials in Electronics**, 29, 6679-6691, **(2018)**.

191. S. Tiwari, G. Rathore, N. Patra, A. K. Yadav, D. Bhattacharya, S. N. Jha, & S. Sen; **Journal of Alloys and Compounds**, 782, 689-698, **(2019)**.

192. M. Zhang, Y. Chen & G. He; **The Scientific World Journal,** (1), 897960, **(2014)**.

193. Y. Seo, M. W. Lee, H. J. Kim, J. W. Choung, C. Jung, C. H. Kim & K. Y. Lee; **Journal of Hazardous Materials**, 415, 125373, **(2021)**.

194. H. R. Khakhal, S. Kumar, D. Patidar, S. Kumar, V. S. Vats, B. Dalela, N. S. Leel & S. Dalela; **Materials Science and Engineering: B**, 297, 116675, **(2023)**.

195. S. M. Chaudhari, O. S. Gonsalves & P. R. Nemade; **Materials Research Bulletin,** 143, 111463, **(2021)**.

196. J. Sahu, S. Kumar, F. Ahmed, P. A. Alvi, B. Dalela, D. M. Phase & S. Dalela," **Journal of Energy Storage,** 59, 106499, **(2023)**.

197. N. Maheswari & G. Muralidharan; **New Journal of Chemistry**, 41(19), 10841-10850, **(2017)**.

198. R. Murugan, G. Ravi, G. Vijayaprasath, S. Rajendran, M. Thaiyan, M. Nallappan & Y. Hayakawa; **Physical Chemistry Chemical Physics**, 19(6), 4396-4404, **(2017)**.

199. M. Fedel, A. Ahniyaz, L. G. Ecco & F. Deflorian; **Electrochimica Acta**, 131, 71-78, **(2014)**.

200. J. Jayachandiran, J. Yesuraj, M. Arivanandhan, A. Raja, S. A. Suthanthiraraj, R. Jayavel & D. J. J. O. I. Nedumaran; **Journal of Inorganic and Organometallic Polymers and Materials**, 28, 2046-2055, **(2018)**.

201. M. Kumar, J. H. Yun, V. Bhatt, B. Singh, J. Kim, J. S. Kim, & C. Y. Lee; **Electrochimica Acta**, 284, 709-720, **(2018)**.

202. S. Phokha, S. Hunpratub, N. Chanlek, S. Sonsupap & S. Maensiri; **Journal of Alloys and Compounds**, 750, 788-797, **(2018)**.

203. A. Kumar, M. Kumar, P. C. Sati, M. K. Srivastava, S. Ghosh & S. Kumar; **Current Applied Physics**, 32, 24-35, **(2021)**.

204. A. Fert & F. N. Dau; **Comptes Rendus Physique**, 20, 817-831, **(2019)**.

205. K. Yakushiji, S. Mitani, F. Ernult, K. Takanashi & H. Fujimori; **Physics Reports,** 451 1-35, **(2007)**.

206. S. Waseem, T. Zeeshan, H. Tariq, F. Majid, M. D. Ali, Z. N. Kayani & M. Amami; **Applied Physics A**, 128(8), 690, **(2022)**.

207. T. Dutta, A. A. Khan, N. Baildya, P. Mondal & N. N. Ghosh; **In Biodegradable and Environmental Applications of Bio-nanocomposites** (pp. 169-187), **(2022)**.

208. A. Kubiak, S. Żółtowska, A. Bartkowiak, E. Gabała, N. Sacharczuk, M. Zalas, & T. Jesionowski; **Materials**, 14(20), 6063, **(2021)**.

209. M. Mylarappa, S. Chandruvasan, K. S. Harisha, S. Kantharaju, S. P. Kumar & K. S. Kumara; **Journal of the Taiwan Institute of Chemical Engineers**,152, 105174, **(2023)**.

210. S. Pansambal, R. Oza, S. Borgave, A. Chauhan, P. Bardapurkar, S. Vyas & S**.** Ghotekar; **Applied Nanoscience**, 13(9), 6067-6092, **(2023).**

211. V. Mihalache, M. Secu & J.C. Grivel; **Materials Chemistry and Physics**, 209, 121-133, **(2018)**.

212. S. B. Putla, M. Kamali, B. Swapna, B. M. Reddy & P. Sudarsanam; **ACS Applied Nano Materials**, 7(7), 6749-6771, **(2024)**.

213. S. Phoka, P. Laokul, E. Swatsitang, V. Promarak, S. Seraphin & S. Maensiri; **Materials Chemistry and Physics**, 115(1), 423-428, **(2009)**.

214. T. Herrling, M. Seifert & K. Jung; **SOFW J.** 139, 10-14, **(2013)**.

215. N. Ai & K. Chen; **Solid State Ionics**, 233, 87-94, **(2013).**

216. P. Li, B. Wang, C. Qin, C. Han, L. Sun & Y. Wang; **Ceramics International**, 46(11), 19232-19240, **(2020)**.

217. K. Sun, G. Zhan, H. Chen & S. Lin; **Sensors**, 21, 8269, **(2021)**.

218. R. Magudieshwaran, J. Ishii, K. C. N. Raja, C. Terashima, R. Venkatachalam, A. Fujishima, & S. Pitchaimuthu; **Materials Letters**, 239, 40-44, **(2019).**

219. K. Zamani, N. Allah-Bakhshi, F. Akhavan, M. Yousefi, R. Golmoradi, M. Ramezani, H. Bach, S. Razavi, G.-R. Irajian, M. Gerami, A. Pakdin-Parizi, M. Tafrihi & F. Ramezani; **BMC Biotechnology**, 21, 68, **(2021)**.

220. H. E. Ahmed, Y. Iqbal, M. H. Aziz, M. Atif, Z. Batool, A. Hanif, N. Yaqub, W. A. Farooq, S. Ahmad, A. Fatehmulla & H. Ahmad; **Molecules**, 26, 4659, **(2021)**.

221. J. Liu, C. Zhu, D. Zhu, X. Jia, Y. Zhang, J. Yu, M. Yang, **Nanomaterials**, 11, 2231, **(2021)**.

222. H. I. Chen, & H. Y. Chang, **Ceramics International**, 31(6), 795-802, **(2005)**.

223. S. V. P. Kumar, L. Suresh, T. Vinodkumar, B. M. Reddy & G. V. P. Chandramouli, **ACS Sustainable Chemistry & Engineering**, 4(4), 2376-2386, **(2016)**.

224. J. Saranya, K. S. Ranjith, P. Saravanan, D. Mangalaraj & R. T. R. Kumar, **Materials Science in Semiconductor Processing**, 26, 218-224, **(2014)**.

225. T. Shittu & M. Altarawneh, **Nanotechnology Reviews**, 11(1), 191-203, **(2021)**.

226. S. K. Alla, K. K. Devarakonda, E. V. P. Komarala, R. K. Mandal, & N. K. Prasad, **Materials & Design**, 114, 584-590, **(2017)**.

227. S. Yuan-Qiang, Z. Huai-Wu, W. Qi-Ye, Z. Hao & J. Q. Xiao, **Chinese Physics Letters,** 25(3), 1106, **(2008)**.

228. V. Fernandes, I. L. Graff, J. Varalda, L. Amaral, P. Fichtner, D. Demaille, Y. Zheng, W.H. Schreiner & D.H. Mosca; **Journal of The Electrochemical Society**, 159, 27-33, **(2011)**.

229. J. M. D. Coey, K. Wongsaprom, J. Alaria & M. Venkatesan; **Journal of Physics D: Applied Physics**, 41, 134012, **(2008)**.

230. S. Soni, V. S. V. Sudhish Kumar, H.R. Khakhal, B. Dalela, S.N. Dolia, P.A.A. Shalendra Kumar & S. Dalela; **Journal of Electron Spectroscopy and Related Phenomena**, 254, 147140, **(2022)**.

231. M. Li, R. Zhang, H. Zhang, W. Feng, & X. Liu; **Micro & Nano Letters**, 5(2), 95-99, **(2010)**.

232. D. Channei, B. Inceesungvorn, N. Wetchakun, S. Ukritnukun, A. Nattestad, J. Chen & S. J. S. R. Phanichphant; **Scientific Reports**, 4(1), 5757, **(2014)**.

233. K. S. Ranjith, P. Saravanan, S. H. Chen, C. L. Dong, C. L. Chen, S. Y. Chen, & R. T. Rajendra Kumar; **The Journal of Physical Chemistry C**, 118(46), 27039-27047, **(2014)**.

234. C. S. Riccardi, R. C. Lima, M. L. Dos Santos, P. R. Bueno, J. A. Varela & E. Longo; **Solid State Ionics**, 180(2-3), 288-291, **(2009)**.

235. O. Andersen, Environmental health perspectives, 54, 249-266, **(1984)**.

236. T. S. Wu, Y. W. Chen, S. C. Weng, C. N. Lin, C. H. Lai, Y. J. Huang & Y. L. Soo; **Scientific Reports**, 7(1), 4715, **(2017)**.

237. C. Li, T. Bai, T. Li, F. Li, W. Dong, Z. Shi & S. Feng; **European Journal of Inorganic Chemistry**" 1204-1209, **(2012)**.

238. A. E. Yacoubi, A. Massit, S. E. Moutaoikel, A. Rezzouk & B. C. E. Idrissi; **Am. J. Mater. Sci. Eng**, 5, 1-5, **(2017)**.

239. H. Borchert, E. V.Shevchenko, A. Robert, I. Mekis, A. Kornowski, G. Grübel & H. Weller; **Langmuir**, 21(5), 1931-1936, **(2005)**.

240. M. Kiran, N. S. Leel, M. K. Kumawat, B. Dalela, P. A. Alvi, S. Kumar & S. Dalela; **Journal of Physics and Chemistry of Solids,** 197, 112438, **(2025)**.

241. M. Kiran, N. S. Leel, B. Dalela, M. A. Khan, A. Bhargava, D. Lovevanshi, & S. Dalela; **Journal of Electronic Materials**, 53(9), 4969-4981, **(2024)**.

242. N. K. Chandar, & R. Jayavel; **Journal of Physics and Chemistry of Solids**, 73(9), 1164-1169, **(2012)**.

243. L. Yue, & X. M. Zhang; **Journal of Alloys and Compounds**, 475(1-2), 702-705, **(2012)**.

244. K. Kumari, R. N. Aljawfi, A. Vij, K. H. Chae, M. Hashim, P. A. Alvi & S. Kumar; **Journal of Materials Science: Materials in Electronics**, 30, 4562-4571, **(2019)**.

245. N. K. Sahoo, S. Thakur & R. B. Tokas; **Journal of Physics D: Applied Physics**, 39(12), 2571, **(2006)**.

246. R. R. Reddy, Y. N. Ahammed, K. R. Gopal & D. V. Raghura; **Optical Materials**, 10(2), 95-100, **(1998)**.

247. R. R. Reddy & Y. N. Ahammed; **Infrared Physics & Technology**, 36(5), 825-830, **(1995)**.

248. A. Kumar, S. Babu, A. S. Karakoti, A. Schulte & S. Seal; **Langmuir**, 25(18), 10998-11007, **(2009)**.

249. B. Soni, S. Makkar & S. Biswas; **Journal of Alloys and Compounds,** 879, 160149, **(2021)**.

250. Z. Liu, B. Guo, L. Hong & H. Jiang; **Journal of Physics and Chemistry of Solids,** 66(1), 161-167, **(2005)**

251. S. Gu, Y. Chen, X. Yuan, H. Wang, X. Chen, Y. Liu & G. Zeng; **RSC Advances**, 5(97), 79556-79564, **(2015)**.

252. M. Elayaraja, I. K. Punithavathy, M. Jothibas, A. Muthuvel & S. J. Jeyakumar **Nanotechnology for Environmental Engineering,** 5, 1-10, **(2020)**.

253. T. Zhai, X. Fang, Y. Bando, Q. Liao, X. Xu, H. Zeng, & D. Golberg; **ACS Nano**, 3(4), 949-959, **(2009)**.

254. M. Y. Ge, H. Wang, E. Z. Liu, J. F. Liu, J. Z. Jiang, Y. K. Li & H. Y. Li, **Applied Physics Letters**, 93(6), **(2008)**.

255. K. Tarui, T. Oomori, Y. Ito & T. Yamamoto; **Physica B: Condensed Matter,** 619, 413158, **(2021)**.

256. A. A. Birajdar, S. E. Shirsath, R. H. Kadam, M. L. Mane, D. R. Mane & A. R. Shitre; **Journal of Applied Physics**, 112, (5), **(2012)**.

257. C. C. Chauhan, A. R. Kagdi, R. B. Jotania, A. Upadhyay, C. S. Sandhu, S. E. Shirsath & S. S. Meena; **Cramics International**, 44(15), 17812-17823 **(2018)**.

258. S. Balsure, V. More, S. Kadam, R. Kadam & A. Kadam; **Engineered Science**, 21(5), 774, **(2022)**.

259. A. Hirohata, K. Yamada, Y. Nakatani, I. L. Prejbeanu, B. Diény, P. Pirro & B. Hillebrands; **Journal of Magnetism and Magnetic Materials,** 509, 166711, **(2020)**.

260. R. C. Kambale, P. A. Shaikh, S. S. Kamble & Y. D. Kolekar; **Journal of Alloys and Compounds,** 478(1-2), 599-603, **(2009)**.

261. S. Soni, K. Kabra, J. Sahu, D. P. Dubey, B. Dalela, P. A. Alvi & S. Dalela; **Journal of Magnetism and Magnetic Materials**, 596, 171965, **(2024)**.

Published Research Papers

LIST OF PUBLICATIONS

Published in international Journal:

1. **Supercapacitor performance, electronic structure and ferromagnetic properties of TM and RE cations of co-doped (Fe, Yb) CeO_2 nanoparticles;** N. S. Leel, **M. Kiran**, P. A. Alvi, B. Dalela, S. Kumar, A. Sharma & S. Dalela; **Applied Surface Science,** 697, (2025), 162934.

2. **Enhanced electrochemical properties for better stability of supercapacitance and electronic structure characteristics of Ag-doped CeO_2 nanoparticles; M. Kiran**, N. S. Leel, P. A. Alvi, B. Dalela, S. Kumar, N. Jakhar & S. Dalela; **Nano-Structures & Nano-Objects,** 41, (2025), 101418.

3. **Ferromagnetic interactions and luminescence in Dy-doped CeO_2 nanoparticles with regard of defects and electronic structure;** M. Dave, N. S. Leel, **M. Kiran**, P. A. Alvi, B. Dalela, S. Kumar & S. Dalela; **Journal of Materials Science: Materials in Electronics,** 36(10), (2025), 1-19.

4. **Effect of oxygen vacancies on enhancing the photo-catalytic activity, photo-luminescence and electronic structure properties of nano-structured Y-doped CeO_2; M. Kiran**, N. S. Leel, M. K. Kumawat, B. Dalela, P. A. Alvi, S. Kumar & S. Dalela; **Journal of Physics and Chemistry of Solids,** 197, (2025), 112438.

5. **Efficient white light-emitting Ag-doped CeO_2 nanoparticles exhibiting colour temperature Tunability and high colour rendering; M. Kiran**, N. S. Leel, B. Dalela, M. A. Khan, A. Bhargava, D. Lovevanshi& S. Dalela; Journal of Electronic Materials, 53(9), (2024), 4969-4981.

6. **Oxygen Vacancies mediated changes in Ferromagnetic, Optical, Photoluminescent and Electronic Structure properties of Ho-doped CeO_2 nanoparticles**; N. S. Leel, **M. Kiran**, P.A. Alvi, B. Dalela, S. Kumar and S. Dalela; **Ceramics International, Elsevier Publication,** 50(5), (2024), 8448-8462.

7. **Oxygen Vacancy driven Luminescence, Ferromagnetic and Electronic Structure Properties of Eu doped CeO_2 nanoparticles;** N. S. Leel, **M. Kiran,** M. K. Kumawat, P.A. Alvi, V. S. Vats, D. Patidar, B. Dalela, Shalendra Kumar and S. Dalela; **Journal of Luminescence, Elsevier Publication,** 263, (2023), 119981.

Nano-Structures & Nano-Objects 41 (2025) 101418

Contents lists available at ScienceDirect

Nano-Structures & Nano-Objects

journal homepage: www.elsevier.com/locate/nanoso

Enhanced electrochemical properties for better stability of supercapacitance and electronic structure characteristics of Ag-doped CeO_2 nanoparticles

M. Kiran [a], N.S. Leel [a], P.A. Alvi [b], B. Dalela [c], Shalendra Kumar [d], N. Jakhar [e], A. Sharma [f], S. Dalela [a,*]

[a] Department of Pure & Applied Physics, University of Kota, Kota 324005, India
[b] Department of Physics, Banasthali Vidyapith, Banasthali 304022, India
[c] Department of Physics, Govt Khaitan Polytechnic College, Jaipur, Rajasthan 302017, India
[d] Department of Physics, School of Engineering, University of Petroleum & Energy Studies, Dehradun 248007, India
[e] Department of Physics, University of Rajasthan Jaipur, Rajasthan 302004, India
[f] Department of Chemistry, PW Institute, Kota, India

ARTICLE INFO

Keywords:
Ag doped CeO_2 nanomaterials
XRD
XPS
Oxygen vacancies
Super capacitance
Electro-chemical properties

ABSTRACT

The structure and functional properties of materials can be significantly influenced by the synthesis of nanoparticles. This manuscript presents undoped CeO_2 and Ag doped CeO_2 nanoparticles (NPs) with different concentration of Ag (x = 0.03, 0.05 and 0.07), prepared using a simple coprecipitation route of synthesis. The prepared NPs have been characterized via X-ray diffraction (XRD), UV-Vis NIR spectroscopy, photoluminescence (PL), X-ray photoelectron spectroscopy (XPS) and electrochemical analysis. The XRD measurement infers the improvement in the crystalline nature with Ag-doping and crystallite size between 13 and 9 nm. The absorption spectra reflect the red shifting of the absorption peaks along with the narrowing of band gap with rise in the Ag concentration. To ascertain the defects and excitation wavelength, PL measurement has been performed. High color rendering index (CRI) of the prepared samples showed good luminescence with white light emission. The development of oxygen vacancies (V_o) upon Ag doping is further confirmed by XPS measurement. In addition, the XPS measurements revealed the charged oxygen vacancies as well as the valence states of Ce with 3+ and 4+ , Ag with 1+ , and O with 2–. The CV test verified that in 2 M KOH electrolyte solution, the 5 % Ag-doped CeO_2 NPs had the maximum specific capacitance (C_{SP}) value of 363.44 F/g at scan rate of 10 mV/s the best cycle stability (retaining 93.90 % after 2100 cycles). It was discovered that the 5 % Ag-doped CeO_2 NPs had an energy density of 125.08 Wh/kg and a power density of 652.48 W/kg. An excellent super capacitive performance of Ag doping in CeO_2 could be used as a unique electrode material to develop high-efficiency and durable energy storage devices and resulted in the enrichment of electrochemical properties of these nanomaterials. Cyclic voltammetry (CV) results are consistent with electrochemical impedance spectroscopy, indicating good voltammetry and impedance spectroscopy performance of Ag-doped CeO_2 NPs. These nano-materials are also better alternatives for solid state electrolyte for fuel cells, UV blockers, photo-catalyst and many other applications.

1. Introduction

In this modern world, the need for electrical power is rising so fast as the capacity to deliver a significant amount of electric power quickly becomes crucial with the rise of electrically powered devices and electric motors. Similarly, there is a growing trend in automobiles to recover power when braking. This necessitates the use of storage devices with rapid charging times and a big capacity to hold the energy generated during braking. These prerequisites bring to the imminence of supercapacitor. The supercapacitor are placed somewhere in between storage batteries and commercial capacitors [1]. An additional draw of supercapacitor is their extended cycle life and environmentally friendly design. The electric double layer capacitor (EDLC) used in supercapacitor was initially made of carbonaceous materials, which offer low

* Corresponding author.
E-mail address: sdphysics@rediffmail.com (S. Dalela).

https://doi.org/10.1016/j.nanoso.2024.101418
Received 1 September 2024; Received in revised form 12 November 2024; Accepted 26 November 2024
Available online 6 December 2024

Journal of Physics and Chemistry of Solids 197 (2025) 112438

Contents lists available at ScienceDirect

Journal of Physics and Chemistry of Solids

journal homepage: www.elsevier.com/locate/jpcs

Effect of oxygen vacancies on enhancing the photo-catalytic activity, photo-luminescence and electronic structure properties of nanostructured Y-doped CeO_2

M. Kiran [a], N.S. Leel [a], M.K. Kumawat [b], B. Dalela [c], P.A. Alvi [d], Shalendra Kumar [e], A. Sharma [f], S. Dalela [a,*]

[a] Department of Pure & Applied Physics, University of Kota, Kota, 324005, India
[b] School of Physical Sciences, Jawaharlal Nehru University, New Delhi, 110067, India
[c] Department of Physics, Govt Khaitan Polytechnic College, Jaipur, 302017, Rajasthan, India
[d] Department of Physics, Banasthali Vidyapith, Banasthali, 304022, India
[e] Department of Physics, School of Engineering, University of Petroleum & Energy Studies, Dehradun, 248007, India
[f] Department of Chemistry, PW Institute, Kota, India

ARTICLE INFO

Keywords:
Y-doped CeO_2 nanoparticles
Defects and oxygen vacancies
Photoluminescence
HRTEM
XPS
Photo-catalyst

ABSTRACT

The exceptional characteristics of CeO_2 and $Ce_{1-x}Y_xO_2$ (x = 0.03, 0.05 and 0.07) nanoparticles were reported in the manuscript supporting that Y^{3+}replaces Ce^{3+}/Ce^{4+}leads to oxygen vacancies formation. The results of XRD measurements revealed FCC structure of decreased crystallite size of CeO_2 with improved crystallinity. To investigate the surface morphology, HRTEM and SAED patterns were performed. EDX analyses were undertaken to discuss the elemental and compositional characteristics. The absorption spectra using UV–Vis–NIR spectroscopy were analyzed and red shifted absorbance was found to enhance with decreasing band gap values for increased Y doping. The Photoluminescence spectra depicted various emissions representing the development of various defects and oxygen vacancy with incorporation of Y content in the lattice with CCT values below 4000 K to be classified as warm yellow light for indoor applications. The development of oxygen vacancies in the CeO_2 lattice was further supported by XPS measurements for core levels Ce 3d, O 1s and Y 3d. Furthermore, the XPS measurements also reported the valence states of elements, Ce with 3+ and 4+, Y with 3+ and O with 2- along with charged oxygen vacancies. The photo-catalytic analysis revealed that Y-doped CeO_2 nanoparticles show better degradation using a variety of characterization. A degradation mechanism that illustrates the impact of oxygen vacancies created by Y-doping on the photo-degradation process has been proposed. The novelty of Y-doped CeO_2 nanoparticles stems from their improved photo-catalytic activities, which are linked to structural changes and the formation of oxygen vacancies. This doping considerably affects the electrical structure, resulting in better light absorption and less electron-hole recombination. The detailed outcomes of present study suggested the use of Y-doped CeO_2 nanoparticles in optoelectronics, spintronics devices and photo-catalyst applications.

1. Introduction

Recently, there has been a huge surge in attention in ceria-based nanoparticles from both basic scientific and business perspectives [1]. Researchers are also working eagerly for developing photo-catalytic materials that possess lower band gap. Some metal oxide semiconductors materials show poor response under visible light but exert better photo-catalytic activity under UV radiations such as CeO_2 which can be utilized as a UV filter in cosmetics, sunscreen, and glass polishing agents [2]. Its superior performance attributes to high oxygen-storage capacity. Because of prominent high capacity to store oxygen (OSC) of ceria, numerous investigations have shown that the material can be utilized as a supporting agent in variety of catalysts [3]. It is a reducible oxide, and at high temperatures, ceria can develop oxygen vacancies (V_o) [4]. For every V_o, this mechanism fallouts in the reduction of $Ce^{4+} \rightarrow Ce^{3+}$cation; depending on the circumstances, this reduction may be reversible [5,6].

* Corresponding author.
E-mail address: sdalela@uok.ac.in (S. Dalela).

https://doi.org/10.1016/j.jpcs.2024.112438
Received 6 September 2024; Received in revised form 18 October 2024; Accepted 3 November 2024
Available online 5 November 2024

Journal of Electronic Materials
https://doi.org/10.1007/s11664-024-11057-1

28TH INTERNATIONAL CONFERENCE ON NUCLEAR TRACKS AND RADIATION MEASUREMENTS

Efficient White Light-Emitting Ag-doped CeO_2 Nanoparticles Exhibiting Color Temperature Tunability and High Color Rendering

M. Kiran[1] · N. S. Leel[1] · B. Dalela[2] · Mohd. A. Khan[1] · A. Bhargava[1] · D. Lovevanshi[1] · P. A. Alvi[3] · Shalendra Kumar[4] · S. Dalela[1]

Received: 3 December 2023 / Accepted: 18 March 2024

Abstract
The present manuscript reports the synthesis of undoped CeO_2 and $Ce_{1-x}Ag_xO_2$ ($x = 0.03$, 0.05, and 0.07) nanoparticles using a microwave-assisted co-precipitation route to understand the Ag doping effect in CeO_2 nanoparticles. The structural and optical properties of these nanoparticles were investigated using x-ray diffraction, UV–Vis–NIR, and PL spectroscopy. The XRD result confirmed the formation of cubic fluorite structures with undoped and Ag-doped CeO_2 nanoparticles. The crystallite size of Ag-doped CeO_2 nanoparticles was observed within the range of 26–47 nm. The absorption peak was observed using UV–Vis–NIR spectroscopy and obtained at below 400 nm, indicating a blue shift with the incorporation of Ag^+ ions in the CeO_2 nanolattice, and the causes are explained in terms of the BM effect and electronic transitions. The PL measurements were taken to determine the defects and excitation wavelength. The prepared samples depicted good luminescence properties with a high value color rendering index (CRI). The results demonstrated that Ag-doped CeO_2 nanoparticles can be used for white light emission, since the structural and optical properties of semiconductors were enhanced upon doping with elements such as Ag. Therefore, these nanoparticles may act as promising candidates for various applications such as UV-absorption, photocatalysis, light-emitting diodes, luminescence, and optoelectronics.

Keywords Ag-doped CeO_2 nanoparticles · absorption spectroscopy · oxygen vacancies and defects · blue shifting · photoluminescence · CRI · white light emission

Introduction

Nanocrystal-based optoelectronic devices have been successful in the area of device research. their emitters have been proven to have wide application, especially in white light sources. Generally, light-emitting diodes (LEDs) are more commonly preferred owing to their good advantages over conventional lamps.[1] Since the light industry, including factories, offices, laboratories, streets, workshops, and public places, require more illumination with white light for performing tasks such as writing, reading, and detection, white LEDs are thus inevitable at such places. The color field of LEDs is characterized as "warm white" (< 3300 K), "neutral white" (3300–5300 K), and "cool light" also known as daylight (> 5300 K), based on the IEC standard. Lamps with a correlated color temperature (CCT) (> 4000 K) or more with the color neutral white are recommended for illumination in professional applications.[2] The main purpose of this manuscript is to lay out the structural, optical, and photoluminescence characteristics of Ag-doped CeO_2 nanoparticles. Cerium oxide (ceria or CeO_2), a rare-earth oxide semiconductor, which has recently attracted much interest due to its exceptional unique features and possible uses, which include solid oxide fuels and superior electrocatalytic performance.[3] The transition of Ce from a Ce^{4+} ion to a Ce^{3+} ion allows it to be widely used for oxidation reactions

✉ S. Dalela
sdalela@uok.ac.in

[1] Department of Pure and Applied Physics, University of Kota, Kota, Rajasthan 324005, India

[2] Department of Physics, Government Khetan Polytechnic College, Jaipur 302017, India

[3] Department of Physics, Banasthali Vidyapith, Banasthali, Rajasthan 304022, India

[4] Department of Physics, University of Petroleum and Energy Studies, Dehradun 248007, India

Published online: 16 April 2024

Conference/Workshop and Seminars Attended

CONFERENCES ATTENDED

1. **International Workshop On "Research Methodology**" Organized by Directorate of Research, University of Kota, Kota, India, (January, 22, 2020).

2. **Orientation Training Workshop On "Daily Science News and Features for Print Version of VaigyanikDrishtikon for Promoting Science Literacy**" Organized by University of Kota, Kota (Rajasthan), (May, 18-20, 2022).

3. **National Conference on "Recent Advances in Science and Technology" (NCRAST-2023)**, Organized by Department of Chemistry Government College Kota, Kota (October, 6-7, 2023).

4. **28th International Conference on "Nuclear Tracks and Radiation Measurements" (28th -ICNTRM-2023)**, Organized by Gurugram University, Sector-51 Gurugram, Haryana, India, (November, 6-10, 2023).

Directorate of Research

University of Kota, Kota

(A State Govt. University Recognized under 12(F) & 12(B) of UGC)

Presents this

CERTIFICATE OF PARTICIPATION

KIRAN MAHAVAR

For his/ her active and invaluable participation during the conduct of One day International Workshop on **"Research Methodology"** held on **22 January 2020** at Directorate of Research, University of Kota, Kota,(INDIA).

Dr. Vipul Sharma
Deputy Registrar (Research)

Dr. O.P. Rishi
Director (Research)

Daily Science News and Features for Digital and Print Versions of Vaigyanik Drishtikon for Promoting Science Literacy

Orientation Training Workshop

NCSTC, DST Govt. of India

In association with

Vaigyanik Drishtikon Society & University of Kota, Kota (Rajasthan)

18 - 20 May, 2022

Certificate

This is certified that Dr./Mr./Ms. ..Kiran Mahavar..... actively participated in 3 days Orientation Training Workshop on '*Daily Science News and Features for Digital and Print Versions of Vaigyanik Drishtikon for Promoting Science Literacy*' at **University of Kota, Kota (Rajasthan).**

Prof. Reena Dadhich	**Dr. Pamposh Kumar**	**Tarun Kumar Jain**
Dean, Faculty of Science	Scientist 'F' & Director	Editor
University of Kota, Kota (Rajasthan)	NCSTC, DST Govt. of India	Vaigyanik Drishtikon

NATIONAL CONFERENCE
ON

RECENT ADVANCES IN SCIENCE AND TECHNOLOGY

(06-07, OCT 2023)
ORGANIZED BY

NCRAST 2023

DEPARTMENT OF CHEMISTRY
GOVERNMENT COLLEGE KOTA
(NAAC 'A' ACCREDITED INSTITUTE)

CERTIFICATE

This is to certify that Prof / Dr. / Mr. / Ms. Kiran M from University of Kota, Kota, has participated / presented a paper / poster entitled Structural and nanoparticles in the two day National Conference, organised by Department of Chemistry, Government College Kota(Raj) on 6th & 7th October 2023.

Prof. MONIKA DAKSHENE	**Prof. RENUKA JAIN**	**Prof. ARUN KUMAR**
CONVENOR	ORGANISING SECRETARY	PAT RON & PRINCIPAL
HEAD, DEPARTMENT OF CHEMISTRY	*DEPARTMENT OF CHEMISTRY*	*GOVERNMENT COLLEGE KOTA*

28th ICNTRM-2023

INTS

28th International Conference on Nuclear Tracks and Radiation Measurements

Certificate of Participation

This certificate is presented to Prof./Dr./Mr./Ms. Kiran Mahavar of Univ. of Kota

for scientific contribution as a Plenary Talk/Invited Talk/Oral Presentation/Poster Presentation/Technical Session Chairperson entitled, "Efficient white light Emitting Ag doped CeO_2 nanoparticles exhibiting colour temperature tunability and high colour rendering", in the 28th International Conference on Nuclear Tracks and Radiation Measurements held at Gurugram University (A State Govt. University Established Under Haryana Act 17 of 2017), Sector 51, Gurugram-122003, India, during 6-10 November, 2023.

Dr. Pratap Singh
Convenor

Prof. Rajesh Kumar
Conference Chair

Dr. Krishan Kant
Conference Chair

Prof. R. P. Chauhan
Conference President